Toward Atomic – Based Understanding of Some Reactive and Non-Reactive Surfaces

A Thesis submitted for the degree of

Doctor of Philosophy in Chemical Engineering

Niveen W Assaf

B.Sc. Chemical Engineering

School of Engineering and Information Technology,

Murdoch University, Western Australia

April, 2018

Statement of originality

I declare that this thesis is my own account of my research and contains as its main content work which has not previously been submitted for a degree at any tertiary education institution. The thesis contains no material previously published or written by another person, except where due reference has been made in text.

Niveen W Assaf

April, 2018

Supervisory statement

We, the undersigned, attest that Higher Research Degree candidate, Niveen W Assaf, has devised, synthesised and carried out the computational quantum-mechanical calculations, experimental work, result analysis, and writing in all papers included in this thesis. Dr Mohammednoor Altarawneh, Professor Bogdan Z Dlugogorski and Professor Marian Radny provided the necessary advice, project direction and assisted with the editing of the papers, consistent with normal supervisors-candidate relations.

Dr Mohammednoor Altarawneh

April, 2018

Professor Bogdan Z Dlugogorski

April, 2018

Professor Marian Radny

April, 2018

Dedications

I dedicate this thesis to

my parents, my husband and my lovely daughter

for their unending support and unfailing love.

LOVE you.

Acknowledgments

I am greatly indebted to my principal supervisor **Dr Mohammednoor Altarawneh** and **my** co-supervisors, **Professor Bogdan Dlugogorski** and **Professor Marian Radny** (University of Newcastle, Australia), for their insightful guidance, long hours of fruitful discussions, valuable inputs, continuous support, and encouragement throughout the time of my study.

I greatly acknowledge **Murdoch University**, Australia, for the award of a postgraduate research scholarship which provided a valuable financial support for this research. All computational work in the thesis was carried out at **The National Computational Infrastructure** (NCI) in Canberra, Australia and **Pawsey Supercomputing** Centre in Perth The project has been supported by the **Australian Research Council** (ARC).

I express my sincere gratitude to **Dr Ibrahim Suleiman** (Taibah University), **Dr Marco De Le Pierre** (Curtin University), **Mr Kris Parker** (Murdoch University) as well as **Dr Jakub Skut** and **Dr Juita (**staffs of the Fire Safety and Combustion Kinetics Research Laboratory) for their professional and technical assistance. My sincere thanks to my fellow student colleagues, **Ibukun Oluwoye**, **Zhe Zeng**, **Arif Abdullah, Kamal Siddique**, **Oday Ahmed**, **Rafiq Mohammed, Jomana Al-Nu'airat, Nassim Zeinali**, **Rukshima Dabare Sidra Jabeen**, **Sana Zahid, Anam Saeed** as well as all my **friends** on and off campus with whom I have shared my journey over these years. My appreciation to all members at the **School of Engineering and Information Technology** for their assistance and cooperation.

I owe a debt of gratitude to a very special person, my greatest treasure, my partner, and my lover, my husband, **AL-Bara'a** for his continued and unfailing love, support, encouragement, prayers, and understanding throughout the realization of this thesis, without which this completion would not be possible. I have been so blessed with you; to stand by me and hold my hand through the hard times and the good times of this journey. Thank you, Bara'a; I love you beyond any words that could be written on paper. I greatly appreciate my baby, my little girl **Wateen**. You have given me the extra strength and motivation to achieve success. Your infectious smile made me happier and made my days a lot more bearable. Thank you, Wateen. I am beyond grateful and blessed to have such lovely and caring family. Words would never express how thankful I am to both of you.

At this moment of accomplishment, I am thankful to my family for their unending support and prayers. **My Father**, you have always been my greatest mentor, my motivation and my deepest root, you gave me my bravery, my strength, and my morality. Thank you, daddy. Thank you for your love. Thank you for the memories. Your spirit will forever dwell in my heart. I am eternally grateful for everything. **My Mum**, my greatest teacher of giving and receiving. I cannot say thank you enough for the patience, devotion, unconditional love, support, blessing, and everything that you have given me throughout my entire life. Mum and Dad, I could not do it without you.

My warm thanks to my brothers and sisters; **Khaled**, **Qais**, **Abdallah**, **Aseel** and **Esra'a** for their love and support.

Thank you all…

Abstract

The thesis is composed of two broad themed sections with the underlying aim of understanding on a precise atomic basis, the electronic and structural factors governing the reactive and non-reactive surfaces of two metal oxides belonging to the same group in the periodic table; boron (B) and aluminium (Al). Using accurate density functional theory (DFT) computations, we first elucidate the initial reaction steps of the surface oxidation of elemental boron into its respective oxide; boron trioxide (B_2O_3). The highly exoergic reaction obtained for the dissociative adsorption of molecular oxygen over the boron surface coincides with the widely used boron oxidation reaction as a secondary energy source in rockets. The relatively large activation energy for the O-O dissociation step marks the non-spontaneity of elemental boron oxidation at room temperature. Having established routes for the formation of B_2O_3-like precursors, we then investigate the relative stability of four low-index surfaces of the low-pressure B_2O_3 phase; namely the B_2O_3-I configuration. We demonstrate that none of the investigated low-index surfaces have dangling bonds, which reasonably relates to the experimentally observed low reactivity of this compound. The most stable surface terminations of B_2O_3 orientations entail tetrahedral BO_4 units. Such termination incurs a lower surface energy than orientations that consist of only triangular BO_3 units. Electronic and structural factors provide atomic-base elucidation of the observed inertness of B_2O_3.

Combined experimental techniques (i.e. diffuse reflectance infrared spectroscopy) and DFT simulation are used to answer some of the most intriguing questions pertinent to factors underpinning the well-documented catalytic inhibition by B_2O_3 and its hygroscopic behaviour. We investigate the adsorption and dissociation mechanisms of two hydrogen chalcogenides,

namely water (H_2O) and hydrogen sulfide (H_2S) molecules over B_2O_3-I (101) surfaces. We show that the diboron trioxide surface exhibits high physiochemical reactivity towards water molecules. The Lewis acid properties of B_2O_3-I lead to the formation of a molecular adsorption state (rather than dissociative adsorption) of the H_2S molecule via the acceptance of an electron pair into the low-energy orbital of the boron valence shell. While acting as water scavenger to generate dissociated radicals, B_2O_3 exhibits an inhibitor characteristic towards the dissociation of H_2S molecules, representing an ideal reactor wall coating in such systems.

Alumina have been widely utilised as independent catalysts or as support materials for other catalysts. From an environmental perspective, alumina nanoclusters dispersed on surfaces of particulate matter PM_{12} generated from various combustion processes play a critical role in the synthesis of environmental persistent free radicals (EPFR). Of particular importance are phenoxy-type EPFR that often acts as building blocks for the formation of notorious pollutants. Herein, we provide a comprehensive thermo-mechanistic account of alumina-surface mediated formation of phenoxy-type EPFR on different structural alumina models encompassing the following surfaces: dehydrated alumina surface, fully hydrated alumina surface, surfaces with different hydration coverage, and silicon-alumina doped surface. We show that fission of the phenol's hydroxyl bond over dehydrated alumina systematically incurs lower energy barriers in reference to the hydrated surfaces. The catalytic activity of the alumina surface in producing the phenoxy/phenolate species reversibly correlates with the degree of hydroxyl coverage. Furthermore, we clarify the effect doping on the catalytic activity of alumina. The activation energy barrier required to form phenoxy moiety on Si-substituted Al_2O_3 (0001) surface is ~40% lower than that of analogous barriers encountered over undoped dehydrated alumina surface. Overall, all considered models of alumina configurations are shown to produce adsorbed

phenolate; however, desorption of the latter into the gas phase requires a rather sizable energy. Thus, the fate of adsorbed phenolate is most likely to be dictated by decomposition affording carboneous layer or self-decomposition into other stable molecules.

List of Publications

Journal articles

1. **Assaf, N. W.**; Altarawneh, M. K.; Radny, M.W.; Jiang, Z. T.; Dlugogorski, B. Z.; Interaction of oxygen with α-rhombohedral boron (001) surface, *J. Phys. Chem. C*, 120 (2016) 5968-5979.

   2016 impact factor: 4.536

2. **Assaf, N. W.**; Altarawneh, M.; Oluwoye, I.; Radny, M.; Lomnicki, S. M.; Dlugogorski, B. Z.; Formation of environmentally persistent free radicals on α-Al_2O_3, *Environ. Sci. Technol.*, 50 (2016) 11094-11102.

   2016 impact factor: 6.198

3. **Assaf, N. W.**; La Pierre, M. De; Altarawneh, M. K.; Radny, M. W.; Jiang, Z. T.; Dlugogorski, B. Z.; Structure, stability, and (non) reactivity of the low-index surfaces of crystalline B_2O_3–I, *J. Phys. Chem. C*, 121 (2017) 11346–11354.

   2016 impact factor: 4.536

4. **Assaf, N. W.**; Altarawneh, M.; Radny, M.; Al-Nu'airat, J.; Dlu**gogor**ski, B. Z.; Formation of environmentally-persistent free radicals (EPFR) on α-Al_2O_3 clusters, **RSC Adv. 7 (2017) 52672-526683.**

   2016 impact factor: 3.108

5. Mosallanejad, S.; Dlugogorski, B. Z.; Kennedy, E. M.; Stockenhuber, M.; Lomnicki, S. M.; **Assaf, N. W.**; Altarawneh, M.; Formation of PCDD/Fs in oxidation of 2-chlorophenol on neat silica surface, *Environ. Sci. Technol.*, 50 (2016) 412-1418.
   2016 imact factor: 6.198

Conferences

1. **Assaf, N. W.**; Altarawneh, M.; Radny, M. Dlugogorski, B. Z.; "Formation of Environmentally-Persistent Free Radicals (EPFR) on α-Al_2O_3. Different hydroxyl coverage." 9th Conference of the Asian Consortium on Computational Materials Science (ACCMS-9), 2017, Kuala Lumpur, Malaysia.

2. **Assaf, N. W.**; Altarawneh, M.; Radny, M.; Dlugogorski, B. Z.; "Formation of Environmentally-Persistent Free Radicals (EPFR) on α-Al_2O_3. A hydrated surface." (ASCC16), 2016, Perth, Australia.

Table of Contents

CHAPTER 5

Structure, Stability and (non) Reactivity of the Low-Index Surfaces of Crystalline B_2O_3-I

CHAPTER 6

Probing the Chemical Reactivity of the B_2O_3 -I (101) Surface: Interaction with H_2O and H_2S

CHAPTER 7

Formation of Environmentally-Persistent Free Radicals (EPFR) on α-Al_2O_3

CHAPTER 8

Formation of Phenoxy-Type EPFR over Hydrated Pure Alumina and Si-alumina Surfaces

List of abbreviations

The following table defines all acronyms used throughout the thesis as well as the page on which each one is defined or first used.

Abbreviation	Meaning	Page
TEM	Transmission electron microscopy	19
STM	Tunnelling microscope	19
EPFR	Environmental persistent free radicals	22
B_2O_3	Diboron trioxide	22
PCDD/Fs	Polychlorinated dibenzo-*p*-dioxin and polychlorinated dibenzofurans	23
DFT	Density function theory	25
IC	Integrated circuit packages	52
TBCs	Thermal barrier coatings	52
α-Al_2O_3	Corundum	53
DOS	Density of states	59
UVB	Upper valence band	59
CB	Conduction band	59
LVB	Lower valence band	60
LDA	Local density approximation	62
δH	Chemical shift changes	63
T_1	Spin-lattice relaxation	63
TPD	Temperature programed desorption	63
IR	Infrared spectroscopy	70
DFT-MD	Density functional theory-based molecular dynamics	74

XPS	X-ray photoelectronic spectroscopy	76
LITD	Laser-induced thermal desorption	76
FT	Fourier transform	77
$PM_{2.5}$	Airborne fine particles	80
ROS	Reactive oxygen species	80
PCDD	Polychlorinated dibenzodioxine	83
PCDF	Polychlorinated dibenzofurans	83
EPR	Electron paramagnetic resonance	84
XANES	X-ray absorption	84
L-H	Langmuir-Hinshelwood mechanism	84
E-R	Eley-Rideal	84
EELS	Energy loss spectrometry	87
2-MCP	2-monochlorophenol precursor	87
2-CP	2-chlorophenol	89
GGA	Generalised gradient approximation	130
LST/QST	Linear synchronous and Quadratic synchronous transit approaches	240
PBE	Perdew-Burke-Ernzerhof functional	150
DNP	Double-polarised numeric basis set	150
$E_{\text{DFT-D}}$	Total corrected energy	155
E_{disp}	Energy dispersion	155

$E_{\text{KS-DFT}}$	Kohn-Sham energy	155
E^{coh}	Cohesive energy	156
E_{b}	Binding energies	156
$E_{\text{b}}^{\text{subst}}$	Substitutional adsorption	157
$\gamma_{\text{ads}}\left(T,P\right)$	Gibbs free energy at a given temperature and pressure	157
μ_{O}	Chemical potential of oxygen	157
v-B_2O_3.	Vitreous (amorphous) form of diboron trioxid	194
γ	Specific surface energy	197
PDOS	Projected density of states	211
HBO_2	metaboric	222
SBZ	Surface Brillouin zones	224
TST	Transition state theory	218
DRIFT	Diffuse reflectance infrared fourier transform (DRIFT) spectroscopy	226
MWI	Municipal waste incinerators	262
TNT	Trinitrotoluene	297
PFR	Plug flow reactor	344
T_{90}%	Temperature of $_{90}$% destruction	345

CHAPTER1

Introduction and Overview

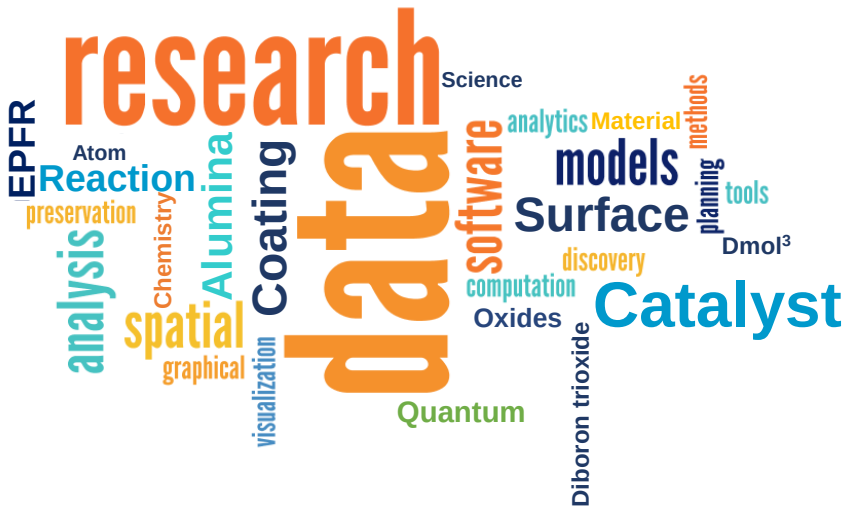

1.1 Introduction

Modelling of molecular-solid interactions offers a valuable insight into the understanding of heterogeneous catalysis/inhibition. Unprecedented advancements in theoretical frameworks, software, and hardware over approximately the last two decades have enabled the description of chemical systems encompassing solid-gas reactions with a profound accuracy in reference to experimental measurements.[1-3] Atomic-based understanding of these interactions is of fundamental importance to optimise pertinent chemical phenomena by either enhancing or eliminating catalytic reactivity, depending on the specific application.

A wide variety of experimental techniques has been instrumental in our understanding of surface science in general, and catalytic/inhibiting systems in particular. These techniques have enabled the control[4], imaging[5], placement[6], and manipulation[7] of individual adsorbate (i.e. atoms and molecules) on surfaces. Common examples include electron microscopy techniques (i.e. transmission electron microscopy (TEM)[8]), surface probing techniques (i.e. tunnelling microscope (STM)[9] and/or noncontact atomic force microscopy (AFM)[9-10]), and spectroscopy techniques (i.e. UPS, TDS, RAIRS, etc.).[11-15] Figure 1.1 shows selected surface science techniques and the corresponding information attained from them.

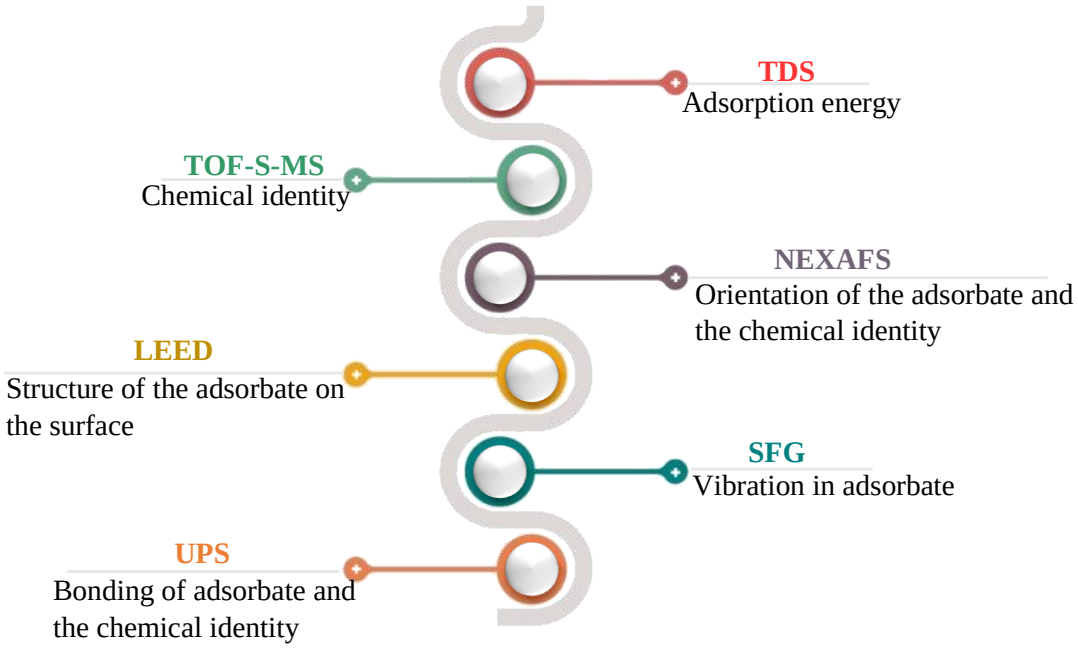

Figure 1.1. Selected surface science techniques and the corresponding information attained from them.[15]

Along the same line of inquiry, theoretical simulation techniques, based on computational quantum-mechanical calculations, are at the heart of our understanding of sophisticated systems in an Ångström spatial domain. Performing theoretical modelling calculations in conjunction with experiments has now become a common approach in both academia and industry (i.e. R& D departments).[16-18] Substitutional progress has been made in terms of computational experiments, which are fast becoming a key requirement. Figure 1.2 displays the selected apparent advantages of applying computational techniques.

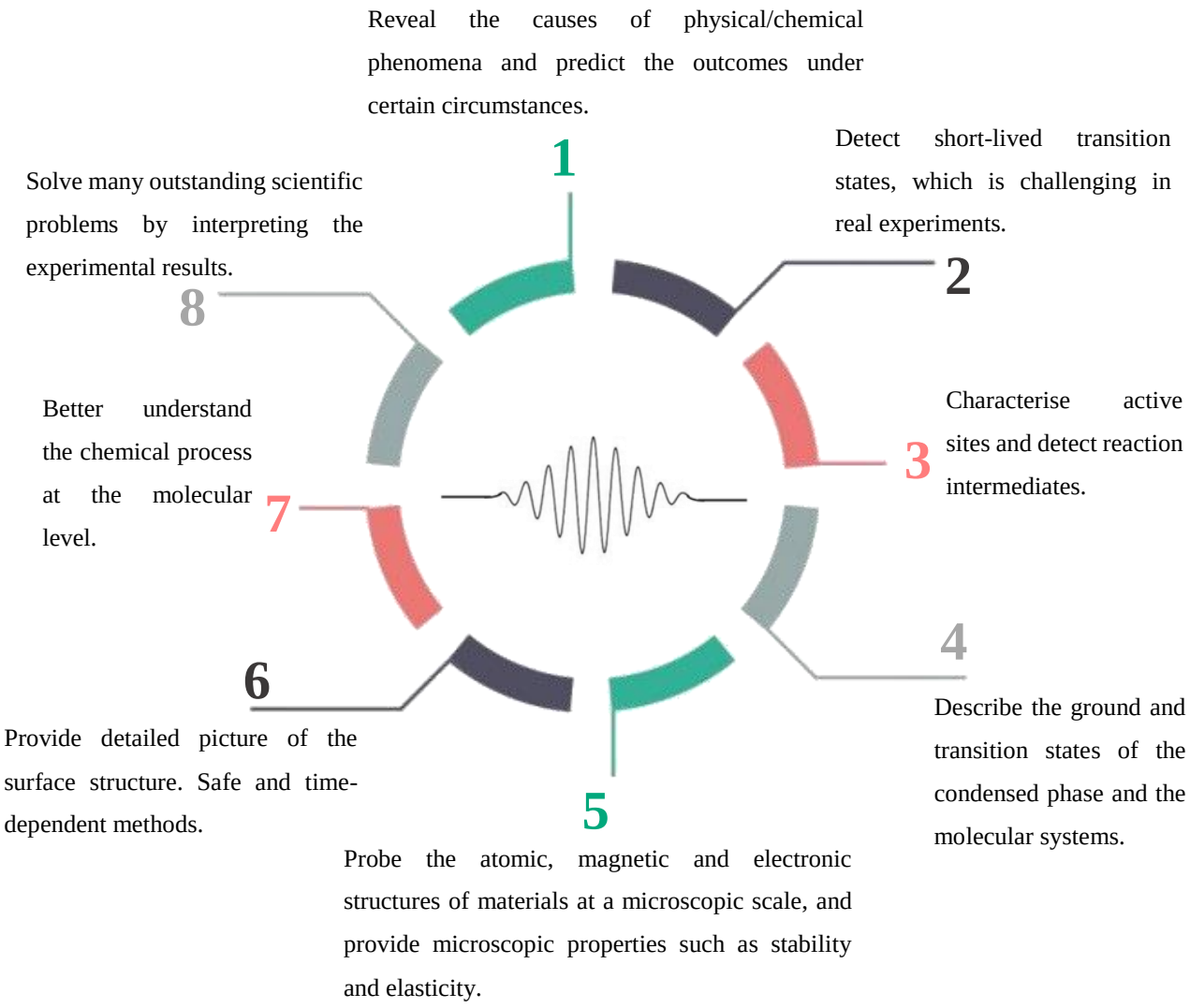

Figure 1.2. Selected advantages of applying computational techniques.

The main aim of performing quantum chemical calculations is to obtain the geometries and total energy of the system under investigation. Then, numerous physical and chemical properties are obtained based on the optimised ground state system (molecules or surfaces). Chapter 3 of this thesis lays out the underlying theoretical background.[19] For instance, calculations of bulk or unit cells typically target the optimisation of the geometries, and thermo-

elastic and optical properties.[20] Surface calculations address different topics, most notably, their reactivity.[21-30] The latter requires modelling of an adsorbate-surface combined system, which in turn provides insights into prominent reaction properties, such as the nature of active sites, adsorption energies, activation barriers for surface-mediated bond fissions, and surface diffusion.[24-25]. Despite the great progress made by using both experimental and theoretical techniques, the details of many molecular-surface interactions remain unclear, especially the dictation of kinetics parameters and the effect of surface dopants on key surface reaction steps.

This thesis presents a series of scientific studies by means of ab initio density function theory calculations, and comprises two parts. In the first part, we focuse on diboron trioxide as a potent oxidation inhibitor extensively deployed in many commerical and laboratory-scale applications. In contrast, in the second part, we investigate the structures and reactivity of alumina (surfaces and clusters) with a focus on their well-documented catalytic role in the synthesis of so-called phenoxy-types environmental persistant fee radicals (EPFR).

1.2 Research Motivations

The two prime motivations behind the present work are as follows:

To prevent/eliminate catalytic-assisted wall reactions in gas phase experiments, several materials are deployed as reactor coatings. The most widely used coating material is diboron trioxide (B_2O_3). The molecular attributes of the truly unreactive functionality of these materials have never been theoretically

investigated in detail. These factors must include a combination of structural and electronic properties that make B_2O_3 surfaces inert chemical entities. Recent studies attempted to link the degree of surface underactivity with certain properties such as band gap and interatomic bond strength. In principle, all solid surfaces have potent adsorption sites; thus, it is very interesting to elucidate why certain materials are specifically chemically inert.

The second theme of the thesis is part of a larger project aimed at revealing the mechanistic and kinetic factors dictating the formation of polybrominated dibenzofurans, PCDD/Fs, and their strucurally-related precursors. A great deal of literature recognises the critical role of alumina in catalysing the formation of PCDD/Fs via surface-assisted coupling of phenoxy-type EPFR. However, the exact reaction steps and underlying energy requirements are not known. Pertinent literature often presents conflicting views in regard to many factors, most notably, the desorption of surface adsorbates versus surface reaction, and the manner in which heterogeneous mechanisms for the formation of EPFR differ from the well-understood gas phase analogous route.

1.3 Thesis Objectives

The overall aim of this thesis is to understand the precise atomic-basis electronic and structural factors dictating reactive and non-reactive surfaces of two metal oxides of the same group in the periodic table; boron (B) and aluminium (Al). Specifically, this thesis sets out to:

1. Theoretically inspect the initial steps governing the conversion of elemental boron into B_2O_3 via adsorption of molecular oxygen into elemental boron.

2. Perform accurate quantum chemistry calculations to provide atomic-based elucidation of the inertness of B_2O_3 and the structure of its crystalline form.

3. Use combined theoretical and experimental approaches (i.e. diffuse reflectance infrared spectroscopy) to explore the mechanistic hygroscopic effect of diboron trioxide.

4. Use computational quantum-mechanical calculations to probe the inhibition role of B_2O_3 surfaces, as a coating material for quartz reactor walls, in the course of the H_2S oxidation process.

5. Use DFT theory to explore the catalytic role of dehydrated and hydrated alumina (with varying hydroxylation degree) surfaces in mediating the formation of phenoxy-type EPFR.

6. Examine theoretically the potential role of atomic dopants in the catalytic activity of alumina in generating EPFR.

1.4 Thesis Outline and an Overview

The thesis is organised as follows:

Chapter 2 presents a critical analysis of the relevant available literature on: (i) the chemistry of borate with a primary focus on reactivity, synthesis procedures, properties and, structures of diboron trioxide; and (ii) the catalytic activity, structures, and electronic properties of the thermodynamically stable phase of alumina i.e. α-Al_2O_3. Basically, Chapter 2 achieves the following:1) critically summarises the industrial synthesis of boron oxide; 2) discusses the catalytic inhibition properties of B_2O_3; 3) presents the molecular structure of diboron trioxide (vitreous and crystalline forms); 4) presents alternative industrial applications of diboron trioxide; 5) summarises the classification of alumina; 6) analyses the acidity and basicity of alumina; 7) surveys the effect of alumina's hydration on its surface reactivity; 8) highlights the role of various transitional metal oxides, particularly alumina, in the formation of notorious PCDD/Fs, and phenoxy-type EPFR.

Chapter 3 introduces the theoretical background of the computational techniques employed in this study, along with a brief review of the basic concepts of ab initio atomistic thermodynamics and the density function theory (DFT) approaches. Moreover, the experimental approaches and computer codes employed within the scope of this thesis (i.e. $DMol^3$ cod and CRYSTAL14 code) are described briefly.

Chapter 4 offers a computational account of the strong and exothermic interaction of atomic and molecular oxygen with the α(001)B12 surface of boron. We found that physisorbed oxygen interacts weakly with the surface, but the dissociative chemisorption entails

considerable exothermicity in the range of 2.47 – 3.45 eV/mol, depending on the adsorbed sites of the two oxygen atoms. Nonetheless, rupture of dioxygen on the surface involves a sizable intrinsic reaction barrier of 3.40 eV. Such a high level of energy clearly explains the chemical inertness (i.e. lack of oxidation) of boron at room temperature. However, elevated temperatures encountered in real applications of boron, such as cutting machinery, overcome the high-energy barrier for the dissociative adsorption of molecular oxygen (3.40 eV). A stability *T-P* phase diagram reveals the spontaneous nature of the substitutional O/α(001)B12 adsorption modes that lead to the formation of diboron trioxide, at temperatures and pressure pertinent to practical applications. The finding of this Chapter conclusively collaborates the experimental observation of the formation of the B_2O_3 phase from the adsorption of oxygen on boron. Finally, charge analysis provides an atomic-scale probe for the predicted stability ordering of the considered O/α(001)B12 configurations.

Chapter 5 presents accurate quantum mechanical calculations using the PW1PW hybrid HF/DFT functional of four low-index surfaces of the low-pressure phase of B_2O_3: (101), (100), (011) and (001). Bond lengths, bond angles, and net Mulliken charges of the surface atoms are analysed in detail. The total and projected density of states and surface energies are discussed. The occurrence of tetrahedral BO_4 units on the lowest energy structures of two of these surfaces is demonstrated for the first time. The corresponding surface orientations incur larger energies in reference to the two orientations featuring only BO_3 units. None of the four investigated lowest energy structures have dangling bonds, which reasonably relates to the experimentally observed low reactivity of this compound. The findings in this Chapter pave the way for potential interest in future studies regarding the surfaces of amorphous B_2O_3, as well as on the hydroxylation of both crystalline and amorphous B_2O_3.

Chapter 6 focuses on the adsorption and dissociation mechanisms of two hydrogen chalcogenides, namely water (H_2O) and hydrogen sulfide (H_2S) molecules, over the B_2O_3-I (101) surface. Aided by both experimental diffuse reflectance infrared spectroscopy and computational first-principle techniques, this Chapter confirms the hygroscopic behaviour of diboron trioxide, elucidating the corresponding enthalpic requirements. We show that the diboron trioxide surface exhibits high physiochemical reactivity towards water molecules with an activation energy of 39 kJ/mol dissociative adsorption. Furthermore, desorption of both molecularly adsorbed and dissociated structures of water molecules from the B_2O_3 -I (101) surface requires activation energies of 124–127 kJ/mol, in agreement with the experimentally derived isoconversional activation energies for the same process. Our investigation on the other hydrogen-chalcogenide compound, i.e. H_2S, reveals that diboron trioxide attracts H_2S molecules and forms molecular adsorption via sp^3 hybridisation between the lone pair electron of the H_2S and the empty *p* orbital of the B_{surf} atom without activation barrier. However, the energy barrier required to dissociate H_2S over the B_2O_3 -I (101) surface appears exceedingly high at 310 kJ/mol. The present insight resolves the two different behaviours of B_2O_3 concerning hydrogen chalcogenides reported in the literature. While acting as a water scavenger to generate dissociated radicals, it exhibits an inhibitor characteristic towards the dissociation of H_2S molecules, representing an ideal reactor wall coating for desired pure gas phase reactions.

Chapter 7 uses first-principle calculations to investigate the activity of the alumina neat α-Al_2O_3(0001) surface in the formation of phenolic EPFR, under conditions relevant to cooling zones of combustion systems. We show that the molecular adsorption of phenol on α-Al_2O_3(0001) entails binding energies in the range of -202–-127 kJ/mol. The dehydroxylated alumina catalyses the conversion of phenol into its phenolate moiety with a modest activation energy of 48 kJ/mol. Kinetic rate parameters, established over the temperature range of 300 to

1000 K, confirm the formation of the phenolate as the preferred pathways for the adsorption of phenol on alumina surfaces, corroborating the role of metal oxides deposited on particulate matter in the cooling zone of combustion systems in the generation of environmentally-persistent free radicals.

Chapter 8 presents a computational study of the catalytic role of the hydrated α-Al_2O_3 (0001) surface and Si modified Al_2O_3 surfaces in producing phenolic EPFR. First, we present the geometric and electronic properties of bulk α-Al_2O_3. Then, we investigate in detail the molecular adsorption of phenol over the α-Al_2O_3 (0001) surface. This is followed by an investigation of surface-mediated dissociation of phenol over both doped and undoped hydroxylated alumina surfaces. Molecular phenol is found to interact in vertical and flat/title configurations with calculated binding energies of -91 and 136 kJ/mol, respectively. The hydrated alumina surface is active toward the attack phenol molecule and forms a phenoxy moiety, via the H_2O elimination mechanism. The Si-α-Al_2O_3 (0001) substituted surface is considered for both hydrated and dehydrated alumina systems. The activation energy barrier required to form phenoxy moiety over the Si- Al_2O_3 (0001) surface was found to be nearly 37% lower than that of the undoped dehydrated alumina surface.

Chapter 9 analyses dissociative adsorption mechanisms of phenol molecules over Al_2O_3 and hydrated $Al_2O_3.nH_2O$ clusters that mimic dehydrated and hydrated alumina structures, respectively. We show that fission of the phenol's hydroxyl bond over dehydrated alumina systematically incurs lower energy barriers than that of the hydrated structures. In contrast, a 1,2-water elimination step marks the most feasible channel in the interaction of phenol and hydrated clusters. It is found that the catalytic activity of the alumina surface in producing the phenoxy/phenolate species reversibly correlates with the degree of hydroxyl coverage.

Desorption of adsorbed phenolates requires sizable desorption energies and is expected to facilitate surface-mediated condensation into dioxin-like moieties.

Finally, **Chapter 10** highlights the concluding remarks of this thesis and provides insights for future research.

Figure 1.3 show thesis map and the relationship between the sections.

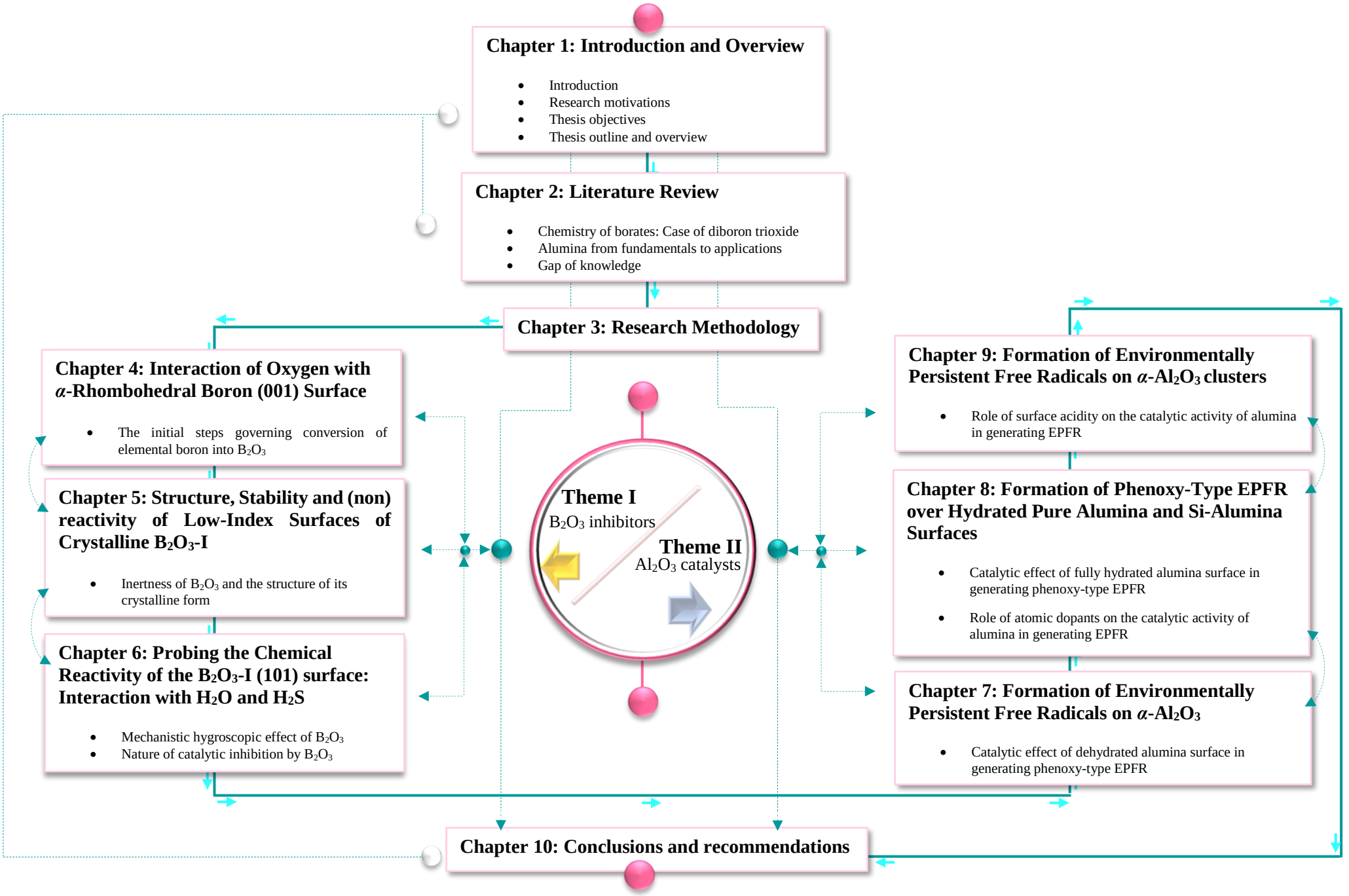

Figure 1.3. Thesis map showing relationships between sections ——▸ Proceeds, ┈┈▸ Relative to.

1.5 References

1. Venables, J., *Introduction to Surface and Thin Film Processes*. Cambridge University Press, 2000.

2. Binnig, G.; Rohrer, H., In touch with atoms. *Rev. Mod. Phys.* **1999**, *71*, S324-S330.

3. Barth, J. V.; Costantini, G.; Kern, K., Engineering atomic and molecular nanostructures at surfaces. *Nature* **2005**, *437*, 671-9.

4. Lin, J.; Balabin, I. A.; Beratan, D. N., The nature of aqueous tunneling pathways between electron-transfer proteins. *Science* **2005**, *310*, 1311-3.

5. Drakova, D., Theoretical modelling of scanning tunnelling microscy: Scanning tunnelling spectroscopy and atomic force microscopy. *Rep. Prog. Phys.* **2001**, *64*, 205-290.

6. Harikumar, K.; Lim, T.; McNab, I. R.; Polanyi, J. C.; Zotti, L.; Ayissi, S.; Hofer, W. A., Dipole-directed assembly of lines of 1, 5-dichloropentane on silicon substrates by displacement of surface charge. *Nat. Nanotech.* **2008**, *3*, 222-228.

7. Ternes, M.; Lutz, C. P.; Hirjibehedin, C. F.; Giessibl, F. J.; Heinrich, A. J., The force needed to move an atom on a surface. *Science* **2008**, *319*, 1066-1069.

8. McDowell, M. T.; Jungjohann, K. L.; Celano, U., Dynamic nanomaterials phenomena investigated with in situ transmission electron microscopy: A nano letters virtual issue. Nano Lett. **2018**, *18*, 657-659.

9. Pavliček, N.; Gross, L., Generation, manipulation and characterization of molecules by atomic force microscopy. *Nat. Rev. Chem.* **2017**, *1*, 0005 DOI: 10.1038/s41570-016-0005.

10. Cui, X.; Troadec, C.; Wee, A. T.; Huang, Y. L., Surface Nanostructure Formation and Atomic-Scale Templates for Nanodevices. *ACS Omega* **2018**, *3*, 3285-3293.

11. Ceyer, S. T., Dissociative chemisorption: Dynamics and mechanisms. *Annu. Rev. Phys. Chem.* **1988**, *39*, 479-510.

12. Arumainayagam, C. R.; Madix, R. J., Molecular beam studies of gas-surface collision dynamics. *Prog. Surf. Sci.* **1991**, *38*, 1-102.

13. Rettner, C. T., *Dynamics of Gas-surface Interactions*. Surendra Kumar, 1991.

14. Hamers, R. J., Scanned probe microscopies in Chemistry. *J. Phys. Chem.* **1996**, *100*, 13103-13120.

15. Bhattacharjee, T., *Towards Understanding Catalytic Processes for the Reactivity of Hydrocarbons on Rh Surface: A Quantum Chemical Study*, University of Heidelberg, 2011.

16. Bischoff, F.; Seufert, K.; Auwärter, W.; Seitsonen, A. P.; Heim, D.; Barth, J. V., Metalation of porphyrins by lanthanide atoms at interfaces: Direct observation and stimulation of cerium coordination to 2H-TPP/Ag (111). *J. Phys. Chem. C* **2018**, *122*, 5083-5092.

17. Barrera, O.; Bombac, D.; Chen, Y.; Daff, T.; Galindo-Nava, E.; Gong, P.; Haley, D.; Horton, R.; Katzarov, I.; Kermode, J., Understanding and mitigating hydrogen embrittlement of steels: A review of experimental, modelling and design progress from atomistic to continuum. *J. Mater. Sci.* **2018**, *53*, 6251–6290.

18. Oudda, H.; Touir, R.; El M'Rabet, M.; Warad, I.; Guenbour, A.; Lakhrissi, B., Coupling of electrochemical and theoretical techniques to study the interaction of steel/terazole based on 8-hydroxyquinoline in 1.0 M Hcl. **2018**, *9*, 1086-1097.

19. Schwarz, K.; Blaha, P., Solid state calculations using WIEN2k. *Comput. Mater. Sci.* **2003**, *28*, 259-273.

20. Anstis, G. R.; Chantikul, P.; Lawn, B. R.; Marshall, D. B., A critical evaluation of indentation techniques for measuring fracture toughness: I, Direct crack measurements. *J. Am. Ceram. Soc.* **1981**, *64*, 533-538.

21. Amin, M. A.; Khaled, K.; Mohsen, Q.; Arida, H., A study of the inhibition of iron corrosion in HCl solutions by some amino acids. *Corros. Sci.* **2010**, *52*, 1684-1695.

22. Obot, I. B.; Obi-Egbedi, N. O., Adsorption properties and inhibition of mild steel corrosion in sulphuric acid solution by ketoconazole: Experimental and theoretical investigation. *Corros. Sci.* **2010**, *52*, 198-204.

23. González-Lezana, T.; Honvault, P.; Jambrina, P.; Aoiz, F. J.; Launay, J.-M., Effects of the rotational excitation of D_2 and of the potential energy surface on the $H^+ + D_2 \rightarrow HD + D^+$ reaction. *J. Chem. Phys.* **2009**, *131*, 044315.

24. Davies, P. R.; Bowker, M., On the nature of the active site in catalysis: the reactivity of surface oxygen on Cu (110). *Catal. Today* **2010**, *154*, 31-37.

25. Zweidinger, S.; Hofmann, J.; Balmes, O.; Lundgren, E.; Over, H., In situ studies of the oxidation of HCl over RuO_2 model catalysts: Stability and reactivity. *J. Catal.* **2010**, *272*, 169-175.

26. Lo, C. S.; Tanwar, K. S.; Chaka, A. M.; Trainor, T. P., Density functional theory study of the clean and hydrated hematite $(1\bar{1}02)$ surfaces. *Phys. Rev. B* **2007**, *75*, 075425.

27. Sinapi, F.; Issakova, T.; Delhalle, J.; Mekhalif, Z., Study of (3-Mercaptopropyl) trimethoxysilane reactivity on zinc: Comparison with organothiol and organosilane thin films. *Thin Solid Films* **2007**, *515*, 6833-6843.

28. Efil, K.; Obot, I. B., Quantum chemical investigation of the relationship between molecular structure and corrosion inhibition efficiency of benzotriazole and Its alkyl-derivatives on iron. *Prot. Met. Phys. Chem. Surf.* **2017,** *53*, 1139.

29. El Adnani, Z.; Mcharfi, M.; Sfaira, M.; Benzakour, M.; Benjelloun, A.; Ebn Touhami, M.; Hammouti, B.; Taleb, M., DFT study of 7-R-3methylquinoxalin-2 (1H)-ones (R = H; CH_3; Cl) as corrosion inhibitors in hydrochloric acid.. *Int. J. Electrochem. Sci* **2012**, *7*, 6738-6751.

30. El Adnani, Z.; Mcharfi, M.; Sfaira, M.; Benzakour, M.; Benjelloun, A.; Touhami, M. E., DFT theoretical Study of 7-R-3methylquinoxalin-2 (1H)-thiones (Rh; CH_3; Cl) as corrosion inhibitors in hydrochloric acid. *Corros. Sci.* **2013**, *68*, 223-230.

CHAPTER 2

Literature Review

2.1 Introduction

The boron family signifies a unique group of fascinating complex elements located in group 13 of the *p*-block in the periodic table (Figure 2.1). It encompasses the semi-metal boron (B) and the metals aluminium (Al), gallium (Ga), indium (In), and thallium (Tl), all of which share the valence electron configuration of ns^2np^1.[1] The elements in the boron group have remarkable similarities and differences.[2] For example, boron, as a semi- metal unlike other elements, features superior hardness, refractivity, and reluctance to participate in metallic-type bonding. Likewise, Tl possess an oxidation state of +1, unlike other elements that adopt oxidation states of +3. Their electrode potential increases down the group, whereas the opposite applies to the ionization energy. Owing to their novel physical and chemical properties, the boron family elements have unique applications.[2-3]

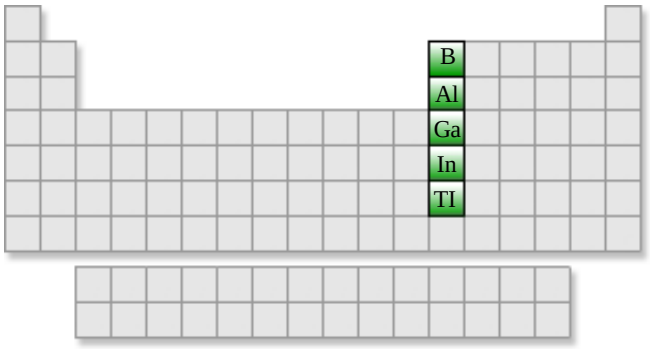

Figure 2.1. Boron family elements.

The existing literature on boron family elements and their compounds is rather extensive and focuses particularly on boron- and/or aluminium-containing compounds owing to increasing applications in many commercial and industrial applications, or simply merely derived by pure scientific curiosity (as it is the case in literature pertinent to the structures of elemental boron).

A significant number of experimental and theoretical studies have addressed many aspects related to boron- and aluminium- containing compounds, mainly focusing on their structures, electronic properties, stability, and most importantly their applications. Herein, we limit this survey to the chemical reactivity of the surfaces with an emphasis on the truly contrasting catalytic behaviour spanning both reactive (catalysts) surfaces and non-reactive (inhibitors) surfaces of alumina and boron oxides, respectively. The structures of both oxides are discussed to shed a light on their relations with the experimentally observed inhibiting/catalysing effects. It follows that this Chapter presents literature pertinent to;

- B_2O_3 as a coating and hygroscopic material, and applications that stem from these unique properties.
- Reactivity of α-Al_2O_3 as one of the most important catalysts with prominent industrial and environmental applications.

This critical review consists of two sections, with the following specific objectives:

1- To briefly discuss the chemistry of borates, the case of diboron trioxide, introducing the importance of boron oxides, their industrial synthesis, and their occurrence and supply;
2- To discuss the *T-P* thermodynamic stability diagrams of diboron trioxide, introducing the most stable crystalline phase;
3- To evaluate the inhibition characterization of diboron trioxide, including its applications as a coating and hygroscopic material;
4- To presents alumina from fundamentals to applications, with a focus on its most thermodynamically stable phase;

5- To discuss the acidity and basicity of alumina; a surface attribute that largely dictates its environmental catalytic capacity;

6- To discuss the reactivity of alumina toward water molecules (i.e. hydration reactions);

7- To evaluate the effect of surface hydration on the catalytic activity of alumina;

8- To critically review the well-documented role of alumina in mediating the formation of notorious PCDD/Fs.

Scheme 2.1 represents the structural configurations of investigated in this Chapter.

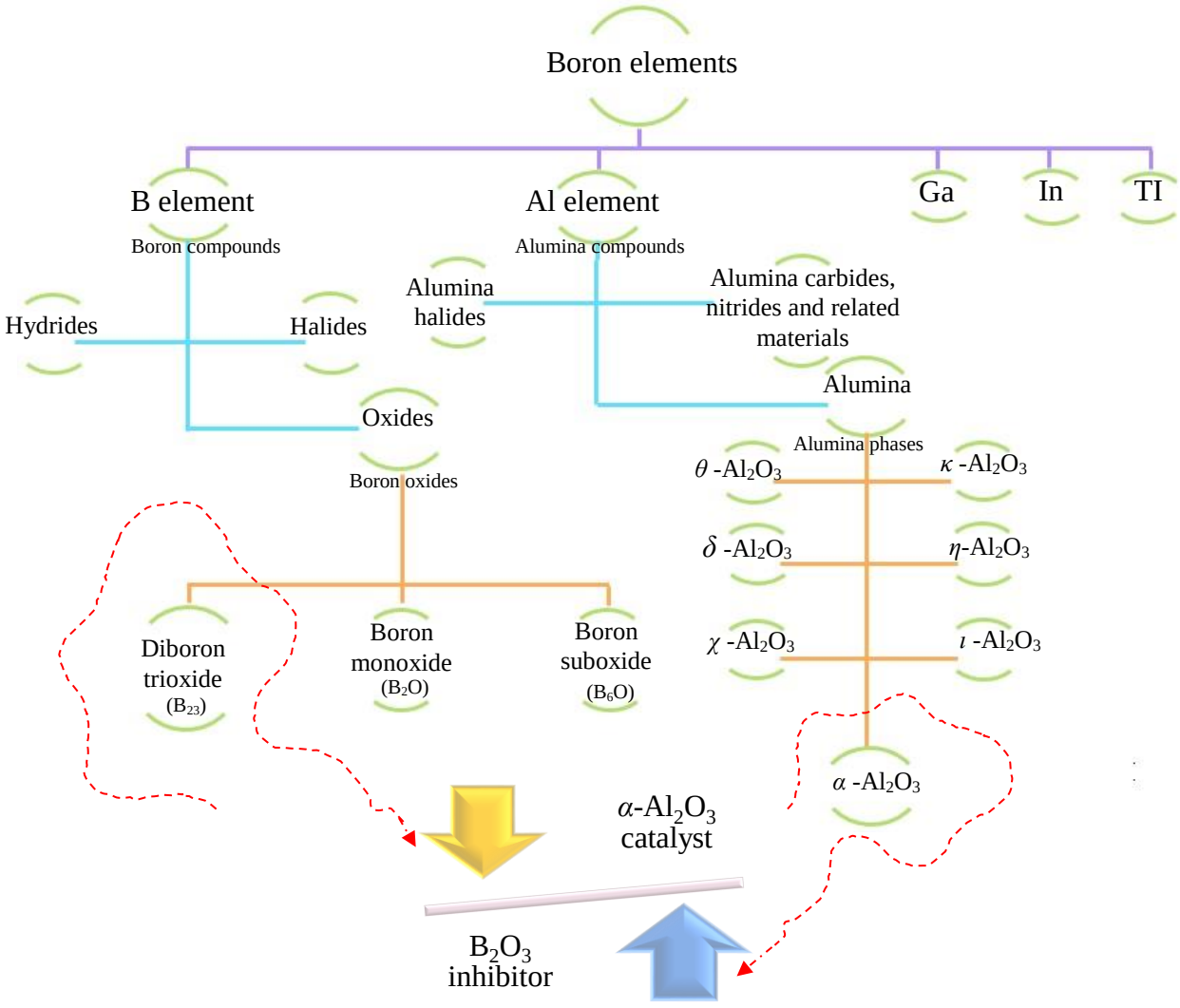

Scheme 2.1. Structural configurations investigated in this Chapter.

2.2 Chemistry of Borates: Diboron Trioxide

2.2.1 Context

Boron-rich compounds display novel properties,[4-13] such as a lightweight structure, superior thermal stability, and high hardness. Because of these unique features, boron and its compounds are employed in many commercial applications. Of particular importance is their deployment as hard, wear-resistant, chemically inert coatings.[14-18] Other applications are an abrasives, nuclear applications, and lightweight armour applications.[19-22] Boron-rich compounds are frequently prescribed in terms of their complex structures. For this reason, numerous theoretical and experimental investigations have studied the structures of elemental boron as a key step in the pursuit to understand their electronic properties.

Boron (B) tends to be chemically inert at room temperature, with a significant hardness, relatively low density, and high melting point.[23-24] The literature on elemental boron has highlighted its crystal structures, constructed a governing thermodynamic stability diagram, and reported its thermal and mechanical properties. Typically, the boron element adopts five different crystallographic structures, namely: α-B12 (α-phase),[25-26] β-B_{106} (β-phase),[27-28] orthorhombic γ-B_{28} (γ-phase),[29] tetragonal *t*-B_{192},[30] and *t*-B_{52} (*t*-phase).[29, 31] Of these phases, γ dominates the stability phase diagram of the elemental boron, as depicted in Figure 2.2.

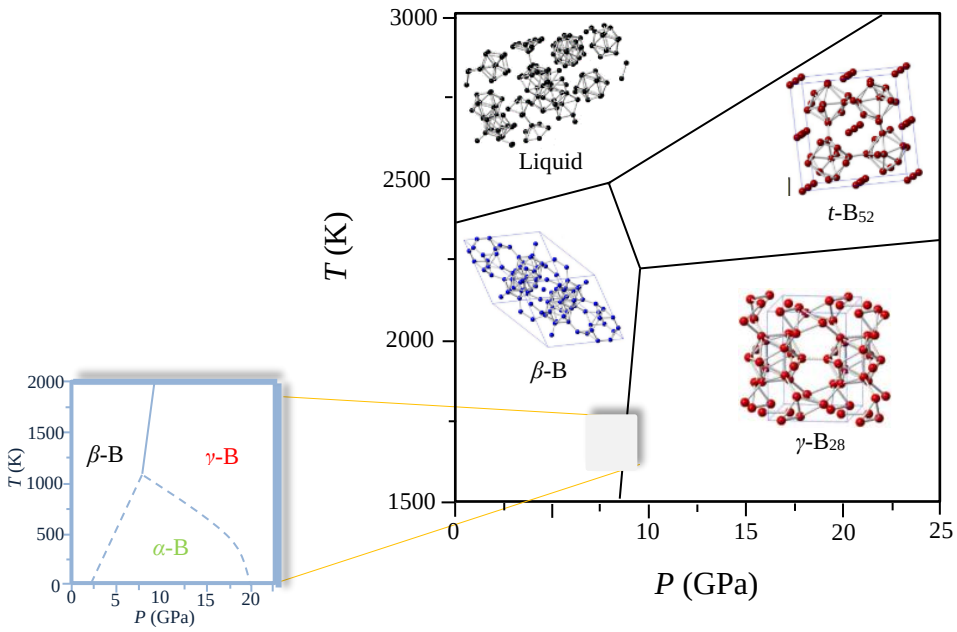

Figure 2.2. Thermodynamic stability phase diagram of elemental boron.[32]

It has been shown that boron clusters, which are produced from the decomposition of boron rich compounds (i.e. in high temperature regimes), are further oxidized in temperature-controlled processes, producing boron oxides.[33] The high enthalpy change in this reaction (303.9 kcal) derives its application as a secondary energy source in rocket fuel.[34]

$$4B+3O \rightarrow 2B_2O_3$$[35-36] R2.1

In nature, boron does not exist in its elemental form, but rather it adapts to the form of boron-containing oxyanions, with the generic formula $B_xO_y^{z-}$ (where O represents the oxygen atom). It is found as an oxide either in minerals and natural water and/or in biological systems (i.e. borate esters). Borate can broadly be defined as any compound that contains B_2O_3.[37-38] Table 2.1 displays selected borate compounds, whereas Table 2.2 enlists common borate minerals that are defined by their B_2O_3 content.

Table 2.1. Selected borate compounds.[37]

Compound	Oxide formula
diboron trioxide (boric oxide)	B_2O_3
orthoboric acid	$B_2O3\_{}_3H_2O$
metaboric acid	$B_2O_3\_ H_2O$
anhydrous sodium tetraborate (anhydrous borax)	$Na_2O\_ 2B_2O_3$
Sodium tetraborate tetrahydrate (kernite)	$Na_2O\_2B_2O_3\_4H_2O$
disodium octaborate tetrahydrate	$Na_2O\_4B_2O_3\_4H_2O$
sodium metaborate	$Na_2O\_B_2O_3\_4H_2O$
sodium metaborate hydrated	$Na_2O\_B_2O_3\_8H_2O$
sodium pentaborate pentahydrate	$Na_2O\_5B_2O_3\_10H_2O$
zinc polytriboratee	$2ZnO\_3B_2O_3\_3H_2O$

Table 2.2. Common borate minerals.[37]

Mineral	Semiempirical formula	Wt% B_2O_3	Location
borax(tincal)	$Na_2B_4O_7.10H_2O$	36.5	United States, Turkey, Argentina
Kernite	$Na_2B_4O_7.4H_2O$	51	United States
ulexite	$NaCaB_5O_9.8H_2O$	43	Turkey, South America
colemanite	$Ca_2B_6O_{11}.5H_2O$	50.8	Turkey
inderite	$Mg_2B_6O_{11}.15H_2O$	37.3	Kazakhstan
szaibelyite (ascharite)	$Mg_2B_2O.5H_2O$	41.4	China
suanite	$Mg_2B_2O_5$	46.3	China
hydroboracite	$CaMgB_6O_{11}.6H_2O$	50.5	Argentina
datolite	$Ca_2B_2Si_2O_9.H_2O$	21.8	Russia

Of the boron oxides, diboron trioxide is an essential oxide for a wide range of technologies. It has received broad attention[39-44] owing to its distinguished performance in electrolysis and ceramics, glass technology, and as oxidation inhibitors.[45-50] Extensive research has shown that B_2O_3 is an excellent glass-former. It largely remains in its vitreous (amorphous) form at ambient pressure conditions, even at temperatures in the vicinity of its melting point and/or at exceedingly slow cooling rates.[51-53] Crystallization from the melting phase is attained when the pressure is within the range of 0.4–1.0 GPa.[52-53]

In the following sections we report the vitreous and crystalline structure of B_2O_3, as well as its chemical reactivity.

2.2.2 Structure of Diboron Trioxide

The molecular structure of vitreous diboron trioxide, *v*-B_2O_3, has been a controversial matter of debate for many years.[54-67] Earlier studies[68-70] indicated that its structure is composed of randomely ordered BO_3 building blocks in which each BO_3 triangle consists of oxygen atoms at the corners and a boron atom at the centre. However, the presumed randomization of the BO_3 unit structure failed to elucidate some physical properties of *v*-B_2O_3.[71] This has made describing the correct structural arrangments of *v*-B_2O_3 a challenging task for a relatively long period of time. Later experimental developments by Jellison. et al.[72] led to a renewed interest in the structure of *v*-B_2O_3. Authors proposed that the O^{17} isotope in *v*-B_2O_3 produces different spectra, affording two distincit sites in the structure. The first site is related to BO_3 triangles (refer to Figure 2.3), and the other to boroxol rings (B_3O_6). The latter is made up of three BO_3

triangles fully connected to each other by their corners. Subsequent experimental studies have attained a similar structural configuration.[73-75]

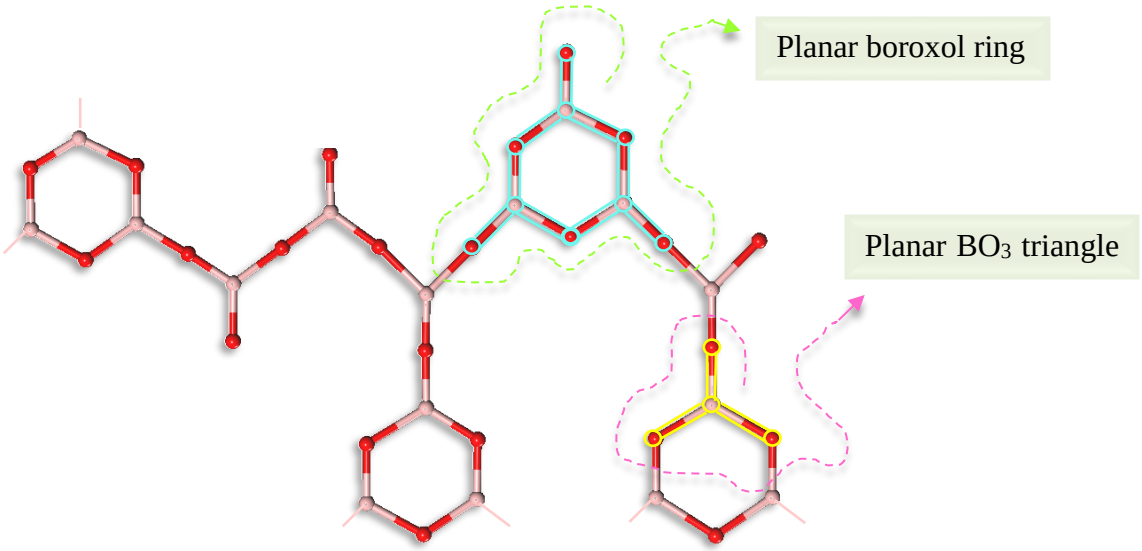

Figure 2.3. Molecular structure of vitreous diboron trioxide *v*-B_2O_3.

Over a wide range of operational pressures and temperatures, above a threshold level of 0.4–1 GPa[52-53], B_2O_3 adopts two crystallographic structures namely, B_2O_3-I and B_2O_3-II.

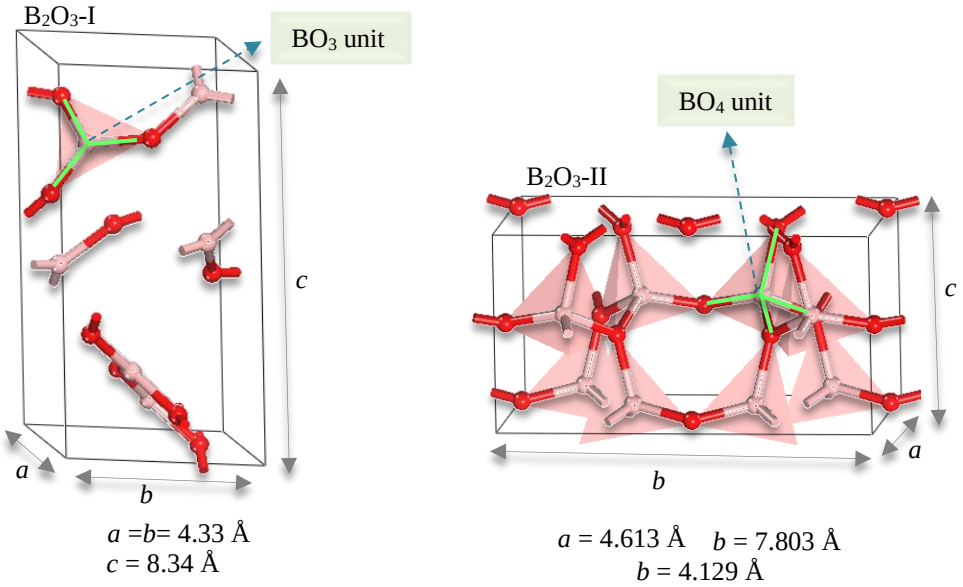

Figure 2.4. Diboron trioxide crystallographic structures; B_2O_3-I (left); B_2O_3-II (right).

With 0.4 GPa (>483.15 K) applied to the amorphous form of B_2O_3, it crystallises to its first crystalline form, B_2O_3-I.[76] It presents a hexagonal structure with lattice parameters of a = 4.33 Å and c = 8.34 Å.[76-77] The exact crystal structure of B_2O_3-I has been a subject of conflicting remarks. The contested point was that the oxygen atoms around boron are either connected to each other in a trigonal coordination (BO_3) and/or tetrahedral configuration (BO_4). Subsequently, some experimental observations[69] have excluded the presence of tetrahedral groups (BO_4) in the structure. This was been confirmed by Gurr et al.[76] who also ruled out the presence of BO_4 units; this is in a clear agreement with the early structures proposed by Berger[78], and Strong and Roy.[79] Following this, the recent refinement structure of crystalline B_2O_3-I was proposed by Effenberger et al.[77] They found that the structure of crystalline B_2O_3-I represents a high space group symmetry $P3_121$ (152), instead of Gurr et al.'s proposed structure with the low symmetric space group of $P3_1$. The planar triangles of BO_3 are lost with the continuity of pressure in difficult processes,[51]; therefore, the coordination number of boron atoms in the crystalline structure transforms from the threefold to fourfold coordination number.[80-81]

An approximately 6.5 GPa (>1000 K)[82-83] high pressure crystal, B_2O_3 –II, with the fourfold coordination number of boron, is the stable crystalline form. It consists of a three-dimensional network of tetrahedral units of BO_4. Based on the aforementioned findings, transformation in the coordination number of boron represents the main source of signficant complexity in the structures of diboron trioxide.[84] Figure 2.5 displays the thermodynamic *P-T* phase diagram of diboron trioxide.[85]

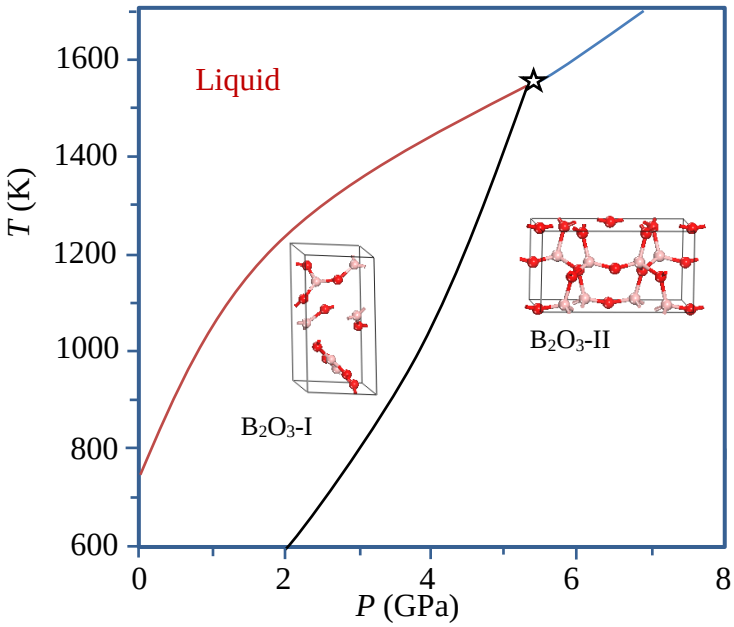

Figure 2.5. Thermodynamically consistent *P*-*T* phase diagram of diboron trioxide.[85]

Theoretically, Huang et al.[86] described the slow conversion of the structure of diboron trioxide as a function of pressure, initiating with the disintegration of the boroxol ring and ultimately leading to the formation of the BO_4 unit, as revealed in Figure 2.6.

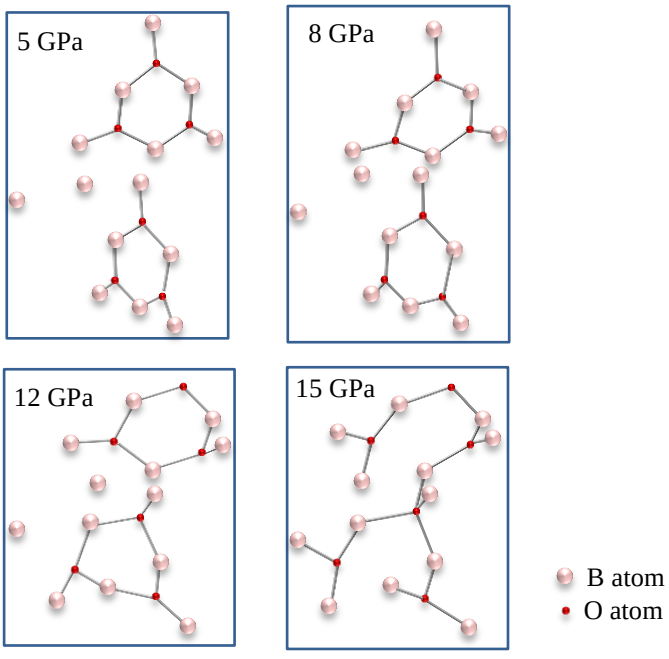

Figure 2.6. Gradual conversion of the structure of diboron trioxide as a function of pressure.[86]

Recent evidence suggests that diboron trioxide is described by its complex structure; consequently, very little is known about its surfaces. One study by Bredow et al.[87] investigated the structures and relative stability of four B_2O_3-I low index surfaces, namely 101,100,001, and $1\bar{1}1$ at 0 K. They found that the stability ordering follows the sequence 101> 111> 100> 001. However, the authors made no attempt to relate the thermodynamic stability to elevated temperatures and pressures, nor did they address the effect of the atomic type termination on the predicted stability order. This indicates that a future study aimed at an atomic–based understanding of B_2O_3 surfaces and their reactivity would be very insghtful.

2.2.3 Reactivity of B_2O_3

2.2.3.1 B_2O_3 Coating

B_2O_3 coatings play a critical role in the maintenance of industrial materials subject to very harsh conditions, allowing higher operating temperature, and most importantly increasing their lifespan.[88] Typically, this can be attained in three basic ways, diffusion coating, overlay coating, and thermal barrier coating.[89]

Common examples includes, boron oxides,[90] boron nitride,[91] silicon silicide,[92] and phosphorus[93]. In particular, B_2O_3 is one of the most widely deployed oxidation inhibitors.[49-50] An important example of its use as an oxidation inhibitor includes carbons-carbon composite oxidation. A thin layer of B_2O_3 is commonly deployed in chemical reaction experiments to eliminate plausible catalytic-wall assisted reactions.[94]

Recent trends in high temperature oxidation resistance have led to a proliferation of studies on carbon-carbon composite oxidation reactions[95-99] as an important composite in many industrial applications.[100-101] Existing research recognises the critical role played by oxidation inhibitors in providing complete protection either short-term and/or at high temperature (i.e. ~1273 K).[93, 102-105]

Of the reported inhibition additives (i.e. boron containing additive, phosphorous containing additive, and halogenated glass), boron-containing inhibitors have the most promising inhibition effect. The mechanistic inhibition effect of boron oxides operates by blockage of the active site; however, oxidative fragmentation of B_2O_3 and its rapid reaction with atmospheric water molecules reduces its inhibition effect.[93, 102, 104-106] B_2O_3 is extremely sensitive to moisture; in moist low-temperature environments, B_2O_3 spontaneously interacts with water molecules; however, heating can reversibly remove the water molecules on the B_2O_3 surfaces, leading to spallation of the coating layer.[107] B_2O_3 exhibits low viscosity which can give rise to uneven spreading.[108] At high temperature, (i.e. 673-873 K), boron oxide forms volatile species (i.e. H_3BO_3 and HB_2), which can decrease its efficiency as a coating during the oxidation processes.[109] For this reason, many studies have aimed to improve its inhibition characterisation by adding some additives as a combination of various inhibitors, to form a hermetic binary system coating. Table 2.3 summarise selected binary system coatings and their effect in enhancing the catalytic inhibition of boron oxide.

Table 2.3. Selected materials and their effect in enhancing the reaction inhibition of B_2O_3.

Material	Description effects	Reference
B_2O_3 modified $MoSi_2$-CrSi-Si/B modified SiC coating	Increases the oxidation protection up to 1173 K for 150 h.	110-111
ZrB_2+ B_2O_3 | SiC coating	Increases the oxidation protection up to 1500 K	112
SiO_2 + B_2O_3 | SiC coating	Increase the oxidation protection up to 1800 K	108, 113
$Al4B_2O_9$ + B_2O_3 on stainless steel	Increases the sintering degree	89
SiO_2-ZrO_2- B_2O_3	Denser and stronger protection layer	114
Ba (Nd_2_xSmx) TiO_{12}	Decreases the sintering temperature	115

Experimental evidence has proven some inhibitors to be unreliable (silicon-based coatings such as Si3N4 and SiC). The major drawback of these coatings is the thermal expansion mismatch between the coating and the substrate layer, which is the leading cause of the formation of the cracks in the coating (873–1373 K). Such cracks lead to the deactivation of the coating layer and allow oxygen molecules to diffuse and oxidise the substrate layer.[116-121] Significant efforts have been devoted to develop more effective coatings to overcome this cracking problem. For this purpose, multi-layer coatings have been synthesised.[112, 119, 122-127]

An effective multi-layer coating is the combination of SiC (outer-layer) and B_4C (inner layer) coating layers.[124] However, thermal expansion cracking of the outer coating layer (i.e. SiC)

allows oxygen diffusion into the second layer (i.e. B_4C). This facilitaes the formation of B_2O_3, which seals the cracks, and accordingly prevents oxidation.

$$B_4C + 4O_2 \rightarrow 2B_2O_3 + CO_2 \qquad \text{R2.2}$$

Diboron trioxide as a crack sealant is of interest because of its important properties, such as low melting point, low oxygen permeability, superior wettability for easy penetration into cracks, and easy sealing treatment.[88, 128] However, the use of a binary system (i.e. B_2O_3 and SiO_2) generally affords better performance.[129]

Several sources of evidence suggest that passifying quartz reactor walls by coating them with boron oxide eliminates the catalytic effects of the surface of the reactor.[130] For instance, some studies have been carried out to investigate B_2O_3 coatings in H_2 and hydrocarbon oxidation processes,[131-135] proving its inert properties toward the decomposition of peroxy species. Along the same line of inquiry, Zhou et al.[136], in a more recent study, investigated H_2S oxidation in a B_2O_3 coated reactor and compared it with an uncoated reactor. The authors found that the oxidation process is strongly catalysed when the oxidation reaction takes pace in an uncoated reactor. The profound wall effect can be completely eliminated by applying a B_2O_3 coating, confirming the inhibition characterisation of diboron trioxide in H_2, S_2, and H_2S oxidation systems. Figure 2.7 contrasts the rate of H_2S oxidation with and without B_2O_3.

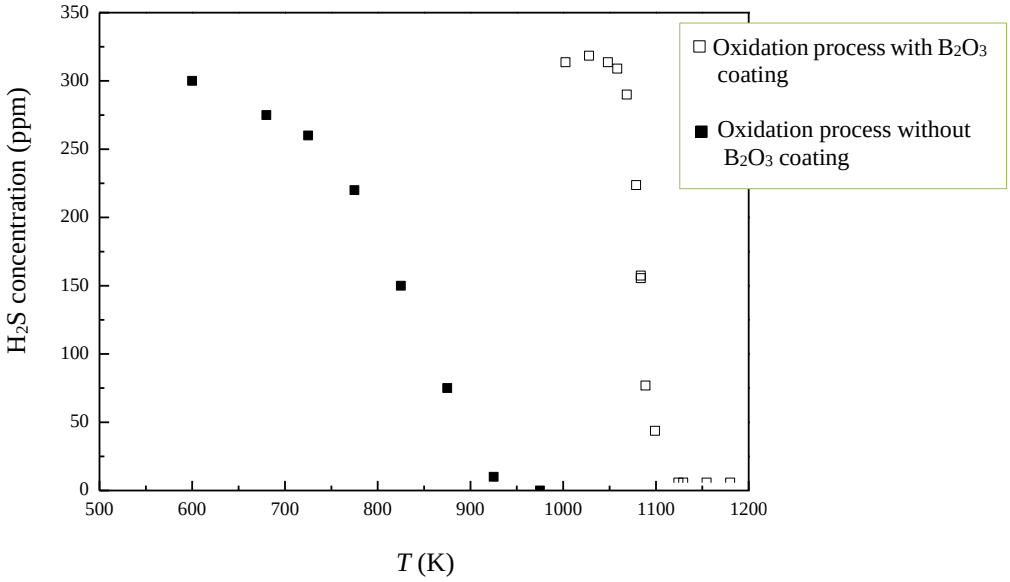

Figure 2.7. H_2S oxidation with and without B_2O_3 coating.[136]

2.2.3.2 B_2O_3 Hygroscopic

B_2O_3 signifies a highly hygroscopic material.[137] When B_2O_3 is produced from the oxidation of boron at high temperature[138], it cools and is converted upon its interaction with atmospheric moisture[139] to boric acid (H_3BO_3), a material that exhibits potent self-lubricating behavior.[138, 140]

Heating process $4B+6O \rightarrow 2B_2O_3$ R2.3

Cooling process $^1/_2B_2O_3+^3/_2H_2O \rightarrow H_3BO_3$ R2.4

The behaviour of self-lubricating films of boric acid is an important industrial problem. Of particular importance is propellant processing, ignition, and combustion[141-144] , as well as B_2O_3 coating applications (as mentioned previously). For instance, the presence of both H_3BO_3 and B_2O_3 in airbreathing propulsion systems undesirably increases the viscosity.[145] Efforts to overcome this problem considered inhibition of the surface oxidation of boron by adding passivating agents such as organic amines and hydroxylamine[146] and/or via adding a coating agent to the surface of boron.[147-148] The latter interacts with B_2O_3 and facilitates its removal during combustion.

In a temperature-controlled process, the interaction of diboron trioxide with water molecules takes place in two stages as shown in Figure 2.8:[149]

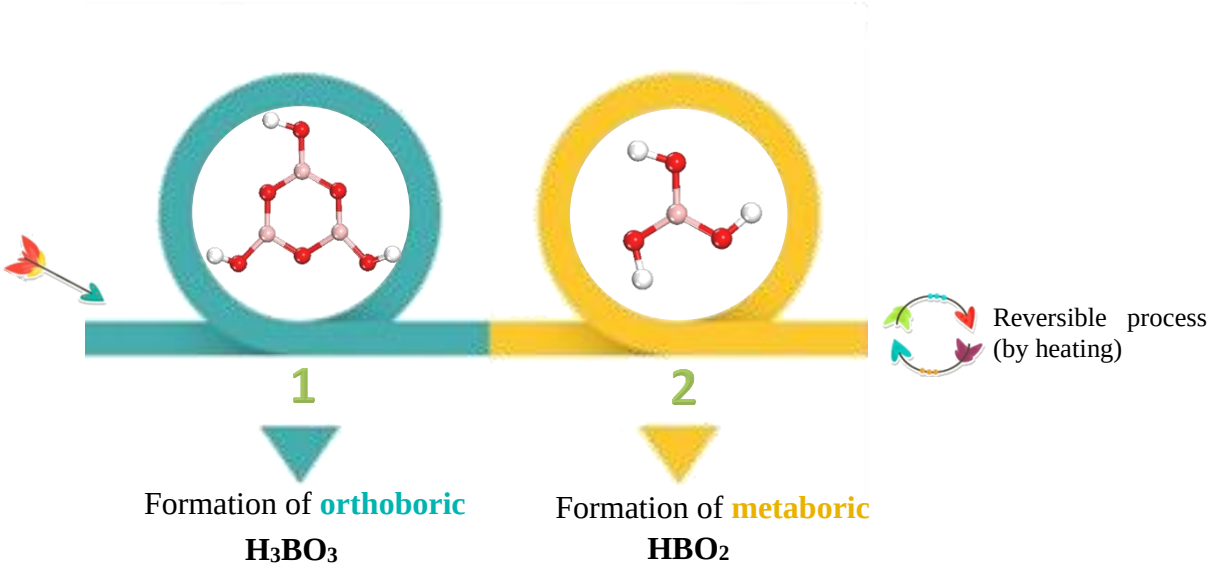

Figure 2.8. Interaction of diboron trioxide with water molecules.

Heating can reversibly remove water molecules on the B_2O_3 surfaces. The surface loses a fraction of its water content and forms HBO_2 at approximately 400 K, whereas it is completely dehydrated at approximately 525 K.[150-151]

2.3 Alumina From Fundamentals to Applications

2.3.1 Context

Alumina have been a focal topic of research owing to their variety of features, such as its hardness, corrosion resistance, abrasion resistance, compression strength, large surface area, good electric insulation, optical properties, and catalytic surface activity.[152-153] Owing to these properties, alumina have unique applications.[154-159] Common examples of its usage include firebricks, abrasives, integrated circuit (IC) packages, electronic, ceramics, catalysis, and in thermal barrier coatings (TBCs).[160-168]

Over a wide range of operational pressures and temperatures, alumina exhibits a variety of crystallographic structures.[169-171] As early as the 1920s, researchers pointed out the presence of several alumina transition phases.[172] According to Haber classification, alumina can be categorized into two main groups, namely α-group and γ-group.[172] Afterwards, aluminium tridroxide-bayerite (β-group) was observed and subsequently added as a new group next to the gibbsite. Table 2.4 lists the early classifications of alumina.[172]

Table 2.4. Early classification of alumina.

	***α*-group**	***β*-group**	***γ*-group**
$Al_2O_3.\ 3H_2O$	Gibbsite $(AlOH)_3$	Bayerite $Al(OH)_3$	Nordstrandite $A(OH)_3$
$Al_2O_3.\ H_2O$	Boehmite AlOOH	diasporeAlOOH	

Stumpf et al. identified new crystallographic structures containing alumina as η, κ, δ, χ, θ, and ι-Al_2O_3 phases.[172-173] In a sequence of thermal decomposition (dehydration) processing of alumina hydroxide, $Al_2O_3.xH_2O$, the six main crystal structures of alumina evolves to afford α-Al_2O_3 (corundum) as portrayed in Figure 2.9:[174-175]

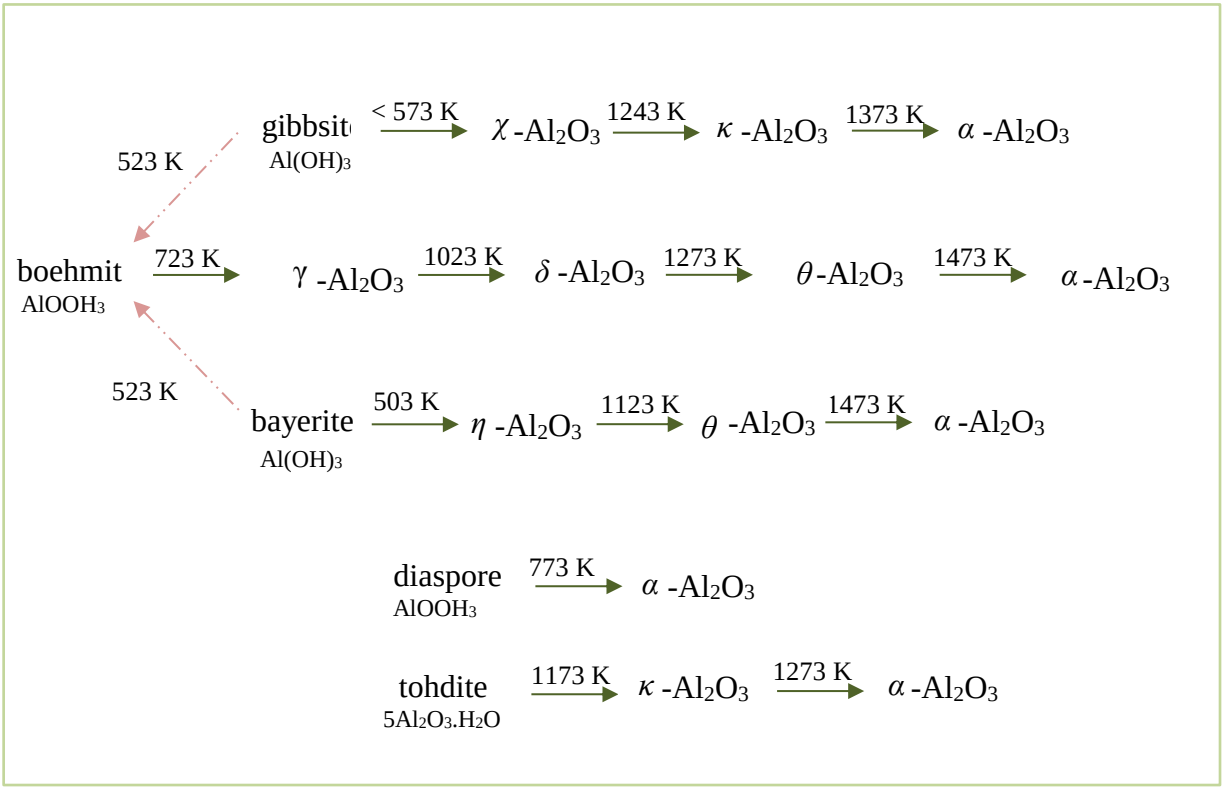

Figure 2.9. Thermal decomposition processing of alumina hydroxides.[175]

In general, two broad groups of alumina are commonly discussed; low-temperature aluminas (T < 873 K) belong to the χ, η, and γ-Al_2O_3 phases, and high temperature aluminas (1173 < T < 1273 K) exist in κ, θ, δ, and α-Al_2O_3 configurations.

The formation of the structural polymorphs of alumina, as seen in Figure 2.9, depends mainly on two basic features; the processing conditions (i.e. temperature) and type of initial alumina hydroxide, $Al_2O_3.xH_2O$. The latter is classified into three main classes are defined by their H_2O content (x):[175]

- Aluminium trihydroxides group, $Al(OH)_3$, where x = 3, such as gibbsite and bayerite.
- Aluminium monohydroxides group, AlOOH, where x = 1, such as boehmite and diaspore
- A tohdite, where x = 0.2.

The aforementioned polymorphs of alumina share several common structural properties; they display a close-packed ABAB alternating sequence stack of oxygen ions and Al ions in octahedral and tetrahedral interstices.[174] Low-temperature alumina features cubic close-packed oxygen lattices, whereas the other group (high temperature) displays hexagonal close-packed oxygen lattices.[171, 176-178] The distinct application of alumina depends on its soda content as demonstrated in Table 2.5.[179]

Table 2.5. Classification of alumina based on soda level (by weight).

Normal soda	**Intermediate soda**	**Low soda**	**High purity**
>0.25%	**0.15-0.25%**	**0.03-0.1%**	**thermally reactive**
White products	Electrical porcelain	Spark plugs	Electronic ceramic
Ceramics tile	White ware porcelain	Electronic ceramic component	High density, high strength wear parts
Sanitary ware	Grinding media	Integrated circuit (IC) substrates	Bioceramics
Refractories	Wear tiles	Laboratory wear	Cutting tools
Fused alumina	85-95% alumina component	Wear resistance components	Thin IC substrates
Glass		Zirconia toughened alumina	Armour

In light of their commercial grades, alumina are often grouped into several categories as shown in Figure 2.10:[180]

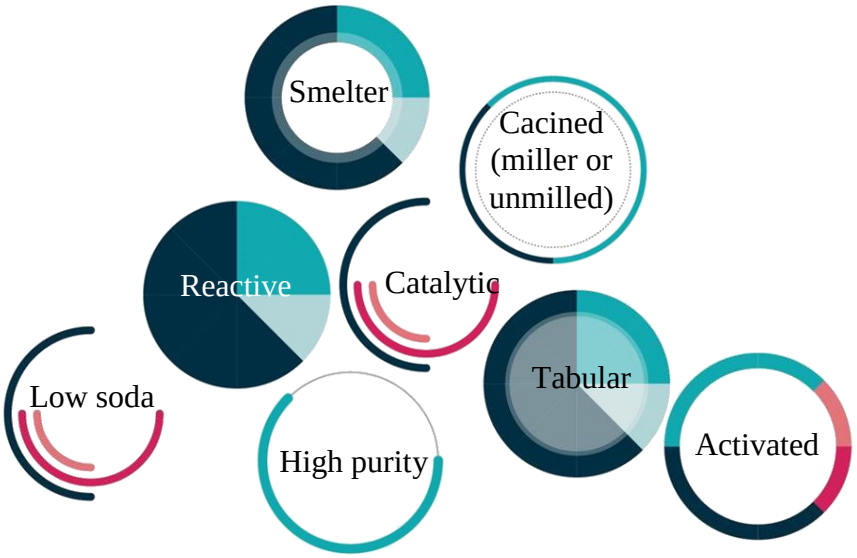

Figure 2.10. Commercial grades of alumina.[180]

Theoretical analysis of the relative stability of the different polymorphs of alumina as a function of temperature was first carried out by Digne et al.[175] Thus, according to the ab initio atomistic thermodynamics approach, the variations in the Gibbs free energy, as a function of temperature, were plotted for each polymorph. The authors confirmed that the transformation occurs at low temperature, forming metastable polymorphs of alumina such as η and γ-Al_2O_3. Further, they found that dehydrated polymorphs of alumina gain more thermodynamic stability with increasing temperature. Lastly, and most importantly, they found that the α-Al_2O_3 polymorph entails a considerable stability beyond the limit of 750 K, a temperature window which spans prominent alumina applications (i.e. catalyst materials at high temperature). Figure 2.11 plots the Gibbs surface energies for the various alumina configurations.

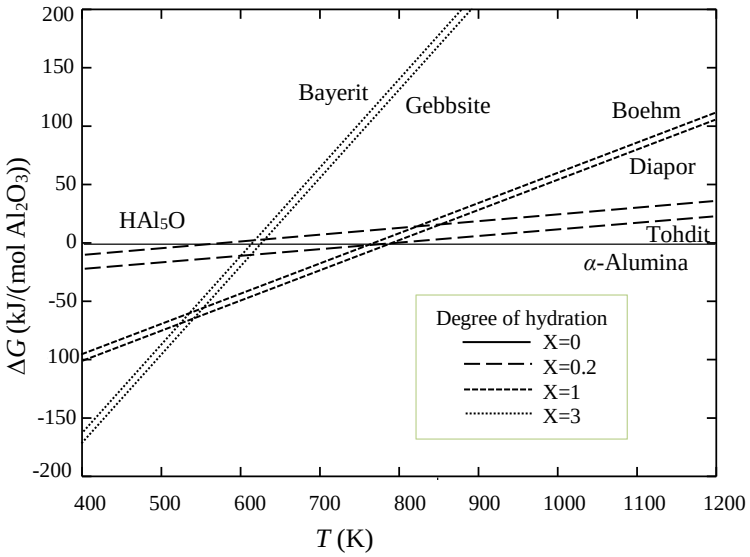

Figure 2.11. Stability phase diagram of alumina.[175]

In this thesis, we focus only on the most thermodynamically stable form of alumina, α-Al_2O_3. In the following sections, we report production procedures of α-Al_2O_3, its crystal structure, and its chemical reactivity.

2.3.2 Production of α-Al_2O_3

Owing to its unique properties, such as stability and strength at high temperature, α-Al_2O_3 has been increasingly deployed in fields as diverse as gas sensors, electronic devices, and catalyst materials at high temperatures.[180] These strategic applications necessitate deploying 99.99 % ultra-high purity α-Al_2O_3 powder.

Currently, the production of highly pure α-Al_2O_3 is carried out based on four synthesis methods:

i. Hydrolysis of alumina, via the following steps, where R is a hydrocarbon radical:[181-183]

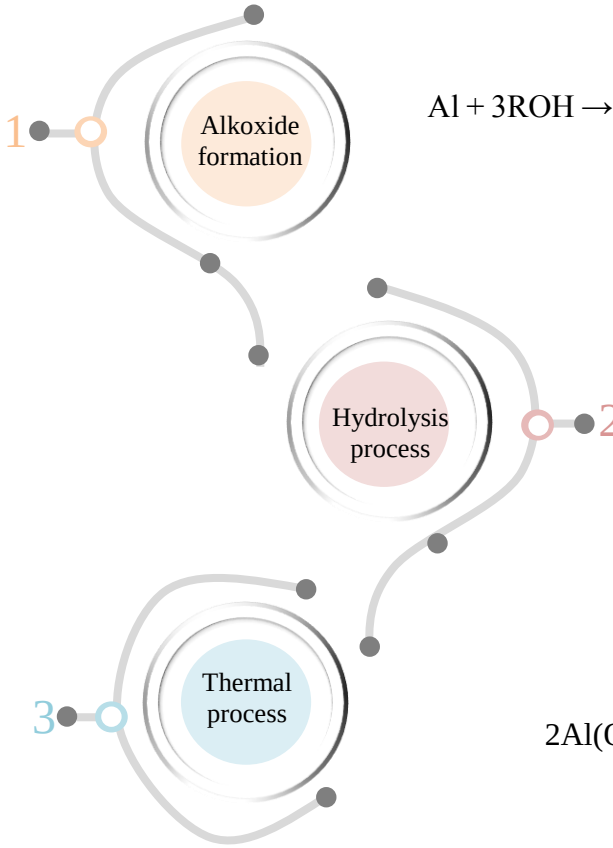

$$Al + 3ROH \rightarrow Al(OR)_3 + {}^3/_2H_2 \quad \text{R2.5}$$

$$Al(OR)_3 + 3H_2O \rightarrow Al(OH)_3 + 3ROH \quad \text{R2.6}$$

$$2Al(OH)_3 \rightarrow Al_2O_3 + 3H_2O \quad \text{R2.7}$$

ii. Chemical vapour deposition between vaporized $AlCl_3$ and water vapour at 1023–1173 K:[184]

$$2AlCl_3 + 3H_2O \rightarrow Al_2O_3 + 6HCl \quad \text{R2.8}$$

iii. Thermal decomposition of aluminium Alum:[185]

$$2NH_4Al(SO_4)_2.12H_2O \rightarrow Al_2O_3 + 2NH_3 + 4SO_3 + 25H_2 \quad \text{R2.9}$$

iv. Thermal decomposition of inorganic aluminium salts, which can generate alpha alumina powder with a purity higher than 99.99%:[186]

$$2NH_4AlO(OH)HCO_3 \rightarrow Al_2O_3 + 2NH_3 + 2CO_2 + 3H_2O \quad \text{R2.10}$$

2.3.3 Crystal Structure and Electronic Properties of Bulk α-Al_2O_3

The crystal structure of α-Al_2O_3 belongs to the $R\bar{3}c$ space group, with either the trigonal unit cell, that is, hexagonal coordinated with six formula units consisting of 30 atoms in total, and/or the rhombohedral unit cell consisting of two molecular units (i.e. ten atoms).[187] The α-Al_2O_3 unit cell displays a close-packed ABAB alternating sequence stack of oxygen ions and Al ions, which occupies two-thirds of the six-fold coordinated sites between the oxygen layers.[188] Figure 2.12 shows the crystallographic classifications of both the trigonal and rhombohedral unit cells of α-Al_2O_3.

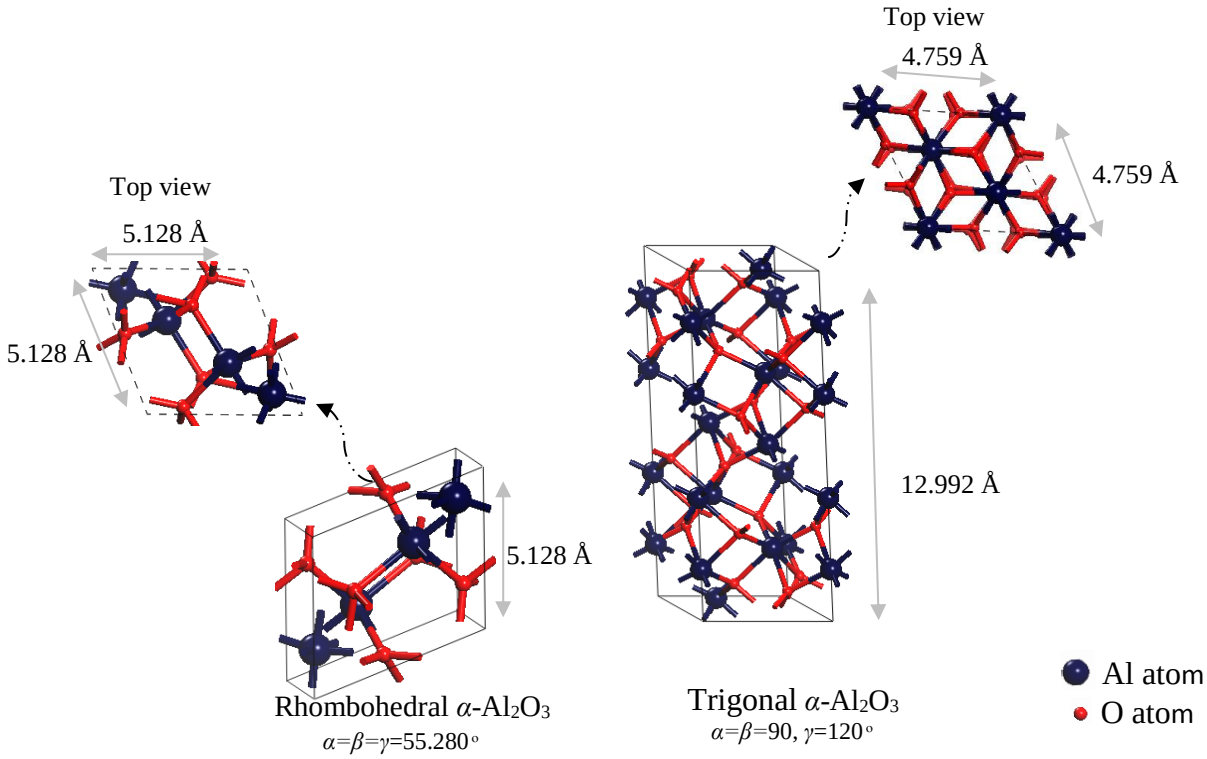

Figure 2.12. Crystallographic classification of both trigonal and rhombohedral unit cells of α-Al_2O_3.

Figure 2.13 illustrates our computed electronic band structure and the total density of states (DOS) of bulk α-Al_2O_3. The system represents a wide insulating gap of 6.31 eV, which is consistent with other theoretically calculated values stated for α-Al_2O_3, namely 6.26 eV[189] and 6.32 eV[187]. A notable difference between the upper valence (UVB) band and the conduction band (CB) was observed by Mousavi et al.[187] Unlike the flat behaviour of the electron states at the top of the VB, CB displays a large curvature, indicating a large effective whole mass of the VB, as well as a good mobility for electrons at the CB.[187]

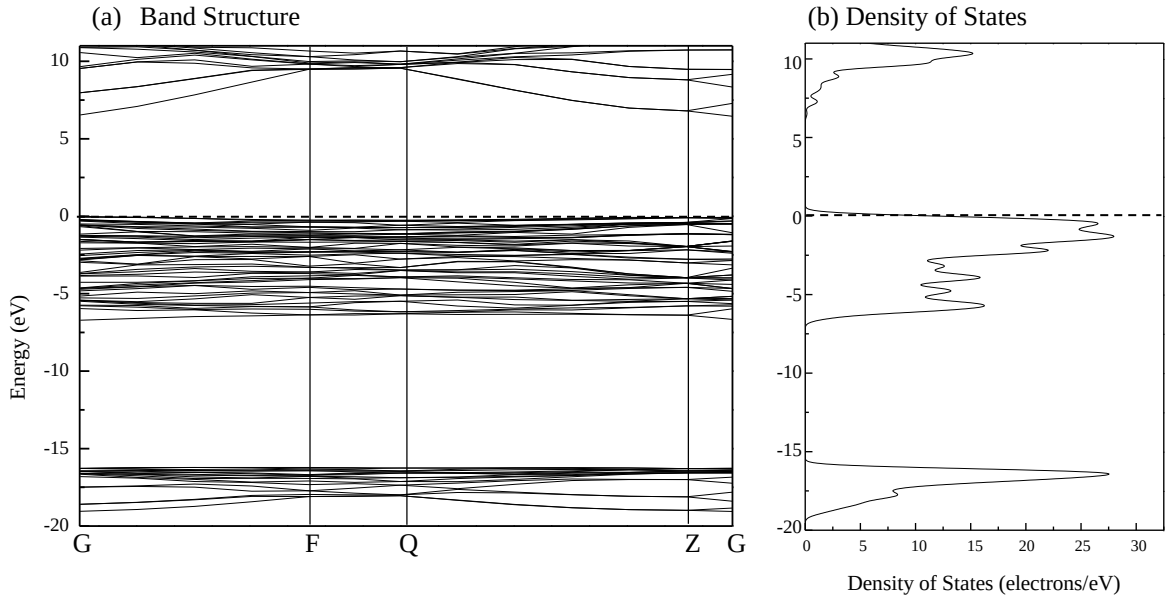

Figure 2.13. Electronic properties of bulk α-Al_2O_3. (a) Electronic band structure. (b)Total density of states.

The calculated DOS contains two valence bands; UVB and lower valence band (LVB). The LVB extends from19.9 to -15.2 eV and mainly consists of two peaks located at approximately -17.6 and -16.4 eV, while the UVB extends from -7.5 to 0.91 eV. The UVB consists of many peaks that act as source of electrons contributing to the transition to the conduction band.[187] The calculated ionic band gap (gap between UVB and LVB) was found to be 7.7 eV; this is consistent with reported results by Perevalov et al.[189] of 8.9 eV. Clearly, such a band gap confirms the ionicity of bulk α-Al_2O_3 (i.e. +1.092*e* and -0.702*e* are reported atomic Mulliken charges for Al and O atoms, respectively.[190])

2.3.4 α-Al_2O_3 (0001) Surface

The structure of a bulk hexagonal unit cell of α-Al_2O_3 affords different non-equivalent low-index plane orientations. Of these orientations, the α-Al_2O_3 (0001) surface is the most thermodynamically stable configuration.[191] The (0001) surface of α-Al_2O_3 has been a subject of numerous experimental[192-197] and theoretical[198-205] investigations since it is a widely used as a substrate in many catalytic-based applications. The (0001) surface of α-Al_2O_3 (shown in Figure 2.14) displays three distinct atomic terminations on the surface: Al termination with Al surface layer followed by an O layer; O termination with oxygen surface layer followed by an Al layer; and Al double termination with an Al surface layer followed by an Al layer (refer to Figure 2.14).

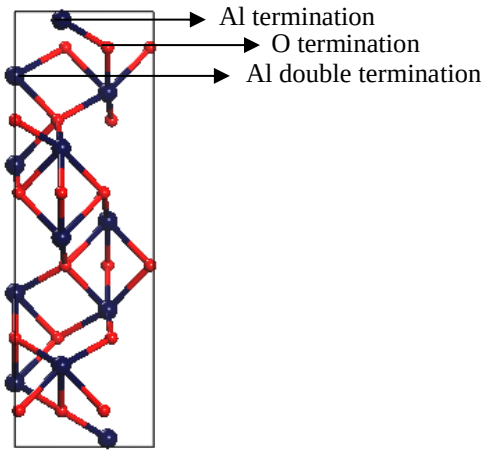

Figure 2.14. α-Al_2O_3 hexagonal unit cell. The terminations labelled Al, O, and Al double can serve as ideal terminations for the 0001 surface (i.e.,a bulk-like termination).

Recent investigations[194-195, 206-207] on α-Al_2O_3 demonstrated the Al termination to be the most energetically stable. Tasker[206] attributed this stability, from electrostatic and electronic considerations, to the non-polarity of this termination. Unlike the other terminations, the net

dipole moment of Al termination, resulting from the staking Al-O-Al, stands at zero. Other analogous studies[202, 204-205] attribute the profound stability of the three terminations to the stoichiometry at the surface, which depends on the alumina/oxygen chemical potential. For instance, the Al-terminated surface assumes a bulk-like termination. Therefore, its energy is independent of the Al and/or O operating chemical potential.

Early research on α-Al_2O_3 focused on estimating the relaxation of the (0001)-Al terminated surface. Theoretical calculations of Manassidis et al.[208] using the density function theory within the local density approximation (LDA) framework predicted that the surface displays a significant inward relaxation, which involves a downward displacement of the Al layer (i.e. the first layer) toward the O layer (i.e. the second layer) of 85% relative to the bulk. This results was later confirmed through a similar theoretical approach by Kruse et al.[209] The large surface relaxation was also confirmed by Verdozzi et al., who obtained a very similar relaxation of 87%.[203] However, x-ray diffraction[203] and ion-scattering[194] experiments conclude a relaxation of 35%, this is significantly lower than the value predicted by theoretical modelling.

The debate regarding the interpretations of the large inward relaxation of the surface Al layer has been expanded with the argument that the large relaxation behaviour of the surface is related to the formation of an sp^2 bond between the Al and O surface atoms.[210] Batyrev et al[201] stated that the large relaxation is unlikely to be related to the formation of sp^2 because there is no evidence of sp^2 bonding in any of the experimental and theoretical studies. However, the authors attribute this strong relaxation to the electrostatic force.

2.3.5 Hydration of Alumina

As a prominant stand-alone and support of catalysts deployed in many chemical reactions, the hydration of alumina has received considerable critical attention, where the chemistry of the surface is affected greatly, and accordingly its reactivity, polarity, and catalytic performance. It has been investigated using various surface science techniques. All of these proved that the interaction occurs via acid-base interactions.[211] The adsorption of water on alumina surfaces principally involves chemisorption, quasichemisorption, physisorption, and capillary condensation, which translates into more profound interactional complexity.[212]

In an experimental study using the NMR technique, Rui et al.[213] investigated the interaction of alumina and water molecules. They showed that through chemical shift changes (δ_H) and spin-lattice relaxation (T_1), water exists over the alumina surface in three different states; bound water, pore water, and bulk water. Adsorbed water constitutes hydrogen atoms bonded with the alumina surface and accordingly it has the highest chemical shift value and the shortest relaxation time. Conversely, bulk water has the lowest chemical shift value and longest relaxation time. The authors also found an inverse correlation between the chemical shift value of the adsorbed water and the temperature, which has been attributed to the effect of the temperature on the speed of the molecular motion. As the temperature increases, the gained molecular speed increases the tendency of the bound water to leave the surface; this process led to a decrease in the average chemical shift. Another experimental study, conducted by McHale et al.[214], showed that 33% of adsorbed water is chemisorbed. Likewise, Coustet and Jupille[215], via resolution electron energy loss spectroscopy, demonstrated that water adsorption over alumina mainly occurs by dissociative adsorption. This was also been confirmed by the temperature programed desorption (TPD) study carried out by Eslam et al.[216]

Initially, it was very challenging to underpin the nature of the surface sites and to ascertain the dissociation sites of water. A number of studies[212, 217-218] postulated that co-ordinately unsaturated Al surface atoms acts as Lewis acid sites and accordingly attract the water's O atom, whereas the O surface atom performs as a Lewis base site attracting the water's H atom, which is the leading cause for the formation of hydroxyl groups over the alumina surface. This concept was subsequently confirmed by several theoretical[219-220] and experimental[221-224] investigations.

2.3.6 Acidity and Basicity of Alumina

The α-Al_2O_3 (0001) surface consists of co-ordinately unsaturated sites. Accordingly, the surface is easily covered by different types of adsorbed species. The difference in the coordination number of Al^{+3} surface atoms (i.e. tetrahedral and/or octahedral) leads to the formation of a variety of chemical sites on the alumina surface, which has a pivotal role in chemical processes.[225] Furthermore, the ratio of the Al^{+3} ion, including both coordination sites, and the oxygen lattice density can result in various transition aluminas, making the surface chemistry of alumina a highly complex subject .[169, 225-226]

Water, as an abundant component, constitutes the most commonly adsorbed species. Depending on the temperature and pressure, water adsorbs on the surfaces either physically (i.e. non-dissociated) via hydrogen bonding and/or chemically (i.e.; dissociated) forming surface hydroxyl groups.[227]

Water dissociation over the alumina surface leads to the formation of a surface hydroxyl group;[227-228] starting from the physisorbed (non-dissociated) interaction at room temperature. With the increase inemperature, water gradually desorbs from the surface changing the chemistry of the surface significantly.[228-230] The extent of the dehydration of alumina has a pivotal role in controlling the surface acid-base properties. For instance, desorbing one water molecule from two adjacent hydroxyl group causes a strained oxygen bridge to form, followed by the appearance of active Lewis acid base sites.[231] However, this change does not terminate at this point. According to Yamadaya (1965),[232] when an alumina surface co-exists with a sufficient amount of water, the surface Lewis acid sites are converted into (very weak) BrØnsted acid sites, arising from the basic properties of the surface. Figure 2.15 illustrates a simple schematic of the generation of acidic-basic sites and BrØnsted acid sites over the alumina surface.[231, 233]

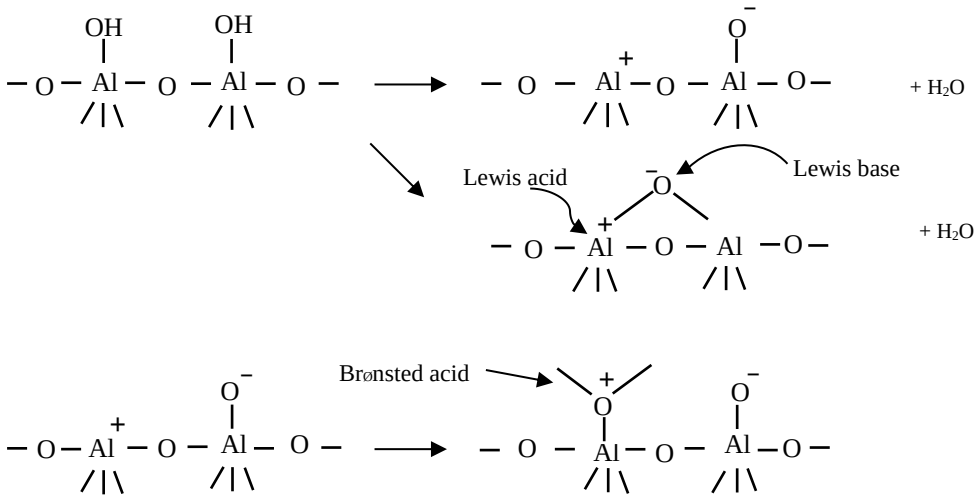

Figure 2.15. Formation of Lewis acid base site over alumina surface. [231, 233]

Both Lewis acid base sites, which are generally generated after dehydration/ dehydroxylations,[234-240] have been thought of as a key factor in deriving the catalytic activity

of alumina surfaces.[231] Different models of surface hydroxyl group have been suggested to elucidate the reactivity of alumina surfaces.[227]

2.3.7 Models of Surface Hydroxyl Group over Alumina Surfaces

2.3.7.1 Peri's Model

Peri's model considers five distinct hydroxyl groups on the γ-Al_2O_3 (100) surface, namely A, D, B, E, and C. The five hydroxyl groups are different from each other in terms of the number of oxide neighbours. (i.e. from zero to four nearest neighbours, respectively).[230] Figure 2.16 displays Peri's model of the hydroxyl group, whereas Table 2.6 presents the calculated frequency and the symbol of the reported hydroxyl group in all models. The key limit of Peri's model is the assumption that the 100 surface constitutes the only possible termination of the crystal. Therefore, Peri's model is unable to encompass the entire hydroxyl group of transition aluminas.

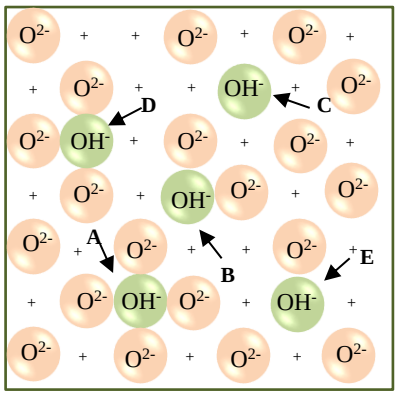

Figure 2.16. Peri model representing five different types of surface hydroxyl group. (+ represents Al^{+3} of lower layer).[233]

Table 2.6. Types of hydroxyl group on alumina transition.[227]

OH bond	Frequency (cm^{-1})	Peri [230]	Tsyganenko [241-242]	Knozinger [226]	Busca's assignment [243]
1	3800	A	I	Ib	Al^{IV}
2	3775	D	I	Ia	-O- Al^{IV}
3	3745	B	II	IIb	Al^{IV}
4	3730	E	II	IIa	-O- Al^{IV}
5	3710	C	III	III	Bridged
6	3690	C	III	III	Bridged
7	3590	H-Bonded		H-bonded	Tribridged

2.3.7.2 Tsyganenko's Model

Tsyganenko et al.[241] repealed Peri's model, arguing that the number of nearest neighbour does not effect the frequency of the hydroxyl group species. The authors considered all passible terminations of the alumina surfaces, and subsequently devised a new classification. Depending on the number of surface cations to which the hydroxyl groups are attached, Tsyganenko et al.[241] classified the surface hydroxyl group into three different types, as portrayed in Figure 2.17.

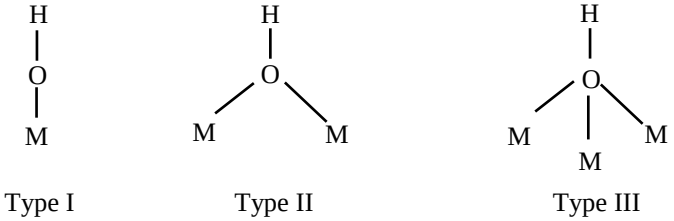

Figure 2.17. Surface hydroxyl groups based on Tsyganenko's classification.[227]

2.3.7.3 Morterra's Model

Unlike Tsyganenko's model, Morterra et al.[244-245] considered the coordination of the surface cation (i.e. Al) as a key factor in determining the surface hydroxyl group frequencies. The authors onsidered all Al-containing systems; thus, this model can only give a general idea of the hydroxyl spectra of different Al oxides. Figure 2.18 displays Morterra's model of the hydroxyl group in transition alumina and other Al-containing oxide systems.

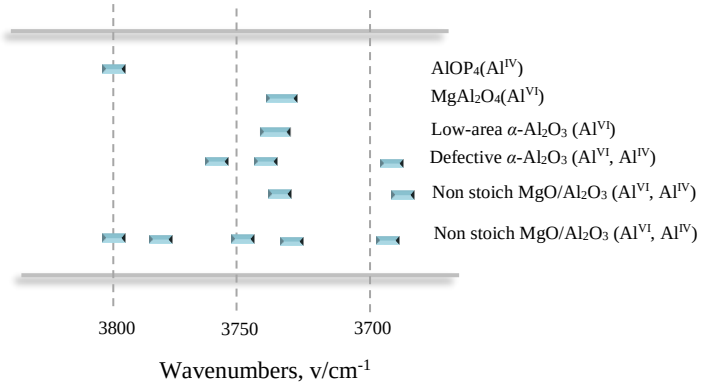

Figure 2.18. Surface hydroxyl groups based on Morterra's model.[227]

2.3.7.4 Knozinger's Model

Knozinger's model is based on three basic assumptions. First, crystalline alumina can exists within the three main possible terminations of 111, 110, and 100. Second, each termination consists of anions and cations array bulk-like exposition. Third, there is no possibility for either surface reconstruction and/or ion migration, even at high temperatures. Herein, the net electrical charge at the hydroxyl group is considered as a key factor in determining the surface hydroxyl group frequencies. Accordingly, hydroxyl groups have been classified into five different groups, as seen in Figure 2.19.[226-227, 246]

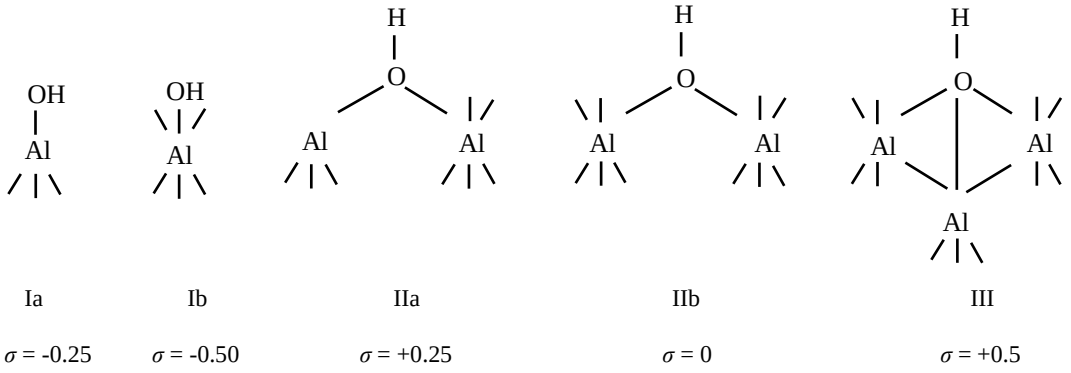

Figure 2.19. Knozinger's model representing five different types of surface hydroxyl group. (σ net electrical charge at hydroxyl group which is determined by the coordination of both hydroxyl group and Al surface cation).[233]

2.3.7.5 Busca's Model

Basca's model represents a modification of the of the previously reported Knozinger's model, which takes into consideration the role of surface cation vacancies as well as the coordination of the cation.[227, 243, 247] Five different hydroxyl groups were characterised, as shown in Figure 2.20.

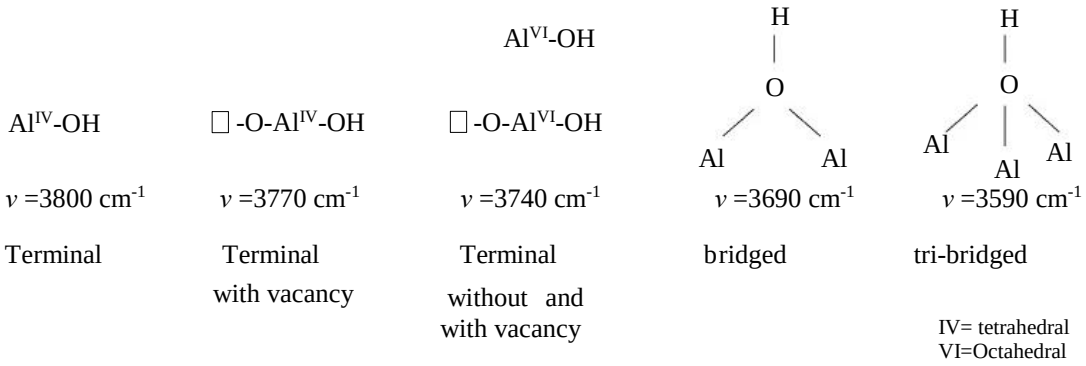

Figure 2.20. Basca's model representing five different types of surface hydroxyl group. □ denotes a cation vacancy. [233]

Chemical sites over alumina surfaces have been detected experimentally either directly by the O-H stretch using infrared (IR) spectroscopy[230, 248] (i.e. Brønsted acids sites, Al-OH) and/or indirectly by the adsorption of IR-absorbing probe molecules (i.e. Lewis acid-base sites, Al^{+3} & O^{-2}).[249-250]

Apart from previous models, authors[225, 230, 248] used the IR spectroscopy observations to classify surface hydroxyl groups into two main groups: isolated hydroxyl groups with sharp infrared bands (>3600 cm^{-1}), and self-associated hydroxyl groups with broad intense bands (<3600 cm^{-1}). Furthermore, self-associated hydroxyl groups differ from the isolated ones in the presence of the hydrogen bond connection between each group. The isolated hydroxyl group has been classified, based on Knozinger's model, into five different types. Figure 2.21 displays a schematic diagram including both types of hydroxyl groups and their frequencies.

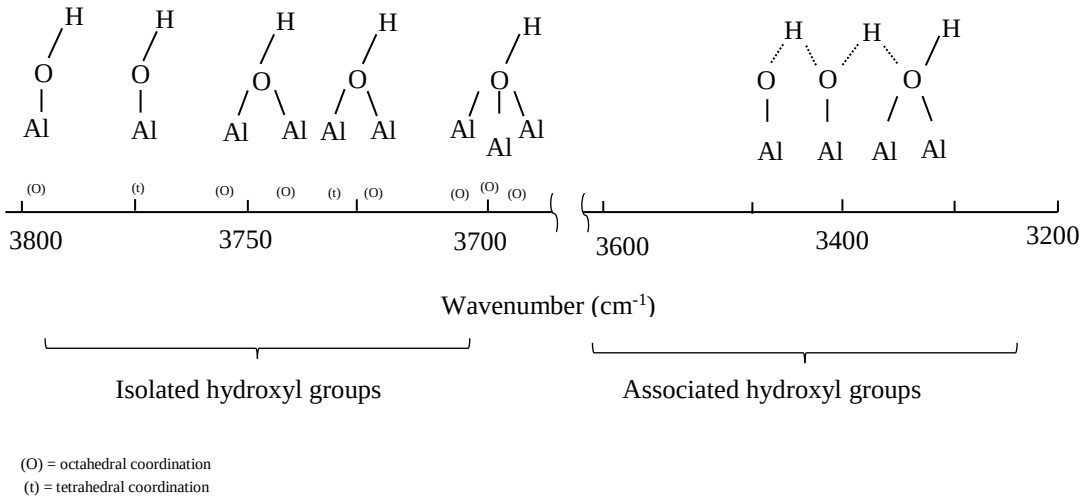

Figure 2.21. Frequency of hydroxyl group over alumina surface. [225]

2.3.8. Water Interaction with the α-Al_2O_3 (0001) Surface

A large and growing body of experimental and theoretical literature has investigated the interaction of the α-Al_2O_3 (0001) surface with water molecules, all of which prove that the α-Al_2O_3 (0001) surface is highly reactive toward water molecules in producing surface hydroxyl groups.[199, 214, 219, 222, 224, 251-256]

A variety of experimental techniques, such as photoemission,[224] thermal desorption,[222] calorimetric[199, 214] and vibrational spectroscopy[253-254], have indicated that the amount of water exposed to the surface is a principal determining factor of the hydrolysis process. For instance, at low water exposure, hydroxylation of the surface occurs through the active defect sites, whereas a high volume of water exposed to the surface results in the breaking of the Al-O surface bond, and accordingly hydroxylation of the basal plane.

Literature DFT investigations[219, 251, 257-259] have confirmed the analogous experimental finding. These studies described in detail the steps of the basal plane hydroxylation, which starts by breaking one of the three equivalent Al_s-O_s surface bonds. Following the fission of multiple surface Al_s-O_s bonds, fully hydroxylated (0001) or gibbsite-like alumina is formed as depicted in Figure 2.22:

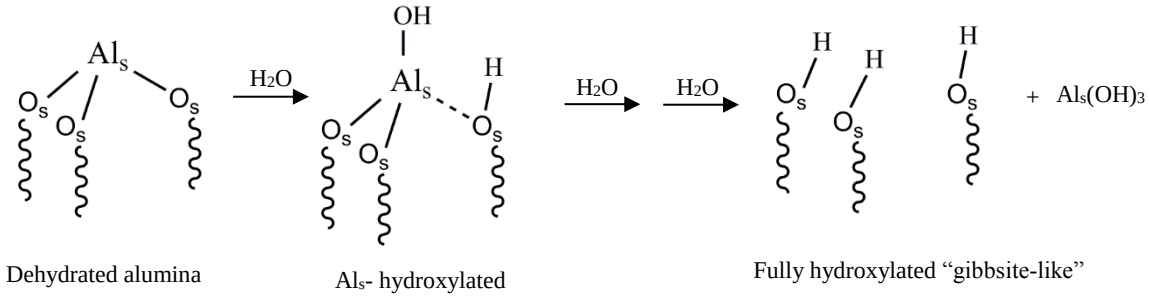

Figure 2.22. Hydrolysis process of α-Al_2O_3 (0001) surface.[256]

Hass et al.[219, 251] reported that the initial dissociation steps (i.e. at low water exposure) are facile and thermodynamically favoured. They even occur at ambient temperature with a trivial activation energy. In a follow-up study, Ranea et al.[256] used plane-wave DFT to determine that the following steps (i.e. at higher water exposure) proceed along more complex reaction coordinates and occur with higher activation energy than that of the opening step. The authors also confirmed that the α-Al_2O_3 surface composition is highly correlated to the sample history, which may in turn be a key factor in the hydrolysis process.

It has been shown that water adsorption over the α-Al_2O_3 (0001) surface produces three different states, as shown in Figure 2.23.

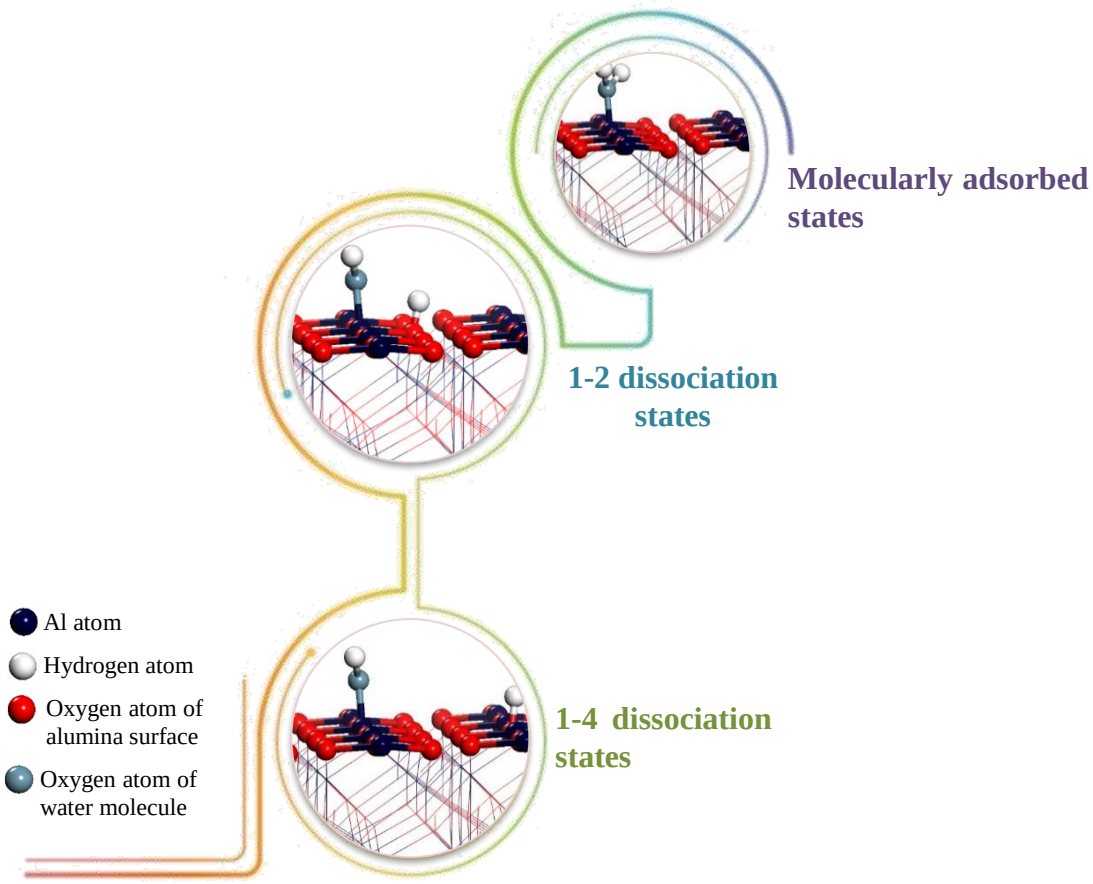

Figure 2.23. Water over α-Al_2O_3 (0001) surface.

A 1-2 dissociative pathway (when a water molecule dissociates on the same Al-O surface bond) is the most kinetically feasible mechanism, where the Al surface atoms are hydroxylated and the nearby oxygen atoms are protonated. This is followed by a 1-4 dissociation pathway, where water dissociates over two different Al-O bonds. The calculated binding energies for the three states, as reported by Hass et al. [219] in their ab initio molecular dynamic study, were predicted to be 97, 139, and 135 kJ/mol, respectively. Wittbrodt et al.[257] employed ab initio computations to investigate the interaction of water molecules with Al_8O_{12} cluster, mimicking the extended α-Al_2O_3 (0001) surface. The authors found that dissociation occurs rapidly over the surface (i.e. 10^{-2} s) after the water has been physically (i.e. molecularly) adsorbed. Figure 2.24 presents a potential energy surface for H_2O dissociation on the α-Al_2O_3 (0001) surface.

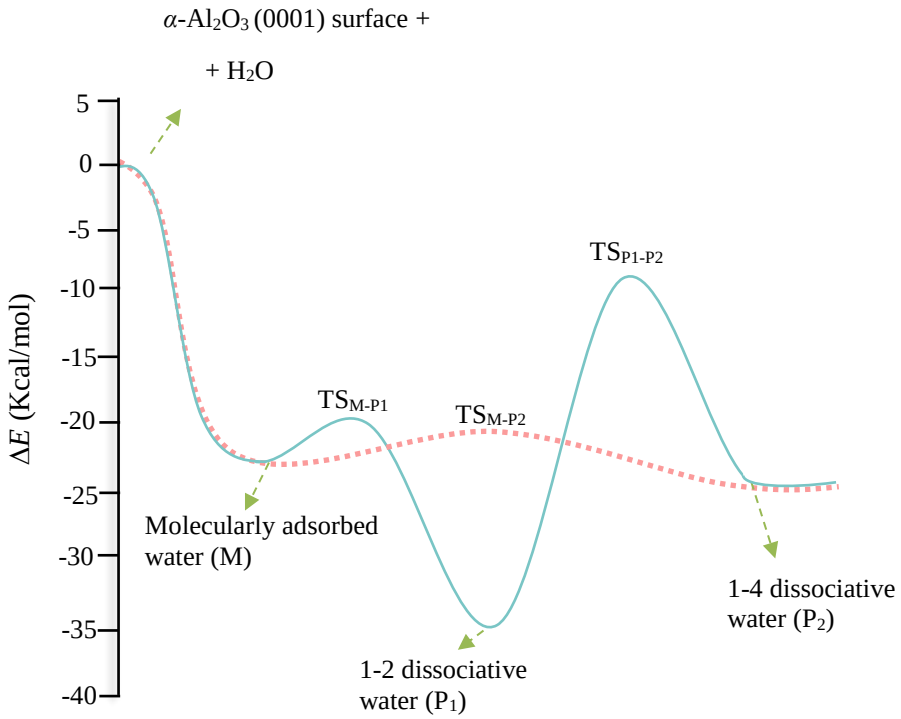

Figure 2.24. Hydrolysis process of the α-Al_2O_3 (0001) surface.[190] TS signifies a transition structure.

Gaigeot et al.[260] used a density functional theory-based molecular dynamics simulation (DFT-MD) to perform a detailed investigation of the behaviour of the (0001) α-Al_2O_3/ water interface as an important aspect in determining the interfacial properties, such as acid/base behaviour, dissolution rate, and surface charging. The authors[260] provide an accurate description of the interfacial hydrogen bonding and electron polarization effects. In addition, based on interfacial hydrogen bonding, they classified the surface hydroxyl groups into two sites; (i) strong and short H-bonding donors, and (ii) weak and long H-bonding acceptors. Alternately, one is in the surface plane and the other is pointing out from the surface, as seen in Figure 2.25.

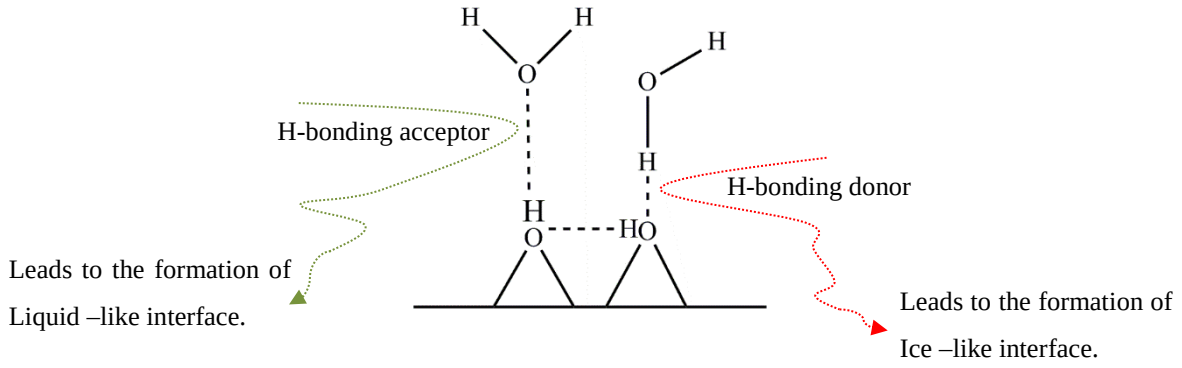

Figure 2.25. Hydrogen bonding network in the (0001) α-Al_2O_3/ water interface.[260]

The calculated average charges on the O and H atoms of the hydroxyl group were found to be -0.84 and 0.28 *e*, respectively, which is the key electronic descriptor dictating the strength and weakness of both sites.[260] The authors[260] also found that both the H-bonding acceptor and H-bonding donor sites lead to the formation of two species of water molecular interfaces namely, liquid-like interface and ice-like interface, respectively. The literature[254, 260-264] provides further information on the vibrational spectroscopy of these two interfaces. Two different spectrum broadbands have been detected; 3200 cm^{-1} peak and 3400 cm^{-1} peak, which are referred to as ice-like interface and liquid-like interface, respectively. Furthermore, the structure of the water/alumina interface was found to be greatly affected by the change in the pH of the reaction medium.[264-266]

The catalytic properties (i.e. activity and selectivity) of the alumina surface are directly correlated to the chemistry of the surface where the hydrolysis process ensues a critical role. Evidence suggests that heating and cooling processes are among the most important factors where the degree of hydration coverage (i.e. acidity and basicity of the surface) is highly sensitive to temperature.[267] Based on the results of the IR and NMR measurements, heating and cooling processes can either reversibly add or remove hydroxyl groups on the surfaces.[268-

[269] Furthermore, it has been observed experimentally, in a microcalorimetry study conducted by McHale et al.[214], that the degree of hydration over the α-Al_2O_3 (0001) surface is mainly associated with the drying temperature, in which heating at temperature of > 1000 K dehydrates the surface to almost < 9 OH/nm^2, whereas at a lower temperature of 600 K, the extent of surface hydroxyl group coverage stands at 15 OH/nm^2. Using X-ray photoelectronic spectroscopy (XPS),[270] TPD and laser-induced thermal desorption (LITD) measurements,[216] it was found that the formation of the surface hydroxyl group over (0001) α-Al_2O_3 is observed at a temperature as low as 300 K.

In a laser-induced thermal desorption and TPD study of alumina hydration, Nelson et al.[223], investigated the desorption of water from the α-Al_2O_3 (0001) surface. They showed that the water desorption process takes place over a wide range of temperature (i.e. 300 to 500 K), concluding that the alumina surface includes different surface hydroxyl groups with different binding energy ranging from 96 to 172 kJ/mol. A seminal study in this area is the work of Hendriksen et al.[271] The authors demonstrated that molecular water is more readily removable compared to surface hydroxyl groups, in which the latter remains on the surface even at 1273 K.

2.3.9 Effect of Surface Hydration on the Catalytic Activity of Alumina

It has become evident that [228-231, 272] the chemical makeup (i.e. adsorption and decomposition) of the hydroxyl groups over the alumina surface constitutes a key factor in clarifying the

reactive/catalytic nature of alumina.[216, 273-274] However, the relationship between the reactivity, surface structure, and the degree of hydrations remains open to debate.[265]

An experimental study by Ballinger and Yates[275] on the behaviour of alumina at high temperature revealed that dehydration of alumina occurs in the temperature range of 475-1200 K. The authors also observed a linear correlation between the decreasing integrated absorbance of the hydroxyl group with the increasing integrated absorbance of physisorbed Al^{+3}-CO. Another experimental study, using Fourier transform (FT) IR spectroscopy, confirmed that the heat of adsorption over alumina surfaces (i.e. both α- and γ-alumina powders) depends primarily on the degree of hydration prior to water adsorption.

Data from several sources have identified that the increased reactivity of the surface atoms on the alumina surfaces is associated with lower atomic coordination numbers, whereby the lower the coordination, the higher the surface acidity or basicity. In a study investigating a selective probe for tri-coordinate Al ‘‘defect’’ sites on 110 and 100 terminations of γ- and δ-alumina, Wischert et al.[276] reported that the fully dehydrated 110 surface in both transitions displays three different Lewis acid sites; tri-coordinated (Al_{III}), tetra-coordinated (Al_{IVa}), and tetra-coordinated (Al_{IVb}), whereas the fully dehydrated 100 surface encompasses two Al_V sites. The authors theoretically addressed the potential of deploying both the 110 and 100 γ- surfaces as scavengers for the N_2 molecular gas; and they found that N_2 molecules are significantly stabilized on the strongest Lewis acid site (i.e. tri-coordinated (Al_{III}), ΔE_{ads} (N_2) -45 kJ/mol). Furthermore, the binding energy correlates with the reduced Lewis acidity of the corresponding sites ($Al_{III} >> Al_{IVb} > Al_V > Al_{Iva}$), as seen in Table 2.7. Along a similar line of enquiry, Joubert et al.[277] demonstrated xperimentally that the tricoordinate Al_{III} strong Lewis acid sites on the

110 surface are the highly reactive sites in dissociating H-H and C-H bonds of H_2 and CH_4 molecules, respectively.

Table 2.7. Calculated adsorption energies of N_2 on the 110 and 100 terminations on γ-alumina.[276]

Adsorption site	ΔE_{ads} (N_2)/kJ/mol
Al_{III}(110)	-41
Al_{IVa}(110)	-8
Al_{IVb}(110)	-15
Al_{V}(100)	-11

In a follow up study by Wichert et al.[278], we investigate the effect of surface hydration on the catalytic activity of the γ-Al_2O_3 (100) surface toward the CH_4 molecule. The authors found that water assumes a pivotal role in the Lewis acidity of the surface in a process that is controlled mainly by temperature. For instance, water physically interacts with Al_{IV} sites, increasing the basicity of the neighbouring O_{surf} atom without making any changes in the Lewis acidity of Al_{III}, which ultimately results in the formation of a highly reactive "frustrated" Al_{III}, O Lewis- acid base site, facilitating dissociation of the C-H bond of CH_4 through lower activation energies. However, prior to the recent work of the same authors,[279] the role of water for the structure, stability, and reactivity of defect sites over the alumina surface was largely unknown. The authors analysed the accuracy and precision of the adsorption of N_2 and CO molecules on the three alumina surface sites (Al_{III}, Al_{IVb}, Al_{IVa}) within different hydration coverages. They confirmed that the reactivity of the surface is not only affected by the atomic

coordination number on the surface, but is also remarkably influenced by the degree of hydration, as demonstrated in Figure 2.26.

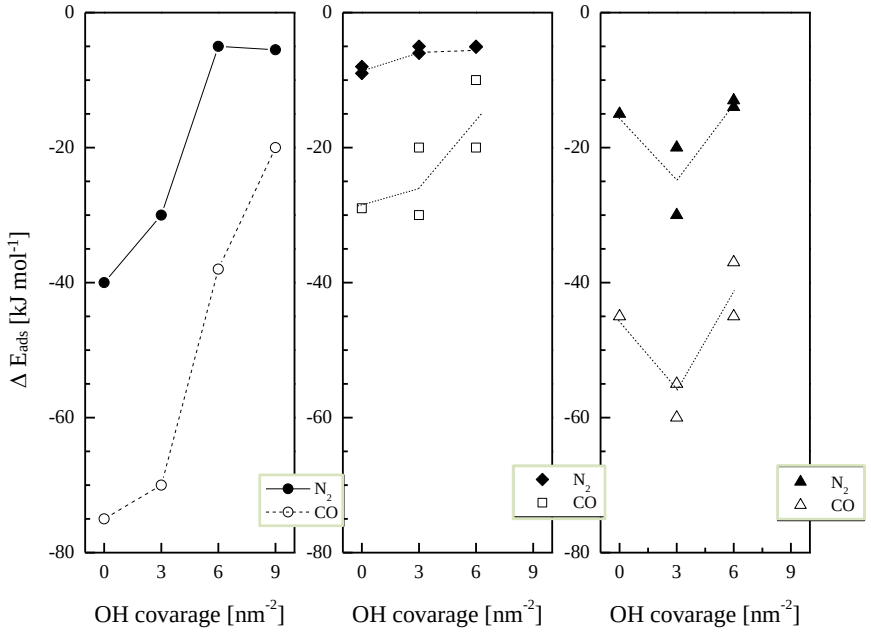

Figure 2.26. Adsorption energy of N_2 and CO molecules on three different Lewis acid sites on the γ-Al_2O_3 (100) surface.[279]

2.3.10 Alumina Mediated Formation of Polychlorinated Dibenzo-*p*-Dioxin and Polychlorinated Dibenzofurans

The main sources of air pollution are typically combustion and thermal processes.[280-281] In light of the size analysis; air pollutants are often divided into three categories as follows [282-286]:

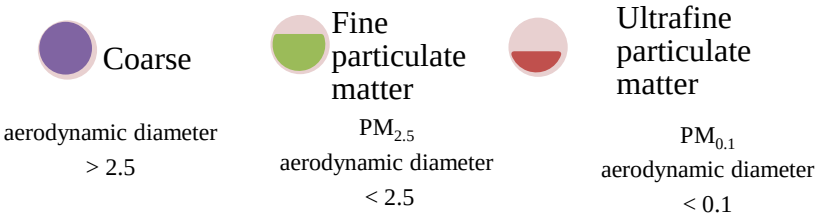

Up to 90% and 70 % of $PM_{0.1}$ and $PM_{2.5}$, respectively, are generally produced from combustion processes (i.e. internal combustion engines, industrial heating, and biomass burning), which are further categorized as either primary particles (i.e. directly emitted particles) or secondary particles (indirectly emitted particles).[287]

Environmentally persistent free radicals are a class of toxic compounds associated with combustion generate airborne fine particles $PM_{2.5}$. They were first demonstrated experimentally by Dellinger et al.[288] in environmental samples collected from different sites, as seen in Figure 2.27. The same research group have later confirmed the presence of the EPFR in irborne fine particles with a high concentration of 10^{1}—10^{18} radicals/g in samples from Baton Rouge city.[289] In addition to the ambient $PM_{2.5}$, EPFR were established on the surface of particles containing active transition metals in the combustion process (i.e.; postflame and cool-zone regions)[288, 290-291] The delocalised electron system of EPFR enables them to resist oxidation by atmospheric oxygen. Oxidative stress induced by the EPFR is analogous to that of reactive oxygen species (ROS, such as OH singlet oxygen, and HO_2). Thus, EPFR can induce serious health problems including chronic respiratory and cardiopulmonary dysfunction [292-293].

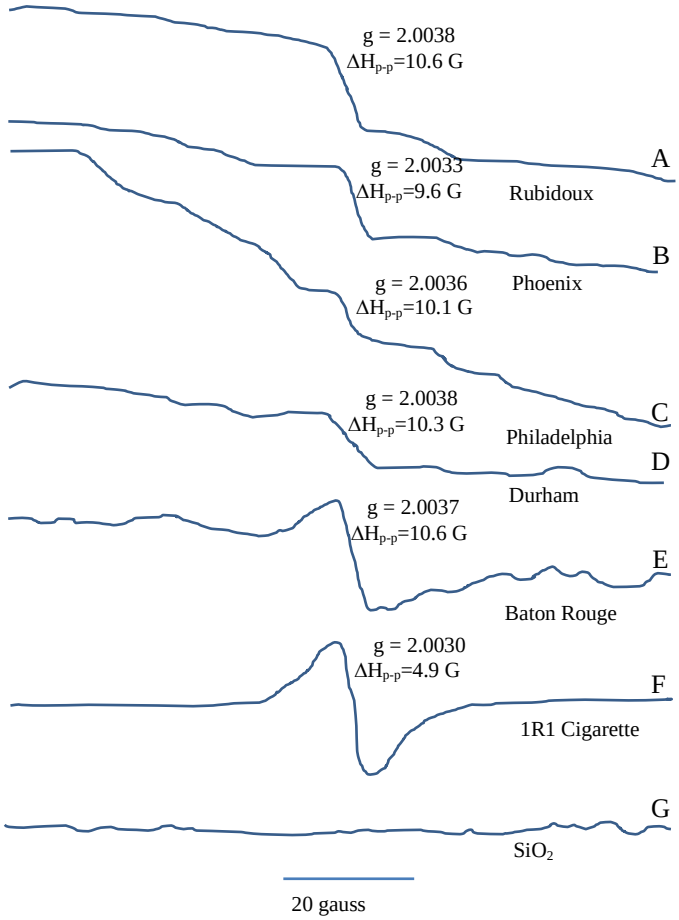

Figure 2.27. EPR spectra of EPFR in $PM_{2.5}$ from different sites in the United States (A-E), tar from one 1R1 research cigarette (F), and ultrapure 0.3 µm, silica (SiO2) (Cab-O-Sil M-5) that was used as a control (G).[288]

Typically, EPFR are produced from the physio-chemical interaction of aromatic hydrocarbons, present in the combustion processes, with metal oxide powder.[291, 294-295] Reliant on the nature of adsorbate (aromatic hydrocarbons) and the temperature, the different EPFR produced are generally classified as either semiquinone and/or phenoxyl type of radicals. Theoretically, it has been demonstrated that the stability of the EPFR stems from resonance stabilization of the phenyl ring. As portrayed in Figure 2.38 EPFR encompasses both carbon-central and oxygen-centred radicals.[290, 296]

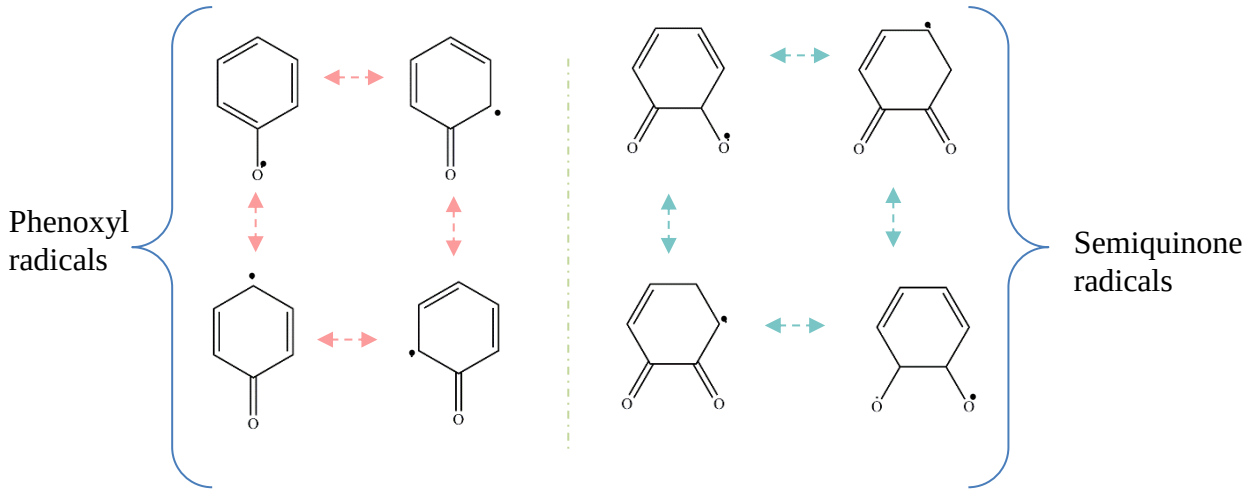

Figure 2.28. EPFR structural types.

The stability of the environmental persistent free radicals primarily depends on two main factors, namely the nature of the precursor molecule and the metal oxides. Figure 2.29 contrasts the half-lives of different EPFR generated over various metal oxides.

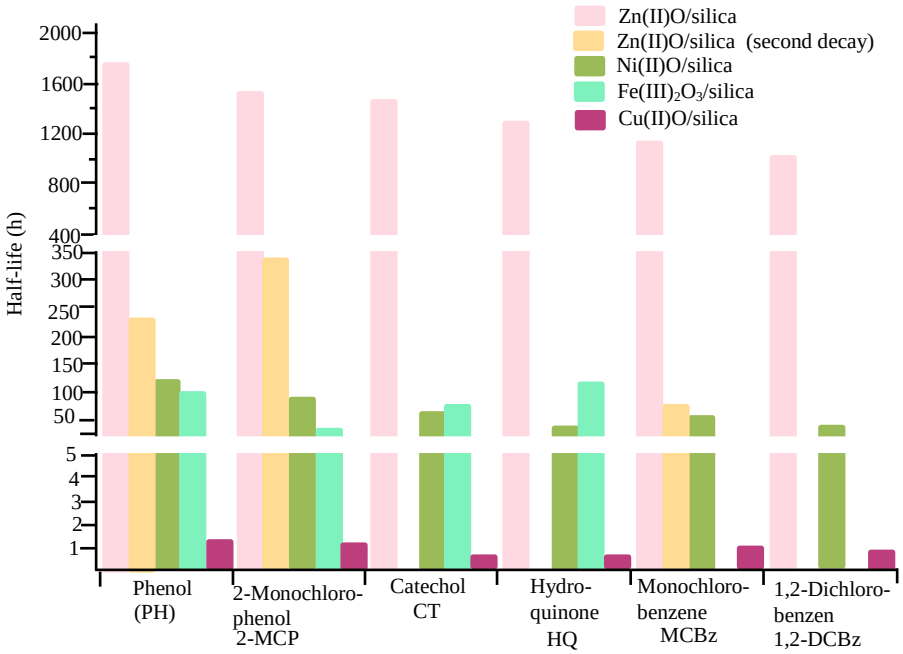

Figure 2.29. Comparison of several half-lives of different EPFR generated over different metal oxides.[297]

EPFR have been recognized as a key intermediate in the formation of persistent organic pollutants, most notably polychlorinated dibenzodioxine (PCDD) and polychlorinated dibenzofurans (PCDF).[298-301] PCDD/Fs are generally formed along two main pathways: (I) high temperature homogeneous synthesis (gas phase reactions in the temperature window of 723–973 K), (II) heterogeneous synthesis (operating in the range of 473 673 K); the latter is divided into two broad channels: precursor synthesis (surface-mediated) and de novo synthesis (oxidation of carbonaceous matrix).

2.3.10.1 Heterogeneous Pathways From the Precursor

In the combustion process, high temperatures produce different type of radicals (i.e. semiquinone and phenoxy), which mainly depend on the precursor present and leads to a series of chemical reactions[302-303] and ultimately the formation of PCDD/Fs and other combustion generated particulate matter.

Figure 2.30 displays the zone theory of combustion for the formation of PCDD/Fs, which provides an overview of the zones of the combustion processes, including the main pathways and the associated temperature window of each zone.

The catalytic formation of PCDD/Fs from the precursor, via forming EPFR, is observed in the last stage of the combustion process, particularly, in the cooling zones of the combustion systems (zone 4). In this part of the combustion process, the temperature typically resides in the range of 423–873 K.

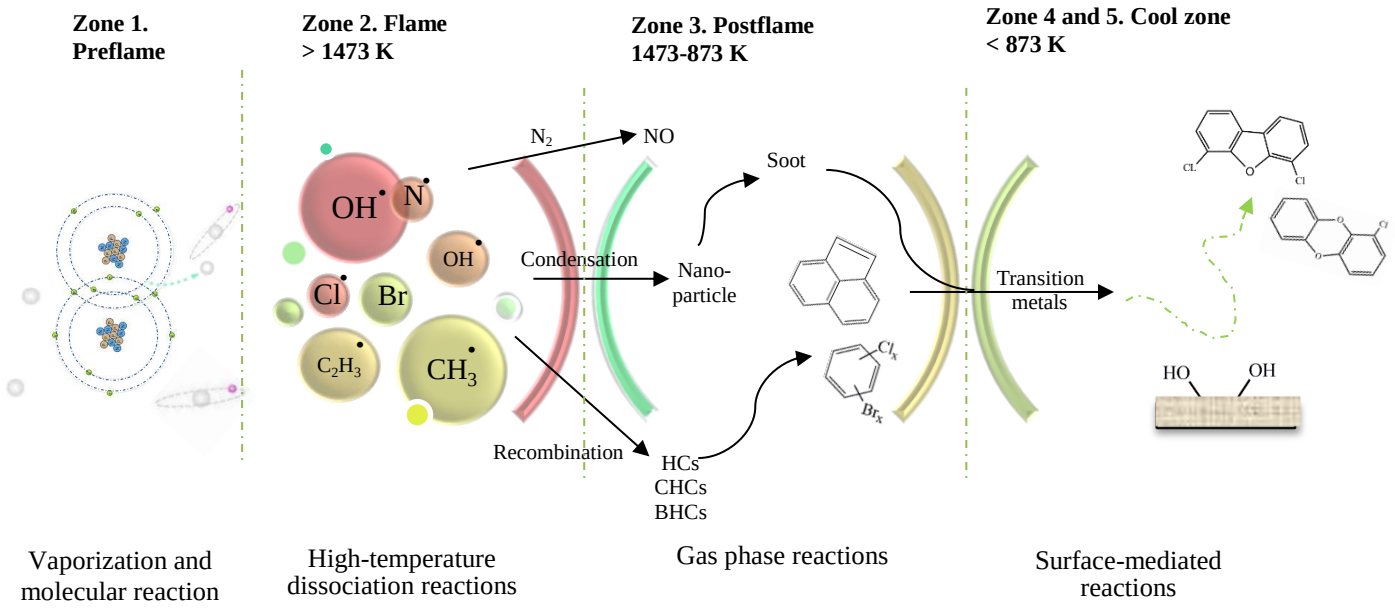

Figure 2.30. Zone theory of combustion in the formation of PCDD/Fs.[289]

EPFR formation has been studied experimentally by many researchers using electron paramagnetic resonance (EPR) spectroscopy and X-ray absorption (XANES) spectroscopy.[290-291, 294-295, 304-307] These studies provided a detailed account of the physiochemical interaction of EPFR precursors with selected metal oxide surfaces (i.e. Fe_2O_3[294]). They indicated that, in the progressive physisorption and chemisorption processes, the surface metal atoms transfer electrons to the adsorbed organic precursors, successively leading to the generation of persistent surface bound radicals. The adsorbed precursor further interacts either with another surface-bound moiety via the Langmuir-Hinshelwood mechanism (L-H, depicted in Figure 2.31) or with a gaseous precursor via the Eley-Rideal (E-R, shown in Figure 2.32) mechanism.

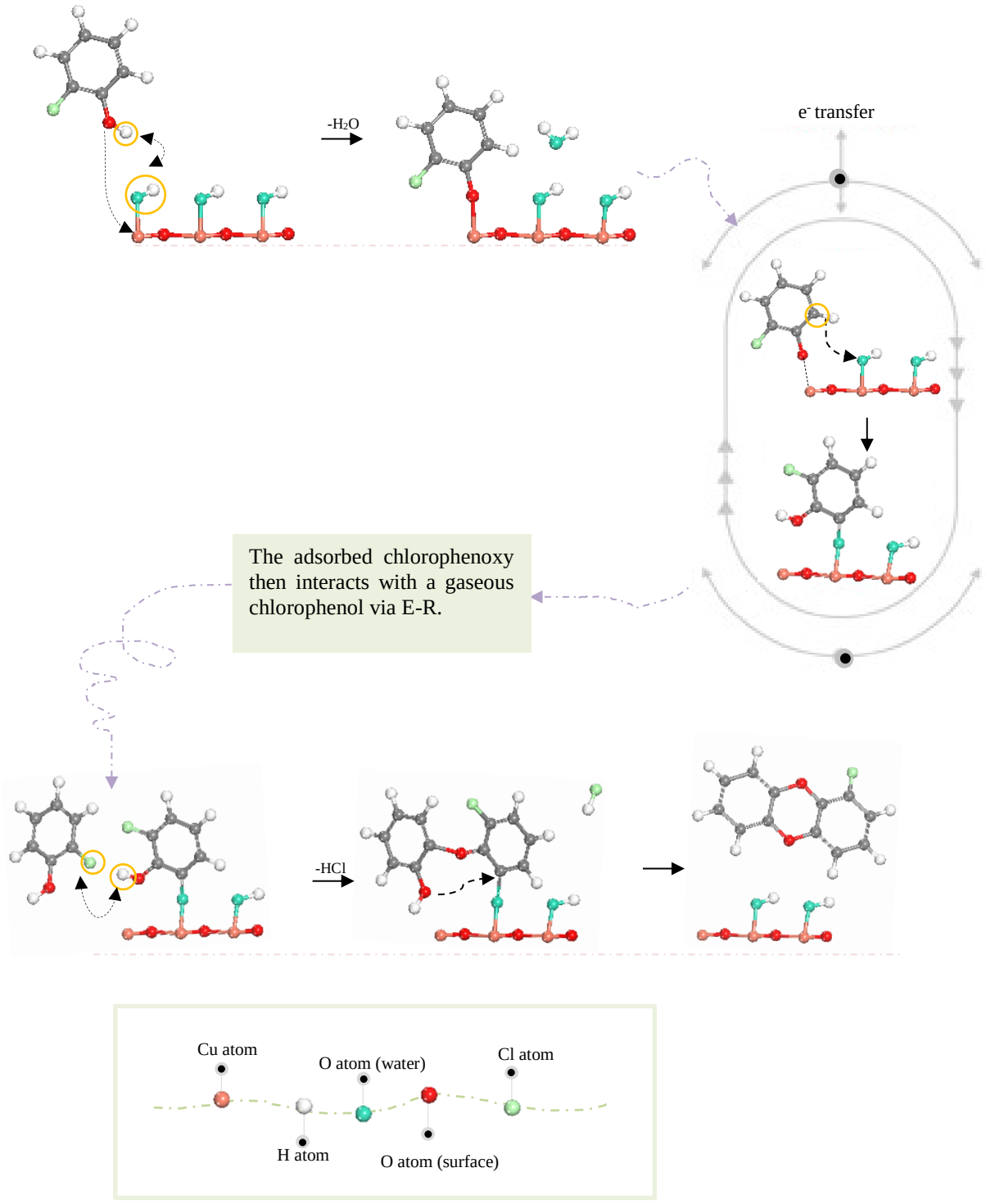

Figure 2.31. Eley-Rideal mechanism for the formation of PCDD/Fs. A case of 2-Chlorophenol on CuO surface. [308]

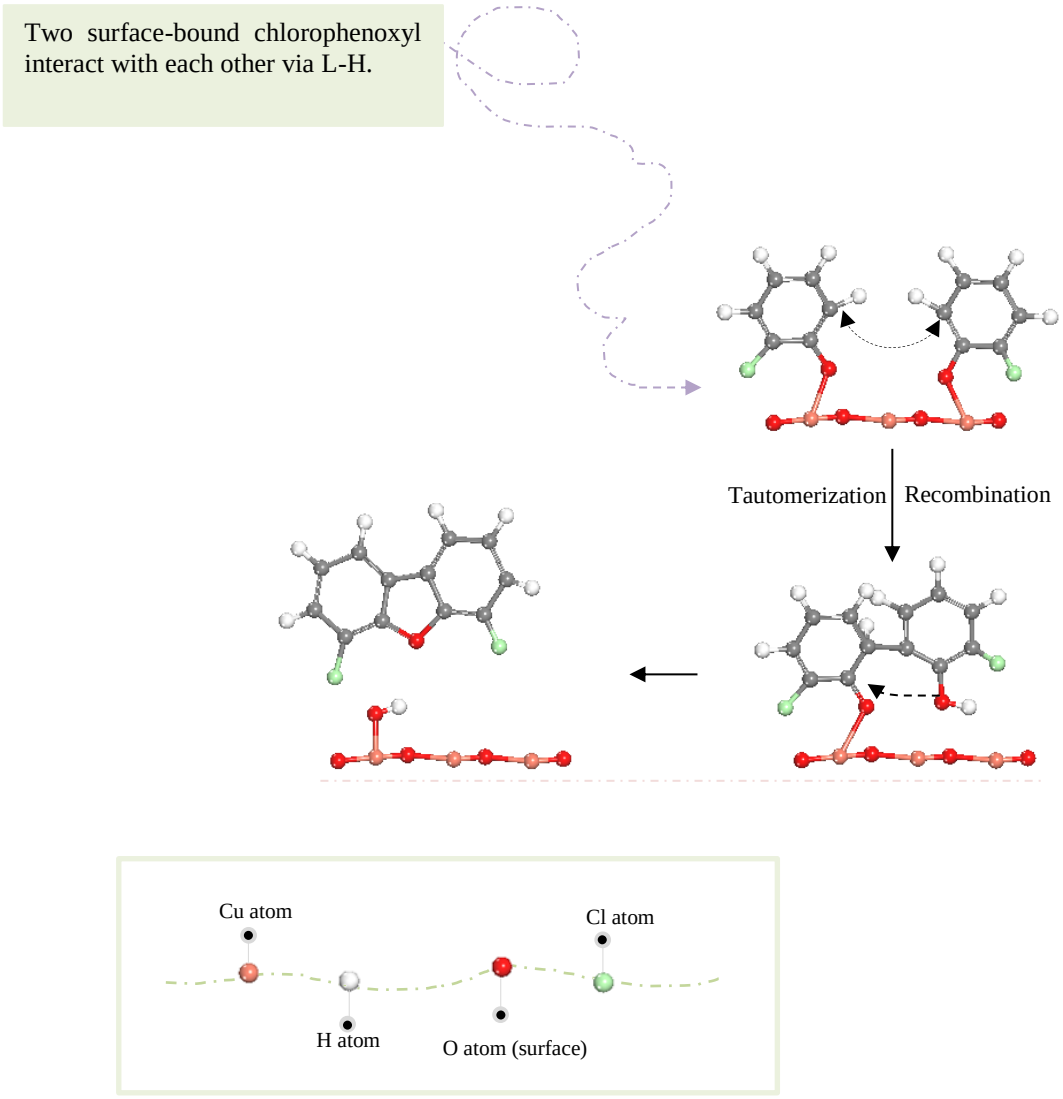

Figure 2.32. Langmuir-Hinshelwood for the formation of PCDD/Fs. A case of 2-Chlorophenol on CuO surface.[308]

2.3.10.2 Role of Alumina

Alumina exists as one of the most abundant metal oxides in $PM_{2.5}$ encountered in combustion systems.[309-311] Its concentration in $PM_{2.5}$ can reach 13-16% by mass.[312] Table 2.8 displays the concentration of alumina and other oxides in fly ash generated from different coal types.

Table 2.8. Concentration of selected oxide in fly ash generated from different coal types.[312]

Component (wt%)	Bituminous	Sub-bituminous	Lignite
SiO_2	20-60	40-60	15-45
Al_2O_3	5-35	20-30	10-25
Fe_2O_3	10-40	4-10	4-15
CaO	1-12	5-30	15-404
MgO	0-5	1-6	3-10
SO_3	0-4	0-2	0-10
Na_2O	0-4	0-2	0-6
K_2O	0-3	0-4	0-4
LOI	0-15	0-3	0-5

A great deal of research has evidenced that alumina, among the most important transition metals in $PM_{2.5}$, plays a crucial role in the formation of PCDD/Fs. For instance, Patterson et al.[304] used electron energy loss spectrometry (EELS) to elucidate the mechanism of EPFR formation over a γ-Al_2O_3 surface. The authors report a noticeable shift in π–π* transition of the chemisorbed phenol, suggesting that the appearance of this precursor governs the generation of phenoxyl EPFR. A recent experimental study by Potter et al.[313] demonstrated the contribution of alumina, α and γ-Al_2O_3, as well as aluminosilicate to the formation of PCDD/Fs from the catalytic oxidation of a 2-monochlorophenol precursor (2-MCP). The authors verified that both alumina and aluminosilicate exhibit an important role in the PCDD/F

formation. However, the yield of PCDD/Fs mediated by α-Al_2O_3 was only 0.4% (by % wt of the initial reactant). Figure 2.33 displays the PCDD/Fs yields from the oxidation of 2-MCP over selected surfaces including both alumina α and γ-Al_2O_3 surfaces. Despite the results of these experiments, a systematic mechanistic understanding of how alumina facilities the formation of EPFR is still lacking.

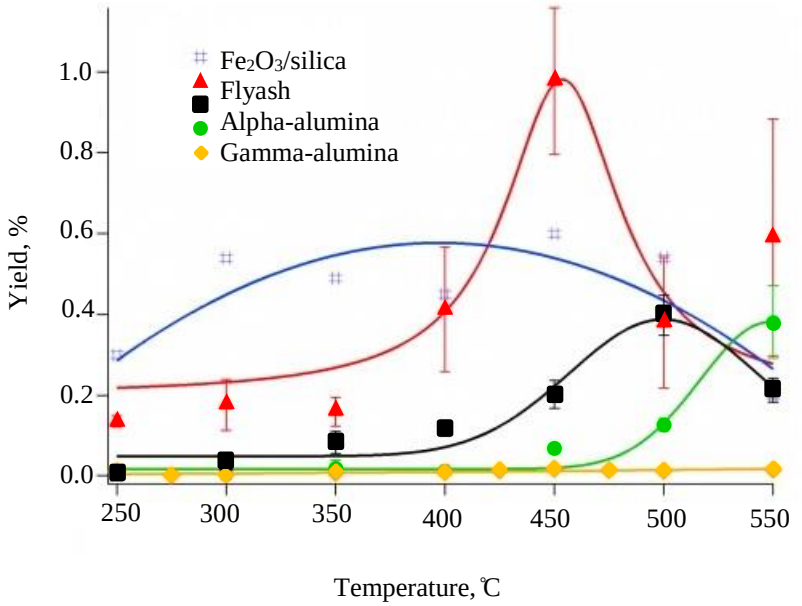

Figure 2.33. PCDD/Fs yields from the oxidation of 2-MCP over selected surfaces.[313]

A series of experimental studies has examined the role of other metal oxides on the formation and persistency of EPFR in particulates. For instance, Lomnicki et al.[291] and Vejerano et al.[294] investigated the catalytic activity of two transition metal oxides, Fe_2O_3 and CuO, deposited on silicon oxide surfaces. They investigated the catalytic activity of both oxides toward five different aromatic hydrocarbons, namely phenol, hydroquinone, 2-monochlorophenol, 1,2-dichlorobenzen, and cachol. They confirmed that both the Fe_2O_3 and CuO surfaces mediate the formation of EPFR species (both phenoxyl and semiquinone type of radicals). They also describe in detail the surface mediated process, starting from the physisorbed interaction of the

precursors, followed by its dissociation states, and ending with the EPFR formation. Furthermore, the authors indicated that surface metal atoms transfer electrons to the bound precursors resulting in the synthesis of EPFR. Some studies have also been carried out to investigate the influence of Ni_2O[295], ZnO[297], and TiO_2[307] on the formation of EPFR, demonstrating their importance in EPFR formation.

Theoretically, Pan et al.[314] investigated the formation of EPFR generated from 2-chlorophenol (2-CP) over hydrated and dehydrated silica surfaces using DFT. The authors demonstrated that the dehydrated silica cluster is more active toward the attack of 2-CP if contrasted with hydrated configurations. Results from the study unequivocally point out the role of surface acidity in the formation of EPFR. However, an intriguing question arises if the same trend applies to alumina and other metal oxides. Along a similar line of inquiry, Mosallanjad et al.[298], conducted a recent study to investigate the formation of PCDD/Fs from neat silica-mediated 2-Chlorophenol, confirming the catalytic role of silica surfaces in the generation of PCDD/Fs. The authors attempted to evaluate the impact of temperature on the surface catalytic activity of silica by applying the process in twotemperature ranges, (523–673 K) and (823–973 K), representing the lower and the upper range, respectively, of the catalytic regime of PCDD/Fs formation. They confirmed that the catalytic pathway over neat silica was observed only in the upper range. However, the authors also recognised the critical role played by the fly ash matrix in PCDD/F formation, even in the absence of transition metals (i.e. neat silica, neat alumina, and alumina-supported iron oxide[315]).

2.4 Summary

The first section in this review analysed several experimental studies carried out to investigate the stability phase diagram of diboron trioxide, and its applications as an important coating material. Analysing the literature pertinent to B_2O_3 in general reveals the apparent lack of theoretical insight into the remarkable inhibition effect of B_2O_3 and its formation mechanism via the oxidation of elemental boron. Collectively, studies discussed in this section outline a critical role for alumina in PCDD/F formation. The second part of the review focused on the functionality of alumina surfaces in faciltating the formation of EPFR and PCDD/Fs. However, despite a great deal of experimental studies, reaction mechanisms for the interaction of structurally related precursors with alumina surfaces leading to EPFR and PCDD/Fs remain largely speculative. In light of the critical literature survey presented in this chapter, Table 2.9 highlight significant knowledge gaps in the two subjects discussed; inhibition characterization of diboron trioxide and catalytic activity of alumina.

Table 2.9. Knowledge gaps in the inhibition characterisation of diboron trioxide and the catalytic activity of alumina.

	Gap	Proposed action
1	The initial steps governing conversion of elemental boron into B_2O_3 are largely unknown.	To investigate chemisorption of the oxygen molecule's elemental boron and to construct a potential energy surface diagram for the formation of B_2O_3
2	Much uncertainty remains regarding the surface, stable, and nonreactive	To investigate the B_2O_3 low index surfaces and perform more accurate single

	structures of diboron trioxide. Results from a previous study of surface termination of B_2O_3 were not chemically sound (i.e. dangling bonds), leading to a well-defined question behind our investigation of the B_2O_3 low index surface: can we identify more chemically sound surface terminations for B_2O_3?	point energy calculations, with an extra layer of ghost atoms on the surfaces.
3	The nature of catalytic inhibition by B_2O_3 remains unclear.	To address adsorption and subsequent decomposition of simple molecules (e.g. H_2S) on clean diboron trioxide.
4	The mechanistic hygroscopic effect of B_2O_3, is not completed understood.	To employ DFT combined with experimental diffuse reflectance infrared spectroscopy to examine the interaction of B_2O_3 with water molecules. This is instrumental in attaining a detailed understanding of the reaction mechanism between the B_2O_3 surface and air moisture.
5	While a great deal of experimental studies using several techniques have unequivocally established the catalytic effect of alumina in generating phenoxy-type EPFR; the exact underlying mechanistic steps are not known.	To employ density function theory to underpin the interaction of phenol with dehydrated and hydrated alumina (with varying hydroxylation degree) surfaces to explore the catalytic role of both surfaces in mediating the formation of phenoxy-type EPFR.
6	The effect of atomic dopants on the catalytic activity of alumina in generating EPFR.	To employ density function theory to study the interaction of phenol with alumina α-Al_2O_3 in which a surface Al

atom is substituted by a Si atom. The underlying aim is to compare activation barriers of prominent steps between clean alumina with a Si-Al_2O_3 surface.

2.5 References

1. Aldridge, S.; Downs, A. J., *The Group 13 Metals Aluminium, Gallium, Indium and Thallium: Chemical Patterns and Peculiarities*. John Wiley & Sons, 2011.

2. Harding, C.; Janes, R.; Johnson, D. A., *Elements of the P Block*. Royal Society of Chemistry, 2002; Vol. 9.

3. Shapiro, P. J.; Atwood, D. A., *Group 13 Chemistry: From Fundamentals to Applications*. ACS Publications, 2002.

4. Mauri, F.; Vast, N.; Pickard, C. J., Atomic structure of icosahedral B_4C Boron Carbide from a first principles analysis of Nmr spectra. *Phys. Rev. Lett.* **2001**, *87*, 085506.

5. Hubert, H.; Devouard, B.; Garvie, L. A. J.; O'Keeffe, M.; Buseck, P. R.; Petuskey, W. T.; McMillan, P. F., Icosahedral packing of B12 icosahedra in Boron Suboxide (B_6O). *Nature* **1998**, *391*, 376-378.

6. Chen, M.; McCauley, J. W.; Hemker, K. J., Shock-induced localized amorphization in Boron Carbide. *Science* **2003**, *299*, 1563-1566.

7. Emin, D., Icosahedral Boron-rich solids. *Phys. Today* **1987**, *40*, 55-62.

8. Domnich, V.; Gogotsi, Y.; Trenary, M.; Tanaka, T., Nanoindentation and Raman spectroscopy studies of Boron Carbide single crystals. *Appl. Phys. Lett.* **2002**, *81*, 3783-3785.

9. He, D.; Zhao, Y.; Daemen, L.; Qian, J.; Shen, T.; Zerda, T., Boron Suboxide: As hard as Cubic Boron Nitride. *Appl. Phys. Lett.* **2002**, *81*, 643-645.

10. Li, D.; Ching, W., Electronic structure and optical properties of the $B_{12}O_2$ crystal. *Phys. Rev. B* **1996**, *54*, 1451.

11. Shirai, K., Central and noncentral forces on the lattice dynamics of Boron-rich solids. *J. Solid State Chem.* **1997**, *133*, 215-223.

12. Orlovskaya, N.; Lugovy, M., *Boron Rich Solids: Sensors, Ultra High Temperature Ceramics, Thermoelectrics, Armor*. Springer, 2010.

13. Lundstron, T., *Boron-Rich Solids.* 1990, p 186.

14. Chung, H. Y.; Weinberger, M. B.; Levine, J. B.; Kavner, A.; Yang, J. M.; Tolbert, S. H.; Kaner, R. B., Synthesis of ultra-incompressible superhard Rhenium Diboride at ambient pressure. *Science* **2007**, *316*, 436-439.

15. Chung, H. Y.; Weinberger, M. B.; Yang, J. M.; Tolbert, S. H.; Kaner, R. B., Correlation between hardness and elastic moduli of the ultraincompressible transition metal diborides Rub#!2, Osb2, and Reb2. *Appl. Phys. Lett.* **2008**, *92*.

16. Gu, Q.; Krauss, G.; Steurer, W., Transition metal borides: Superhard versus ultra-incompressible. *Adv. Mater.* **2008**, *20*, 3620-3626.

17. Levine, J. B.; Tolbert, S. H.; Kaner, R. B., Advancements in the search for superhard ultra-incompressible metal borides. *Adv. Funct. Mater.* **2009**, *19*, 3519-3533.

18. Weinberger, M. B.; Levine, J. B.; Chung, H. Y.; Cumberland, R. W.; Rasool, H. I.; Yang, J. M.; Kaner, R. B.; Tolbert, S. H., Incompressibility and hardness of solid solution transition metal diborides: Os 1-Xru Xb 2. *Chem. of Mater.* **2009**, *21*, 1915-1921.

19. Lazzari, R.; Vast, N.; Besson, J.; Baroni, S.; Dal Corso, A., Atomic structure and vibrational properties of icosahedral B_4C Boron Carbide. *Phys. Rev. Lett.* **1999**, *83*, 3230.

20. Saal, J. E.; Shang, S.; Liu, Z.-K., The structural evolution of Boron Carbide via Ab Initio calculations. *Appl. Phys. Lett.***2007**, *91*, 231915.

21. Schwetz, K. A., Boron Carbide, Boron Nitride, and Metal Borides. *Ullmann's Encyclopedia of Industrial Chemistry.* **1985**.

22. Thevenot, F., *Properties of Ceramics*. 1989; Vol. 2, p 21.

23. Zhai, H.-J.; Kiran, B.; Li, J.; Lai-Sheng, W., Hydrocarbon analogues of Boron clusters--planarity, aromaticity and antiaromaticity. *Nature Mater.* **2003**, *2*, 827.

24. Solozhenko, V.; Kurakevych, O.; Oganov, A., On the hardness of a new Boron phase, orthorhombic Γ-B28. *J. Superhard Mater.* **2008**, *30*, 428-429.

25. McCarty, L.; Kasper, J.; Horn, F.; Decker, B.; Newkirk, A., A new crystalline modification of Boron. *J. Am. Chem. Soc.* **1958**, *80*, 2592-2592.

26. He, C.; Zhong, J. X., Structures, stability, mechanical and electronic properties of A-Boron and A*-Boron. *AIP Adv.* **2013**, *3*.

27. Hughes, R. E.; Kennard, C. H. L.; Sullenger, D. B.; Weakliem, H. A.; Sands, D. E.; Hoard, J. L., The structure of B-rhombohedral Boron. *J. Am. Chem. Soc.* **1963**, *85*, 361-362.

28. Sands, D. E.; Hoard, J. L., Rhombohedral elemental Boron. *J. Am. Chem. Soc.* **1957**, *79*, 5582-5583.

29. Oganov, A. R.; Chen, J.; Gatti, C.; Ma, Y.; Ma, Y.; Glass, C. W.; Liu, Z.; Yu, T.; Kurakevych, O. O.; Solozhenko, V. L., Ionic high-pressure form of elemental Boron. *Nature* **2009**, *457*, 863-867.

30. Vlasse, M.; Naslain, R.; Kasper, J. S.; Ploog, K., Crystal structure of tetragonal Boron related to A-Alb12. *J. Solid State Chem.* **1979**, *28*, 289-301.

31. Solozhenko, V. L.; Kurakevych, O. O., Equilibrium P-T phase diagram of Boron: Experimental study and thermodynamic analysis. *Sci. Rep.* **2013**, *3*.

32. Solozhenko, V. L.; Kurakevych, O. O., Equilibrium P-T phase diagram of Boron: Experimental study and thermodynamic analysis. *Sci. Reports* **2013**, *3*.

33. Tai, T. B.; Nguyen, M. T., Structure and electron delocalization of the Boron Oxide cluster $B_3(Bo)_3$ and its anion and dianion. *Chem. Phys. Lett.* **2009**, *483*, 35-42.

34. King, M. K., Ignition and combustion of Boron particles and clouds. *J. Spacecraft* **1982**, *19*, 294-306.

35. Wang, Y.; Fan, J.; Trenary, M., Surface chemistry of Boron oxidation. 1. Reactions of Oxygen and water with Boron films grown on tantalum (110). *Chem. Mater.* **1993**, *5*, 192-198.

36. Wang, Y.; Trenary, M., Surface chemistry of Boron oxidation. 2. The reactions of boron oxides B_2O_2 and B_2O_3 with boron films grown on tantalum (110). *Chem. Mater.* **1993**, *5*, 199-205.

37. Schubert, D., Boron oxides, boric acid, and borates. *Kirk-Othmer Encyclopedia of Chemical Technology* **2000**.

38. Kistler, R. B.; Helvaci, C., Boron and borates. *Ind. Min. Rocks* **1994**, *6*, 171-186.

39. Youngman, R.; Haubrich, S.; Zwanziger, J.; Janicke, M.; Chmelka, B., Short-and intermediate-range structural ordering in glassy Boron Oxide. *Sci.-AAAS-Weekly Paper Ed.* **1995**, *269*, 1416-1419.

40. Umari, P.; Pasquarello, A., Fraction of boroxol rings in vitreous Boron Oxide from a first-principles analysis of Raman and Nmr spectra. *Phys. Rev. Lett.* **2005**, *95*, 137401.

41. Ferlat, G.; Charpentier, T.; Seitsonen, A. P.; Takada, A.; Lazzeri, M.; Cormier, L.; Calas, G.; Mauri, F., Boroxol rings in liquid and vitreous B_2O_3 from first principles. *Phys. Rev. Lett.* **2008**, *101*, 065504.

42. Huang, L.; Kieffer, J., Thermomechanical anomalies and polyamorphism in B_2O_3 glass: A molecular dynamics simulation study. *Phys. Rev. B* **2006**, *74*, 224107.

43. Wright, A. C., Borate structures: Crystalline and vitreous. Physics and chemistry of glasses. *Eur J. Glass Sci. Technol. Part B* **2010**, *51*, 1-39.

44. McCulloch, L., A crystalline Boric Oxide. *J. Am. Chem. Soc.* **1937**, *59*, 2650-2652.

45. dos Santos-Loff, D.; Micoulaut, M.; Kerner, R., Statistics of boroxol rings in vitreous Boron Oxide. *EPL (Europhysics Letters)* **1994**, *28*, 573.

46. Heitjans, P.; Indris, S., Diffusion and ionic conduction in nanocrystalline ceramics. *J. Phys.: Condens. Matter* **2003**, *15*, R1257.

47. Indris, S.; Heitjans, P.; Roman, H. E.; Bunde, A., Nanocrystalline versus microcrystalline Li_2O: B_2O_3 composites: Anomalous ionic conductivities and percolation theory. *Phys. Rev. Lett.* **2000**, *84*, 2889.

48. Chawla, N.; Kerr, M.; Chawla, K., Monotonic and cyclic fatigue behavior of high-performance ceramic fibers. *J. Am. Ceram. Soc.* **2005**, *88*, 101-108.

49. Chawla, K. K., *Composite Materials: Science and Engineering*. Springer Science & Business Media, 2012.

50. Deborah, D. C., Composite materials: Science and applications. *Eng. Mater. Proc.* **2010**.

51. Kracek, F.; Morey, G.; Merwin, H., The system, water-boron oxide. *Am. J. Sci. A* **1938**, *35*, 143-171.

52. Uhlmann, D.; Hays, J.; Turnbull, D., The Effect of High Pressure on B_2O_3: Crystallisation, densification, and the crystallisation anomaly. *Phys. Chem. Glasses* **1967**, *8*, 1-1.

53. Aziz, M. J.; Nygren, E.; Hays, J. F.; Turnbull, D., Crystal growth kinetics of Boron Oxide under pressure. *J. Appl. Phys.* **1985**, *57*, 2233-2242.

54. Barrow, N. S.; Ashbrook, S. E.; Brown, S. P.; Holland, D., Developing 11b solid state Mas Nmr methods to characterise medium range structure in borates. Physics and chemistry of glasses. *Eur. J. Glass Sci. Technol. Part B* **2009**, *50*, 201-204.

55. Ferlat, G.; Charpentier, T.; Seitsonen, A. P.; Takada, A.; Lazzeri, M.; Cormier, L.; Calas, G.; Mauri, F., Boroxol rings in liquid and vitreous B_2O_3 from first principles. *Phys. Rev. Lett.* **2008**, *101*.

56. Hannon, A. C.; Grimley, D. I.; Hulme, R. A.; Wright, A. C.; Sinclair, R. N., Boroxol groups in vitreous boron oxide: New evidence from neutron diffraction and inelastic neutron scattering studies. *J. Non-Cryst. Solids* **1994**, *177*, 299-316.

57. Huang, L.; Kieffer, J., Thermomechanical anomalies and polyamorphism in B_2O_3 glass: A molecular dynamics simulation study. *Phys. Rev. B - Condens. Matter Mater. Phys.* **2006**, *74*.

58. Hung, I.; Howes, A. P.; Parkinson, B. G.; Anupõld, T.; Samoson, A.; Brown, S. P.; Harrison, P. F.; Holland, D.; Dupree, R., Determination of the bond-angle distribution in vitreous B_2O_3 by 11b double rotation (Dor) Nmr spectroscopy. *J. Solid State Chem.* **2009**, *182*, 2402-2408.

59. Jellison, G. E., Jr.; Panek, L. W.; Bray, P. J.; Rouse, G. B., Jr., Determinations of structure and bonding in vitreous B_2O_3 by means of B10, B11, and O17 Nmr. *J. Chem. Phys.* **1977**, *66*, 802-812.

60. Joo, C.; Werner-Zwanziger, U.; Zwanziger, J. W., Erratum: The ring structure of boron trioxide glass. (J. Non-Cryst. Solids (2000) 261 (282-286)). *J. Non-Cryst. Solids* **2000**, *271*, 265-266.

61. Joo, C.; Werner-Zwanziger, U.; Zwanziger, J. W., Ring structure of boron trioxide glass. *J. Non-Cryst. Solids* **2000**, *261*, 282-286.

62. Suzuya, K.; Yoneda, Y.; Kohara, S.; Umesaki, N., High energy X-ray study of the structure of vitreous B_2O_3. *Phys. Chem. Glasses* **2000**, *41*, 282-285.

63. Swenson, J.; Börjesson, L., Fraction of boroxol rings in vitreous boron trioxide. *Phys. Rev. B - Condens. Matter Mater. Phys.* **1997**, *55*, 11138-11143.

64. Swenson, J.; Börjesson, L., Comment on "fraction of boroxol rings in vitreous boron oxide from a first-principles analysis of Raman and Nmr spectra". *Phys. Rev. Lett.* **2006**, *96*.

65. Umari, P.; Pasquarello, A., Fraction of boroxol rings in vitreous boron oxide from a first-principles analysis of Raman and Nmr spectra. *Phys. Rev. Lett.* **2005**, *95*.

66. Verhoef, A. H.; den Hartog, H. W., A molecular dynamics study of B_2O_3 glass using different interaction potentials. *J. Non-Cryst. Solids* **1992**, *146*, 267-278.

67. Wright, A. C.; Vedishcheva, N. M.; Shakhmatkin, B. A., Vitreous borate networks containing superstructural units: A challenge to the random network theory? *J. Non-Cryst. Solids* **1995**, *192-193*, 92-97.

68. Svanson, S.; Johansson, R., The configuration of three-coordinated Boron in vitreous and crystalline Boron Oxide. *Acta Chem. Scand.* **1969**, *23*, 635-646.

69. Warren, B.; Krutter, H.; Morningstar, O., Fourier analysis of X-ray patterns of vitreous SiO_2 and B_2O_2. *J. Am. Ceram. Soc.* **1936**, *19*, 202-206.

70. Zachariasen, W. H., The atomic arrangement in glass. *J. Am. Chem. Soc.* **1932**, *54*, 3841-3851.

71. Fajans, K.; Barber, S. W., Properties and structures of vitreous and crystalline Boron Oxide1. *J. Am. Chem. Soc.* **1952**, *74*, 2761-2768.

72. Jellison Jr, G.; Panek, L.; Bray, P.; Rouse Jr, G., Determinations of structure and bonding in vitreous B_2O_3 by means of B10, B11, and O17 Nmr. *J. Chem. Phys.* **1977**, *66*, 802-812.

73. Johnson, P. A.; Wright, A. C.; Sinclair, R. N., A neutron diffraction investigation of the structure of vitreous Boron Trioxide. *J. Non-Cryst. Solids* **1982**, *50*, 281-311.

74. Mozzi, R. L.; Warren, B., The structure of vitreous Boron Oxide. *J. Appl. Crystallogr.* **1970**, *3*, 251-257.

75. Suzuya, K.; Yoneda, Y.; Kohara, S.; Umesaki, N., High energy X-ray study of the structure of vitreous B_2O_3. *Phys. Chem. Glasses* **2000**, *41*, 282-285.

76. Gurr, G.; Montgomery, P.; Knutson, C.; Gorres, B., The crystal structure of trigonal Diboron Trioxide. *Acta Crystallogr. Section B: Struct. Crystallogr. Crystal Chem.* **1970**, *26*, 906-915.

77. Effenberger, H.; Lengauer, C. L.; Parthé, E., Trigonal B_2O_3 with higher space-group symmetry: Results of a reevaluation. *Monatsh. Chem./Chemical Monthly* **2001**, *132*, 1515-1517.

78. Berger, S. V., The crystal structure of Boron Oxide. *Acta Chem. Sound* **1953**, *7*.

79. Strong, S.; Kaplow, R., The structure of crystalline B_2O_3. *Acta Crystallogr. Section B: Struct. Crystallogr. Crystal Chem.* **1968**, *24*, 1032-1036.

80. Brazhkin, V.; Katayama, Y.; Trachenko, K.; Tsiok, O.; Lyapin, A.; Artacho, E.; Dove, M.; Ferlat, G.; Inamura, Y.; Saitoh, H., Nature of the structural transformations in B_2O_3 glass under high pressure. *Phys. Rev. Lett.* **2008**, *101*, 035702.

81. Lee, S. K.; Eng, P. J.; Mao, H.-k.; Meng, Y.; Newville, M.; Hu, M. Y.; Shu, J., Probing of bonding changes in B_2O_3 glasses at high pressure with inelastic X-ray scattering. *Nat. Mater.* **2005**, *4*, 851.

82. Prewitt, C.; Shannon, R., Crystal structure of a high-pressure form of B_2O_3. *Acta Crystallogr. Section B: Structural crystallogr. Crystal Chem.* **1968**, *24*, 869-874.

83. Nieto-Sanz, D.; Loubeyre, P.; Crichton, W.; Mezouar, M., X-ray study of the synthesis of boron oxides at high pressure: Phase diagram and equation of state. *Phys. Rev. B* **2004**, *70*, 214108.

84. Efimov, A. M., *Optical Constants of Inorganic Glasses*. CRC Press, 1995; Vol. 9.

85. Solozhenko, V. L.; Kurakevych, O. O.; Le Godec, Y.; Brazhkin, V. V., Thermodynamically consistent P–T phase diagram of boron oxide B_2O_3 by in situ probing and thermodynamic analysis. *J. Phys. Chem. C* **2015**, *119*, 20600-20605.

86. Huang, L.; Nicholas, J.; Kieffer, J.; Bass, J., Polyamorphic transitions in vitreous B_2O_3 under pressure. *J. Phys.: Condens. Matter* **2008**, *20*, 075107.

87. Bredow, T.; Islam, M. M., Theoretical study of low-index surfaces of trigonal B_2O_3. *Surf. Sci.* **2008**, *602*, 2217-2221.

88. Agüero, A., Ingeniería de superficies y su impacto medioambiental. *Rev. Metal.* **2007**, *43*, 63-75.

89. Roussel, R.; Kolarik, V.; Lorenzo, M. J.; Fietzek, H., Effect of boron addition on micro-aluminum-particle-based multifunctional high-temperature coatings. *Oxid. Met.* **2014**, *81*, 179-189.

90. McKee, D.; Spiro, C.; Lamby, E., The effects of boron additives on the oxidation behavior of carbons. *Carbon* **1984**, *22*, 507-511.

91. Hannache, H.; Quenisset, J.; Naslain, R.; Heraud, L., Composite materials made from a porous 2d-Carbon-Carbon oreform densified with Boron Nitride by chemical vapour infiltration. *J. Mater. Sci.* **1984**, *19*, 202-212.

92. Chown, J.; Deacon, R.; Singer, N.; White, A., Special Ceramics—1962. **1963**.

93. Ehrburger, P.; Baranne, P.; Lahaye, J., Inhibition of the oxidation of Carbon-Carbon composite by Boron Oxide. *Carbon* **1986**, *24*, 495-499.

94. Zeng, Z.; Dlugogorski, B. Z.; Altarawneh, M., Flammability of Cs 2 and other reduced Sulfur species. *Fire Saf. J.* **2017**.

95. Radovic, L. R.; Karra, M.; Skokova, K.; Thrower, P. A., The role of substitutional Boron in Carbon oxidation. *Carbon* **1998**, *36*, 1841-1854.

96. Bacos, M.-P.; Dorvaux, J.-M.; Lavigne, O.; Renollet, Y., C/C composite oxidation model: I. Morphological experimental investigations. *Carbon* **2000**, *38*, 77-92.

97. Bacos, M.-P.; Cochon, J.-L.; Dorvaux, J.-M.; Lavigne, O., C/C composite oxidation model: Ii. Oxidation experimental investigations. *Carbon* **2000**, *38*, 93-103.

98. Bacos, M.-P.; Dorvaux, J.-M.; Lavigne, O.; Talandier, J., C/C composite oxidation model: Iii. Physical basis, limitations and applications. *Carbon* **2000**, *38*, 105-117.

99. Lee, Y.-J.; Joo, H.-J.; Radovic, L. R., Preferential distribution and oxidation inhibiting/catalytic effects of Boron in carbon fiber reinforced carbon (Cfrc) composites. *Carbon* **2003**, *41*, 2591-2600.

100. Fitzer, E., The future of Carbon-Carbon composites. *Carbon* **1987**, *25*, 163-190.

101. Buckley, J. D., Carbon-Carbon: An overview. **1988**.

102. Ho, C. T.; Chung, D. D. L., Inhibition of the oxidation of Carbon-Carbon composites by bromination. *Carbon* **1990**, *28*, 815-824.

103. Lobiondo, N. E.; Jones, L. E.; Clare, A. G., Halogenated glass systems for the protection of structural Carbon-Carbon composites. *Carbon* **1995**, *33*, 499-508.

104. McKee, D. W.; Spiro, C. L.; Lamby, E. J., The effects of Boron additives on the oxidation behavior of carbons. *Carbon* **1984**, *22*, 507-511.

105. Romine, P. R.; Ochoa, O. O., An assessment of the effect of inhibitor oxidation on the response of oxidation-resistant Carbon/Carbon composites. *Compos. Sci. Technol.* **1996**, *56*, 569-579.

106. Zhu, Y. C.; Ohtani, S.; Sato, Y.; Iwamoto, N., Influence of Boron ion implantation on the oxidation behavior of Cvd-Sic coated Carbon-Carbon composites. *Carbon* **2000**, *38*, 501-507.

107. Chang, C. E.; Wilcox, W. R., Vitreous boron oxide: Drying and moisture absorption. *Mater. Res. Bull.* **1971**, *6*, 1297-1304.

108. McKee, D., Borate Treatment of carbon fibers and Carbon/Carbon composites for improved oxidation resistance. *Carbon* **1986**, *24*, 737-741.

109. Cullinan, J.; Schaeffer, J.; Gulbransen, E.; Meier, G.; Pettit, F. *Program to Study the Oxidation of Carbon-Carbon Composites and Coatings on These Materials*. Pittsburgh Uni PA Dept of Materials Csience and Engineering: 1989.

110. Feng, T.; Li, H.-J.; Yang, X.; Shi, X.-H.; Wang, S.-l.; He, Z.-B., Multilayer and multi-component oxidation protective coating system for carbon/carbon composites from room temperature to 1873k. *Corr. Sci.* **2013**, *72*, 144-149.

111. Feng, T.; Li, H.-J.; Shi, X.-H.; Yang, X.; Li, Y.-X.; Yao, X.-Y., Sealing role of B_2O_3 in Mosi 2–Crsi 2–Si/B-modified Sic coating for C/C composites. *Corr. Sci.* **2012**, *60*, 4-9.

112. McKee, D. W., Oxidation behavior and protection of Carbon/Carbon composites. *Carbon* **1987**, *25*, 551-557.

113. Zhu, Y.-C.; Ohtani, S.; Sato, Y.; Iwamoto, N., Influence of Boron ion implantation on the oxidation behavior of Cvd-Sic coated Carbon-Carbon composites. *Carbon* **2000**, *38*, 501-507.

114. Liu, F.; Yang, G., Solidification of superalloy in a Sio 2–Zro 2–B_2O_3 coating mould. *J. Non-Crystall. Solids* **2001**, *290*, 105-114.

115. Chang, L.-C.; Chiou, B.-S., Effect of B_2O_3 nano-coating on the sintering behaviors and electrical microwave properties of Ba (Nd 2− X Sm X) Ti_4O_{12} ceramics. *J. Electroceram.* **2004**, *13*, 829-837.

116. Buckley, J. D., Carbon-Carbon, an overview. *Am. Ceram.Soc. Bull.* **1988**, *67*, 364-368.

117. Meetham, G. W., High-temperature materials - a general review. *J. Mater. Sci.* **1991**, *26*, 853-860.

118. Sheehan, J. E.; Buesking, K. W.; Sullivan, B. J., Carbon-Carbon composites. *Ann. Rev. Mater. Sci.* **1994**, *24*, 19-44.

119. Strife, J. R.; Sheehan, J. E., Ceramic coatings for Carbon-Carbon composites. *Am. Ceram. Soc. Bull.* **1988**, *67*, 369-374.

120. Westwood, M. E.; Webster, J. D.; Day, R. J.; Hayes, F. H.; Taylor, R., Oxidation protection for carbon fibre composites. *J. Mater. Sci.* **1996**, *31*, 1389-1397.

121. Zhu, Y. C.; Ohtani, S.; Sato, Y.; Iwamoto, N., The improvement in oxidation resistance of Cvd-Sic coated C/C composites by silicon infiltration pretreatment. *Carbon* **1998**, *36*, 929-935.

122. Buchanan, F. J.; Little, J. A., Oxidation protection of Carbon-Carbon composites using chemical vapour deposition and glaze technology. *Corr. Sci.* **1993**, *35*, 1243-1250.

123. Buchanan, F. J.; Little, J. A., Particulate-containing glass sealants for Carbon-Carbon composites. *Carbon* **1995**, *33*, 491-497.

124. Fergus, J. W.; Worrell, W. L., Silicon-carbide/boron-containing coatings for the oxidation protection of graphite. *Carbon* **1995**, *33*, 537-543.

125. McKee, D. W., Borate treatment of carbon fibers and Carbon/Carbon composites for improved oxidation resistance. *Carbon* **1986**, *24*, 737-741.

126. Sheehan, J. E., Oxidation protection for carbon fiber composites. *Carbon* **1989**, *27*, 709-715.

127. Tsou, H. T.; Kowbel, W., A multilayer plasma-assisted Cvd coating for oxidation protection of Carbon-Carbon composites. *J. Adv. Mater.* **1996**, *27*, 9-13.

128. Schlichting, J., Oxygen transport through glass layers formed by a gel process. *J. Non-Crystall. Solids* **1984**, *63*, 173-181.

129. Hatta, H.; Sohtome, T.; Sawada, Y.; Shida, A., High temperature crack sealant based on SiO_2-B_2O_3 for Sic coating on Carbon–Carbon composites. *Adv. Compos. Mater.* **2003**, *12*, 93-106.

130. Kalinovski, I. J.; Gutman, D.; Krasnoperov, L. N.; Goumri, A.; Yuan, W.-J.; Marshall, P., Kinetics and thermochemistry of the reaction Si (Ch3) 3+ Hbr⇌ Si (Ch3) 3h+ Br: determination of the (Ch3) 3Si-H bond energy. *J. Phys. Chem.* **1994**, *98*, 9551-9557.

131. Egerton, A.; Warren, D., Kinetics of the Hydrogen/Oxygen reaction. I. The explosion region in boric acid-coated vessels. *Proc. R. Soc. London. Ser. A, Mathematical and Physical Sciences* **1951**, 465-476.

132. Baldwin, R.; Walker, R.; Langford, D., Oxidation of propionaldehyde in aged boric-acid-coated vessels. Part 1—kinetic results. *Trans. Farad. Soc.* **1969**, *65*, 792-805.

133. Baldwin, R.; Walker, R.; Langford, D., Oxidation of propionaldehyde in aged boric-acid-coated vessels. Part 2.—analytical results. *Trans. Farad. Soc.* **1969**, *65*, 806-815.

134. Baldwin, R.; Mayor, L., The mechanism of the Hydrogen+ Oxygen reaction in aged boric-acid-coated vessels. *Trans. Farad. Soc.* **1960**, *56*, 103-114.

135. Lodhi, Z. H.; Walker, R. W., Decomposition of 4, 4-dimethylpent-1-ene in the presence of oxygen between 400 and 500 C: Oxidation chemistry of allyl radicals. *J. Chem. Soc., Farad. Trans.* **1991**, *87*, 681-689.

136. Zhou, C. R.; Sendt, K.; Haynes, B. S., Experimental and kinetic modelling study of H_2S oxidation. *Proc. Combust. Inst.* **2013**, *34*, 625-632.

137. Pérez-Enciso, E.; Ramos, M.; Vieira, S., Low-temperature specific heat of different B_2O_3 glasses. *Phys. Rev. B* **1997**, *56*, 32.

138. Erdemir, A.; Bindal, C.; Zuiker, C.; Savrun, E., Tribology of naturally occurring boric acid films on boron carbide. *Surf. Coat. Technol.* **1996**, *86*, 507-510.

139. Findik, F., Latest progress on tribological properties of industrial materials. *Mater. Des.* **2014**, *57*, 218-244.

140. Hernandez-Sanchez, E.; Chino-Ulloa, A.; Velazquez, J.; Herrera-Hernández, H.; Velázquez-Mancilla, R.; Carrera-Espinoza, R., Effect of relative humidity on the tribological properties of self-lubricating H_3BO_3 films formed on the surface of steel suitable for biomedical applications. *Adv. Mater. Sci. Eng.* **2015**, *2015*.

141. King, M. K., A review of studies of boron ignition and combustion phenomena at Atlantic Research Corporation over the past decade. *Int. J. Energ. Mater. Chem. Propuls.* **1993**, *2*.

142. Hsieh, W. H.; Peretz, A.; Huang, I. T.; Kuo, K. K., Combustion behavior of boron-based Bamo/Nmmo fuel-rich solid propellants. *J. Propul. Power* **1991**, *7*, 497-504.

143. King, M. K., Ignition and combustion of Boron particles and clouds. *J. Spac. Rock.* **1982**, *19*, 294-306.

144. Meinkohn, D., The ignition of Boron particles. *Combust. Flame* **1985**, *100*, 634-644.

145. Nandi, A. K.; Ghosh, M.; Newale, S. P.; Jadhav, A. J.; Prasanth, H.; Pandey, R. K., Formation of boric acid by surface oxidation of amorphous Boron powder: Characterization and quantitative estimation. *Cent. Eur. J. Energ. Mater.* **2012**, *9*, 387-398.

146. Nieder, E. G., Chemical Passivation of Amorphous Boron Powder. Google Patents: 1987.

147. Liu, T. K.; Luh, S. P.; Perng, H. C., Effect of Boron particle surface coating on combustion of solid propellants for ducted rockets. *Propellants Explos. Pyrotech.* **1991**, *16*, 156-166.

148. Shyu, I. M.; Liu, T. K., Combustion characteristics of gap-coated Boron particles and the fuel-rich solid propellant. *Combust. Flame* **1995**, *100*, 634-644.

149. Myers, J. E., Xix.—Boric anhydride and its hydrates. *J. Chem. Soc., Trans.* **1917**, *111*, 172-179.

150. Slutskii, V.; Severin, E.; Polenov, L., An Ab initio study of reactions in the $H_3BO_3/B_2O_3/H_2O$ system. *Russ. J. Phys. Chem. B, Focus on Physics* **2007**, *1*, 549-552.

151. Mülazim, Y.; Kızılkaya, C.; Kahraman, M. V., Thermal and neutron shieldin properties of $10B_2O_3$/polyimide hybrid materials. *Polym. Bull.* **2011**, *67*, 1741-1750.

152. Richards, G., Aluminum oxide ceramics. *Pergamon Press Ltd., Ency. Mater. Sci. Eng.* **1986**, *1*, 158-162.

153. Ruberto, C.; Yourdshahyan, Y.; Lundqvist, B. I., Surface properties of metastable alumina: A comparative study of K-and A− Al_2O_3. *Phys. Rev. B* **2003**, *67*, 195412.

154. Lazcano, P.; Batzill, M.; Diebold, U.; Häberle, P., Oxygen adsorption on Cu⁄ Zn O (0001)− Zn. *Phys. Rev. B* **2008**, *77*, 035435.

155. Lahtonen, K.; Hirsimäki, M.; Lampimäki, M.; Valden, M., Oxygen adsorption-induced nanostructures and island formation on Cu {100}: Bridging the gap between the formation of surface confined oxygen chemisorption layer and oxide formation. *J. Chem.Phys.* **2008**, *129*, 124703.

156. Miller, S. D.; Kitchin, J. R., Relating the coverage dependence of oxygen adsorption on Au and Pt Fcc (111) surfaces through adsorbate-induced surface electronic structure effects. *Surf. Sci.* **2009**, *603*, 794-801.

157. Zhang, W.-B.; Tang, B.-Y., First-principles studies of the oxygen adsorption on unreconstructed and reconstructed Ni (110) surfaces. *Surf.Sci.* **2009**, *603*, 1002-1009.

158. Zhang, W.-B.; Tang, B.-Y., Surface adsorption phase diagram of O/Ni (110) system: An Ab initio atomistic thermodynamics investigation. *Appl. Phys. Lett.* **2009**, *94*, 091901.

159. Sun, B.; Zhang, P.; Wang, Z.; Duan, S.; Zhao, X.-G.; Ma, X.; Xue, Q.-K., Atomic oxygen adsorption and incipient oxidation of the Pb (111) surface: A density-functional theory study. *Phy. Rev. B* **2008**, *78*, 035421.

160. Padture, N. P.; Gell, M.; Jordan, E. H., Thermal barrier coatings for gas-turbine engine applications. *Science* **2002**, *296*, 280-284.

161. Campbell, C. T., Ultrathin metal films and particles on oxide surfaces: Structural, electronic and chemisorptive properties. *Surf. Sci. Rep.* **1997**, *27*, 1-111.

162. Gates, B., Supported metal clusters: Synthesis, structure, and catalysis. *Chem. Rev.* **1995**, *95*, 511-522.

163. Henrich, V.; Cox, P., The Surface Science of Metal Oxides. Cambridge U. *New York* **1994**.

164. Freund, H.-J.; Kuhlenbeck, H.; Staemmler, V., Oxide surfaces. *Rep. Prog. Phys.* **1996**, *59*, 283.

165. Hart, L. D., Alumina Chemicals: Science and Technology Handbook. **1989**.

166. Datta, A., Evidence for cluster sites on catalytic Alumina. *J. Phys. Chem.* **1989**, *93*, 7053-7054.

167. Pompeo, F., Characterization of A-Al_2O_3 supports modified with CeO_2 and ZrO_2. *Mater. Lett.*, *63*, 477-479.

168. Moreno, M. S., Electron microscopy study of Ceox–Pd/A-Al_2O_3 catalysts for methane dry reforming. *J. Appl. Phys.*, *105*, 083531.

169. Wefers, K.; Misra, C., Oxides and hydroxides of Aluminum (Report). *Aluminum Company of America, 92,* **1987**.

170. Gitzen, W. H., Alumina as a Ceramic Material. **1970**.

171. Levin, I.; Brandon, D., Metastable alumina polymorphs: Crystal structures and transition sequences. *J. Am. Ceram. Soc.* **1998**, *81*, 1995-2012.

172. Fiedorow, R., Aluminium hydroxids and oxides—their preparation properties. *Wiad. Chem.* **1967**, *21*.

173. Kuczyński, W.; Fiedorow, R., *Prace Komisji Matematyczno-przyrodniczej* **1968**, *12*.

174. Lippens, B. C.; Steggerda, J. J., *Physical and Chemical Aspects of Adsorbents and Catalysts*. **1970**.

175. Digne, M.; Sautet, P.; Raybaud, P.; Toulhoat, H.; Artacho, E., Structure and stability of aluminum hydroxides: A theoretical study. *J. Phys. Chem. B* **2002**, *106*, 5155-5162.

176. Kosmulski, M., *Chemical Properties of Material Surfaces.* **2001**.

177. Plyasova, L. M.; Kefeli, L. M., On the structure of aluminum oxides. *Kinet. Katal.* **1965**, *6*.

178. Sposito, G., *The Environmental Chemistry of Aluminum.* **1989**.

179. Evans, K. In *The Manufacture of Alumina and Its Use in Ceramics and Related Applications*, Key Engineering Materials, Trans. Tech. Publ.: 1996; pp 489-526.

180. Shirai, T.; Watanabe, H.; Fuji, M.; Takahashi, M., Structural Properties and Surface Characteristics on Aluminum Oxide Powders. **2010**.

181. Yoldas, B. E., Hydrolysis of aluminium alkoxides and Bayerite conversion. *J. Chem. Technol. Biotechnol.* **1973**, *23*, 803-809.

182. Endl, H.; Kruse, B.; Hausner, H., Effects of processing parameters in the preparation of ultrapure aluminum oxide from aluminum isopropylate. *Berichte der Deutschen Keramischen Gesellschaft* **1977**, *54*, 105-110.

183. Kadokura, H.; Umezaki, H.; Higuchi, Y., Process for Producing High Purity Metallic Compound. Google Patents: 1987.

184. Wong, P.; Robinson, M. *Chemical Vapor Deposition of Polycrystalline Aluminum Oxide*. Army Materials and Mechanics Research Center Watertown. MASS: 1969.

185. Park, H. C.; Park, Y. J.; Stevens, R., Synthesis of Alumina from high purity alum derived from coal fly ash. *Mater. Sci. Eng.: A* **2004**, *367*, 166-170.

186. Kato, S.; Iga, T.; Hatano, S.; Isawa, Y., Sintered Alumina. Pt. 10. Effects of synthetic conditions of Nh 4 Alo (Oh) Hco 3 on sinterability of alumina obtained by thermal decomposition. *Yogyo Kyokai Shi* **1976**, *84*, 255-258.

187. Mousavi, S.; Abolhassani, M.; Hosseini, M.; Sebt, S., Comparison of electronic and optical properties of the A and K phase alumina using density functional theory. *Chin. J. Phys.* **2009**, *48*.

188. Kim, Y.; Hsu, T., A reflection electron microscopic (Rem) study of A-Al_2O_3 (0001) surfaces. *Surf. Sci.* **1991**, *258*, 131-146.

189. Perevalov, T. V.; Shaposhnikov, A.; Gritsenko, V. A.; Wong, H.; Han, J.; Kim, C., Electronic structure of A-Al_2O_3: Ab Initio simulations and comparison with experiment. *JETP Lett.* **2007**, *85*, 165-168.

190. Wang, B.; Hou, H.; Luo, Y.; Li, Y.; Zhao, Y.; Li, X., Density functional/all-electron basis set slab model calculations of the adsorption/dissociation mechanisms of water on A-Al_2O_3 (0001) surface. *J. Phys. Chem. C* **2011**, *115*, 13399-13411.

191. Wander, A.; Searle, B.; Harrison, N., An Ab Initio study of A-Al_2O_3 (0001): The effects of exchange and correlation functionals. *Surf. Sci.* **2000**, *458*, 25-33.

192. Chang, C. C., Leed studies of the (0001) face of A-Alumina. *J. Appl. Phys.* **1968**, *39*, 5570-5573.

193. French, T.; Somorjai, G. A., Composition and surface structure of the (0001) face of alpha - Alumina by low-energy electron diffraction. *J. Phys. Chem.* **1970**, *74*, 2489-2495.

194. Ahn, J.; Rabalais, J., Composition and structure of the Al_2O_3 {0001}-(1× 1) surface. *Surf. Sci.* **1997**, *388*, 121-131.

195. Guenard, P.; Renaud, G.; Barbier, A.; Gautier-Soyer, M., Determination of the A-Al_2O_3 (0001) surface relaxation and termination by measurements of crystal truncation rods. *MRS Online Proc. Lib. Arch.* **1996**, *437*.

196. Toofan, J.; Watson, P., The termination of the A-Al_2O_3 (0001) surface: A Leed crystallography determination. *Surf. Sci.* **1998**, *401*, 162-172.

197. Suzuki, T.; Hishita, S.; Oyoshi, K.; Souda, R., Structure of A-Al_2O_3 (0001) surface and Ti deposited on A-Al_2O_3 (0001) substrate: Caiciss and Rheed study. *Surf. Sci.* **1999**, *437*, 289-298.

198. Manassidis, I.; Gillan, M. J., Structure and energetics of alumina surfaces calculated from first principles. *J. Am. Ceram. Soc.* **1994**, *77*, 335-338.

199. McHale, J.; Auroux, A.; Perrotta, A.; Navrotsky, A., Surface energies and thermodynamic phase stability in nanocrystalline aluminas. *Science* **1997**, *277*, 788-791.

200. Puchin, V.; Gale, J.; Shluger, A.; Kotomin, E.; Günster, J.; Brause, M.; Kempter, V., Atomic and electronic structure of the corundum (0001) surface: Comparison with surface spectroscopies. *Surf. Sci.* **1997**, *370*, 190-200.

201. Batyrev, I.; Alavi, A.; Finnis, M. W., Ab initio calculations on the Al_2O_3 (0001) surface. *Farad. Disc.* **1999**, *114*, 33-43.

202. Di Felice, R.; Northrup, J. E., Theory of the clean and hydrogenated Al_2O_3 (0001)−(1× 1) surfaces. *Phys. Rev. B* **1999**, *60*, R16287.

203. Verdozzi, C.; Jennison, D.; Schultz, P.; Sears, M., Sapphire (0001) surface, clean and with D-metal overlayers. *Phys. Rev. Lett.* **1999**, *82*, 799.

204. Tepesch, P.; Quong, A., First-principles calculations of A-Alumina (0001) surfaces energies with and without Hydrogen. *Physica Status Solidi (b)* **2000**, *217*, 377-387.

205. Wang, X.-G.; Chaka, A.; Scheffler, M., Effect of the environment on A− Al_2O_3 (0001) surface structures. *Phys. Rev. Lett.* **2000**, *84*, 3650.

206. Tasker, P., Surfaces of Magnesia and Alumina. *Adv. Ceram.* **1984**, *10*, 176.

207. French, R. H.; Heuer, A. H., International workshop on the science of Alumina. *J. Am. Ceram. Soc.* **1994**, *77*, 292-292.

208. Manassidis, I.; De Vita, A.; Gillan, M., Structure of the (0001) surface of A-Al_2O_3 from first principles calculations. *Surf. Science* **1993**, *285*, L517-L521.

209. Kruse, C.; Finnis, M. W.; Milman, V. Y.; Payne, M. C.; Vita, A.; Gillan, M. J., First-principles calculations for niobium atoms on a sapphire surface. *J. Am. Ceram. Soc.* **1994**, *77*, 431-436.

210. Godin, T.; LaFemina, J. P., Atomic and electronic structure of the corundum (A-Alumina)(0001) surface. *Phys. Rev. B* **1994**, *49*, 7691.

211. Brown, G. E.; Henrich, V. E.; Casey, W. H.; Clark, D. L.; Eggleston, C.; Felmy, A.; Goodman, D. W.; Grätzel, M.; Maciel, G.; McCarthy, M. I., Metal oxide surfaces and their interactions with aqueous solutions and microbial organisms. *Chem. Rev.* **1999**, *99*, 77-174.

212. Desai, R.; Hussain, M.; Ruthven, D., Adsorption of water vapour on activated Alumina. I—-equilibrium behaviour. *Can. J. Chem. Eng.* **1992**, *70*, 699-706.

213. Rui, Z.; Yan, Z.; Kai, H.; Zhen-ping, J.; Gong-zhen, C., Nmr revealed activated Alumina-water interaction. *Wuhan Uni. J. Nat. Sci.* **2005**, *10*, 572-576.

214. McHale, J.; Navrotsky, A.; Perrotta, A., Effects of increased surface area and chemisorbed H_2O on the relative stability of nanocrystalline Γ-Al_2O_3 and A-Al_2O_3. *J. Phys. Chem. B* **1997**, *101*, 603-613.

215. Coustet, V.; Jupille, J., High-resolution electron-energy-loss spectroscopy of hydroxyl groups at the surface of bulk insulating oxides. *Surf. Interface Anal.* **1994**, *22*, 280-283.

216. Elam, J. W.; Nelson, C. E.; Cameron, M. A.; Tolbert, M. A.; George, S. M., Adsorption of H_2O on a single-crystal A-Al_2O_3(0001) surface. *J. Phys. Chem. B* **1998**, *102*, 7008-7015.

217. Kotoh, K.; Enoeda, M.; Matsui, T.; Nishikawa, M., A multilayer model for adsorption of water on activated alumina in relation to adsorption potential. *J. Chem. Eng. Jpn.* **1993**, *26*, 355-360.

218. Kotoh, K.; Enoeda, M.; Matsui, T.; Nishikawa, M., Multilayer adsorption characteristics of heavy water on activated alumina. *J. Chem. Eng. Jpn.* **1993**, *26*, 570-572.

219. Hass, K. C.; Schneider, W. F.; Curioni, A.; Andreoni, W., The chemistry of water on alumina surfaces: Reaction dynamics from first principles. *Science* **1998**, *282*, 265-268.

220. Thissen, P.; Grundmeier, G.; Wippermann, S.; Schmidt, W. G., Water adsorption on the $\Ensuremath{\Alpha}{\Text{-Al}}_{2}{\Text{O}}_{3}(0001)$ surface. *Phys. Rev. B* **2009**, *80*, 245403.

221. Coustet, V.; Jupille, J., High-resolution electron-energy-loss spectroscopy of isolated hydroxyl groups on A-Al_2O_3 (0001). *Surf. Sci.* **1994**, *307*, 1161-1165.

222. Elam, J.; Nelson, C.; Cameron, M.; Tolbert, M.; George, S., Adsorption of H_2O on a single-crystal A-Al_2O_3 (0001) surface. *J. Phys. Chem. B* **1998**, *102*, 7008-7015.

223. Nelson, C.; Elam, J.; Cameron, M.; Tolbert, M.; George, S., Desorption of H_2O from a hydroxylated single-crystal A-Al_2O_3 (0001) surface. *Surf. Sci.* **1998**, *416*, 341-353.

224. Liu, P.; Kendelewicz, T.; Brown, G. E.; Nelson, E. J.; Chambers, S. A., Reaction of water vapor with A-Al_2O_3 (0001) and A-Fe_2O_3 (0001) surfaces: Synchrotron X-ray photoemission studies and thermodynamic calculations. *Surf. Sci.* **1998**, *417*, 53-65.

225. Ballinger, T. H.; Yates Jr, J. T., Interaction and catalytic decomposition of 1, 1, 1-trichloroethane on high surface area Alumina: An infrared spectroscopic study. *J. Phys. Chem.* **1992**, *96*, 1417-1423.

226. Knözinger, H.; Ratnasamy, P., *Catal. Rev. Sci.* **1978**, *17*, 642.

227. Morterra, C.; Magnacca, G., A case study: Surface Chemistry and surface structure of atalytic Aluminas, as studied by vibrational spectroscopy of adsorbed species. *Catal. Today* **1996**, *27*, 497-532.

228. Lippens, B.; Linsen, J. S. B.; Fortuin, M.; Okkersee, C.; Steggerda, J., *Physical and Chemical Aspects of Adsorbents and Catalysts.* Acad. Press, London-New York **1970**.

229. Peri, J. B.; Hannan, R. B., Surface hydroxyl groups on Γ-Alumina1. *J. Phys. Chem.* **1960**, *64*, 1526-1530.

230. Peri, J., A model for the surface of Γ-Alumina1. *J. Phys. Chem.* **1965**, *69*, 220-230.

231. Cornelius, E.; Milliken, T.; Mills, G.; Oblad, A., Surface strain in oxide cata1ysts– A1umina. *J. Phys. Chem.* **1955**, *59*, 809-813.

232. Yamadaya, M., Shimomura, K., Huckida, H., *Shokubay* **1965**, *7*, 3113

233. Kasprzyk-Hordern, B., Chemistry of Alumina, reactions in aqueous solution and its application in water treatment. *Adv. Colloid Interface Sci.* **2004**, *110*, 19-48.

234. Morris, H. D.; Ellis, P. D., Aluminum-27 cross polarization of Aluminas. The Nmr spectroscopy of surface Aluminum atoms. *J. Am. Chem. Soc.* **1989**, *111*, 6045-6049.

235. Majors, P. D.; Ellis, P. D., Surface site distributions by solid-state multinuclear Nmr spectroscopy. Pyridine binding to gamma-Alumina by Nitrogen-15 and Deuterium Nmr. *J. Am. Chem. Soc.* **1987**, *109*, 1648-1653.

236. Huggins, B. A.; Ellis, P. D., Aluminum-27 nuclear magnetic resonance study of Aluminas and their surfaces. *J. Am. Chem. Soc.* **1992**, *114*, 2098-2108.

237. Coster, D.; Blumenfeld, A. L.; Fripiat, J. J., Lewis acid sites and surface Aluminum in Aluminas and Zeolites: A high-resolution Nmr study. *J. Phys. Chem.* **1994**, *98*, 6201-6211.

238. Blumenfeld, A. L.; Fripiat, J. J., Acid sites topology in Aluminas and Zeolites from high-resolution solid-state Nmr. *Top. Catal.* **1997**, *4*, 119-129.

239. Lunsford, J. H., Characterization of acidity in zeolites and related oxides using Trimethylphosphine as a probe. *Top. Catal.* **1997**, *4*, 91-98.

240. Ripmeester, J. A., Surface acid site characterization by means of Cp/Mas Nitrogen-15 Nmr. *J. Am. Chem. Soc.* **1983**, *105*, 2925-2927.

241. Tsyganenko, A.; Filimonov, V., Infrared spectra of surface hydroxyl groups and crystalline structure of oxides. *Spectrosc. Lett.* **1972**, *5*, 477-487.

242. Tsyganenko, A.; Filimonov, V., Infrared spectra of surface hydroxyl groups and crystalline structure of oxides. *J. Mol. Struct.* **1973**, *19*, 579-589.

243. Busca, G.; Lorenzelli, V.; Escribano, V. S.; Guidetti, R., Ft-113 study of the surface properties of the spinels Nial2o4 and Coal2o4 in relation to those of transitional Aluminas. *J. Catal.* **1991**, *131*, 167-177.

244. Morterra, C.; Ghiotti, G.; Garrone, E.; Boccuzzi, F., Infrared spectroscopic characterization of the A-Alumina surface. *J. Chem. Soc., Farad. Trans. 1: Phys. Chem. Condens. Phases* **1976**, *72*, 2722-2734.

245. Morterra, C.; Ghiotti, G.; Boccuzi, F.; Coluccia, S., An infrared spectroscopic investigation of the surface properties of Magnesium Aluminate spinel. *J. Catal.* **1978**, *51*, 299-313.

246. Kabalka, G. W.; Pagni, R. M., Organic reactions on Alumina. *Tetrahedron* **1997**, *53*, 7999-8065.

247. Busca, G.; Lorenzelli, V.; Ramis, G.; Willey, R. J., Surface sites on spinel-type and corundum-type metal oxide powders. *Langmuir* **1993**, *9*, 1492-1499.

248. Zaki, M.; Knözinger, H., Carbon Monoxide—a low temperature infrared probe for the characterization of hydroxyl group properties on metal oxide surfaces. *Mater. Chem. Phys.* **1987**, *17*, 201-215.

249. Knöuzinger, H., Specific poisoning and characterization of catalytically active oxide surfaces. *Adv. Catal.* **1976**, *25*, 184-271.

250. Kung, M. C.; Kung, H. H., Ir studies of Nh3, Pyridine, Co, and No adsorbed on transition metal oxides. *Catal. Rev. Sci. Eng.* **1985**, *27*, 425-460.

251. Hass, K.; Schneider, W.; Curioni, A.; Andreoni, W., First-principles molecular dynamics simulations of H_2O on A-Al_2O_3 (0001). *J. Phys. Chem. B* **2000**, *104*, 5527-5540.

252. Eng, P. J.; Trainor, T. P.; Brown Jr, G. E.; Waychunas, G. A.; Newville, M.; Sutton, S. R.; Rivers, M. L., Structure of the hydrated A-Al_2O_3 (0001) surface. *Science* **2000**, *288*, 1029-1033.

253. Al-Abadleh, H. A.; Grassian, V., Ft-Ir study of water adsorption on Aluminum Oxide surfaces. *Langmuir* **2003**, *19*, 341-347.

254. Zhang, L.; Tian, C.; Waychunas, G. A.; Shen, Y. R., Structures and charging of A-Alumina (0001)/water interfaces studied by sum-frequency vibrational spectroscopy. *J. Am. Chem. Soc.* **2008**, *130*, 7686-7694.

255. Ranea, V. A.; Schneider, W. F.; Carmichael, I., Dft characterization of coverage dependent molecular water adsorption modes on A-Al_2O_3 (0001). *Surf. Sci.* **2008**, *602*, 268-275.

256. Ranea, V. c. A.; Carmichael, I.; Schneider, W. F., Dft investigation of intermediate steps in the hydrolysis of A-Al_2O_3 (0001). *J. Phys. Chem. C* **2009**, *113*, 2149-2158.

257. Wittbrodt, J.; Hase, W.; Schlegel, H., Ab initio study of the interaction of water with cluster models of the Aluminum terminated (0001) A-Aluminum oxide surface. *J. Phys. Chem. B* **1998**, *102*, 6539-6548.

258. Shapovalov, V.; Truong, T. N., Ab initio study of water adsorption on A-Al_2O_3 (0001) crystal surface. *J. Phys. Chem. B* **2000**, *104*, 9859-9863.

259. Łodziana, Z.; Nørskov, J. K.; Stoltze, P., The stability of the hydroxylated (0001) surface of A-Al_2O_3. *J. Chem. Physics* **2003**, *118*, 11179-11188.

260. Gaigeot, M.-P.; Sprik, M.; Sulpizi, M., Oxide/water interfaces: How the surface Chemistry modifies interfacial water properties. *J. Phys.: Condens. Matter* **2012**, *24*, 124106.

261. Braunschweig, B.; Eissner, S.; Daum, W., Molecular structure of a mineral/water interface: Effects of surface nanoroughness of A-Al_2O_3 (0001). *J. Phys. Chem. C* **2008**, *112*, 1751-1754.

262. Flörsheimer, M.; Kruse, K.; Polly, R.; Abdelmonem, A.; Schimmelpfennig, B.; Klenze, R.; Fanghänel, T., Hydration of mineral surfaces probed at the molecular level. *Langmuir* **2008**, *24*, 13434-13439.

263. Sung, J.; Zhang, L.; Tian, C.; Shen, Y. R.; Waychunas, G. A., Effect of Ph on the water/A-Al_2O_3 ($1\bar{1}02$) interface structure studied by Sum-frequency vibrational spectroscopy. *J. Phys. Chem. C* **2011**, *115*, 13887-13893.

264. Sung, J.; Shen, Y.; Waychunas, G., The interfacial structure of water/protonated A-Al_2O_3 () as a function of Ph. *J. Phy.: Condens. Matter* **2012**, *24*, 124101.

265. Huang, P.; Pham, T. A.; Galli, G.; Schwegler, E., Alumina (0001)/water interface: Structural properties and infrared spectra from first-principles molecular dynamics simulations. *J. Phys. Chem. C* **2014**, *118*, 8944-8951.

266. Sung, J.; Zhang, L.; Tian, C.; Shen, Y. R.; Waychunas, G. A., Effect of Ph on the water/A-Al_2O_3 (1102) Interface structure studied by sum-frequency vibrational spectroscopy. *J. Phys. Chem. C* **2011**, *115*, 13887-13893.

267. Mawhinney, D. B.; Rossin, J. A.; Gerhart, K.; Yates, J. T., Adsorption and reaction of 2-Chloroethylethyl Sulfide with Al_2O_3 surfaces. *Langmuir* **1999**, *15*, 4789-4795.

268. Glemser, O.; Rieck, G., Die Bindung Des Wassers in Den Durch Thermische Zersetzung Von Aluminiumhydroxyden Entstandenen Phasen. *Angewandte Chemie* **1956**, *68*, 182-182.

269. Glemser, O., Ergebnisse Und Probleme Von Verbindungen Der Systeme Oxyd-Wasser. *Angewandte Chemie* **1961**, *73*, 785-805.

270. Liu, P.; Kendelewicz, T.; Brown, G. E.; Nelson, E. J.; Chambers, S. A., Reaction of water vapor with A-Al_2O_3(0001) and A-Fe_2O_3(0001) surfaces: Synchrotron X-ray photoemission studies and thermodynamic calculations. *Surf. Sci.* **1998**, *417*, 53-65.

271. Hendriksen, B. A.; Pearce, D. R.; Rudham, R., Heats of adsorption of water on A- and Γ-Alumina. *J. Catal.* **1972**, *24*, 82-87.

272. Medema, J., Isomerization of Butene over Alumina. *J. Catal.* **1975**, *37*, 91-100.

273. Eng, P. J.; Trainor, T. P.; Brown Jr., G. E.; Waychunas, G. A.; Newville, M.; Sutton, S. R.; Rivers, M. L., Structure of the hydrated A-Al₂O₃ (0001) surface. *Science* **2000**, *288*, 1029-1033.

274. Hass, K. C.; Schneider, W. F.; Curioni, A.; Andreoni, W., First-principles molecular dynamics simulations of H_2O on A-Al_2O_3 (0001). *J. Phys. Chem. B* **2000**, *104*, 5527-5540.

275. Ballinger, T. H.; Yates Jr, J. T., High-temperature behavior of Rhodium/Alumina catalysts. *J. Phys. Chem.* **1991**, *95*, 1694-1698.

276. Wischert, R.; Copéret, C.; Delbecq, F.; Sautet, P., Dinitrogen: A selective probe for tri-coordinate Al "defect" sites on Alumina. *Chem. Comm.* **2011**, *47*, 4890-4892.

277. Joubert, J.; Salameh, A.; Krakoviack, V.; Delbecq, F.; Sautet, P.; Copéret, C.; Basset, J. M., Heterolytic splitting of H_2 and CH_4 on Γ-Alumina as a structural probe for defect sites. *J. Phys. Chem. B* **2006**, *110*, 23944-23950.

278. Wischert, R.; Copéret, C.; Delbecq, F.; Sautet, P., Optimal water coverage on Alumina: A key to generate Lewis acid–base pairs that are reactive towards the C-H bond activation of Methane. *Angewandte Chem. Int. Ed.* **2011**, *50*, 3202-3205.

279. Wischert, R.; Laurent, P.; Copéret, C.; Delbecq, F. o.; Sautet, P., *γ*-Alumina: The essential and unexpected role of water for the structure, stability, and reactivity of "defect" sites. *J. Am. Chem. Soc.* **2012**, *134*, 14430-14449.

280. Zambon, P.; Ricci, P.; Bovo, E.; Casula, A.; Gattolin, M.; Fiore, A. R.; Chiosi, F.; Guzzinati, S., Sarcoma risk and dioxin emissions from incinerators and industrial plants: A population-based case-control study (Italy). *Environ. Health* **2007**, *6*, 19.

281. Floret, N.; Lucot, E.; Badot, P.-M.; Mauny, F.; Viel, J.-F., A municipal solid waste incinerator as the single dominant point source of PCDD/Fs in an area of increased non-Hodgkin's lymphoma incidence. *Chemosphere* **2007**, *68*, 1419-1426.

282. Sioutas, C.; Delfino, R. J.; Singh, M., Exposure assessment for atmospheric ultrafine particles (UFPs) and implications in epidemiologic research. *Environ. Health Perspect.* **2005**, *113*, 947.

283. Ntziachristos, L.; Froines, J. R.; Cho, A. K.; Sioutas, C., Relationship between Redox activity and chemical speciation of size-fractionated particulate matter. *Part. Fib. Toxicol.* **2007**, *4*, 5.

284. Zhu, Y.; Hinds, W. C.; Kim, S.; Sioutas, C., Concentration and size distribution of ultrafine particles near a major highway. *J. Air Waste Manage. Assoc.* **2002**, *52*, 1032-1042.

285. Barmpadimos, I.; Keller, J.; Oderbolz, D.; Hueglin, C.; Prévôt, A., One decade of parallel fine ($PM_{2.5}$) and coarse (Pm 10–Pm 2.5) particulate matter measurements in Europe: Trends and variability. *Atmos. Chem. Phys.* **2012**, *12*, 3189-3203.

286. Cusack, M.; Alastuey, A.; Pérez, N.; Pey, J.; Querol, X., Trends of particulate matter ($PM_{2.5}$) and chemical composition at a regional background site in the Western Mediterranean over the last nine years (2002–2010). *Atmos. Chem. Phys.***2012**, *12*, 8341-8357.

287. Bølling, A. K.; Pagels, J.; Yttri, K. E.; Barregard, L.; Sallsten, G.; Schwarze, P. E.; Boman, C., Health effects of residential wood smoke particles: The importance of combustion conditions and physicochemical particle properties. *Part. Fib. Toxicol.* **2009**, *6*, 29.

288. Dellinger, B.; Pryor, W. A.; Cueto, R.; Squadrito, G. L.; Hegde, V.; Deutsch, W. A., Role of free radicals in the toxicity of airborne fine particulate matter. *Chem. Res. Ttoxicol.* **2001**, *14*, 1371-1377.

289. Walsh, M.; Cormier, S.; Varner, K.; Dellinger, B., By-products of the thermal treatment of hazardous waste: Formation and health effects. *EM (Pittsburgh, Pa.)* **2010**, 26.

290. Dellinger, B.; Lomnicki, S.; Khachatry/an, L.; Maskos, Z.; Hall, R. W.; Adounkpe, J.; McFerrin, C.; Truong, H., Formation and stabilization of persistent free radicals. *Proc. Combust. Inst.* **2007**, *31*, 521-528.

291. Lomnicki, S.; Truong, H.; Vejerano, E.; Dellinger, B., Copper oxide-based model of persistent free radical formation on combustion-derived particulate matter. *Environ. Sci. Technol.* **2008**, *42*, 4982-4988.

292. Peters, A.; Dockery, D. W.; Muller, J. E.; Mittleman, M. A., Increased particulate air pollution and the triggering of myocardial infarction. *Circulation* **2001**, *103*, 2810-2815.

293. Nel, A., Air pollution-related illness: Effects of particles. *Science* **2005**, *308*, 804-806.

294. Vejerano, E.; Lomnicki, S.; Dellinger, B., Formation and stabilization of combustion-generated environmentally persistent free radicals on an Fe $(III)_2O_3$/Silica surface. *Environ. Sci. Technol.* **2010**, *45*, 589-594.

295. Vejerano, E.; Lomnicki, S. M.; Dellinger, B., Formation and stabilization of combustion-generated, environmentally persistent radicals on Ni (II) O supported on a silica surface. *Environ. Sci. Technol.* **2012**, *46*, 9406-9411.

296. Cass, G. R.; Hughes, L. A.; Bhave, P.; Kleeman, M. J.; Allen, J. O.; Salmon, L. G., The chemical composition of atmospheric ultrafine particles. *Philos. Trans. R. Soc. London A: Math. Phys. Eng. Sci.* **2000**, *358*, 2581-2592.

297. Vejerano, E.; Lomnicki, S.; Dellinger, B., Lifetime of combustion-generated environmentally persistent free radicals on Zn (II) O and other transition metal oxides. *J. Environ. Monit.* **2012**, *14*, 2803-2806.

298. Mosallanejad, S.; Dlugogorski, B. Z.; Kennedy, E. M.; Stockenhuber, M.; Lomnicki, S. M.; Assaf, N. W.; Altarawneh, M., Formation of Pcdd/Fs in oxidation of 2-chlorophenol on neat silica surface. *Environ. Sci. Technol.* **2016**, *50*, 1412-1418.

299. Altarawneh, M.; Dlugogorski, B. Z., Formation and chlorination of Carbazole, Phenoxazine, and Phenazine. *Environ. Sci. Technol.* **2015**, *49*, 2215-2221.

300. Altarawneh, M.; Dlugogorski, B. Z., Formation of Dibenzofuran, Dibenzo-P-Dioxin and their hydroxylated derivatives from Catechol. *Phys. Chem. Chem. Phys.* **2015**, *17*, 1822-1830.

301. Altarawneh, M.; Radny, M. W.; Smith, P. V.; Mackie, J. C.; Kennedy, E. M.; Dlugogorski, B. Z.; Soon, A.; Stampfl, C., A first-principles density functional study of Chlorophenol adsorption on Cu_2O (110): CuO. *J. Chem. Phys.* **2009**, *130*, 184505.

302. Lomnicki, S.; Truong, H.; Dellinger, B., Mechanisms of product formation from the pyrolytic thermal degradation of Catechol. *Chemosphere* **2008**, *73*, 629-633.

303. Truong, H.; Lomnicki, S.; Dellinger, B., Mechanisms of molecular product and persistent radical formation from the pyrolysis of Hydroquinone. *Chemosphere* **2008**, *71*, 107-113.

304. Patterson, M. C.; Keilbart, N. D.; Kiruri, L. W.; Thibodeaux, C. A.; Lomnicki, S.; Kurtz, R. L.; Poliakoff, E.; Dellinger, B.; Sprunger, P. T., Epfr formation from Phenol adsorption on Al_2O_3 and TiO_2: Epr and Eels studies. *Chem. Phys.* **2013**, *422*, 277-282.

305. Farquar, G. R.; Alderman, S.; Poliakoff, E.; Dellinger, B., X-ray spectroscopic studies of the high temperature reduction of Cu(II) O by 2-Chlorophenol on a simulated fly ash surface. *Environ. Sci. Technol.* **2003**, *37*, 931-935.

306. Alderman, S.; Farquar, G. R.; Poliakoff, E.; Dellinger, B., Reaction of 2-Chlorophenol with CuO: Xanes and sem analysis. *Proc. Combust. Inst.* **2005**, *30*, 1255-1261.

307. Patterson, M. C.; Thibodeaux, C. A.; Kizilkaya, O.; Kurtz, R. L.; Poliakoff, E.; Sprunger, P. T., Electronic signatures of a model pollutant–particle system: Chemisorbed Phenol on TiO_2 (110). *Langmuir* **2015**, *31*, 3869-3875.

308. Lomnicki, S.; Dellinger, B., A detailed mechanism of the surface-mediated formation of Pcdd/F from the oxidation of 2-Chlorophenol on a CuO/Silica surface. *J. Phys. Chem. A* **2003**, *107*, 4387-4395.

309. Takasuga, T.; Makino, T.; Tsubota, K.; Takeda, N., Formation of dioxins (PCDDs/PCDFs) by dioxin-free fly ash as a catalyst and relation with several Chlorine-sources. *Chemosphere* **2000**, *40*, 1003-1007.

310. Seames, W. S., An initial study of the fine fragmentation fly ash particle mode generated during pulverized coal combustion. *Fuel Process.Technol.* **2003**, *81*, 109-125.

311. Cains, P. W.; McCausland, L. J.; Fernandes, A. R.; Dyke, P., Polychlorinated Dibenzo-P-Dioxins and Dibenzofurans formation in incineration: Effects of fly ash and Carbon source. *Environ. Sci. Technol.* **1997**, *31*, 776-785.

312. Ahmaruzzaman, M., A review on the utilization of fly ash. *Prog. Energy Combust. Sci.* **2010**, *36*, 327-363.

313. Potter, P. M.; Dellinger, B.; Lomnicki, S. M., Contribution of Aluminas and Aluminosilicates to the formation of Pcdd/Fs on fly ashes. *Chemosphere* **2016**, *144*, 2421-2426.

314. Pan, W.; Zhong, W.; Zhang, D.; Liu, C., Theoretical study of the reactions of 2-Chlorophenol over the dehydrated and hydroxylated Silica clusters. *J. Phys. Chem. A* **2011**, *116*, 430-436.

315. Mosallanejad, S.; Dlugogorski, B. Z.; Altarawneh, M.; Kennedy, E. M.; Yokota, M.; Nakano, T.; Stockenhuber, M., Decomposition of 2-Chlorophenol on surfaces of neat Alumina and Alumina supported Iron (III) Oxide catalysts. *Organohalogen Compd.* **2014**, *76*, 396-399.

CHAPTER 3

Theoretical Background

Theoretical chemistry is the backbone of chemistry. It is a mathematical description chemists use to solve chemical problems by employing computer simulations. It can be applied when a calculated method is established well enough to be automated for computerisation. Depending on the methodology, different tools can be deployed.

The theoretical tools on which this thesis is based centre around ab initio thermodynamic approach along with density function theory and the properties attained within the framework of these widely used methods. In this chapter we briefly elucidate the theories involved in the development of these tools, followed by a brief description of the computer codes employed within the scope of this thesis (i.e. DMol^3 cod and CRYSTAL14 code).

3.1 Schrödinger Equation

Describing the electronic structure of a many-body system depends upon an approximate solution of the Schrödinger equation.[1-2]

$$H\Psi = E\Psi \qquad 3.1$$

Where: Ψ signifies many-body wave functions, H stands for the many-body Hamiltonian and E is the total energy. For a molecular system, H involves different parts comprising kinetic, T, and potential, V, energies of the molecular system as follows:

$$H = T_I + T_i + V_{I,I} + V_{i,i} + V_{ext} \qquad 3.2$$

where: uppercase *I* signifies nuclei and lowercase *i* denotes electrons. T_I is the kinetic energy of the nuclei, T_i is the kinetic energy of the electrons, $V_{I,I}$ is the nuclei-nuclei interactions, $V_{i,i}$ is the electron-electron interactions and V_{ext} is the electron-nuclei interactions or the so called external potential (e.g. This expression applies only for the electronic subsystem described by Eq. 3.3)

Based on the fact that the electron motion is much faster than that of the nuclei, the Born-Oppenheimer approximation is employed which disregards the nuclear motion.[3] Therefore, the solution of the equation will be simplified by adopting only the electronic energy as well as the position of the nuclei as follows:

$$H = T_i + V_{i,i} + V_{ext} \tag{3.3}$$

The terms in the above Eq. (3.3) are given as:

$$T_i = -\frac{1}{2}\sum_i \nabla_i^2 \tag{3.4}$$

$$V_{i,i} = \frac{1}{2}\sum_i \sum_{j,i\neq j} \frac{1}{|r_j - r_i|} \tag{3.5}$$

$$V_{ext} = -\sum_I \sum_i \frac{Z_I}{|R_I - r_i|} \tag{3.6}$$

where *r* is the location of electrons and *R* is the location of nuclei. Atomic units are adopted throughout, meaning $e = \alpha_0 = m_e = \hbar = (4\pi\varepsilon_0)^{-1} = 1$ for unit charge, Bohr radius, electronic mass and reduced Planck, respectively.

Practically, the many-body Schrödinger equation cannot be solved without a reliance on some approximation methods. Such approximations provides assumptions (i.e., describing the energy as a function of density in density function theory), and make finding the solution of the equation a tractable problem. We will describe this approach, density function theory, in the following section.

3.2 Density Function Theory

Density functional theory depends on a principle of expressing the energy as a function of density. The root of this principle is the Thomas-Fermi model, where the total energy of an electronic many-body system can be computed in terms of its electronic density.[4] Employing a uniform electron gas to treat the electron-electron repulsion and nuclear-electron interaction and modelling the kinetic energy, the functional energy can be written as:

$$E_{TF}[\rho(r)] = \frac{3}{10}(3\pi^2)^{2/3} \int \rho^{5/3}\,(\mathrm{r})dr - Z\int \frac{\rho(r)}{r}dr + \iint \frac{\rho(r_1)\rho(r_2)}{r_{12}}dr_1 dr_2 \qquad 3.7$$

The absence of exchange and correlation in the Thomas-Fermi model results in non-accuracy of the results attained from this model. Corrections to the electron density of the Thomas-Fermi model have later been demonstrated by applying the variational principle to Eq. 3.7. This correction was first demonstrated by Hohenberg and Kohn in 1964.[5]

3.2.1 The Hohenberg-Kohn Theorems

Hohenberg and Kohn[5] derived two main theorems, both, adopted the electron density as a main variable, rather than the wave function, in attaining the total energy of the system. The first theorem includes formulating the external potential in terms of the electron density as follows:[6-7]

$$E\left[\rho(r)\right] = \int \rho(r) V_{ext}\, dr + F_{HK}\left[\rho(r)\right] \tag{3.8}$$

where F_{HK} signifies Hohenberg-Kohn energy functional which is a representation of an electron-electron interaction $E_{ii}[\rho]$ as well as the kinetic energy of the electrons $T_i[\rho]$.

$$F_{HK}\left[\rho(r)\right] = E_{ii}\left[\rho\right] + T_i\left[\rho\right] \tag{3.9}$$

The term $E_{ii}[\rho]$ in the above Eq. (3.9) is divided into two terms, namely; Coulomb repulsion $J[\rho]$ and non-classical component $E_{ncl}[\rho]$. It is given as:

$$E_{ii}\left[\rho\right] = \frac{1}{2}\int\int \frac{\rho(r_1)\rho(r_2)}{r_{12}} dr_1\, dr_2 + E_{ncl}\left[\rho\right] = J\left[\rho\right] + E_{ncl}\left[\rho\right] \tag{3.10}$$

In the second theorem, using the vibrational type approach, Hohenberg and Kohn revealed that the lowest energy of the system is an upper bound to the true ground stat energy:

$$F_0 = E\left[\rho_0(r)\right] \leq E\left[\rho(r)\right] \tag{3.11}$$

The latter provides new insights toward the use of the ground state density in calculating the properties of the systems.

3.2.2 The Kohn-Sham Equation

Kohn and Sham[8] provided an approximation to solve the universal functional $F_{HK}[\rho(r)]$. They interpreted the kinetic energy functional T_i by means of kinetic energy of a non-interacting reference system T_s and an unknown part T_c. The latter covers the corrections in reference to the electron interactions in the real systems.

The Hohenberg-Kohn energy functional is then given as:

$$F_{HK} = T_s[\rho] + J[\rho] + E_{xc}[\rho] \qquad 3.12$$

where $T_s[\rho]$ is the kinetic energy of the non-interacting electrons and $E_{xc}[\rho]$ is the exchange-correlation energy. The former is calculated using one-particle wave function φ. Both terms are given as:

$$T_s[\rho] = \sum_{i=1}^{N} \left\langle \varphi_i \left| -\frac{1}{2}\nabla^2 \right| \varphi_i \right\rangle \qquad 3.13$$

$$E_{xc}[\rho] = T_i[\rho] - T_s[\rho] + E_{ii}[\rho] - J[\rho] \qquad 3.14$$

Again, $T_i[\rho]$ and $T_s[\rho]$ represents kinetic energies in interacting and non-interacting systems, respectively.

Following the Kohn-Sham methodology, the many-body system can be treated as a single, and all unknown variables are integrated into the exchange-correlation term. This can be formulated by the so called Kohn-Sham equation as follows:

$$\left[-\frac{1}{2}\nabla^2 + V_{eff}(r)\right]\varphi_i = \varepsilon_i \varphi_i \qquad 3.15$$

where $V_{eff}(r)$ is the effective potential which defined by the external $V_{ext}(r)$, the classical Coulomb and the exchange-correlation $V_{xc}(r)$ potentials, as follows:

$$V_{eff}(r) = V_{ext}(r) + \int \frac{\rho(r')}{|r - r'|} dr' + V_{xc}(r) \qquad 3.16$$

The density of the real systems is given by the following formula

$$\rho(r) = \sum_i^N |\varphi_i(r)|^2 \qquad 3.17$$

where φ_i represents the Kohn-Sham orbitals.

The derivative of equation 3.14 with respect to density gives the exchange- correlation potential, $V_{xc}(r)$. The latter is the only unknown parameter in the Kohn-Sham equation, which can be expressed as:

$$V_{xc}(r) = \frac{\delta E_{xc}[\rho(r)]}{\delta \rho(r)} \qquad 3.18$$

3.2.3 Exchange- Correlation Functional

Finding a good approximation to the exchange- correlation term in the Kohn-Sham equation is one of the main obstacles in modern DFT. A wide variety of methods has been developed for treating this term and completing the solution of the equation. In this section, we will briefly discuss two widely used methods/approximations - the local density approximation and the generalised gradient approximation (GGA).

The local density approximation treats the exchange-correlation of an inhomogeneous system as a local homogeneous electron gas, where its exchange-correlation terms are known[9]:

$$E_{xc}^{LDA}[\rho] = \int \rho(r)\varepsilon_{xc}[\rho(r)]dr \qquad 3.19$$

where $\varepsilon_{xc}[\rho(r)]$ illustrates the exchange-correlation of the homogeneous electron gas or the so called LDA energy functional, which in turn can be split into two terms, namely: exchange and correlations:

$$\varepsilon_{xc}\left[\rho(r)\right] = \varepsilon_x\left[\rho(r)\right] + \varepsilon_c\left[\rho(r)\right] \qquad 3.20$$

The first term in Eq. 3.20, exchange energy, is given by Dirac's expression[10]:

$$E_x\left[\rho\right] = -C_x\int \rho(r)^{4/3} dr \qquad 3.21$$

and,

$$\varepsilon_x\left[\rho\right] = -\frac{3}{4}\left(\frac{3}{\pi}\right)^{1/3}\rho^{1/3} = -\frac{3}{4}\left(\frac{9}{4\pi^2}\right)^{1/3}\frac{1}{r_s} \qquad 3.22$$

where r_s is the inter-electronic distance. The second term in Eq. 3.20 is given by different accurate numerical approximations[11-13].

The generalised gradient approximations (GGA) offer an improvement to the LDA. It considers the electron density as well as its gradient:

$$E_{xc}^{GGA} = \int \rho(r)\varepsilon_{xc}\left(\rho(r), \nabla\rho(r)\right) dr \qquad 3.23$$

GGA provides more accurate results when compared to LDA, hence, it is the mainly used approximation in calculations presented in the thesis.

In addition to LDA and GGA approximations, Hybrid functionals, such as PBE0, B3LYP and HSE03, provides a substantial improvement over both approximation descriptions. It includes a combination of conventional DFT and Hartree-Fock method (HF).[14-17]

$$E_{xc}^{Hybrid}[\rho] = \mu\left(E_x^{HF}[\rho] - E_x^{GGA}[\rho]\right) + E_{xc}^{GGA}[\rho] \qquad 3.24$$

where $E_x^{HF}[\rho]$ is the HF exchange term, and μ is the amount of exact-exchange.

Each chapter contains a detailed description of the specific computational method, including the exchange-correlation approximation, as well as the geometric and electronic calculation parameters.

3.3 Ab Initio Atomistic Thermodynamic

The use of DFT is a well-established approach for electronic structure calculations. Using this approach, a deeper insight into the microscopic regime can be attained. However, a complete understanding of the real image of a system (i.e.; heterogeneous catalysis) requires obtaining further in-depth information on a macroscopic time and length scale. For example, all DFT calculations are implemented at zero pressure and zero temperature (i.e.; T=0 K and P=0 KPa), on the other hand the actual real reactions occur at high pressure and temperature. To clarify the macroscopic system on the basis of a microscopic consideration, a multi-scale modelling

approach is needed. A common example is the ab initio thermodynamic approach.[18-19] Figure 3.1 displays the time and scale regime used to represent material science applications.

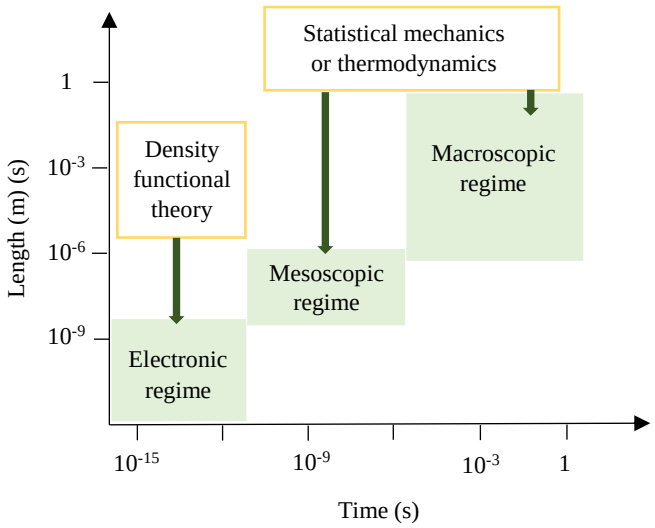

Figure 3.1. The time and scale regime used to represent material science applications.[18]

Using the results attained from DFT as an input to statistical mechanics or a thermodynamic approach is a way to actually connect the time and scale regimes which results in describing the system of finite temperature and pressers.[20-23]

The key variable in an investigating a (*T*, *P*)-ensemble is the Gibbs free energy, *G*.

$$G(T,V,N) = H(T,V,N) - TS^{conf}(T,V,N) \qquad 3.25$$

$$H(T,V,N) = U(T,V,N) + PV(T,V,N) \qquad 3.26$$

where $H(T,V,N)$ is enthalpy, $TS^{conf}(T,V,N)$ is configurational energy, $U(T,V,N)$ is internal energy, and P and V in the last term, $PV(T,V,N)$, represent the pressure and volume, respectively.

The internal energy term, $U(T,V,N)$, is given by the total energy, E^{tot}, which is directly attained from DFT calculations or the so called electronic structure calculations, as well as the vibrational free energy, F^{vib}, as follows:

$$U(T,V,N) = E^{tot}(V,N) - F^{vib}(T,V,N) \qquad 3.27$$

By combining the three equations Eq. 3.25-3.27 the Gibbs free energy is then defined as:

$$G(T,V,N) = E^{tot}(V,N) - F^{vib}(T,V,N) + PV(T,V,N) - TS^{conf}(T,V,N) \qquad 3.28$$

For solid surface calculations, the $E^{tot}(V,N)$ term has the most substantial contribution to the value of the Gibbs free energy. A number of approximations can be applied to Eq. 3.28, making the contribution of the three last terms of the equation, $F^{vib}(T,V,N)$, $PV(T,V,N)$ and $TS^{conf}(T,V,N)$, negligible. For example, the input of the *PV* term can be estimated by employing simple dimensional analysis. The surface energy values within DFT calculations is calculated per surface area, and therefore, the *PV/A* dimension is bar Å^3/Å^2. The latter is approximately equal to 10^{-3} meV/ Å^2 when applying 1 bar of pressure (100 kPa). Even at high pressure, P~100, the *PV* term will also be trivial (less than 0.1) making this part negligible when compared to the total energy value..

In regard to the configuration entropy term, TS^{conf}, for well-ordered system, the configurational entropy stems from trivial disorder (i.e.; surface defects). Hence the energy contribution of this term to the Gibbs free energy is negligible. The configurational contribution for a system like boron, used in this work, can be estimated using the atomistic thermodynamic approach. Such approach is a direct screening method can be used only for the well-ordered surface phases to compare the stability order of all plausible structures.

Finally, the vibrational term, F^{vib}, can generally be attained from DFT calculations. However, it is realized that the contribution of this term is directly related to the system. The effect of lattice vibrations, often neglected in semiconductor alloy thermodynamic calculations, correspondingly the influence of this term in our system is neglected. Thus, the Gibbs free energy can be attained from the total energy of the system solely.[24-32]

$$G(T,P) = E^{tot} \qquad 3.29$$

3.3.1 Surface Free Energy Phase Diagram

In equilibrium, the energy of a one-component system, E, can be attained by its internal energy which is reliant on the entropy, S, the number of the particle, N and the volume, V, of the system.

$$E_{bulk} = TS - PV + N\mu \qquad 3.30$$

where μ is chemical potential of the system. Solid surface calculations require cleavage of a homogeneous solid or the so called bulk. This results in the formation of two surfaces of size A. Such a process does not occur spontaneously, hence, the energy of the system has to upgrade by an amount proportional to the size of the surface. The constant of proportionality is illustrated as surface energy, γ,[33] therefore the internal energy of a cleaved bulk (surface) can be given as:

$$E_{slab} = TS - PV + N\mu + \gamma A \qquad 3.31$$

Substituting the Gibbs free energy, $G = E - TS + PV$, and a subsequent rearrangement of Eq. 3.31, the surface free energy can be formulated as:

$$\gamma = \frac{1}{A}\left[G_{slab} - N\mu\right] \qquad 3.32$$

where G_{slab} stands for the surface free energy of a cleaved surface. For a multi-component system (i.e., adsorbed molecule over a solid surface), Eq. 3.32 can be expressed by the general formula of:

$$\gamma = \frac{1}{A}\left[G_{slab} - \sum_i N_i \mu_i\right] \qquad 3.33$$

where *i* represents the species present in the system.

In Chapter 4 the adsorption of oxygen on a pure boron surface has been investigated in order to determine the most stable structure over a wide range of operational pressure and temperature conditions. For this purpose, the phase diagram of oxygen adsorption on α-rhombohedral boron (001) surface has been calculated using Eq.3.33.

Introducing Gibbs free energy of adsorption, G_{ads} ,

$$G_{ads} = G_{O/slab} - G_{slab} \tag{3.34}$$

where $G_{O/slab}$ denotes the Gibbs free energy of the boron surface with N_O adsorbed oxygen atoms, and G_{slab} signifies the Gibbs free energy of the clean boron surface. By substituting Eq. 3.33 can then be given as:[24-27, 29-30, 34-37]

$$\gamma_{ads} = \frac{1}{A}\left[G_{ads} - \sum_i N_i \mu_i(T, P_i) \right] \tag{3.35}$$

$$\gamma_{ads} = \frac{1}{A}\left[\; G_{O/slab} - G_{slab} - \Delta N_B \, \mu_B(T,P) - N_O \, \mu_O(T,P) \; \right] \tag{3.36}$$

where ΔN_B is the difference in the number of boron atoms between the unreconstructed (ideal surface) and reconstructed (with missing or adding atoms) surface. Again using some approximations[24-32]; Eq. 3.36 can then be given as:

$$\gamma_{ads} = \frac{1}{A}\left[\ E_{O/slab} - E_{slab} - \Delta N_B\,\mu_B(T,P) - N_O\,\mu_O(T,P)\ \right] \qquad 3.37$$

where $E_{O/slab}$ is total energy of a boron surface with N_O adsorbed oxygen, E_{slab} is the total energy of a clean boron surface and A is the surface area.

Considering the excess/deficiency of boron atoms in the adsorbates phase and the clean surface, ΔN_B , $\Delta N_B \mu_B(T,P)$ term in Eq. 3.37 can then be defined by the Gibbs free energy of the bulk phase, g_B^{bulk} .

The surface Gibbs free energy at a given temperature and pressure, $\gamma_{ads}(T,P)$ is now given as:

$$\gamma_{ads}(T,P) = \frac{1}{A}\left[N_O E_b - \Delta N_B E_B^{bulk} - N_O\,\mu_O(T,P)\right] \qquad 3.37$$

where N_O is the number of oxygen atoms, ΔN_B is the difference in the number of B atoms between the O/α(001)B12 system and the clean O/α(001)B12 surface, $\mu_O(T,\mathrm{P})$ is the chemical potential of oxygen and E_b is the average binding energy. The latter is formulated as:

$$E_b = \frac{1}{n}\left[E_{O/\,slab} - (E_{slab} + \frac{n}{2}E_{O_2})\right] \qquad 3.39$$

where n represents a number of adsorbed oxygen atoms. For the ideal gas, the chemical potential in Eq. 3.38 is a function of *T* and *P* as follows:

$$\mu_o(T,P) = \tilde{\mu}_o(T,P^o) + \frac{1}{2}kT\ln\left(\frac{P}{P^o}\right) \qquad 3.40$$

where the standard thermodynamic tables[38] provide values $\tilde{\mu}_o(T,P^o)$, as calculated from the variation of entropy and enthalpy of pure oxygen with temperature at standard pressure, P^o (i.e., 1 bar).

3.4 Transition State Determinations

Transition state structure is at the heart of our understanding of chemical reactions; it plays a key role in attaining a deeper insight into the nature of chemical reactions.

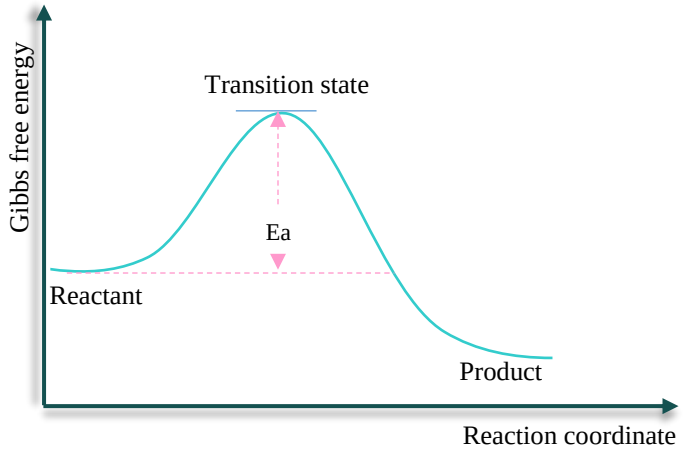

Scheme 3.1. Potential energy surface diagram of a chemical reaction. Ea signifies the activation energy.

The synchronous transit methods LST/QST have been implemented to explain the minimum energy path of chemical reactions illustrated in the thesis. Such methods are normally used to find a reaction path when sensible structures for the reactants and products exist, but the location of the maximum energy along the path (transition state, TS) is unknown and usually requires further refinement.

Starting from reactants and products, the synchronous transit methods find a transition state by linear synchronous transit (LST) method,[39] where a single interpolation is performed to find a maximum energy. A refinement of the transition state is then made by applying quadratic synchronous transit (QST). [39] The latter, is an automatic search for an energy maximum with constrained minimizations in order to refine the transition state to a high degree. The LST method connects the reactant and product structures and build the reaction path by interpolating (geometrically) between both of them. Hence, the maximum energy is found on the path as a guess. On the contrary, the QST method finds the reaction path by interpolating between the geometry of three structures - reactant, product and an intermediate. Figure 3.2. presents an algorithm flow diagram of the synchronous transit methods, LST/QST.

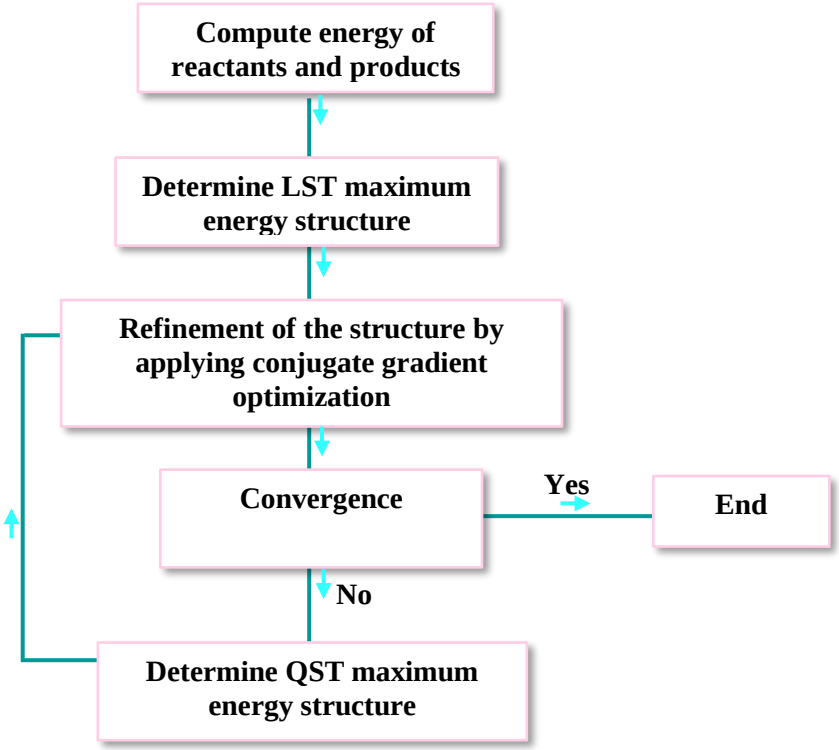

Figure 3.2. Algorithm flow diagram of the synchronous transit methods, LST/QST.[39]

In LST method, the reactant and product structures are connected to each other by a set of idealized structures connecting all distances between pairs of atoms according to the following equations:[40]

$$r_{ab}^{i}(f) = (1-f)r_{ab}^{R} + fr_{ab}^{P} \qquad 3.41$$

where r_{ab}^{R} and r_{ab}^{P} denote the inter-nuclear spaces among atoms *a* and *b* in the reactant and product, respectively, and *f* stands for the interpolation parameter (0-1). A LST path is defined by reaching the molecular geometry in which the atomic distances are close to corresponding values attained from interpolating the Cartesian coordinates between both reactant and product structures. The structure is then found as follows:

$$s(f) = \frac{1}{2}\sum_{a \neq b} \frac{\left[r_{ab} - r_{ab}^{i}(f)\right]^2}{\left[r_{ab}^{i}(f)\right]^4} + 10^{-6}\sum_{a}\left[x_a - x_a^{i}(f)\right]^2 \qquad 3.42$$

where x_a^i denote the interpolated Cartesian position of an atom and x_a is the actual coordinate.

$s(f) \geq 0$

QST method, in contrast, requires substituting Eq. 3.41 with:

$$r_{ab}^{i} = \alpha + \beta + \gamma f^2 \qquad 3.41$$

The maximum energy attained from Eq. 3.41 represents the transition state. In the subsequent chapters we provide details on vibrational frequency calculations.

3.5. Optimisation of the Atomic Structure of a System within Density Functional Theory

The geometry optimisation using density function theory aim to locate a stable geometry of the molecule corresponding to the minimum energy structure. It is an iterative procedure where the coordinates of the atoms are modulated so that the total energy of the predicted structure is fetched to a stationary point, i.e., minima of the potential energy surface where forces on the atoms are zero. By computing the energy of the initial geometry and its first derivatives, at the input point, we can determine how close resemblance it is to the actual physical structure of the system at equilibrium. The first derivatives of energy can also provide an indication of the direction along the surface where the energy declines most rapidly from the existing point as

well as the forces that act on the nuclei. Together, this will afford information about the curvature of the surface at that point and offer additional useful information for determining the next step.

Several different algorithms can be used to perform geometry optimisation or the so-called geometry minimisation. These includes, conjugate gradient, steepest descent and Newton-Raphson methods. For example, DMol^3 code when performing geometry minimisation, chooses the appropriate method automatically. Furthermore, optimisation can generally be performed using Cartesian coordinates and/or internal coordinates input geometries in which both can be applied for molecular and crystalline systems.

3.6 Codes

3.6.1 DMol^3

DMol^3 is a reliable, unique and highly accurate computationally efficient modelling program[41-42] and uses DFT to calculate the electronic structure and energetics of atoms, molecules in gas phase boundary conditions and/or solids and surfaces in 3D periodic boundary conditions. It has long been one of the fastest computational methods combines speed with the accuracy to predict structural properties both quickly and reliably, an advantage that become obvious particularly for huge systems (i.e.; > 600 atoms). A wide range of systems can be considered using DMol^3, including, organic/inorganic molecules, metallic solids, covalent solids, molecular crystals and infinite surfaces of a material. Type and quality of the calculations can be easily controlled in DMol^3 via basic input options such as spin state, the basis set, the pseudopotential, total charge and the DFT functional. It is a user friendly interface code with

a visualization tool allow the user to build structures via the graphical interface. Furthermore, it is a flexible client-server architecture. The only disadvantage of this code, is the highly sensitivity of the geometry optimization to the initial geometry of the system, especially in calculations of highly complex surfaces. DMol[3] provides two sets of DFT functional, including: LDA such as PWC of Perdew and Wang[12] and VWN functional of Vosko et al.[12] and GGA functionals such as PW91,[43-44] PBE,[44] BP,[43-44] HCTH,[45] RPBE[46] and BLYP,[47-48] along with dispersion correction for DFT such as Grimm correction[49] and Tkatchenko and Scheffler correction.[50]

DMol[3] offers different types of atomic orbitals used to specify the atomic basis set from small to large sets[51] containing; minimal basis set (Min), double-numeric quality basis set (DN), DN basis with polarization functions (DNP), double-numeric plus d-function (DND) and triple numerical plus polarization (TNT). Pseudopotential, in contrast, can be treated in three different ways, by effective core potential (ECP), density function semi-core pseudopotential (DSPP) and scalar relativity.

DMol[3] provides optimized geometries, excited states of molecules (via time-dependent density functional theory methods[41]), reaction energies, potential barriers (via LST/QST method[39-40]), vibrational spectra, bond order, Fukui indices, charge analysis (Mulliken, Hirshfeld and EPS) as well as thermodynamic properties.

3.6.2 CRYSTAL 14

CRYSTAL is an accurate program[52-53] which uses DFT and HF methods to calculate the electronic structure and energetics of (periodic systems) crystalline solids. A special feature of the code is that it applies the Gaussian-type functions along with the atomic nuclei as the basis set. The latter, makes it very suitable for insulating systems such as minerals (less suitable for metals). Besides, the extensive exploitation of symmetry to achieve computational efficiency.[52] The implementation of hybrid HF/DFT functionals in CRYSTAL is particularly efficient compared to different codes, in partly due to the adoption of localised basis sets, but also due to the decades long effort in the code's development in this direction.

With CRYSTAL, we can attain, structural features, electronic structure, dielectric properties, thermodynamic properties, magnetic properties, transport properties, elastic, piezoelectric and photoelastic properties as well as vibrational properties.

3.7. References

1. Schrödinger, E., Quantisierung Als Eigenwertproblem. *Ann. Phys.* **1926**, *385*, 437-490.
2. Kaxiras, E., *Atomic and Electronic Structure of Solids*; Cambridge university press: **2003**.
3. Born, M.; Oppenheimer, R., Zur quantentheorie der molekeln. *Ann. Phys.* **1927**, *389*, 457-484.
4. Thomas, L. H. In *The Calculation of Atomic Fields*. Cambridge university press: **1927**.
5. Hohenberg, P.; Kohn, W., Inhomogeneous electron gas. *Phys. Rev.* **1964**, *136*, 864-871.

6. Cramer, C. J., *Essentials of Computational Chemistry: Theories and Models*; John Wiley & Sons: **2013**.

7. Parr, R.; Yang, W., *Density Functional Theory of Atoms and Molecules*, New York: Oxford Univ. Press: **1989**.

8. Kohn, W.; Sham, L. J., Self-consistent equations including exchange and correlation effects. *Phys. Rev.* **1965**, *140*, 1133-1138.

9. Kohanoff, J., *Electronic Structure Calculations for Solids and Molecules: Theory and Computational Methods*; Cambridge University Press: **2006**.

10. Dirac, P. A. In *Note on Exchange Phenomena in the Thomas Atom*. Mathematical Proceedings of the Cambridge Philosophical Society, Cambridge University Press: **1930**.

11. Von Barth, U.; Hedin, L., A Local exchange-correlation potential for the spin polarized case. I. *J. Phys. C* **1972**, *5*, 1629-1642.

12. Vosko, S. H.; Wilk, L.; Nusair, M., Accurate spin-dependent electron liquid correlation energies for local spin density calculations: A critical analysis. *Can. J. Phys.* **1980**, *58*, 1200-1211.

13. Perdew, J. P.; Zunger, A., Self-interaction correction to density-functional approximations for many-electron Systems. *Phys. Rev. B* **1981**, *23*, 5048-5079.

14. Heyd, J.; Scuseria, G. E.; Ernzerhof, M., Hybrid functionals based on a screened coulomb potential. *J. Chem.Phys.* **2003**, *118*, 8207-8215.

15. Paier, J.; Marsman, M.; Hummer, K.; Kresse, G.; Gerber, I. C.; Ángyán, J. G., Screened Hybrid density functionals applied to solids. *J. Chem. Phys.* **2006**, *124*, 154709.

16. Paier, J.; Hirschl, R.; Marsman, M.; Kresse, G., The Perdew–Burke–Ernzerhof exchange-correlation functional applied to the G2-1 test set using a plane-wave basis set. *J. Chemical Phys.* **2005**, *122*, 234102.

17. Jaramillo, J.; Scuseria, G. E.; Ernzerhof, M., Local hybrid functionals. *J. Chem. Phys.* **2003**, *118*, 1068-1073.

18. Reuter, K.; Stampf, C.; Scheffler, M., *Ab Initio Atomistic Thermodynamics and Statistical Mechanics of Surface Properties and Functions.* Handbook of Materials Modeling **2005**.

19. Nieminen, R. M., From atomistic simulation towards multiscale modelling of materials. *J. Phys.s: Conden.Matt.* **2002**, *14*, 2859-2876.

20. Kaxiras, E.; Bar-Yam, Y.; Joannopoulos, J.; Pandey, K., Ab initio theory of polar semiconductor surfaces. II. (22) Reconstructions and related phase transitions of gaas ($\overline{111}$). *Phys. Rev. B* **1987**, *35*, 9636-9643.

21. Scheffler, M.; Koukal, J., *Physics of Solid Surfaces*. Elsevier, Amsterdam: **1987**.

22. Scheffler, M.; Dabrowski, J., Parameter-free calculations of total energies, interatomic forces and vibrational entropies of defects in semiconductors. *Philos. Mag. A* **1988**, *58*, 107-121.

23. Qian, G.-X.; Martin, R. M.; Chadi, D., First-principles study of the atomic reconstructions and energies of Ga-and As-stabilized GaAs (100) Surfaces. *Phys. Rev. B* **1988**, *38*, 7649-7663.

24. Wieckowski, A., *Fuel Cell Catalysis: A Surface Science Approach*. John Wiley and Sons: **2009**.

25. Li, W.-X.; Stampfl, C.; Scheffler, M., Insights into the function of silver as an oxidation catalyst by Ab initio atomistic thermodynamics. *Phys. Rev. B* **2003**, *68*, 165412-165427.

26. Peljhan, S.; Kokalj, A., Adsorption of chlorine on Cu (111): A density-functional theory study. *J. Phy. Chem. C* **2009**, *113*, 14363-14376.

27. Reuter, K.; Scheffler, M., First-principles atomistic thermodynamics for oxidation catalysis: Surface phase diagrams and catalytically interesting regions. *Phys. Rev. Lett.* **2003**, *90*, 046103-046107.

28. Rogal, J. *Function of Palladium Surfaces in Oxidizing Environments: A First-Principles Statistical Mechanics Approach*. Dissertation, Free University of Berlin, **2006**.

29. Rogal, J.; Reuter, K.; Scheffler, M., Co oxidation at Pd (100): A first-principles constrained thermodynamics study. *Phys. Rev. B* **2007**, *75*, 205433-205444.

30. Rogal, J.; Reuter, K.; Scheffler, M., First-principles statistical mechanics study of the stability of a subnanometer thin surface oxide in reactive environments: Co oxidation at Pd (100). *Phys. Rev. Lett.* **2007**, *98*, 046101-046105.

31. Stampfl, C., Surface processes and phase transitions from Ab initio atomistic thermodynamics and statistical mechanics. *Catal. Today* **2005**, *105*, 17-35.

32. Stampfl, C.; Soon, A.; Piccinin, S.; Shi, H.; Zhang, H., Bridging the temperature and pressure gaps: Close-packed transition metal surfaces in an oxygen environment. *J. Phys.: Conden. Matt.* **2008**, *20*, 184021-184040.

33. Zangwill, A., *Physics at Surfaces*; Cambridge university press: **1988**.

34. Xu, Y.; Shelton, W. A.; Schneider, W. F., *Synthesis, Properties, and Applications of Oxide Nanomaterials*;John Wiley and Sons: **2007**.

35. Rogal, J. Stability, *Composition and Function of Palladium Surfaces in Oxidizing Environments: A First-Principles Statistical Mechanics Approach.* Freie Universität Berlin Berlin, **2006**.

36. Piccinin, S.; Zafeiratos, S.; Stampfl, C.; Hansen, T. W.; Hävecker, M.; Teschner, D.; Bukhtiyarov, V. I.; Girgsdies, F.; Knop-Gericke, A.; Schlögl, R., Alloy catalyst in a reactive environment: The example of Ag-Cu particles for ethylene epoxidation. *Phys. Rev. Lett.* **2010**, *104*, 035503-035507

37. Soon, A.; Todorova, M.; Delley, B.; Stampfl, C., Thermodynamic stability and structure of copper oxide surfaces: A first-principles investigation. *Phys.l Rev. B* **2007**, *75*, 125420-125429.

38. Chase, M. W. 1998, *NIST-JANAF Thermochemical Tables* (4th ed.; Washington, DC: Am. Chem. Soc.)

39. Govind, N.; Petersen, M.; Fitzgerald, G.; King-Smith, D.; Andzelm, J., A generalized synchronous transit method for transition state location. *Comp. Mater. Sci.e* **2003**, *28*, 250-258.

40. Halgren, T. A.; Lipscomb, W. N., The synchronous-transit method for determining reaction pathways and locating molecular transition states. *Chem. Phys. Lett.* **1977**, *49*, 225-232.

41. Delley, B., Time dependent density functional theory with DMol^3. *J. Phys.: Conden. Matt.* **2010**, *22*, 384208-384214.

42. Delley, B., From molecules to solids with the DMol^3 approach. *J. Chem. Phys.* **2000**, *113*, 7756-7764.

43. Perdew, J. P.; Burke, K.; Ernzerhof, M., Generalized gradient approximation made simple. *Phys. Rev. Lett.* **1996**, *77*, 3865-3868.

44. Perdew, J. P.; Burke, K.; Wang, Y., Generalized gradient approximation for the exchange-correlation hole of a many-electron system. *Phys.Rev. B* **1996**, *54*, 16533-16539.

45. Boese, A. D.; Handy, N. C., A New parametrization of exchange–correlation generalized gradient approximation functionals. *J. Chem. Phys.* **2001**, *114*, 5497-5503.

46. Hammer, B.; Hansen, L. B.; Nørskov, J. K., Improved adsorption energetics within density-functional theory using revised perdew-Burke-Ernzerhof functionals. *Phys. Rev. B* **1999**, *59*, 7413-7421.

47. Becke, A. D., A multicenter numerical integration scheme for polyatomic molecules. *J. Chem. Phys.* **1988**, *88*, 2547-2553.

48. Lee, C.; Yang, W.; Parr, R. G., Development of the colle-salvetti correlation-energy formula into a functional of the electron density. *Phys. Rev. B* **1988**, *37*, 785-789.

49. Grimme, S., Semiempirical GGa-type density functional constructed with a Long-range dispersion correction. *J. Comp. Chem.* **2006**, *27*, 1787-1799.

50. Tkatchenko, A.; Scheffler, M., Accurate molecular van der waals interactions from ground-state electron density and free-atom reference data. *Phys. Rev. Lett.* **2009**, *102*, 073005-073007.

51. Delley, B., An all-electron numerical method for solving the local density functional for polyatomic molecules. *J. Chem. Phys.* **1990**, *92*, 508-517.

52. Dovesi, R.; Orlando, R.; Erba, A.; Zicovich-Wilson, C. M.; Civalleri, B.; Casassa, S.; Maschio, L.; Ferrabone, M.; De La Pierre, M.; D'Arco, P., Crystal14: A Program for the ab initio investigation of crystalline solids. *Int. J. Quantum Chem.* **2014**, *114*, 1287-1317.

53. Dovesi, R.; Roetti, C.; Orlando, R.; Zicovich-Wilson, C. M.; Pascale, F.; Civalleri, B.; Doll, K.; Harrison, N. M.; Bush, I. J.; D'Arco, P.; Llunell, M.; Causà M. Noël, Y. *Crystal 2014 User's Manual*, 2014.

CHAPTER 4

Interaction of Oxygen with α-Rhombohedral Boron (001) Surface

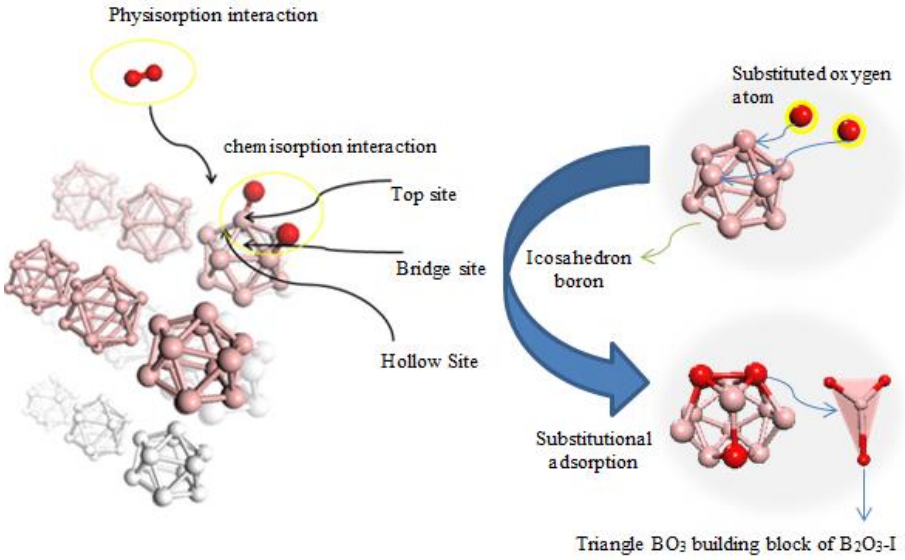

The following is a modified version of the published paper:

Assaf, N. W.; Altarawneh, M. K.; Radny, M. W.; Jiang, Z. T.; Dlugogorski, B. Z., Interaction of Oxygen with *α*-Rhombohedral Boron (001) Surface. *J. Phys. Chem. C* **2016,** *120*, 5968-5979.

2016 impact factor: 4.536

4.1 Introduction

Boron (B) is a unique element of fascinating complexity. Boron and boron-based compounds find applications in diverse areas of energy, environment, electronics and chemical sensing. In most of these applications, boron surfaces interact with atomic and/or molecular oxygen, prompting us to elucidate the chemical and physical characteristics of oxygen-boron systems on a precise atomic scale. Neighbouring carbon in the periodic table, boron affords remarkable similarities and differences in reference to this element.[1] For example, its sp^2 hybridisation – like that of carbon – enables it to form fullerene-like cage configurations and 2D graphene-like monolayer sheets.[2] However, the nature of chemical bonds varies between purely covalent in carbon compounds to non-covalent in boron species, with the latter accompanied by the unique charge distribution. Boron displays chemical inertness at room temperature, significant hardness, low density and, at elevated pressure, also super conductivity.[3-5]

Owing to these properties, elemental boron finds unique applications. Common examples of its usage include igniters in airbags,[6] protective coatings of nuclear reactors,[7] cutting and polishing materials,[8] as well as semiconductors, thermo-electric and high-energy devices.[6, 9] Over a wide range of operational pressures and temperatures, boron exhibits a variety of crystallographic structures such as α-B12 (α-phase),[10-11] β-B106 (β-phase),[12-13] orthorhombic γ-B28 (γ-phase),[14] tetragonal *t*-B192[15] and *t*-B52 (*t*-phase).[14, 16] For this reason, several studies on elemental boron have constructed its governing thermodynamic stability diagram and have reported its thermal and mechanical properties.[5, 11, 16-28] Two phases, α and β dominate the stability phase diagram of the elemental boron.[26, 29-30] Under ambient conditions, the two phases are energy degenerate.[29] In comparison to the β-phase, the α-B12 phase displays less

complexity, higher density and electronic neutrality. Consequently, we elect herein to consider a surface that terminates the α-B12 phase.

Recent theoretical investigations address the potential of deploying boron surfaces as a scavenger for CO_2, N_2 and CH_4 gases. Sun et al.[31] studied the interaction of CO_2 with α and γ(001)B12 surfaces, demonstrating that, the physisorbed states of CO_2 on these two surfaces acquire a rather marginal binding energy corresponding to weak van der Waals complexes. On the contrary, dissociation of CO_2 (i.e., formation of chemisorbed states) displays considerable exothermicity in the range of 1.30 eV – 2.00 eV. The same research group[32] found that, the α and γ(001)B12 surfaces serve as extractors for N_2 and CH_4 from gas mixtures. Along a similar line of enquiry, Marlid et al.[33] investigated both chemical and physical interactions of elemental hydrogen and bromine with the α(001)B12 surface, discovering that, despite its presumed chemically inert nature at the ambient temperature, this boron surface can effectively capture certain gas-phase species.

Virtually all potential applications of boron in industrial and catalytic processes occur in oxidative media, motivating further investigation into the adsorption of atomic and molecular oxygen on clean boron surfaces. Earlier experimental data[34] suggest that, adsorption of molecular oxygen on boron surfaces, in temperature-controlled processes, produces two boron oxides - B_2O_3 and B_2O_2. However, recent XPS measurements indicate that, diboron trioxide represents the only distinguishable form of boron oxide, produced from reaction of oxygen with elemental boron.[35]

$$4B + 3O_{2(g)} \rightarrow 2B_2O_3 \qquad \text{R4.1}$$

Due to the high enthalpy change of this reaction (13.18 eV),[34] oxidation of boron constitutes a secondary energy source in rocket fuel.[36] B_2O_3 also find applications as unreactive coating material for walls of chemical reactors (i.e. quartz tubular flow reactors).[37]

In the present Chapter, we examine theoretically the interaction of molecular and atomic oxygen with the clean α(001)B12 surface. The choice of this particular surfaces stems from a three-fold rationale. Firstly, 001 surface represents a termination of one of the two most stable forms of elemental boron, the α-B12 phase. Secondly, this surface incurs less complexity than surfaces terminating other forms (i.e., β-phase) of boron. These two points allow narrowing down the plausible oxygen adsorption sites. Finally, while there is an example of experimental studies on bulk boron, the only available experimental account of boron surfaces relates to the electronic equidensity of the α(001)B12 surface.[38] Our calculated neutral charge of this surface serves as an additional benchmark for the accuracy of reported results. The present Chapter aims to assess the thermodynamic feasibility of the formation of bulk-like B_2O_3 structure via substitutional adsorption of oxygen atoms on the clean α(001)B12 surface. Oxidation of boron at elevated temperature may affect its performance as a super hard coating material.

4.2 Computational Methodology

All unrestricted spin polarised, total energy and electronic-structure calculations were performed using the DFT[39] functional implemented in the DMol^3 code.[40-41] The computational methodology comprised a generalised gradient approximation of Perdew-Burke-Ernzerhof functional (PBE),[42] along with the Grimme dispersion correction,[43] and a double-polarised numeric basis set of DNP. The Grimme methodology corrects binding energies and

geometrical features of noncovalent systems that characterise the long-range electron correlations. In this formalism, the total corrected energy ($E_{\text{DFT-D}}$) represents the addition of an energy dispersion term (E_{disp}) to the Kohn-Sham energy ($E_{\text{KS-DFT}}$):

$$E_{\text{DFT-D}} = E_{\text{KS-DFT}} + E_{\text{disp}} \qquad 4.1$$

The E_{disp} term is an empirical function estimated based on fitted dispersion coefficients and interatomic distances between each atomic pair. For the system at hand, we found that, introducing the Grimme dispersion correction marginally modifies the binding energies. A test on one structure (T3) indicates that, implementing the Grimme dispersion correction changes the binding energy only by 2.0 %, in reference to the standard GGA-PPE approach.

We modelled the α(001)B12 face within a 1 × 1 surface unit cell using asymmetric slab consisting of 10 layers (30 B atoms), and relaxing, in the total energy calculations, the eight top-most layers and the adsorbates. Dipole correction was taken into account to compensate the slab symmetry. A vacuum region of 20 Å in length separated adjacent slabs along the *z*-direction. The energies and total forces converged to within 7×10^{-8} Ha and 1×10^{-5} Ha/Å tolerances, respectively. The integration of the surface Brillouin zone involved a 4 × 4 × 1 κ-point sampling according to the Monkhorst-Pack scheme.[44] We set the real space cutoff at 4.4 Å. Test computations employing a 6 × 6 × 1 κ-point sampling, a 4.8 Å space cut-off, and slabs consisting of 12 and 14 layers, performed in view of total energy for one structure, verified the reliability of the results. A 6 × 6 × 1 κ-point sampling has also been tested in view of charge distributions where the latter has changed only by ~ 0.001*e*. Test calculations using 30 Å in

length separated adjacent slabs in the z-direction changed the total energy by ~1 $*10^{-6}$ Ha. As demonstrated in Section 3, we have also tested the convergence of surface relaxations and constructions with respect to the number of layers and the size of the unit cells. All energy values reported in the discussion were estimated at 0 K.

Cohesive energy E^{coh} of bulk boron follows from a simple expression:

$$E^{coh} = E_B^{gas} - E_B^{bulk} \qquad 4.2$$

where E_B^{bulk} and E_B^{gas} denote energies of a bulk boron atom and a gas phase boron atom, respectively.

We estimate average adsorption energy for on-surface (E_b) from the following formulae:

$$E_b = \frac{1}{n}\left[E_{O/Slab} - \left(E_{slab} + \frac{n}{2}E_{O_2}\right)\right] \qquad 4.3$$

where *n* represents a number of adsorbed, $E_{O/slab}$ stands for the energy of O/α(001)B12 system, E_{slab} is the energy of the clean α(001)B12 slab, and E_{O_2} signifies the energy of an isolated oxygen molecule. The deformation energy associated with structural modification of the substrate is attained by subtracting the energy of the O/α(001)B12 system, $E_{O/slab}$, frozen but with the adsorbate removed, from the energy of the clean α(001)B12 slab, E_{slab}. Taking into

consideration the energies and the numbers of substituted bulk B atoms, we estimate average adsorption energy for substitutional (E_b^{subst}) adsorption:

$$E_b^{subst} = \frac{1}{n}[E_{O/slab} + nE_B^{bulk} - \left(E_{slab} + \frac{n}{2}E_{O_2}\right)] \quad 4.4$$

Applying the approach of the ab initio atomistic thermodynamics, we calculate the stability *T*-*P* diagram that incorporates all on-surface and substitutional phases in the O/*α*(001)B12 system. References 45 and 46 discuss the details of the methodology, as implemented in the present contribution. Briefly, in this approach, the surface Gibbs free energy at a given temperature and pressure, $\gamma_{ads}(T,P)$, varies with the chemical potential of the adsorbed oxygen according to:

$$\gamma_{ads}(T,P) = \frac{1}{A}[N_O E_b - \Delta N_B E_B^{bulk} - N_O \mu_O] \quad 4.5$$

where N_O denotes the number of oxygen atoms, ΔN_B is the difference in the number of B atoms between the O/*α*(001)B12 system (only pertinent to substitutional configurations) and the clean *α*(001)B12 surface, and μ_0 signifies the chemical potential of oxygen. For the ideal gas, the chemical potential of oxygen in Eq. (4.4), μ_0, is a function of *T* and *P*

$$\mu_o(T,P) = \mu_o(T,P^o) + \frac{1}{2}kT\ln\left(\frac{P}{P^o}\right) \quad 4.6$$

where the standard thermodynamic tables[47] provide values $\mu_O(T,P^O)$, as calculated from the variation of entropy and enthalpy of pure oxygen with temperature at standard pressure, P^o

(i.e., 1 bar). The total energy of oxygen in an isolated molecule ($\frac{1}{2}E_{O_2}^{tot}$) has been elected as the zero reference energy for the oxygen chemical potential μ_O. The term $\mu_{\mathrm{O}}\left(T, P^{\mathrm{o}}\right)$ is then given by:

$$\mu_{\mathrm{O}}\left(T, P^{\mathrm{o}}\right) = \frac{1}{2}[H(T, P^0, O_2) - H(0\mathrm{K}, P^0, O_2)] - \frac{T}{2}[S(T, P^0, O_2) - S(0\mathrm{K}, P^0, O_2)] \qquad 4.7$$

4.3 Results and Discussion

4.3.1 Bulk Boron

Among possible phases of bulk boron, *α*-boron(B12) possesses the simplest crystalline structure. Figure 4.1 presents the optimised unit cell. In this geometry, boron atoms occupy two non-equivalent sites: polar (Bp), on the triangular face of the icosahedron, and equatorial (Be) at the middle of the icosahedron.[48-49] Table 4.1 presents the calculated lattice parameters (*a* and *c*), band gaps and cohesive energies, along with experimental and theoretical values from literature.[21-22, 30, 38, 50-55] Our calculated lattice parameters deviate only marginally (i.e., 0.25 %) from the corresponding experimental values.[51]

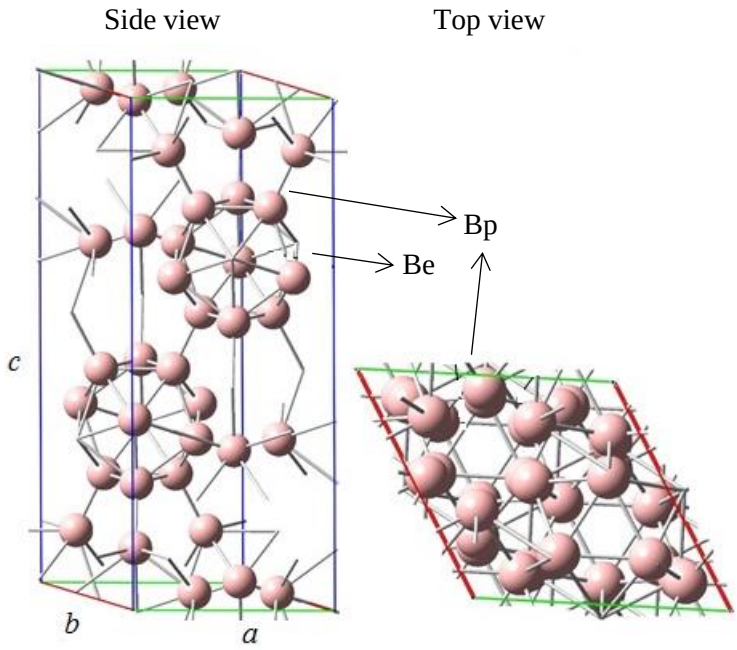

Figure 4.1. Top and side views of the unit cell of bulk *α*-boron(B12).

Table 4.1. Selected properties of bulk *α*-boron (B12).

Calculated parameters	***a*/Å**	***b*/Å**	***c*/Å**	E^{g}**/eV**	E^{coh}**/eV**
This work	a = 4.895	b = 4.895	c =12.554	Direct = 1.91 Indirect = 1.63	6.23
Other theoretical predictions	a = 4.93	b = 4.93	c = 12.56[22]	Direct = 1.80 - 2.6[30, 49-51]	6.68[30]
	a = 4.92	b = 4.92	c = 12.60[52]	Indirect = 1.40-2.00[30, 49-51]	6.76[21]
Experiment	a = 4.908	b = 4.908	c = 12.567[48]	Direct = 2.00	

Figures 4.2 and 4.3 illustrate, respectively, the electronic band structure and the electronic density of states of bulk α-boron(B12). The system is semiconducting with calculated direct and indirect band gap energies of 1.91 eV and 1.63 eV, respectively. These values coincide with the findings of the recent theoretical work of Setten et al.[30], who reported the direct and indirect band energies as 1.94 eV and 1.54 eV, correspondingly. Figure 4.2 also indicates the highest peak of the valence band appearing at the *Z* symmetry index, while the *F* symmetry point marks the location of the lowest position of the conduction band. The analysis of Figure 4.3 shows that, the contribution from p states dominates the total DOS above -5 eV, and that of s states below -10 eV. The calculated DOS agrees with the corresponding data of Wang et al.[22]

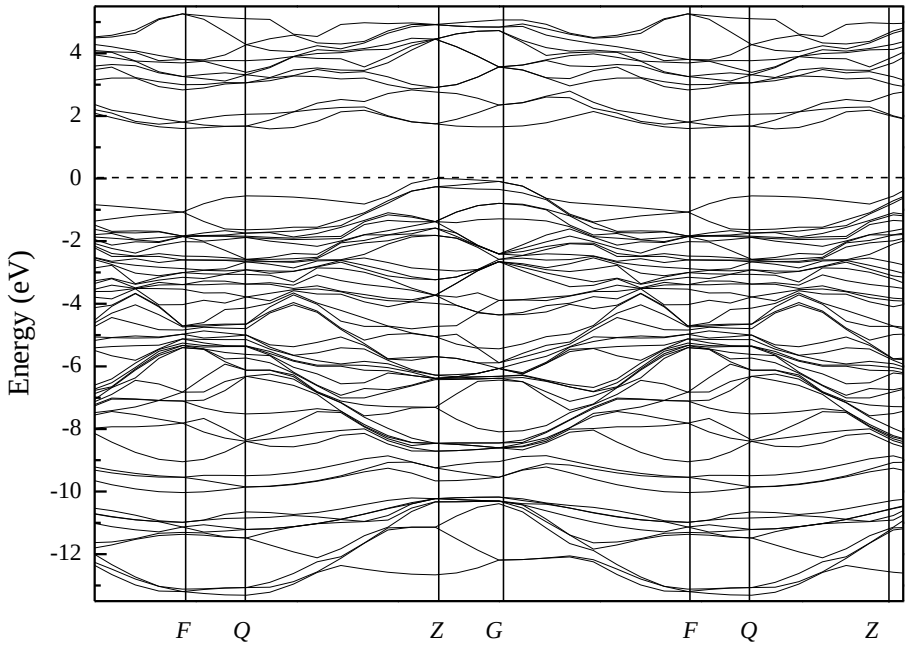

Figure 4.2. The electronic band structure of bulk α-boron(B12).

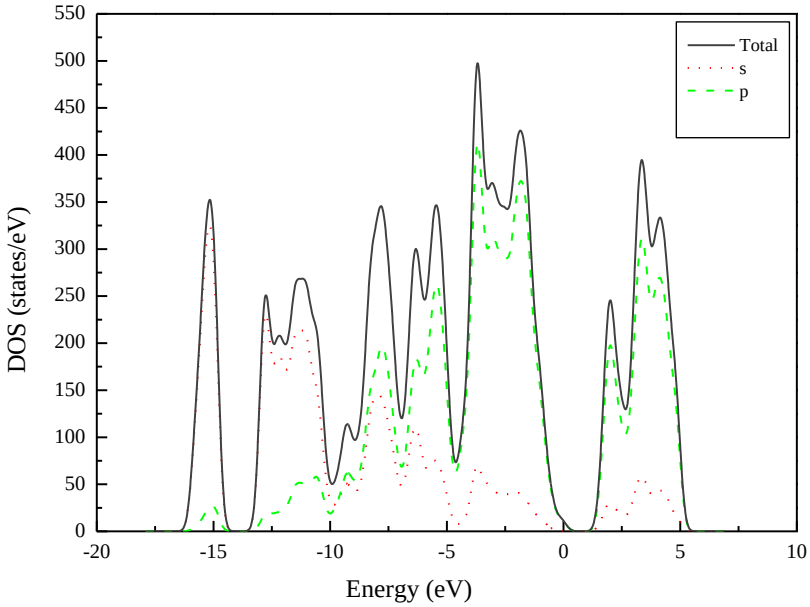

Figure 4.3. Total density of states of bulk α-boron(B12).

4.3.2 Clean α(001)B12 Surface

The optimised geometry of the clean α(001)B12 surface, as presented in Figure 4.4, involves relaxation of only the two topmost atomic layers in the absence of any surface reconstruction. Our test calculations performed for slabs consisting of 10, 12 and 14 atomic layers display lack of sensitivity of the distances between the two topmost layers in the slabs (Δd_{12}) and between the second and third layers (Δd_{23}) with respect to bulk positions. For example, calculated values of Δd_{12} and Δd_{23} for slabs containing of 10, 12 and 14 atomic layers amount to 0.41 Å, 0.41 Å 0.41 Å and 0.01 Å, 0.01 Å and 0.01 Å, respectively. Therefore, we deploy a slab consisting of 10 layers with 1 × 1 surface unit cell in all calculations.

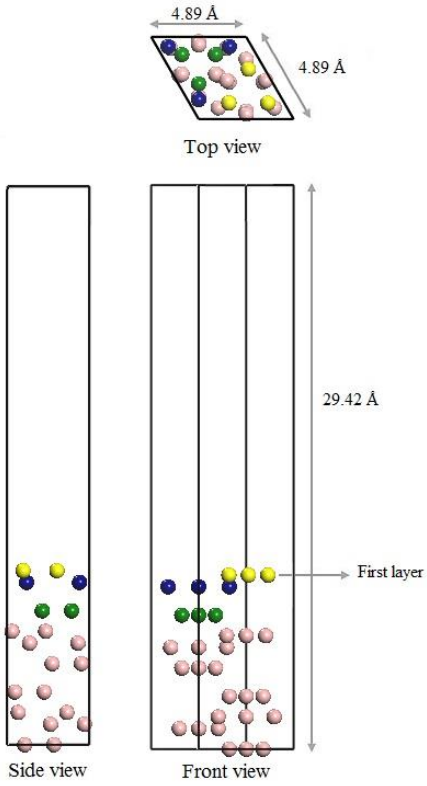

Figure 4.4. Vacuum slab of the *α*(001)B12 surface.

Figures 4.5a and 4.6 present the density of state, DOS, projected onto the atomic orbitals of both the surface and subsurface atoms, as well as the electronic structure calculated for the clean *α*(001)B12 surface, respectively. We observe that, in contrast to the semiconducting nature of bulk *α*-boron (B12), the clean *α*(001)B12 surface exhibits a metallic character. While it is beyond the scope of this work to analyse the surface electronic structure in detail, it bears to mind that, the metallic character of the *α*(001)B12 surface originates from the surface electronic states that may trap electrons or holes at the surface. Our DOS analyses coincide with the corresponding data of Amsler et al.[55] for the *α*(111)B12 surface. This character of the surface states corroborates the reactivity of boron surfaces toward adsorption of various gas species (e.g., CO_2[31], N_2[32]).

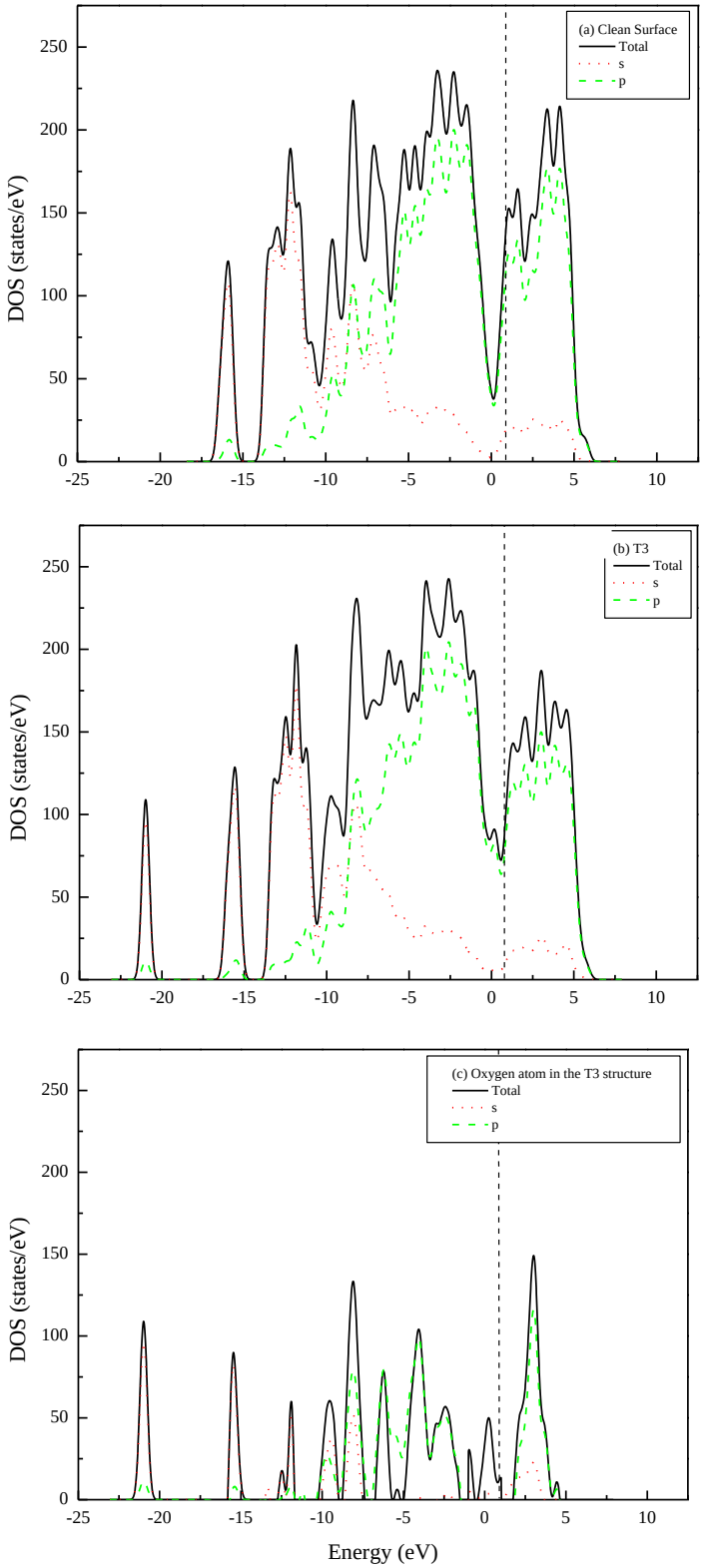

Figure 4.5. DOS for (a) the *α*(001)B12 surface, (b) the T3 adsorption configuration (see Fig. 6) and (c) the difference between them. We only display positive values in c.

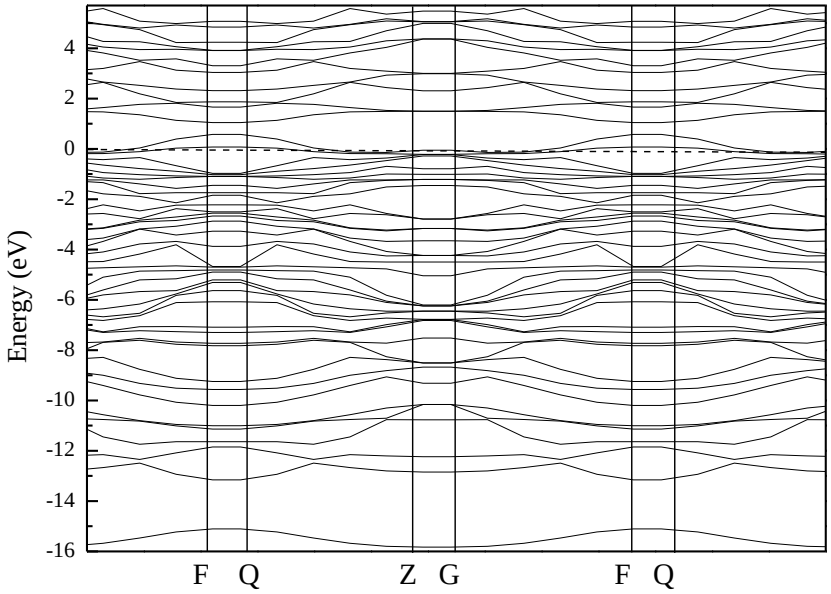

Figure 4.6. Electronic structure of the clean α(001)B12 surface.

4.3.3 Geometric and Energetic Properties for On-Surface and Substitutional Adsorption

4.3.3.1 Adsorption of Atomic Oxygen on the α(001)B12 Surface

The 1 × 1 surface unit cell of α(001)B12 provides eight distinct adsorption sites, shown in Figure 4.7. The sites include three top sites (T1, T2 and T3), three bridge sites (B1, B2 and B3) and two hollow sites (H1 and H2). Initially, we placed the oxygen atoms at all eight adsorption sites, but found that only T3, B1, H1 and H2 converged into distinct stable adsorption geometries. B1 does not exist in the optimum bridge positions, but for clarity, we describe this structure as a bridge configuration. Figure 4.8 displays all stable geometries, and Table 4.2 lists binding energies, the distance between an oxygen atom and the nearest boron atom and the vertical distances between adsorbed oxygen atoms and the first substrate layer. The calculated energetics indicate strong interaction of atomic oxygen with the α(001)B12

surface, with the following stability order of top (T3) > bridge (B1) > hollow (H1 and H2). This indicates that, three-fold coordinated structures (H1 and H2) do not provide favourable adsorption sites when compared with the one and two-fold organised T3 and B1 assemblies, respectively (refer to top views of structures in Figure 4.8 The predicted trend concurs with that obtained for the adsorption of H on α(001)B12.[33] Interestingly, by inspecting the configurations in Figure 4.8, the oxygen atoms in structure B1 share the same two-fold coordination number with oxygen atoms in bulk B_2O_3, albeit with somewhat distinct angles of 75.6˚and 59.7˚, respectively.

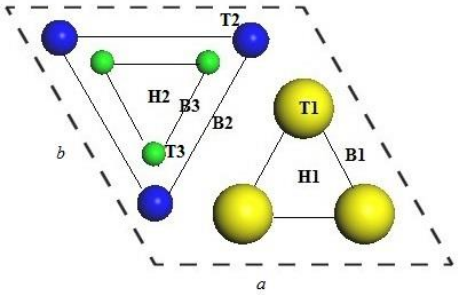

Figure 4.7. Top view of the adsorption sites on the α(001)B12 surface. Yellow spheres represent the B atoms on the surface layer, the blue and green spheres show the B atoms in the second and third layers, respectively.

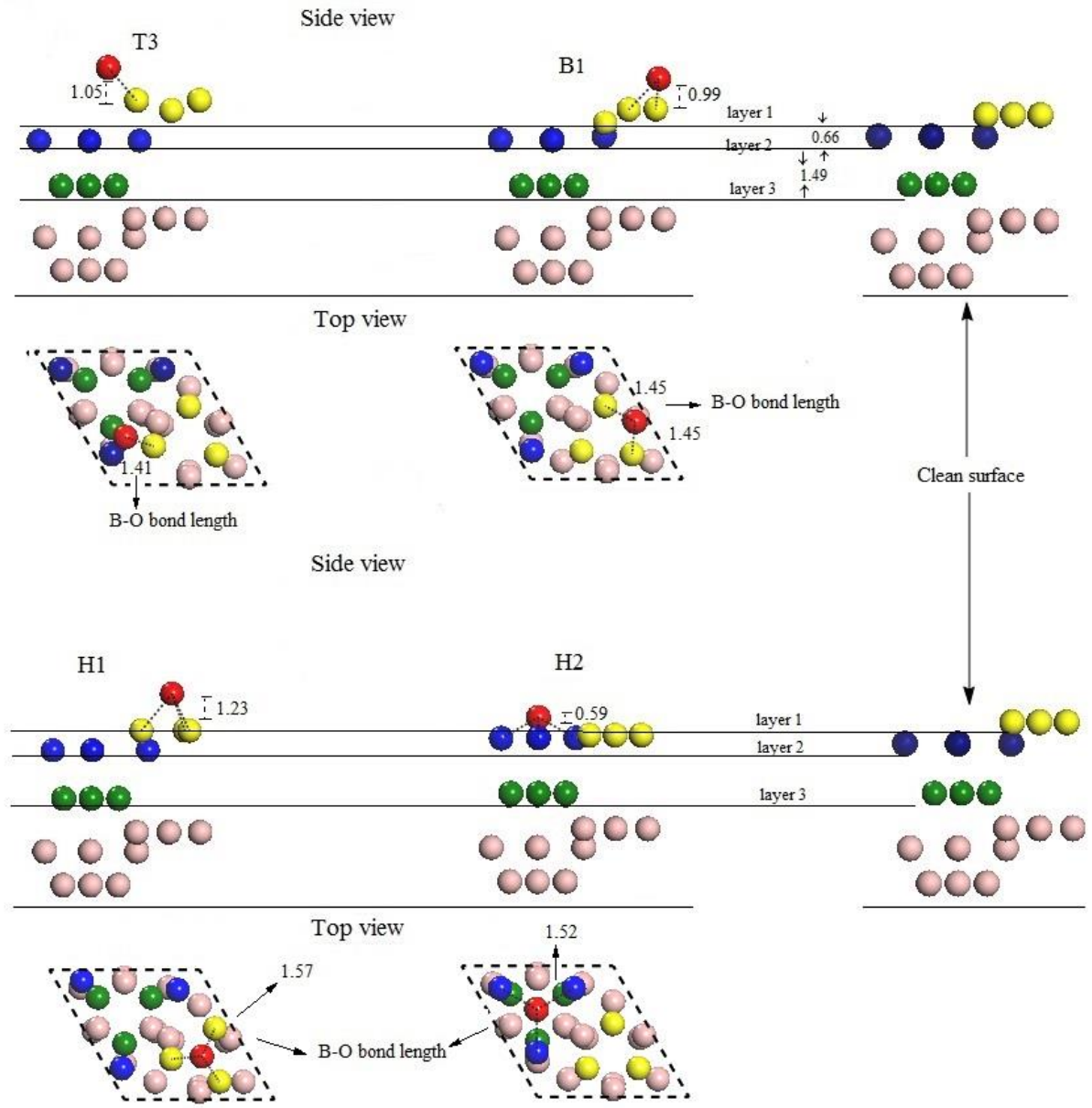

Figure 4.8. Top and side views of the stable geometries induced by atomic oxygen adsorbed on the *α*(001)B12 surface. Oxygen atoms are red-coloured. Yellow, blue and green spheres denote boron atoms in the first, second and third layers, respectively. The oxygen atom in the B1 configuration does not lie in the optimum bridge position, but for clarity we describe this structure as the bridge. (Bond length and distances are in Å).

Table 4.2. Binding energies (E_b) for adsorption of atomic oxygen, vertical distance between adsorbed oxygen atoms and first layer of the surface (O-B) and the distance (bond length) between oxygen atoms and the nearest boron atom.

Site name	E_b/eV	(O-B)/Å	D(B-O)/Å
T3	-3.38	1.05	1.41
B1	-2.99	0.99	1.45
H1	-2.45	1.23	1.57
H2	-1.63	0.59	1.52

For the calculated structural effects induced by the adsorption of atomic oxygen within the 1 × 1 and 2 × 2 surface unit cells, we observe that, changes in the B-B distances (i.e. reconstruction) are very small, in the order of 0.04 – 0.11 Å. By contrast, the interlayer spacing pertinent to the T3 site differs by 0.59 Å from the corresponding distance in the clean α(001)B12 surface. Clean surface displays a downward relaxation of -0.41 Å in the topmost layer, compared to the bulk interlayer distance, while T3 exhibits a corresponding outward relaxation of 0.17 Å. Changes in interlayer spacing between the second and third layers in the T3 configuration are minimal with respect to the clean α(001)B12 surface (e.g., -0.03 Å). This amplified surface deformation has resulted in a significant destabilization of the surface, where the calculated deformation energy of T3 amounts to 0.68 eV.

By inspecting the structures in Figure 4.8, one observes considerable sensitivity of the structural adjustment to the adsorption site. For example, the outward relaxation of the first two layers of B1 is less than that in T3. H1 and H2 experience the downward relaxation of the first layer. H2 also displays the outward relaxation of the second layer, resulting in the first

two layers merging to form one layer. We conclude therefore that, the highly reactive nature of boron atoms towards the oxygen atom exerts the most dominating structural effect. The significant relaxations in all O/α(001)B12 structures (Table 4.2) corresponds to their noticeable binding energies.

In order to assess the effects of the adsorbed oxygen atom on the electronic structure of the clean α(001)B12 surface, Figure 4.5b displays the DOS calculated for the T3 configuration and Figure 4.5c depicts the difference between the DOS obtained for the clean α(001)B12 and that with the adsorbed oxygen in the T3 structure. We observe that, the new bands that originate from the interaction between electronic states of oxygen and valence states of boron enhance the electron density at the Fermi level. We also notice the emergence of a new band located at -22 eV, belonging to the s orbitals of the oxygen atoms. Our observations concur with those reported by Hu et al.[56] in their study of oxygen adsorption on boron-substituted graphite surfaces (BC5).

4.3.3.2 Molecular Oxygen Adsorption on the α(001)B12 Surface

In this section, we investigate the physisorbed (non-dissociative) and chemisorbed (dissociative) adsorption of molecular oxygen on the α(001)B12 surface. In both cases, we consider the two oxygen atoms comprising the O_2 molecule to be positioned at one of the four plausible atomic adsorption sites, namely, T3, B1, H1 and H2.

In physisorbed (non-dissociative) interaction, oxygen molecule initially positions itself vertically in T3, B1, H1 and H2. We have found that, orientation of the oxygen molecule

converges either to horizontal or slightly tilted geometries, with the stability order similar to that found for the adsorption of atomic oxygen of top (T3) > bridge (B1) > hollow (H1 & H2). Figure 4.9 shows the stable geometries of the physisorbed systems (P1-P7). We observe that, the O-O bond lengths (in the P1-P7 structures) of 1.22 Å correspond closely to the values calculated for an isolated gas phase O_2 molecule (1.23 Å). Furthermore, the nearest O atom is separated from the surface by ~ 3.00 Å. Table 4.3 summarises the binding energies, the O-O lengths and the vertical distances between the oxygen atom in the O_2 molecule nearest to the α(001)B12 surface and the surface itself. The data indicate that, the O_2 molecule adsorbs very weakly on the α(001)B12 surface, in agreement with the reported low-energy physisorption of CH_4[32], CO_2[31] and N_2[32] on boron surfaces. Test conversion of 2 × 2 of the molecular oxygen adsorption has been performed; the precision of the binding energy converges to ~0.02 eV, confirming that the 1 × 1 surface cell is sufficient and that there is no interaction between oxygen molecule and its periodic image.

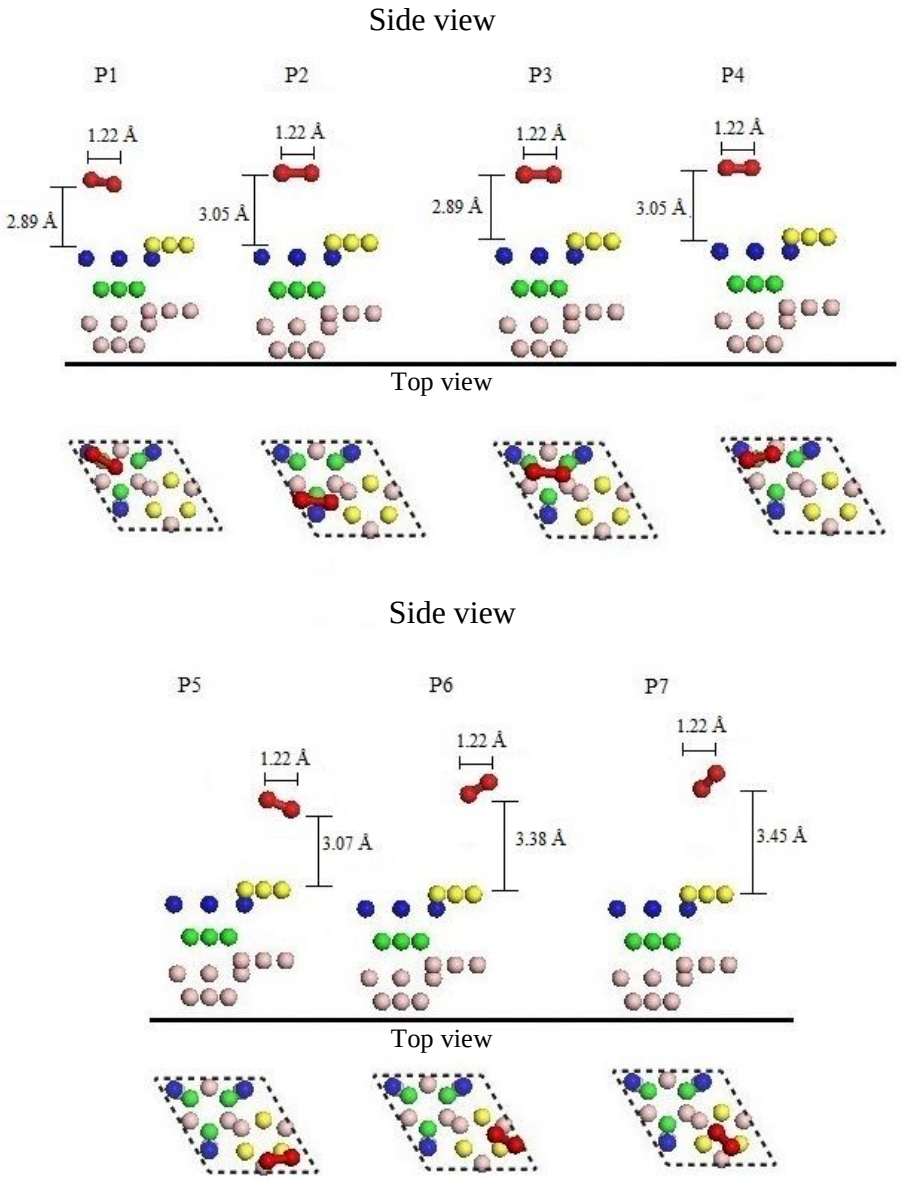

Figure 4.9. Top and side views of the stable geometries induced by molecular oxygen physisorbed on *α*(001)B12. Yellow, blue and green spheres denote boron atoms in the first, second and third layers, respectively. Oxygen atoms are red-coloured.

Table 4.3. Binding energies and geometric parameters for the molecular oxygen physisorbed on a clean α(001)B12 surface. (B in (O_2-B) represents boron atom at the surface directly below the oxygen molecule.)

Adsorption sites	E_b/eV	(O_2-B)/Å	D(O-O)/Å	Tilted angle (°)
P1	-0.03	2.89	1.22	-5.00
P2	-0.03	3.05	1.22	0.003
P3	-0.03	2.98	1.22	0.003
P4	-0.02	3.05	1.22	0.002
P5	-0.02	3.07	1.22	-28.00
P6	-0.02	3.38	1.22	+27.00
P7	-0.01	3.45	1.22	+30.00

On the contrary, the dissociative adsorption configurations (C1-C5), shown in Figure 4.10, display sizable binding energies (-2.47 to -3.45 eV) and shorter vertical spacing between the first layer of the substrate and the dissociated O_2 molecule (with O-O separation of ~ 2.50 Å). Table 4.4 enlists binding energies and geometrical features pertinent to the chemisorbed structures C1-C5. Initially, the two oxygen atoms were placed in the four adsorption sites (T3, B1, H1 & H2), in the following configurations: (T3-T3), (T3-B1), (T3-H1), (T3-H2), (B1-B1), (B1-H1), (B1-H2) and (H1-H2). We have found that, only the (T3-B1), (T3-H1) and (B1-B1) configurations afford stable molecular adsorption geometries with the stability order of C1, C2, C3 (T3-B1) > C4 (B1-B1) > C5 (T3-H1). The most stable structure, C1, attains a binding energy of -3.45 eV. Relative ordering in the calculated binding energies, accompanied by the dissociation of the molecules on boron surfaces, follows their corresponding bond dissociation enthalpies in the gas phase, i.e., CO_2 (5.53 eV), H_2 (4.51 eV), O_2 (3.04 eV) and Br_2 (1.99 eV).[57-58] Our calculated binding energy in the most stable structure C1 is in line with the

corresponding theoretical prediction for dissociations of CO_2[31] (-2.07 eV), H_2 (-3.01 eV) and Br_2[33] (-4.12 eV). Figure 4.11 elucidates the general physisorbed and chemisorbed adsorption behaviour of oxygen molecule on the α(001)B12 surface. Calculated deformation energy, in both C1 and P1 structures, amount to 3.24 eV and 0.0, respectively. Two concluding remarks can be drawn from this finding. First, as expected, the larger molecular deformation allows for stronger interactions with the surface that largely compensate for the greater strain. This has been confirmed theoretically in the literature.[59] The second important finding is that although the adsorption energy of both T3 and C1 configurations are essentially equal, the higher deformation energy at C1, 3.24 eV, must be compensated for by a superior electronic interaction of oxygen molecule with boron surface.[60]

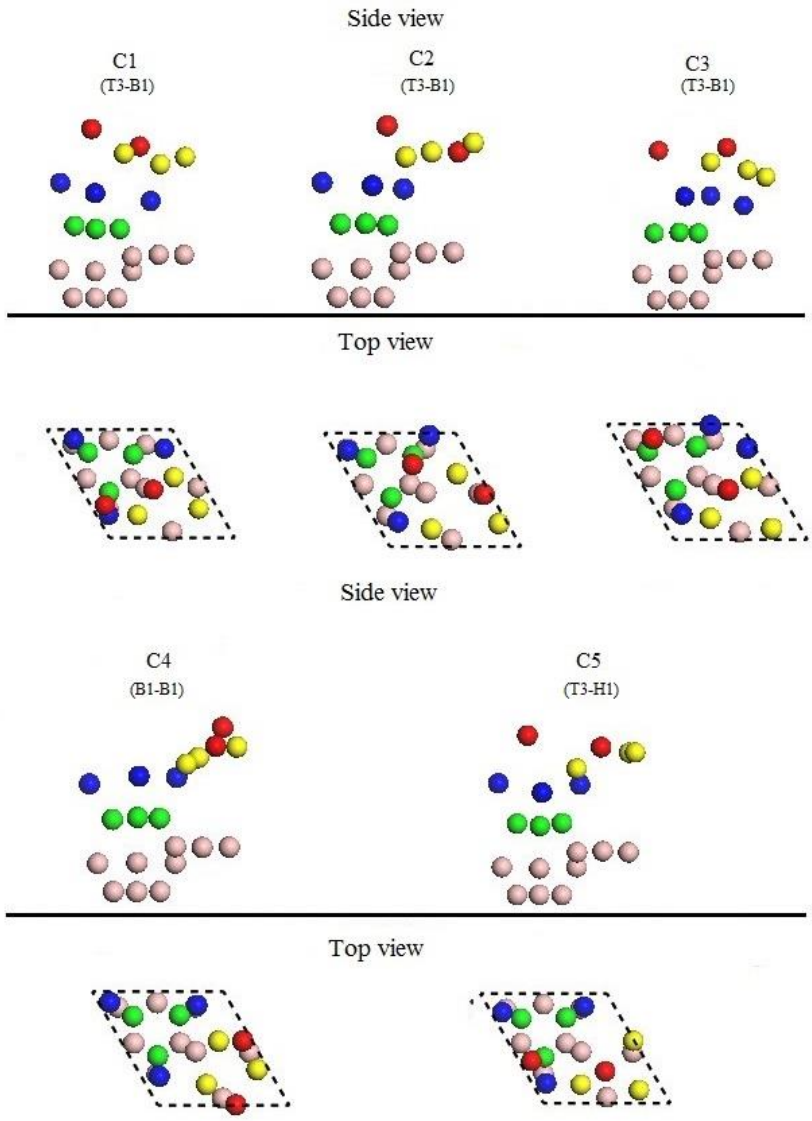

Figure 4.10. Top and side view of the chemisorption O/*α*(001)B12 configurations. Yellow, blue and green spheres denote boron atoms in the first, second and third layers, respectively. Oxygen atoms are red-coloured.

Table 4.4 Binding energies and geometrical parameters for the molecular oxygen chemisorption on the clean α(001)B12 surface.

Structure	E_b/eV	(O_2-B)/Å	D(O-O)/Å
C1	-3.45	0.34	2.38
C2	-3.30	0.0	2.48
C3	-3.04	0.34	2.50
C4	-2.87	0.48	3.36
C5	-2.47	0.23	2.91

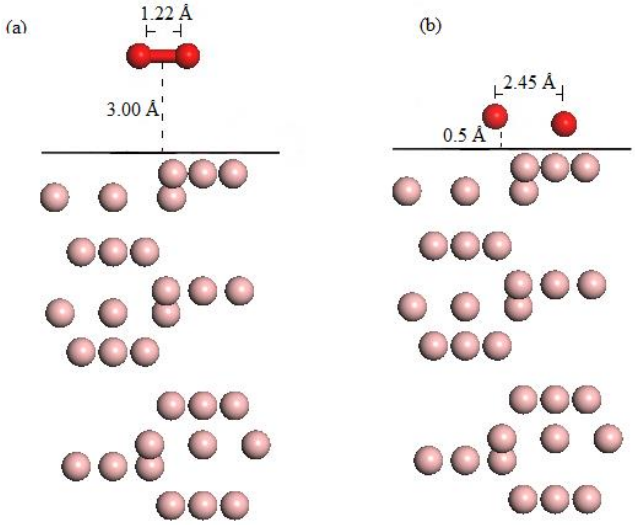

Figure 4.11. Details of the geometrical features induced by molecular oxygen physisorbed (a) and chemisorbed (b) on α(001)B12. Oxygen atoms are red-coloured.

Dissociation of oxygen molecule on the titled surface does not occur spontaneously, despite of the considerable exothermicity of the chemisorbed states. Figure 4.12 depicts the potential

energy diagram for the decomposition of an oxygen molecule on the (001)B12 surface following the pathway from the physisorbed P1 structure to the chemisorbed C1 configuration. The calculated overall reaction barrier amounts to 3.4 eV. This exceedingly high value clearly explains the resistance of crystalline boron to oxidation at room temperature. Elevated temperature makes this barrier possible to overcome. Moreover, gas-phase and catalytic reactions induce fission of the O-O bonds releasing atomic oxygen.

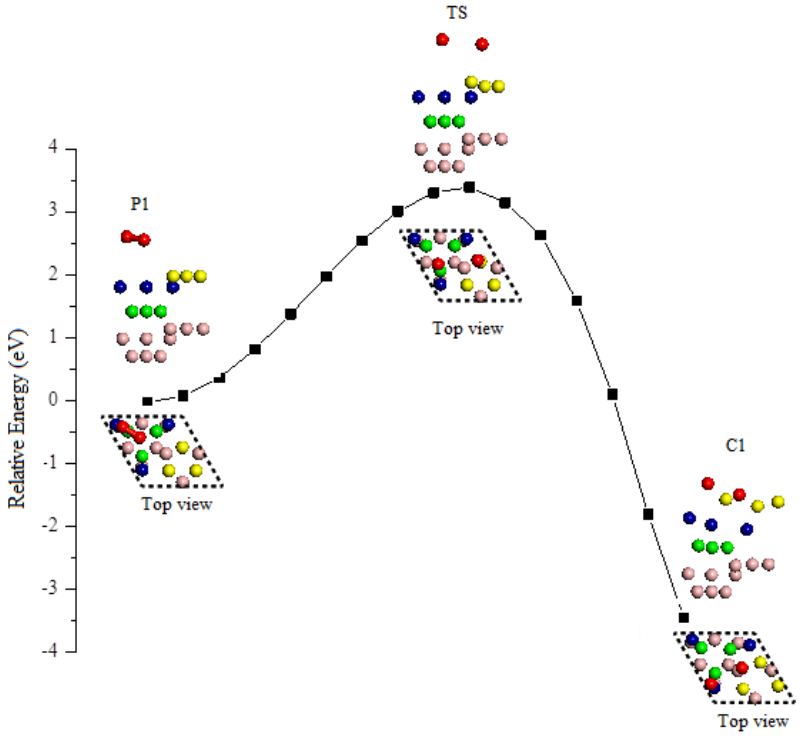

Figure 4.12. Potential energy diagram for the interaction of O_2 molecule with the α(001)B12 surface.

4.3.3.3 Substitutional Adsorption

Substitutional adsorption represents a first step toward assessing the thermodynamic feasibility of forming the B_2O_3 bulk-like structures from the interaction of a gas phase oxygen with a clean α(001)B12 surface. We explore seven different substitutional configurations at coverage of 1/3 ML, 2/3 ML, 1 ML and 2 ML. Figure 4.13 illustrates all stable configurations and Table 4.5 lists the calculated binding energies for each of them.

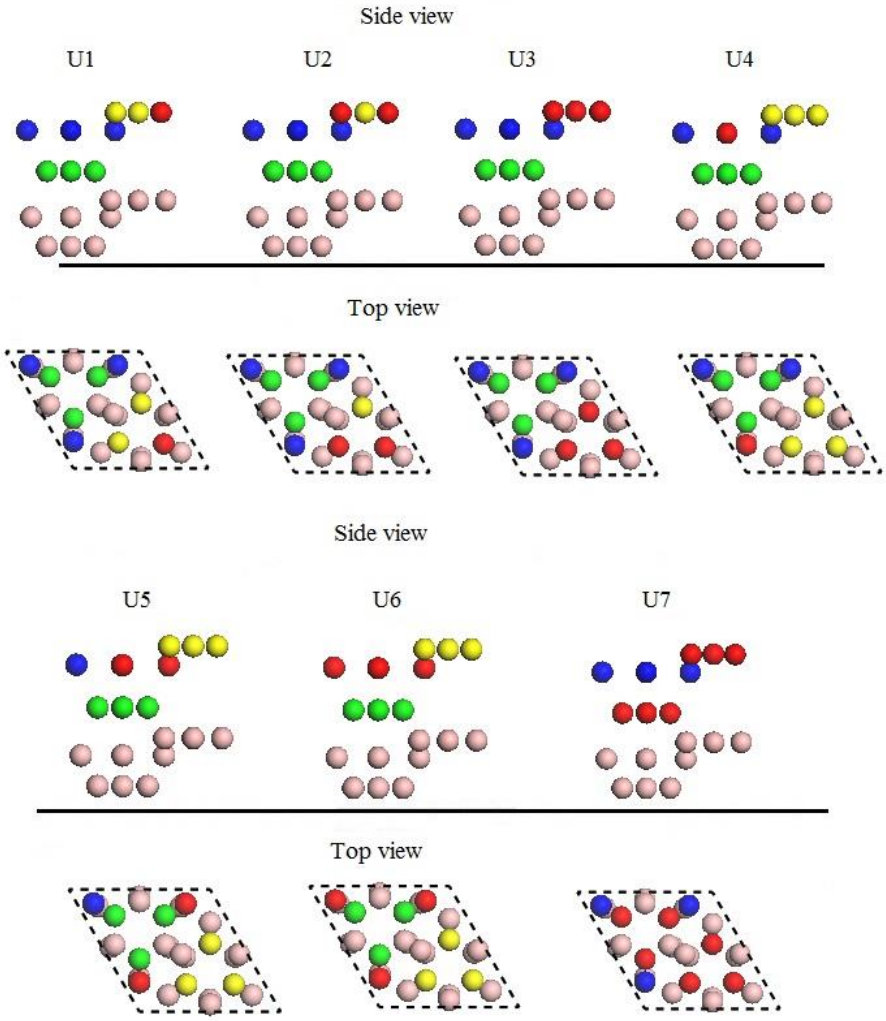

Figure 4.13. Top and side views of the structures induced by substitutional adsorption of O on α(001)B12. Red spheres denote oxygen, yellow spheres signify the first layer B atoms, blue and green spheres represent second and third layer B atoms. Light pink spheres are B atoms located deeper in the slabs.

Table 4.5. Coverage (Φ) and chemisorption energies for substituted O/α(001)B12 configurations.

Sub Site	Description	Φ	E_b^{subst} /eV
U1	One first layer B atom is substituted with an oxygen atom	1/3	-1.65
U2	Two first layer B atoms are substituted with oxygen atoms	2/3	-3.93
U3	Three first layer B atom are substituted with oxygen atoms	1	-3.29
U4	One second layer B atom is substituted with an oxygen atom	1/3	-1.63
U5	Two second layer B atom are substituted with oxygen atoms	2/3	-2.75
U6	Three second layer B atom are substituted with oxygen atoms	1	-2.80
U7	All first and third layer boron atoms are substituted with oxygen atoms	2	-3.28

In configurations U1 and U4, an oxygen atom substitutes one boron atom from the first and second layer, respectively. In the U2 and U5 assemblies, two boron atoms in the first or second layer, correspondingly, are replaced with oxygen atoms. We construct the U3 and U6 structures by swapping all boron atoms in first and second layers with oxygen atoms, while in the U7 configuration, all boron atoms in the first and third layer are exchanged with the oxygen atoms. It should be noted that, the first three layers of U7 structure resemble the low index surface of B_2O_3 (110). Figure 4.14 illustrates side views of substitutional structure U7 and the low-index (110) surface of B_2O_3. The similarity between the U7 structure and a B_2O_3-

constructed configuration manifests itself by bond lengths O-O/B-O and distances between the layers in the two structures. For example, the O-O and B-O bond lengths in the U7 structure deviate only marginally from the corresponding bonds in bulk B_2O_3; i.e., within 0.03-0.1 Å and 0.01-0.1 Å, respectively. Furthermore, as Figure 4.14 depicts, the substituted oxygen atoms in U7, together with boron surface atoms in the second layer, compose a triangular BO_3 building block.

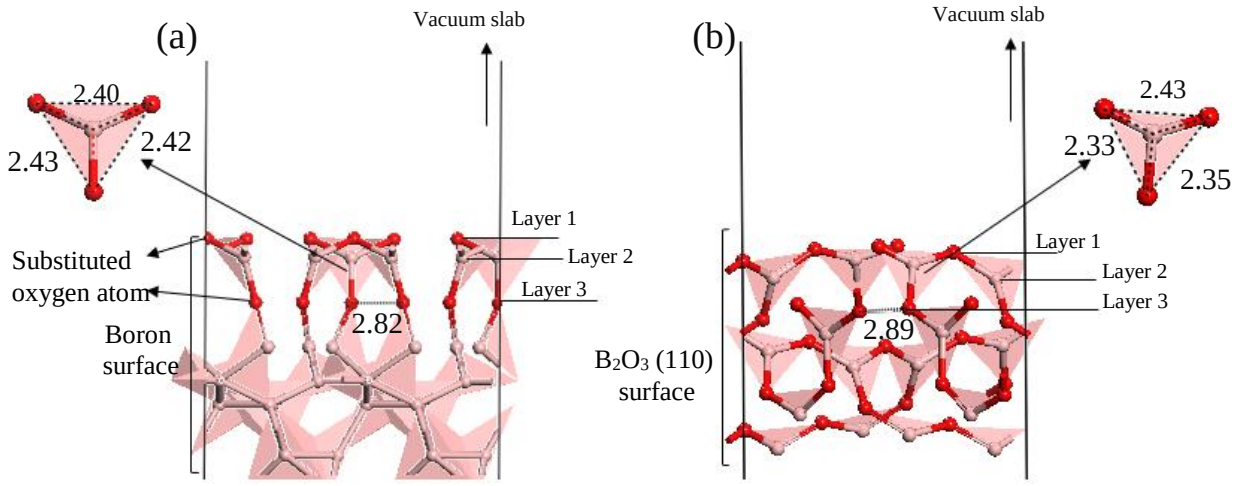

Figure 4.14. (a) Side view of the first three layers of substitutional structure U7. (b) Side view of the low index (110) surface of B_2O_3. Red spheres denote oxygen atoms and light pink spheres are boron atoms. (The substitutional structure U7 is presented in the Figure by supercell range of 2 × 2).

Our data indicate that, considerable exoergicity (-3.29 eV, refer to Table 4.5) accompanies the formation of U7 via substitutional adsorption of O_2. This signifies that, thermodynamics permit the formation of bulk-like B_2O_3 structures through the sub-surface adsorption.

4.3.3.4 Phase Diagram

In this section, we discuss a stability phase diagram for oxygen interaction with the α(001)B12 surface by relating surface energies $\gamma_{ads}(T,P)$ with the change in the chemical potential of oxygen, $\mu_o(T,P)$. Under experimentally accessible conditions, $\mu_o(T,P)$ could only vary between two boundaries corresponding to lean and rich limits.[61] The lean-limit signifies the $\mu_o(T,P)$ at which the bulk B_2O_3 phase commences to form via adsorption of an oxygen molecule on a clean surface, whereas an oxygen rich limit denotes the condensation of a gaseous O_2. Approximate values of oxygen-lean and oxygen-rich limits are those of a third of the $\Delta_f H^o_0$ for bulk B_2O_3 and condensed O_2, i.e., -13.18 eV (divided by three) and 0.00 eV, respectively.[62] Table 4.6 assembles calculated $\gamma_{ads}(T,P)$ at oxygen-lean and oxygen-rich limits. Between the two boundaries of $\mu_o(T,P)$, a thermodynamic equilibrium establishes itself and governs the relative stability of O/α(001)B12 structures.

Table 4.6. Values of $\gamma_{ads}(T,P)$ in eV Å^{-2} for all configurations at O-lean and O-rich limits

	Rich-limit	**Lean-limit**
T3	-0.17	0.16
B1	-0.14	0.16
H1	-0.12	0.17
H2	-0.08	0.19
C1	-0.33	0.31
C2	-0.32	0.32
C3	-0.29	0.33

C4	-0.28	0.33
C5	-0.29	0.34
U1	-0.08	0.19
U2	-0.19	0.15
U3	-0.48	1.49
U4	-0.08	0.19
U5	-0.26	1.35
U6	-0.40	1.52
U7	-0.95	0.98

Figure 4.15 displays lines of $\gamma_{ads}(T,P)$ for the atomic, molecular, and substitution adsorption on the clean α(001)B12 surface. Up to the value of -4.0 eV of $\mu_o(T,P)$, at pressure and temperature corresponding to less than 10^9 Pa and 800 K, respectively, the clean surface represents the most stable configuration. This reveals that, the adsorption of oxygen on clean α(001)B12 is not feasible from a thermodynamic perspective when the $\mu_o(T,P)$ falls below -4.0 eV. For the chemical potential of oxygen in the range of -4.0 < $\mu_o(T,P)$< -3.0, several structures hold very comparable stability. These configurations comprise the on-surface atomic (T3, B1, H1 and H2) and molecular (C1, C2, C5) structures, as well as one substitutional adsorption geometry (U4). Bearing in mind that, the very narrow stability differences between these structures overlap within the accuracy margin of the adopted methodology, i.e. 10.0 – 20.0 eV Å^{-2},[63] we conclude that, these structures coexist at $\mu_o(T,P)$ ranging from -3.40 eV and -3.00 eV. Beyond $\mu_o(T,P)$ of -3.0 eV , the profound stability of the B_2O_3-bulk like structure U7 dominates the phase diagram. The predominant stability of this configuration supports experimental XPS observations of the formation of B_2O_3 from adsorption of oxygen on bulk boron.[34-35] However, note that, kinetic factors may play a significant role in determining the

most plausible O/α(001)B12 configurations. For instance, these factors may prevent the formation of a structure even if it is energetically favourable. Some of the issues emerging from this finding relate specifically to the unqualified stability of U7 at higher values of $\mu_o(T,P)$. All substitutional structures other than U7 are thus only accessible kinetically.

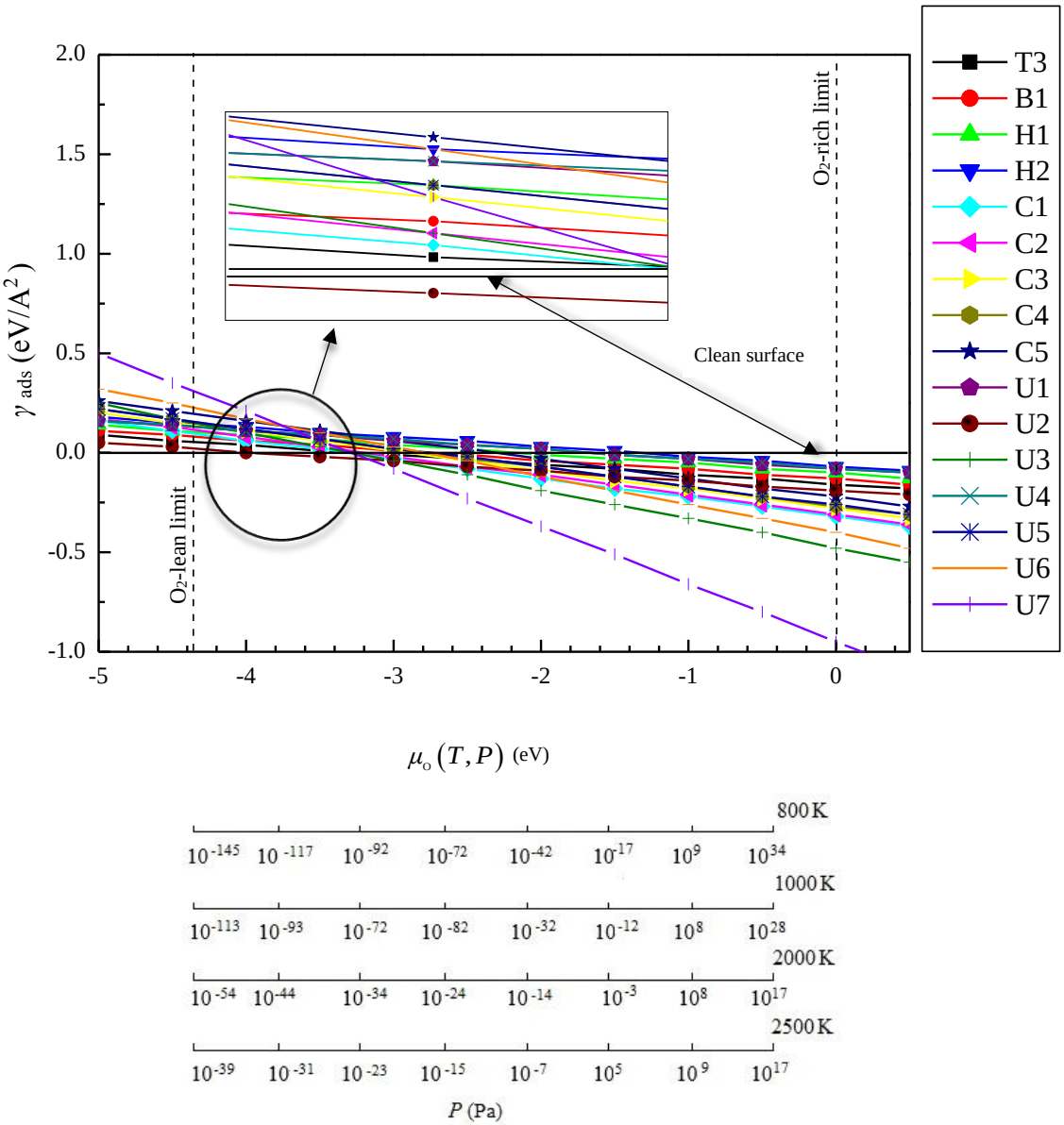

Figure 4.15. The stability phase diagram for the adsorption of atomic oxygen, including the substitutional configurations, as a function of oxygen chemical potential, and *T* and *P*.

4.3.4 Charge Analysis

Mulliken charge analysis[64] describes the electronic properties of a system, and the analysis often serves as a helpful tool in rationalising the interaction strength and the thermodynamic stability ordering of solid state. Table 4.7 summarises atomic Mulliken charges for clean *α*(001)B12, an isolated gas phase oxygen molecule, the most stable chemisorbed structures (C1) and the physisorbed (P1) configuration of the O_2/*α*(001)B12 system. The neutral charge density distributed over the *α*(001)B12 surface is in accord with the experimental finding of Fujimori et al.[38] By inspecting the data in Table 4.7, we note a net charge transfer occurring across the slab of the clean *α*(001)B12 surface, from atoms in the middle of the slab (positive charge of 0.03 *e*) towards atoms in the first layer (negative charge of 0.07 *e*). The observed difference in the charge accumulated between the top and the middle of the clean *α*(001)B12 surface confirms the previously observed amphoteric nature of boron surfaces.[31, 65] This in turn indicates that, boron surfaces have potential to comprise both acidic and basic sites alike.

Table 4.7. Mulliken atomic charges (***e***) on oxygen and boron atoms for the clean *α*(001)B12 surface, an isolated oxygen molecule in gas phase, and in P1 and C1 structures. Charge transfer (CT) values are calculated as the difference in atomic charges between the clean *α*(0001)B12 surface and the corresponding atoms in the P1 and C1 configurations. B1-B3, B4-B6, B7-B9, B10-B12, B13-B15 B16-B18 denote boron atoms in the first – sixth layers, respectively. Sum of the charges are based on all 30 B atoms (although only 14 of them are shown below), confirming that, charge transfer from the surface = charge transfer to oxygen atoms.

Atom label	**Charge for clean surface and isolated O_2**	**P1**	**CT**	**C1**	**CT**
O1	0.00	-0.02	-0.02	-0.52	-0.52
O2	0.00	-0.02	-0.02	-0.50	-0.50
Sum of charge	0.00	-0.04	-0.04	-1.02	-1.02
B1	-0.07	0.07	0.14	0.45	0.52
B2	-0.07	0.06	0.13	0.32	0.39
B3	-0.07	0.07	0.14	0.36	0.43
B4	-0.07	-0.16	-0.09	-0.31	-0.24
B5	-0.14	-0.16	-0.02	-0.04	0.10
B6	-0.15	-0.16	-0.01	0.03	0.17
B7	0.05	0.05	0.00	-0.01	-0.05
B8	0.05	0.05	0.00	0.01	-0.05
B9	0.05	0.05	0.00	0.05	0.00
B10	0.03	0.05	0.02	-0.02	-0.05
B11	0.03	0.05	0.02	0.02	-0.01
B12	0.03	0.03	0.00	0.05	0.02
B13	0.03	0.04	0.01	-0.01	-0.04
B14	0.04	0.06	0.02	0.03	-0.01
B15	0.04	0.06	0.02	0.02	-0.02
B16	0.02	0.03	0.01	0.03	0.01
B17	0.03	0.03	0.00	0.03	0.00

B18	0.02	0.04	0.01	0.04	0.02
B19	0.08	0.01	-0.08	0.09	0.01
B20	0.08	0.01	-0.07	0.09	0.01
B21	0.08	0.01	-0.08	0.08	0.00
B22	0.07	-0.08	-0.14	0.07	0.00
B23	0.06	-0.08	-0.13	0.07	0.01
B24	0.07	-0.08	-0.14	0.05	-0.02
B25	0.05	0.00	-0.05	0.05	0.00
B26	0.05	0.00	-0.05	0.05	0.00
B27	0.04	0.00	-0.04	0.04	0.00
B28	0.00	0.00	0.00	-0.20	-0.20
B29	-0.21	0.00	0.21	-0.21	0.00
B30	-0.21	0.00	0.21	-0.21	0.00
Sum of the charges	0.00	0.04	0.04	1.02	1.02

The very marginal value of the total charge transfer observed in the physisorbed structure P1 (0.04 *e*) substantiates its very low binding energy (i.e. 0.03 eV). In the same manner, a considerable total charge transfer of 1.02 *e* serves as an indicator of the strong interaction in the case of chemisorbed configuration C1 (i.e., 3.33 eV). Further analysis indicates that, the adsorbed oxygen atom in the C1 structure holds a partial charge of -0.50 *e*, while their adjacent boron atoms are associated with partial positive charges of 0.45 *e*, confirming the ionic nature of the formed B-O bonds. The ionicity of the B-O bonds in the C1 configuration concurs with the nature of bulk B_2O_3, in which O and B atoms bear net electronic charges of – 2.0 *e* and 3.0 *e*, respectively. Our finding correlates well with a recent charge analysis by Sun et al.[31] of CO_2 interaction with a boron surface.

Similarly, the most stable (T3) and the least stable (H2) O/*α*(001)B12 structures (not shown in Table 7) are associated with total charge transfer values of 0.46 *e* and 0.35 *e*, respectively. (Note that, the calculations of the total charge transfer involve 30 atoms, with only 14 of them

shown in Table 7.) Although the difference in charge transfer between the two configurations is relatively small, it is an important factor to elucidate their respective reactivities. This observation is consistent with the Lewis acid–base interaction. Our findings match those reported in earlier studies.[31]

4.4 Conclusions

In this Chapter, we have investigated geometric and electronic properties of bulk α-boron(B12) as well as the interaction of this phase with the atomic and molecular oxygen. The structural data computed for the α(001)B12 surface show a significant relaxation of the topmost layers but no surface reconstruction. We found that, the atomic and molecular oxygen interacts strongly with the α(001)B12 surface with binding energies in the range of -1.63 eV to -3.38 eV. Three stable adsorption sites of boron surface arise with their stability ordered as top (T3) > bridge (B1) > and hollow (H1, H2). The molecular adsorption affords a number of weakly physisorbed structures. On the other hand, dissociation of O_2 on the α(001)B12 surface is considerably exoergic, however, a sizable reaction barrier of 3.4 eV hinders chemisorbed (dissociative) adsorption of molecular oxygen at ambient conditions. The formed B-O surface bonds display noticeable ionicity. We found that, the three-fold coordination is not a favorable adsorption site. The *T-P* phase diagram, comprising energetics of all calculated adsorption structures, shows that, the formation of a B_2O_3-bulk like structure via substitutional adsorption dictates the stability of oxygen/boron configurations at temperatures and pressure pertinent to practical applications. We highlighted geometrical and electronic similarities (i.e., charge distributions) between O/α(001)B12 structures and bulk B_2O_3. Our results indicate that, the B_2O_3 surfaces provide limited case scenarios for adsorption of oxygen on boron surfaces and

warrant further investigation. Finally, the surfaces of α-B12 unit cell appear more dense when compared with those of the β-B106 cell. Accordingly, addressing comprehensively the interaction of oxygen with boron surfaces necessitates considering surfaces derived from other forms of elemental boron, especially β-B106.

4.5 References

Hosmane, N. S., *Boron Science: New Technologies and Applications*; CRC Press, New York, 2012.

2. Lau, K. C.; Yap, Y. K.; Pandey, R. *Boron and Boron Carbide Materials: Nanostructures and Crystalline Solids. Lecture Notes in Nanoscale Science and Technology*; Springer: New York, 2009.

3. Eremets, M. I.; Struzhkin, V. V.; Mao, H.-k.; Hemley, R. J., Superconductivity in boron. *Science* **2001**, *293*, 272-274.

4. Shirai, K.; Dekura, H.; Masago, A. Superconductivity research on boron solids and an efficient doping method. *J. Phys. Conf. Ser.* **2009**, *176*, 012001-012019.

5. Shang, S.; Wang, Y.; Arroyave, R.; Liu, Z.-K., Phase stability in α-and β-rhombohedral boron. *Phys. Rev. B* **2007**, *75*, 092101-092105.

6. Albert, B.; Hillebrecht, H., Boron: Elementary challenge for experimenters and theoreticians. *Angew. Chem. Int. Edit.* **2009**, *48*, 8640-8668.

7. Braganza, C.; Vepřek, S.; Groner, P., Boron compound protective coatings prepared by means of low pressure plasma CVD. *J. Nucl. Mater.* **1979**, *85*, 1133-1137.

8. Knyshev, E. A.; Kobyakov, V. A.; Tkatchev, K. V.; Tsomaya, K. P.; Mashkovskii, E. I.; Karyuk, G. G., Crystalline boron and its abrasive properties. *J. Less Common Met.* **1979**, *67*, 477-484.

9. Oganov, A. R.; Solozhenko, V. L., Boron: A hunt for superhard polymorphs. *J. Superhard Mater.* **2009**, *31*, 285-291.

10. McCarty, L. V.; Kasper, J. S.; Horn, F. H.; Decker, B. F.; Newkirk, A. E., A new crystalline modification of boron. *J. Am. Chem. Soc.* **1958**, *80*, 2592-2592.

11. He, C.; Zhong, J. X., Structures, stability, mechanical and electronic properties of *α*-boron and *β*-Boron. *AIP Adv.* **2013**, *3*, 042138-042145.

12. Hughes, R. E.; Kennard, C. H. L.; Sullenger, D. B.; Weakliem, H. A.; Sands, D. E.; Hoard, J. L., Thestructure of *β* -rhombohedral boron. *J. Am. Chem. Soc.* **1963**, *85*, 361-362.

13. Sands, D. E.; Hoard, J. L., Rhombohedral elemental boron. *J. Am. Chem. Soc.* **1957**, *79*, 5582-5583.

14. Oganov, A. R.; Chen, J.; Gatti, C.; Ma, Y.; Ma, Y.; Glass, C. W.; Liu, Z.; Yu, T.; Kurakevych, O. O.; Solozhenko, V. L., Ionic high-pressure form of elemental boron. *Nature* **2009**, *457*, 863-867.

15. Vlasse, M.; Naslain, R.; Kasper, J. S.; Ploog, K., Crystal structure of tetragonal boron related to *α*-AlB_{12}. *J. Solid State Chem.* **1979**, *28*, 289-301.

16. Solozhenko, V. L.; Kurakevych, O. O., Equilibrium Pt phase diagram of boron: experimental study and thermodynamic analysis. *Sci. Rep.* **2013**, *3*, 2351-2359.

17. Masago, A.; Shirai, K.; Katayama-Yoshida, H., Crystal stability of *α*-and *β*-Boron. *Phys. Rev. B* **2006**, *73*, 104102-104112.

18. Will, G.; Kiefer, B., Electron deformation density in rhombohedral *α*-Boron. *Z. Anorg. Allg. Chem.* **2001**, *627*, 2100-2104.

19. Schöttke, H., The electronic band structure of *α*-rhombohedral boron. *J. Less Common Met.* **1983**, *91*, 159-165.

20. Li, D.; Ching, W. Y., Electronic structures and optical properties of low-and high-pressure phases of crystalline B_2O_3. *Phys. Rev. B* **1996**, *54*, 13616-13622.

21. Li, D.; Xu, Y.-N.; Ching, W. Y., Electronic structures, total energies, and optical properties of *α*-rhombohedral B12 and *α*-tetragonal B50 crystals. *Phys. Rev. B* **1992**, *45*, 5895-5905.

22. Wang, L., Master thesis, *Electronic Stucture of Elemental Boron.* University of Missouri, 2010.

23. Shalamberidze, S. O.; Kalandadze, G. I.; Khulelidze, D. E.; Tsurtsumia, B. D., Production of *α*-rhombohedral boron by amorphous boron crystallization. *J. Solid State Chem.* **2000**, *154*, 199-203.

24. Horn, F. H., Some electrical and optical properties of simple rhombohedral boron. *J. Appl. Phys.* **1959**, *30*, 1611-1612.

25. Zarechnaya, E. Y.; Dubrovinsky, L.; Dubrovinskaia, N.; Filinchuk, Y.; Chernyshov, D.; Dmitriev, V.; Miyajima, N.; El Goresy, A.; Braun, H. F.; Van Smaalen, S.; Kantor, I.; Prakapenka, V.; Hanfland, M.; Mikhaylushkin, A. S.; Abrikosove, I. A.;Simake, S. I., Superhard semiconducting optically transparent high pressure phase of boron. *Phys. Rev. Lett.* **2009**, *102*, 185501-185505.

26. Parakhonskiy, G.; Dubrovinskaia, N.; Bykova, E.; Wirth, R.; Dubrovinsky, L., Experimental pressure-temperature phase diagram of boron: resolving the long-standing enigma. *Sci. Rep.* **2011**, *1*, 96-103.

27. Shirai, K.; Masago, A.; Katayama-Yoshida, H., High-pressure properties and phase diagram of boron. *Phys. Status Solidi B* **2007**, *244*, 303-308.

28. Polian, A.; Chervin, J. C.; Munsch, P.; Gauthier, M., *α*-Boron at very high pressure: Structural and vibrational properties. *J. Phys. Conf. Ser.* **2008**, *121*, 042017-042021.

29. White, M. A.; Cerqueira, A. B.; Whitman, C. A.; Johnson, M. B.; Ogitsu, T., Determination of phase stability of elemental boron. *Angew. Chem.* **2015**, *127*, 3697-3700.

30. Van Setten, M. J.; Uijttewaal, M. A.; de Wijs, G. A.; de Groot, R. A., Thermodynamic stability of boron: The role of defects and zero point motion. *J. Am. Chem. Soc.* **2007**, *129*, 2458-2465.

31. Sun, Q.; Wang, M.; Li, Z.; Du, A.; Searles, D. J., A computational study of carbon dioxide adsorption on solid boron. *PCCP* **2014**, *16*, 12695-12702.

32. Sun, Q.; Wang, M.; Li, Z.; Li, P.; Wang, W.; Tan, X.; Du, A., Nitrogen removal from natural gas using solid boron: A first-principles computational study. *Fuel* **2013**, *109*, 575-581.

33. Mårlid, B.; Larsson, K.; Carlsson, J.-O., Chemical interaction of H_2, Br_2, and HBr with *α*-boron surfaces. *J. Phys. Chem. B* **2001**, *105*, 12797-12802.

34. Wang, Y.; Fan, J.; Trenary, M., Surface chemistry of boron oxidation. 1. Reactions of oxygen and water with boron films grown on tantalum (110). *Chem. Mater.* **1993**, *5*, 192-198.

35. Wang, Y.; Trenary, M., Surface chemistry of boron oxidation. 2. The reactions of boron oxides B_2O_2 and B_2O_3 with boron films grown on tantalum (110). *Chem. Mater.* **1993**, *5*, 199-205.

36. King, M. K., Ignition and combustion of boron particles and clouds. *J. Spacecraft Rockets* **1982**, *19*, 294-306.

37. Krasnoperov, L. N.; Niiranen, J. T.; Gutman, D.; Melius, C. F.; Allendorf, M. D., Kinetics and thermochemistry of $Si(CH_3)_3$ + No Reaction: direct determination of a Si-N bond energy. *J. Phys. Chem.* **1995**, *99*, 14347-14358.

38. Fujimori, M.; Nakata, T.; Nakayama, T.; Nishibori, E.; Kimura, K.; Takata, M.; Sakata, M., Peculiar covalent bonds in *α*-rhombohedral boron. *Phys. Rev. Lett.* **1999**, *82*, 4452-4455.

39. Gross, E. K.; Dreizler, R. M., *Density Functional Theory*; Springer Science & Business Media, 2013.

40. B. Delley, An all-electron numerical method for solving the local density functional for polyatomic molecules. *J. Chem. Phys.* **1990**, *92*, 508-517.

41. B. Delley, From molecules to solids with the $DMol^3$ approach. *J. Chem. Phys.* **2000**, *113*, 7756-7764.

42. Perdew, J. P.; Burke, K.; Ernzerhof, M., Generalized gradient approximation made simple. *Phys. Rev. Lett.* **1996**, *77*, 3865-3868.

43. Grimme, S., Semiempirical gga-type density functional constructed with a long-range dispersion correction. *J. Comput. Chem.* **2006**, *27*, 1787-1799.

44. Monkhorst, H. J.; Pack, J. D., Special points for brillouin-zone integrations. *Phys. Rev. B* **1976**, *13*, 5188-5192.

45. Rogal, J.; Reuter, K.; Scheffler, M., First-principles statistical mechanics study of the stability of a subnanometer thin surface oxide in reactive environments: co oxidation at Pd (100). *Phys. Rev. Lett.* **2007**, *98*, 046101-046105.

46. Stampfl, C., Surface processes and phase transitions from ab Initio atomistic thermodynamics and statistical mechanics. *Catal. Today* **2005**, *105*, 17-35.

47. Chase, M. W. 1998, *NIST-JANAF Thermochemical Tables* (4th ed.; Washington, DC: Am. Chem. Soc.)

48. Tallant, D.; Aselage, T.; Campbell, A.; Emin, D., Boron carbide structure by raman spectroscopy. *Phys. Rev. B* **1989**, *40*, 5649-5656.

49. He, J.; Wu, E.; Wang, H.; Liu, R.; Tian, Y., Ionicities of boron-boron bonds in B12 icosahedra. *Phys. Rev. Lett.* **2005**, *94*, 015504-015508.

50. Terauchi, M.; Kawamata, Y.; Tanaka, M.; Takeda, M.; Kimura, K., Electron energy-loss spectroscopy study of the electronic structure of *α*-Rhombohedral boron. *J. Solid State Chem.* **1997**, *133*, 156-159.

51. Decker, B.; Kasper, J., The crystal structure of a simple rhombohedral form of boron. *Acta Crystallogr.* **1959**, *12*, 503-506.

52. Häussermann, U.; Simak, S.; Ahuja, R.; Johansson, B., Metal-nonmetal transition in the boron group elements. *Phys. Rev. Lett.* **2003**, *90*, 065701-065705.

53. Lee, S.; Bylander, D.; Kleinman, L., Bands and bonds of B12. *Phys. Rev. B* **1990**, *42*, 1316-1320.

54. R. Caputo, A. Zuttel, First principles study of *α*-Boron: Can the B12 cage host hetero-atoms? *Mol. Phys.* **2009**, *107*, 1831-1842.

55. Amsler, M.; Botti, S.; Marques, M. A.; Goedecker, S., Conducting boron sheets formed by the reconstruction of the *α*-Boron (111) surface. *Phys. Rev. Lett.* **2013**, *111*, 136101-136107.

56. Hu, Q.; Wu, Q.; Sun, G.; Luo, X.; Liu, Z.; Xu, B.; He, J.; Tian, Y., First-principles study of atomic oxygen adsorption on boron-substituted graphite. *Surf. Sci.* **2008**, *602*, 37-45.

57. Afeefy, H. Y.; Liebman, J. F.; Stein, S. E.; Linstrom, P. J.; Mallard, W. G., *NIST Chemistry Webbook, NIST Standard Reference Database Number 69*, 2005.

58. Linstrom, P. J.; Mallard, W., *NIST Chemistry Webbook; NIST Standard Reference Database Number* 69, **2001**.

59. Raffaini, G.; Ganazzoli, F., Molecular dynamics simulation of the adsorption of a fibronectin module on a graphite surface. *Langmuir* **2004**, *20*, 3371-3378.

60. Krekelberg, W. P.; Greeley, J.; Mavrikakis, M., Atomic and molecular adsorption on Ir (111). *J. Phys. Chem. B* **2004**, *108*, 987-994.

61. Bergermayer, W.; Schweiger, H.; Wimmer, E., Ab initio thermodynamics of oxide surfaces: O_2 on Fe_2O_3 (0001). *Phys. Rev. B* **2004**, *69*, 195409-195421.

62. Rossini, F. D.; Wagman, D. D.; Evans, W. H.; Rossini, F. D.; Rossini, F. D., *Selected values of chemical thermodynamic properties*; Washington, DC: US Government Printing Office, 1952.

63. Rogal, J.; Reuter, K.; Scheffler, M., Thermodynamic stability of Pdo surfaces. *Phys. Rev. B* **2004**, *69*, 075421-075429.

64. R. S. Mulliken, Report on notation for the spectra of polyatomic molecules. *J. Chem. Phys* **1955**, *23*, 1997-2011.

65. Muya, J. T.; De Proft, F.; Geerlings, P.; Nguyen, M. T.; Ceulemans, A., Theoretical study on the regioselectivity of the B80 buckyball in electrophilic and nucleophilic reactions using DFT-based reactivity indices. *J. Phys. Chem. A* **2011**, *115*, 9069-9080.

CHAPTER 5

Structure, Stability and (non) Reactivity of the Low-Index Surfaces of Crystalline B_2O_3-I

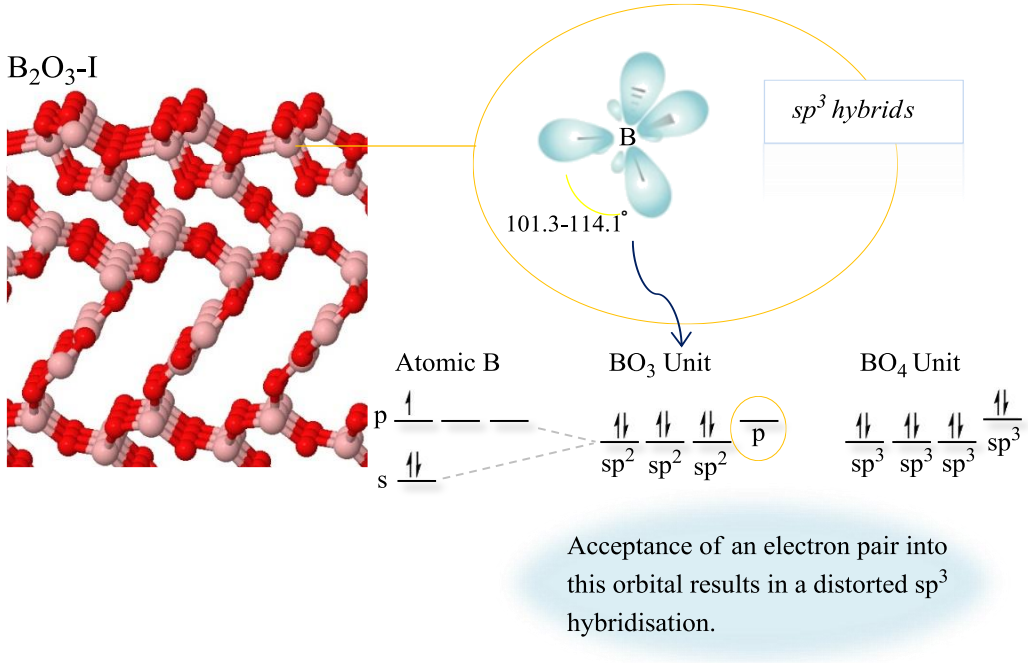

The following is a modified version of the published paper:

Assaf, N. W.; La Pierre, M. De; Altarawneh, M. K.; Radny, M. W.; Jiang, Z.-T.; Dlugogorski, B. Z. ; Structure, Stability, and (Non) Reactivity of the Low-Index Surfaces of Crystalline B_2O_3–I, *J. Phys. Chem. C* **2017,** *121*, 11346–11354.

2016 impact factor: 4.536

5.1 Introduction

Diboron trioxide is one of the most widely deployed oxidation inhibitors[1, 2] and as such finds direct applications in electrolysis,[3] ceramic and glass technology.[4-6] At ambient conditions, B_2O_3 adopts a vitreous (amorphous) form, v-B_2O_3. Earlier studies[7-9] on v-B_2O_3 reported its structure as composed of randomly oriented BO_3 building blocks, in which three oxygen atoms located at the corners of a triangle surround a boron atom. However, an experimental study by Jellison et al.[10] involving the ^{17}O isotope revealed that oxygen in v-B_2O_3 occupies two distinct sites, depending on whether an oxygen atom forms part of a boroxol ring or whether it links two boroxol rings. Each boroxol ring represents a hexagon with three alternating vertices occupied by B atoms and the other three by O atoms. In addition, each B coordinates to an additional O, which in turn bonds to a B atom on an adjacent ring. Thus, a boroxol ring (B_3O_6) comprises three BO_3 triangles, with one oxygen atom in each triangle lying on the outer of the ring. Subsequent experimental investigations have yielded similar conclusions.[11-13]

Over a wide range of operational pressures and temperatures, crystalline B_2O_3 exhibits two crystallographic structures - B_2O_3-I at low pressure[14] and B_2O_3-II at high pressure.[15, 16] At a pressure of 400 MPa (> 483.15 K), the amorphous form of B_2O_3 transforms into crystalline B_2O_3-I. The planar triangles of BO_3 present in B_2O_3-I form a hexagonal structure (space group $P3_121$) with lattice parameters of a = 4.33 Å and c = 8.34 Å.[14, 17] With increasing pressure, the optimal coordination number of boron atoms changes from a three-fold to a four-fold arrangement.[18, 19] At ~6.5 GPa (> 1000 K),[16, 18, 20] the second B_2O_3–II crystal structure is formed, which consists of three-dimensional networks of tetrahedral units of BO_4 adopting an orthorhombic lattice (space group $Ccm2_1$). Two in three oxygens in this structure form dative bonds and have a three-fold rather than two-fold coordination, resulting in the BO_4 tetrahedra

being disorted, with 3 B-O lengths larger than the 4th one (1.51 vs 1.37 Å).[15] Note that the three-fold coordinated boron in B_2O_3-I has got a sp^2 hybridisation, with an empty low-energy p orbital in the valence shell that is mainly responsible for the Lewis acid behaviour of this compound. In the case of the high pressure phase B_2O_3–II, acceptance of an electron pair into this orbital results in a sp^3 hybridization and the observed distorted four-fold coordination.[21]

Despite the amorphous form being the most exploited in practical applications, the crystalline phases can serve as significant model systems to get insights into the properties of B_2O_3, especially at an atomistic scale. As regards the structure and energetics of B_2O_3-I surfaces, Bredow and Islam[22] are so far the only authors in the literature to have investigated them by means of quantum mechanical methods. In their pioneering work, they focused on the low-index surfaces and found the following stability order: (101) < $(1\bar{1}1)$ (or, equivalently, (011)) < (100) < (001). Notably, the authors found out that 3 out of the 4 investigated surfaces feature dangling bonds, which partially contrasts with the experimental observation of B_2O_3 surfaces not being reactive.

In this Chapter, we report the results from a comprehensive investigation on the low-index (*hkl*) surfaces of B_2O_3-I, as obtained through hybrid Hartree-Fock/Density Functional Theory (HF/DFT) calculations. Building on the early work by Bredow and Islam,[22] we have explored sp^3 in addition to sp^2 hybridised surface boron, as well as alternative atomic arrangements for surface terminations, and have successfully identified new lowest energy surface structures, providing significant connections with the inertness of B_2O_3 and the structure of its vitreous form.

5.2 Computational Methodology

Calculations were performed using the ab initio CRYSTAL14 code.[23, 24] Surfaces were simulated by using the 2D periodic slab model, consisting of a film formed by a set of atomic layers parallel to the *hkl* crystalline plane of interest. All the calculations were performed at the DFT level. In particular, the PW1PW Hamiltonian was adopted,[25] which contains a hybrid HF/DFT exchange term, that has already been used in previous studies on B_2O_3.[22, 26] Additional calculations were performed using the PW91,[27] PBEsol[28] (GGA), B3LYP[29-31] and PBE0[32] (hybrid) Hamiltonians. Hybrid functionals have been successfully applied to the investigation of surfaces of a variety of minerals, including diamond,[33] silica,[34, 35] spinel[36] and olivine.[37, 38]

Boron and oxygen were described by the m-6-311G(d) basis-sets proposed by Heyd et al. to investigate a large set of semiconductor solids.[39] The exponents (in units of $bohr^{-2}$) of the most diffuse sp shells are 0.16 (B) and 0.26 (O), whereas the exponents of the d shells are 0.80 (B) and 1.29 (O).

DFT Exchange and correlation contributions were numerically evaluated by integrating, over the cell volume, functions of the electron density and of its gradient. Choice of the integration grid is based on an atomic partition method, originally developed by Becke.[40] In the present Chapter, the extra-large pruned (75, 974) *p* grid was chosen (XLGRID in the code[24]), which ensures a satisfactory accuracy in the integrated electron charge density, the corresponding error for the studied surfaces being smaller than $1 \cdot 10^{-4}$ |e| over either 408 [(101), (011) and (001)] or 476 [(100)] |e|. Diagonalization of the Hamiltonian for the studied surfaces was performed at either 13 [(101), (011) and (001)] or 16 [(100)] irreducible k points in the

reciprocal space (Monkhrost net[41]) by setting the shrinking factor to 6 (more details are provided in ref. 24). The thresholds controlling the accuracy in the evaluation of Coulomb and exchange integrals (ITOL1, ITOL2, ITOL3, ITOL4 and ITOL5 in the code[24]) were set to 10^{-8} (ITOL1 to ITOL4) and 10^{-18} (ITOL5). Threshold on the SCF energy was set to 10^{-8} hartree. Structures were optimized by using the analytical energy gradients with respect to atomic coordinates[42-44] and a BFGS algorithm; convergence was checked on both gradient components and nuclear displacements, whose tolerances where set to 0.0003 Hartree·bohr^{-1} and 0.0012 bohr, respectively. Vibrational frequencies at the Γ point were computed within the harmonic approximation by numerical differentiation of the analytical gradients with respect to the atomic Cartesian coordinates[45]. This permitted to verify that the optimised structures lie on minima of the potential energy surface.

The specific surface energy γ at T = 0 K was calculated by using the following relation:[46]

$$\gamma = \lim_{n\to\infty} E_s(n) = \lim_{n\to\infty} \frac{E(n) - nE_{bulk}}{2A} \qquad 5.1$$

where $E(n)$ denotes the energy of a n-layer slab; E_{bulk} signifies the energy of the bulk; A is the area of the primitive unit cell of the surface; the factor 2 in the denominator accounts for the upper and lower surfaces of the slab. $E_s(n)$ is thus the energy per unit area required for the formation of the surface from the bulk. As more layers are added in the calculation ($n \rightarrow \infty$), $E_s(n)$ will converge to the surface energy per unit area (γ). All values were corrected for Basis Set Superposition Error (BSSE, e.g. ref. 46).

The number of atomic layers to be considered in each slab, *n*, was set to 60, and chosen to satisfy the following criteria: surface energy for all orientations converged within 0.01 J/m^2, bond lengths converged within 0.01 Å, bond angles converged within 1°.

5.2.1 Effect of the Hamiltonian

The impact of the choice of the Hamiltonian was analysed for both bulk and slab calculations, by comparing the results obtained using PBEsol, PW91 (GGA), B3LYP, PBE0 and PW1PW (hybrid). Table 5.1 shows cell parameters and B-O distances in bulk B_2O_3-I for the different functionals. The most affected quantity turns out to be the *c* lattice parameter: Whereas PBE0 and PW1PW reproduce it very well, yielding a +0.3 and +0.4% discrepancy compared to the experiment, respectively, the other functionals show significant deviations: -2.9% (PBEsol), +1.9% (PW91), +4.5% (B3LYP). The case of B3LYP is peculiar: even if this functional is known to overestimate lattice parameters,[47] such a large overestimation probably relates to its poorer description of dispersion interactions,[48] and suggests to avoid its use for the purposes of the present investigation. On the other hand, both PBE0 and PW1PW show a nearly coincident, excellent agreement with the experimental data, in line with the known accuracy of hybrid methods; we decided to adopt PW1PW as the main method for the sake of increased comparability with the previous work by Bredow and Islam.[22] As regards the *a* cell parameter, B-O distances and O-B-O angles, all of them are always reproduced with an accuracy better than 1%.

Table 5.1. Structural and electronic properties of bulk B_2O_3–I.

	Current study					Islam, Bredow and Minot[26]	Exp.[17]
	PBEsol	PW91	B3LYP	PBE0	PW1PW	PW1PW	
A	4.313	4.367	4.371	4.330	4.334	4.35	4.3358
C	8.095	8.501	8.718	8.366	8.376	8.39	8.3397
Δc (%)	-2.9	+1.9	+4.5	+0.3	+0.4	+0.6	--
d(B-O_a)	1.378	1.380	1.373	1.370	1.371	1.376	1.376
d(B-O_a')	1.375	1.375	1.367	1.365	1.366	1.374	1.374
d(B-O_b)	1.368	1.369	1.362	1.360	1.361	1.370	1.357
θ(O_a-B-O_a')	120.1	120.5	120.6	120.5	120.4	--	120.5
θ(O_a-B-O_b)	116.3	116.3	116.6	116.4	116.5	--	116.4
θ(O_a'-B-O_b)	123.0	122.9	122.6	122.8	122.8	--	123.2
q(B)	+0.934	+0.935	+1.015	+1.048	+1.029	--	--
q(O_a)	-0.616	-0.614	-0.665	-0.688	-0.676	--	--
q(O_b)	-0.637	-0.642	-0.700	-0.718	-0.705	--	--
E_{gap}	6.44	6.41	8.57	9.21	8.66	9.1	--

Lengths are in Å, angles in °, net Mulliken charges in |e| units, E_{gap} in eV. *Δc* is the percent deviation of the *c* cell parameter with respect to the experimental value. Data obtained with the PW1PW Hamiltonian in the present Chapter are in bold for ease of reading.

Let us now assess the adopted Hamiltonians against the surface energies of the four low-index surfaces considered in this Chapter (see Table 5.2). The most important aspect is that the stability order is preserved regardless the adopted functional; the same applies for the overall atomic arrangements of the surfaces (not reported). This outcome is very significant as it implies that results presented in the following sections may be considered to be independent from the chosen Hamiltonian. One minor point to note is that, in the case of the functionals

with large *c* parameter discrepancies in the bulk, PW91 and B3LYP, the two lowest energy surfaces become more stabilised as opposed to the highest energy ones, as compared to the other functionals; on the contrary PBEsol (which largely underestimates *c* in the bulk) yields a relative destabilisation of the two lowest energy surfaces. The (100) surface orientation, i.e. the 2nd most stable, has the *c* parameter parallel to its plane and exhibits the largest dependence of its formation energy upon the *c* value.

Table 5.2. Surface energies γ (J/m^2) of the low-index surfaces of B_2O_3-I.

	Current study					**Bredow and Islam[22]**
	PBEsol	PW91	B3LYP	PBE0	**PW1PW**	PW1PW
(001)	0.780	0.816	0.875	0.884	**0.882**	2.21
(011)	0.675	0.691	0.824	0.743	**0.735**	1.12
(100)	0.576	0.311	0.240	0.400	**0.396**	1.29
(101)	0.329	0.210	0.188	0.254	**0.254**	0.34

Data obtained with the PW1PW Hamiltonian in the present Chapter are in bold for ease of reading.

5.3 Results and Discussion

5.3.1 Bulk Properties

The atomic structure of the hexagonal unit cell of B_2O_3-I, as obtained through our PW1PW simulations, is shown in Figure 5.1; it contains 6 B and 9 O atoms, 1 and 2 of which are irreducible by symmetry.[17, 49] The structure is made up of a three-dimensional network of planar BO_3 triangles,[14, 17] with three-fold coordinated, sp^2 hybridised B atoms.

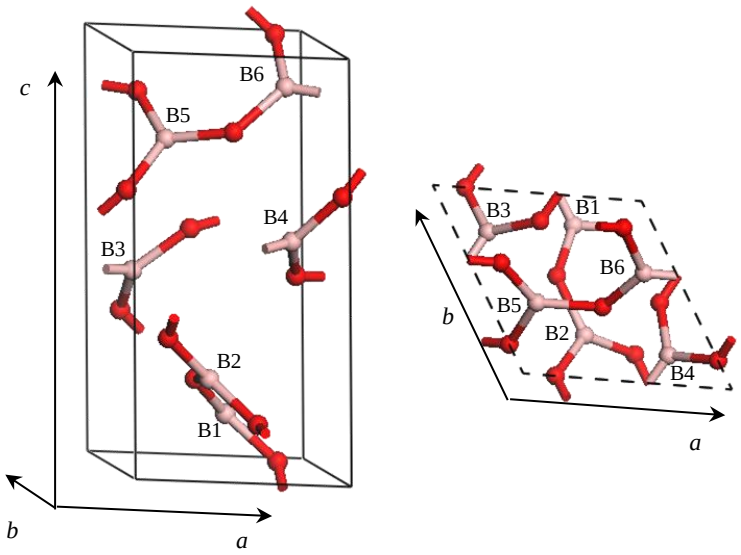

Figure 5.1. The primitive unit cell of bulk B_2O_3-I (side and top views). Light pink and red spheres refer to boron and oxygen atoms, respectively.

Table 5.1 provides a set of structural and electronic properties, in excellent agreement with experimental measurements and theoretical data available in the literature:[17, 18, 26, 49-51] lattice parameters, bond lengths and angles, band gap, Mulliken net charges. Bond angles reveal a very limited distortion of the BO_3 groups from an ideal triangular coordination, as their values range between 116˚ and 123˚.

Figure 5.2 displays the calculated total density of states of bulk B_2O_3-I, as well as its projections on the B and O atoms. There is a wide insulating gap of 8.66 eV, which is consistent with the value reported by Bredow and Islam[22] (9.1 eV). The valence band consists of two continuum regions of energy levels, the lower one stretching between -21.4 and -18.7 eV, and the upper one extending from -9.3 eV up to the top of the valence band. Except for the lower half of the latter, where there is a significant contribution from the B atomic orbitals, the valence band is

mostly contributed by O orbitals. On the other hand, the bottommost portion of the conduction band (from +8.6 eV on) mainly relates to electronic states involving B orbitals.

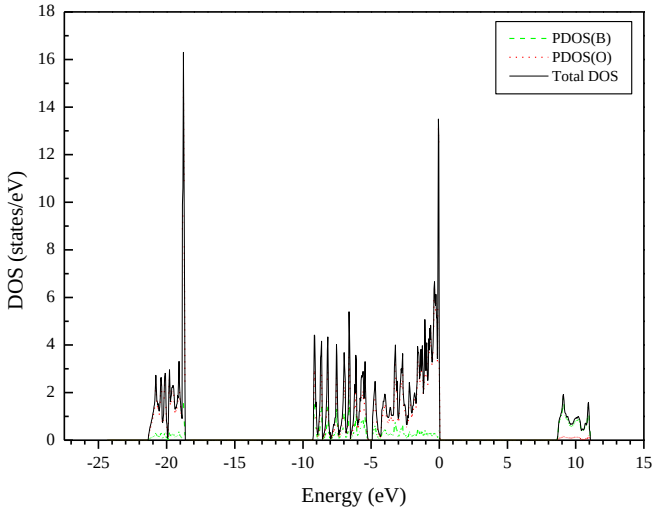

Figure 5.2. Total (DOS) and projected (PDOS) electronic densities of states for bulk B_2O_3-I.

5.3.2 Structure of the Low-Index Surfaces

We started our analysis by considering all the plane orientations featuring 0, 1 or -1 in their Miller indices. Symmetry relations reduce this set to just six irreducible orientations: (100), (001), (011), (101), (110) and (111); in this regard, the $(1\bar{1}1)$ orientation presented by Bredow and Islam[22] is equivalent to (011) by symmetry. It was then noted that there exist no (110) nor (111) slabs with symmetry related surfaces, and then null perpendicular dipole moment. As a result, we ended up investigating four low-index surfaces: (001), (011), (100) and (101). Atomic structures of the lowest energy terminations for these surfaces are represented in Figure 5.3-5.6; bond lengths and angles for the surface B atoms are listed in Table 5.3. At variance with the study by Bredow and Islam,[22] none of the atoms in these structures have got dangling bonds.

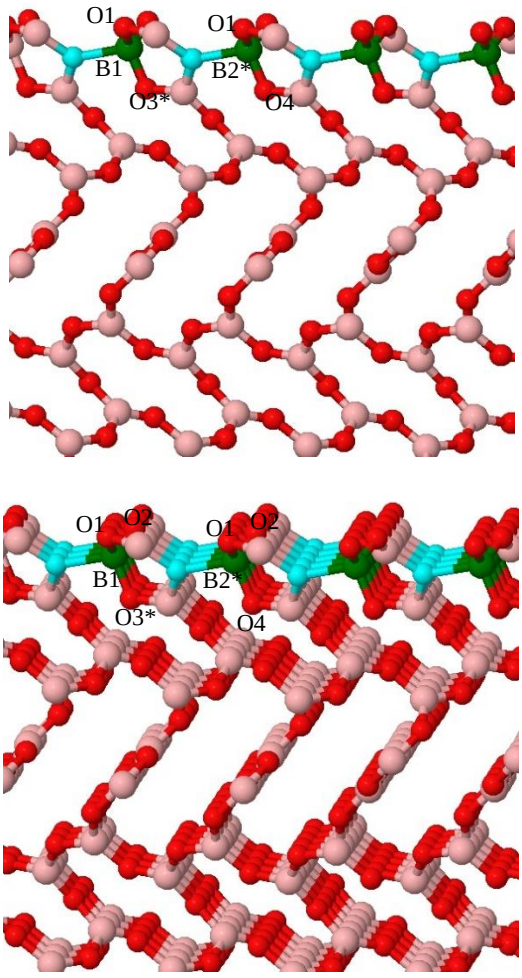

Figure 5.3. Atomic structure of the B_2O_3-I (001) surface. Both side and tilted views are shown. Labels are used to name rows (orthogonal to the plane of the document) of symmetry irreducible surface B atoms, as well as rows of the O atoms that are bound to the former. Asterisks are used to mark either four-fold coordinated B (green spheres) atoms or three-fold coordinated O atoms (cyan spheres).

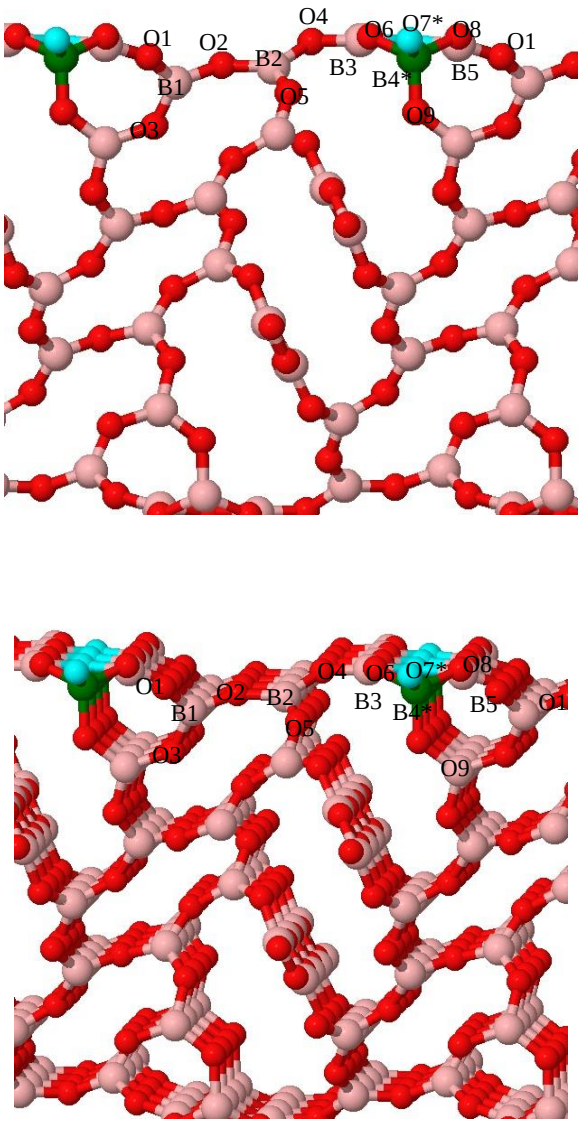

Figure 5.4. Atomic structure of the B_2O_3-I (011) surface. Refer to the caption to Figure 5.3 for more details.

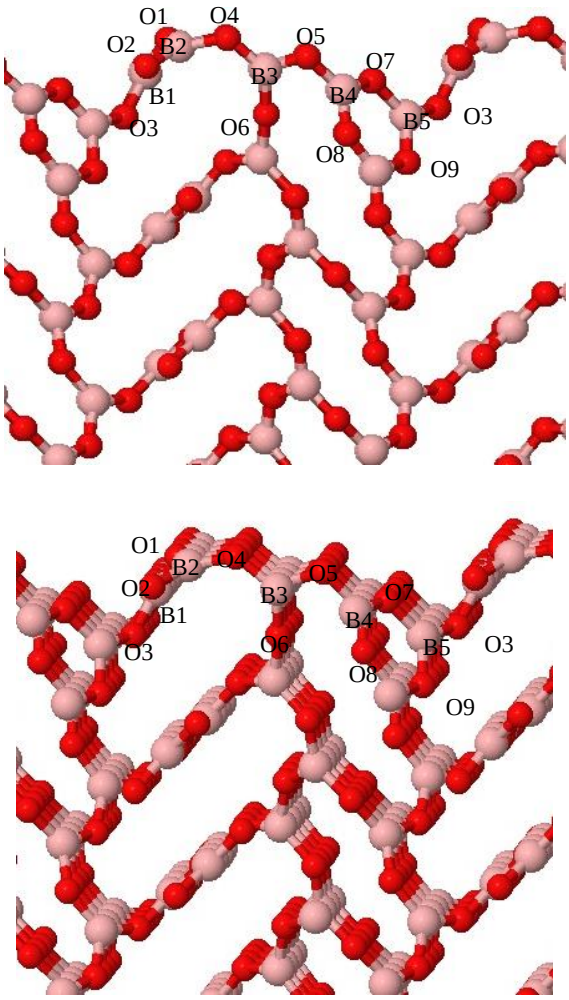

Figure 5.5. Atomic structure of the B_2O_3-I (100) surface. Refer to the caption to Figure 5.3 for more details.

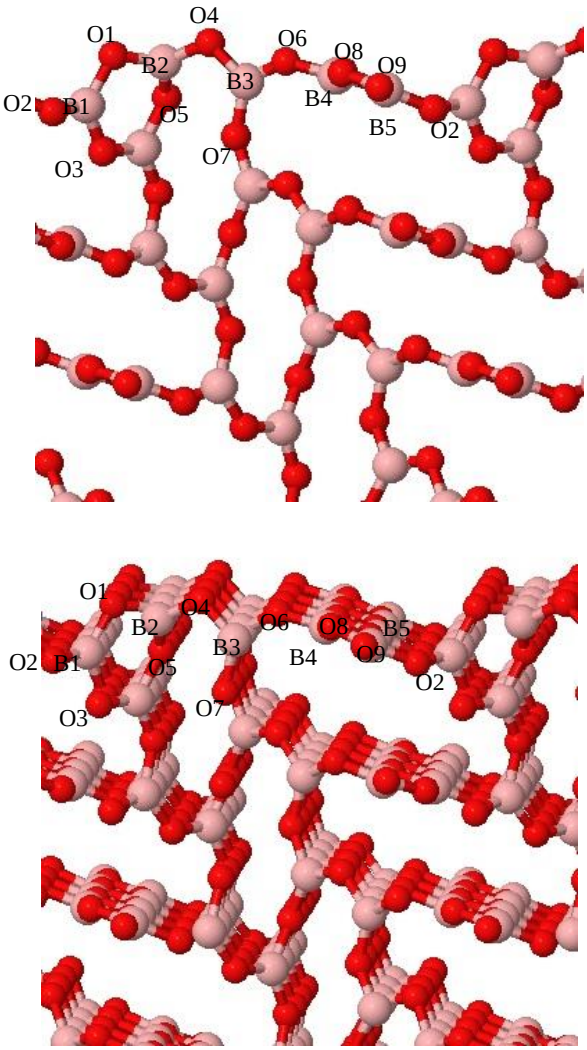

Figure 5.6. Atomic structure of the B_2O_3-I (101) surface. Refer to the caption to Figure 5.3 for more details.

Table 5.3. Bond lengths (d, Å) and angles (θ, ˚) for surface B atoms of the low-index surfaces of B_2O_3-I**.**

			d			**θ**	
		O1	O2	O3*	O1,O2	O1,O3*	O2,O3*
	B1	1.335	1.334	1.455	117.2	119.0	123.5
		O1	O2	O3*	O1,O2	O1,O3*	O1,O4
(001)	B2*	1.383	1.378	1.847	114.1	101.3	113.7
		O4	--	--	O2,O3*	O2,O4	O3*,O4
	“	1.431	--	--	109.9	113.6	102.7
		O1	O2	O3	O1,O2	O1,O3	O2,O3
	B1	1.384	1.374	1.386	120.2	120.6	119.2
		O2	O4	O5	O2,O4	O2,O5	O4,O5
	B2	1.371	1.411	1.348	121.8	121.5	116.8
		O4	O6	O7*	O4,O6	O4,O7*	O6,O7*
	B3	1.355	1.328	1.526	119.9	126.6	113.6
(011)		O6	O7*	O8	O6,O7*	O6,O8	O6,O9
	B4*	1.400	1.642	1.467	104.8	108.0	116.3
		O9	--	--	O7*,O8	O7*,O9	O8,O9
	“	1.428	--	--	115.4	103.1	109.5
		O1	O7*	O8	O1,O7*	O1,O8	O7*,O8
	B5	1.344	1.469	1.347	119.8	122.0	118.2
		O1	O2	O3	O1,O2	O1,O3	O2,O3
	B1	1.348	1.362	1.365	121.2	122.6	116.2
		O1	O2	O4	O1,O2	O1,O4	O2,O4
	B2	1.364	1.358	1.347	120.1	119.7	120.0
(100)		O4	O5	O6	O4,O5	O4,O6	O5,O6
	B3	1.344	1.356	1.368	118.0	124.5	117.5
		O5	O7	O8	O5,O7	O5,O8	O7,O8
	B4	1.360	1.362	1.371	118.5	120.0	121.3
		O3	O7	O9	O3,O7	O3,O9	O7,O9

	B5	1.354	1.358	1.371	121.5	118.5	119.9
(101)		O1	O2	O3	O1,O2	O1,O3	O2,O3
	B1	1.367	1.357	1.381	121.1	119.0	118.1
		O1	O4	O5	O1,O4	O1,O5	O4,O5
	B2	1.376	1.353	1.379	120.3	118.5	120.1
		O4	O6	O7	O4,O6	O4,O7	O6,O7
	B3	1.368	1.346	1.378	117.8	117.8	124.1
		O6	O8	O9	O6,O8	O6,O9	O8,O9
	B4	1.339	1.371	1.377	117.0	123.1	119.7
		O2	O8	O9	O2,O8	O2,O9	O8,O9
	B5	1.354	1.356	1.375	122.5	116.5	121.0

Atomic labels as in Figures 5.3 to 5.6. Asterisks are used to mark either four-fold coordinated B atoms or three-fold coordinated O atoms.

In the case of (101) and (100) orientations all surface borons are three-fold coordinated, with a nearly ideal triangular geometry that closely resembles the bulk case: bond lengths are in the range 1.339÷1.381 Å for (101) and 1.344÷1.371 Å for (100). These values compare well with 1.361÷1.371 Å in the bulk, the maximum shortening and lengthening being only 0.022 and 0.010 Å, respectively. Similarly, bond angles are 116.5÷124.1˚ in (101) and 116.2÷124.5˚ in (100), to be compared with 116.5÷122.8˚ in the bulk.

Interestingly, the other two orientations, (011) and (001), both feature four-fold coordinated B atoms and three-fold coordinated O atoms, which result in pronounced distortions from the bulk geometry. In the case of (011) one surface B atom out of five is four-fold coordinated (B4* in Figure 5.4 and Table 5.3), and one surface O atom out of six is three-fold coordinated (O7*). The B4* atom shows much longer bonds compared to the bulk: 1.400, 1.428 and 1.467 Å when bound to two-fold coordinated oxygens, up to 1.642 Å when bound to O7*; the corresponding bond angles are within 103.1÷116.3˚, indicating a distorted tetrahedral

geometry. The remaining surface borons show large, though less marked, deviations from the bulk when bound to two-fold coordinated O atoms, with bond lengths spreading over the range 1.328÷1.411 Å; however, this quantity can raise up to 1.469 and 1.526 Å for the B-O7* bonds. Besides, all the three-fold coordinated borons show bond angles that are in line with a slightly distorted triangular geometry, 113.6÷126.6˚.

Finally, the (001) orientation has one four-fold coordinated surface boron in two (B2* in Figure 5.3 and Table 5.3) and one three-fold coordinated surface oxygen in three (O3*). The B2* atom forms bonds with three-fold coordinated oxygens whose length is moderately longer than in the bulk, 1.378÷1.431 Å, whereas the bond with O3* is as long as 1.847 Å; bond angles (101.3÷114.1˚) again suggest a distorted tetrahedral geometry. The only three-fold coordinated surface boron, B1, has short bonds with two-fold coordinated oxygens, 1.334 and 1.335 Å, and a 1.455 Å long bond with O3*; all bond angles involving B1 lie in the range 117.2÷123.5, which are typical for a triangular geometry.

5.3.3 Electronic Properties of the Low-Index Surfaces

Table 5.4 presents the Mulliken net charges for the surface B atoms and all the O atoms that are chemically bound to the former. In general, surface atoms are less charged than in the bulk: compare the ranges +0.802÷+1.019 |e| and -0.522÷-0.710 |e| for three-fold coordinated B and two-fold coordinated O, respectively, with the bulk values of +1.029 |e| and -0.676, -0.705 |e|. In the case of B atoms, charges smaller than +0.89 |e| are only found in the surfaces which do not contain four-fold coordinated borons. As regards higher coordinated atoms (i.e. four-fold B and three-fold O), they carry larger charges than the average: in this case B values are very

close to the bulk ones, +0.992 |e| in (011) and +0.986 |e| in (001), whereas O values are even larger than in the bulk, -0.797 |e| in (011) and -0.804 |e| in (001).

Table 5.4. Net Mulliken charges (|e|) for the surface B atoms, and corresponding chemically bound O atoms, of the low-index surfaces of B_2O_3-I.

	B1	**B2**	**B3**	**B4**	**B5**				
(001)	+0.893	+0.986*	--	--	--				
(011)	+1.019	+0.955	+0.927	+0.992*	+0.910				
(100)	+0.896	+0.852	+0.820	+0.830	+1.003				
(101)	+0.978	+0.802	+0.959	+0.908	+0.917				
	O1	O2	O3	O4	O5	O6	O7	O8	O9
(001)	-0.552	-0.548	-0.804*	-0.710	--	--	--	--	--
(011)	-0.593	-0.634	-0.643	-0.579	-0.580	-0.548	-0.797*	-0.625	-0.610
(100)	-0.551	-0.617	-0.675	-0.531	-0.522	-0.637	-0.578	-0.630	-0.674
(101)	-0.558	-0.666	-0.687	-0.539	-0.619	-0.579	-0.668	-0.588	-0.649

Notation as in Table 5.3.

Figure 5.7 shows the total and projected DOS curves for the four low-index surfaces, indicating an insulating character for all of them. The band gap amounts to 8.57, 7.97, 8.53 and 8.50 eV for the (001), (011), (100) and (101) orientations, respectively (Bredow and Islam[22] report 8.5 eV for the (011) surface). The gap reduction as compared to the bulk crystal (8.66 eV) relates in all cases to the occurrence of occupied electronic states that lie just above the top of the valence band (which again agrees with the corresponding analysis by Bredow and Islam[22]).

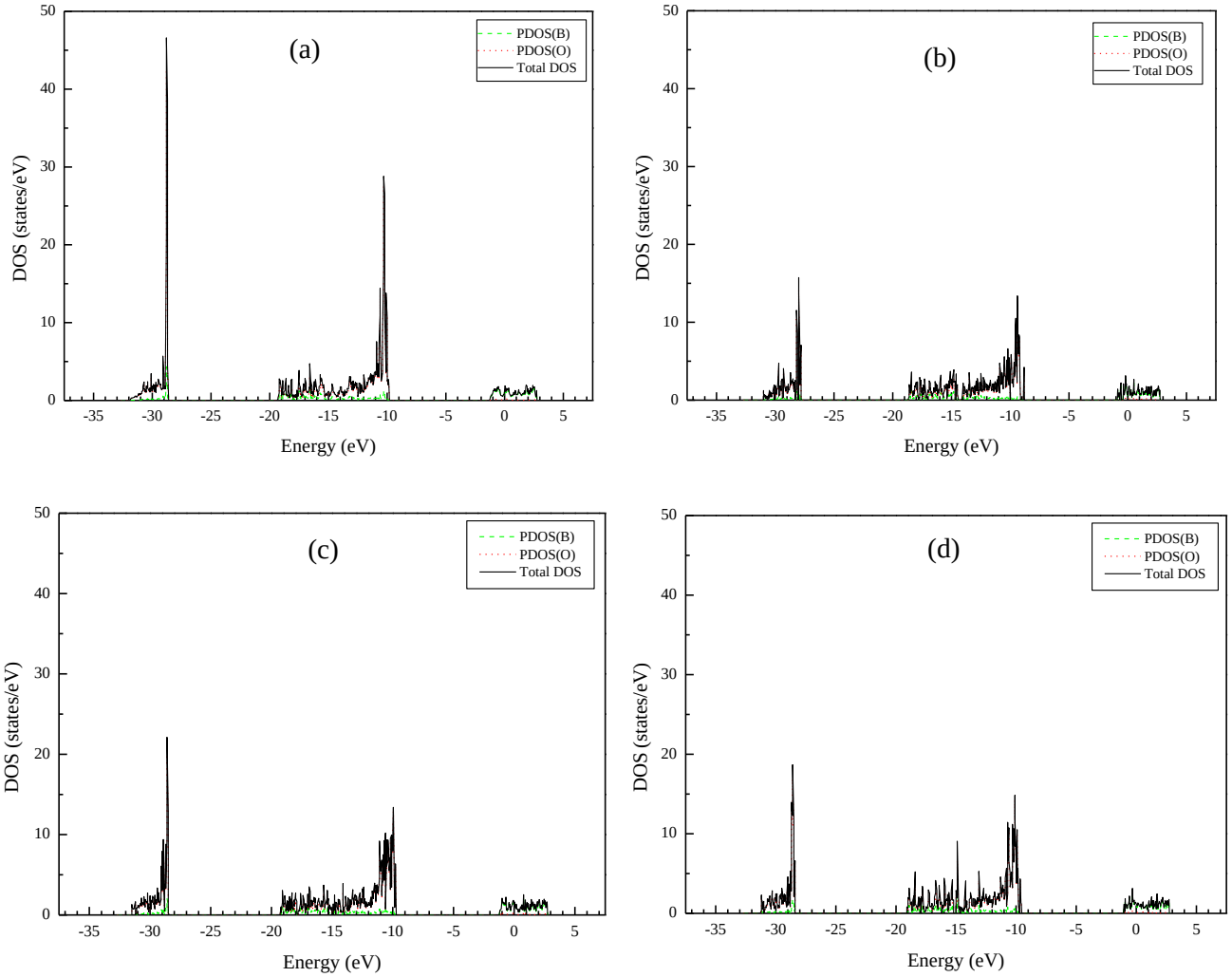

Figure 5.7. Total density of states (DOS) and projected density of states (PDOS) for the (a) (001), (b) (011), (c) (100), and (d) (101) surfaces of B_2O_3-I.

5.3.4 Surface Energies

Surface energy values for the investigated low-index surfaces, as calculated through Eq. (5.1), are reported in Table 2. The stability order is as follows: (101) < (100) < (011) < (001), corresponding to energies of 0.254, 0.396, 0.735 and 0.882 J/m^2, respectively. Interestingly, the two orientations featuring only three-fold coordinated B atoms are lower in energy than the two orientations that also contain four-fold coordinated borons.

A few differences come out when comparing our results with the ones by Bredow and Islam.[22] They got surface energies of 0.34, 1.29, 1.12 and 2.21 J/m^2 for the same four orientations, which they correlated with an increased number of dangling bonds per surface area when increasing the energy. The stability of (100) and (011) surfaces is reversed. Moreover, all surfaces but the most stable one show considerably larger surface energy values compared to ours. Finally, all of our structures display no dangling bonds. These issues are related to two key differences between our study and the literature one: we exteneded our search for low energy surface structures to 1) structures featuring four-fold coordinated B atoms, and 2) structures with alternative atomic terminations. This latter point relates to symmetry analysis revealing that for all the four orientations there exists a repeating unit along the non-periodic direction perpendicular to the slab that is made up of 3 B_2O_3 formula units. This implies that there are at least three different ways of terminating each surface; this number gets even larger when considering that, for a given choice of terminating B_2O_3 unit, there are several possible choices of atomic arrangements within the surface unit cell. Exploitation of this property permitted us to identify the lowest energy structure for the (100) surface.

5.4 Conclusions

In this Chapter, we have adopted a quantum-mechanical approach exploiting a hybrid HF/DFT Hamiltonian to investigate the structural, electronic and energetic properties of four low-index surfaces of crystalline B_2O_3-I: (001), (011), (100) and (101).

This compound shows a great flexibility in terms of bond lengths and angles, thanks to the possibility of adopting both triangular BO_3 and tetrahedral BO_4 coordinations, and in addition to the further distortions allowed by both these structural units. We have demonstrated for the first time that the most stable surface terminations for the (011) and (001) orientations contain tetrahedral BO_4 units, featuring four-fold coordinated borons as well as three-fold coordinated oxygens. Energy for these two surfaces turns out to be higher than (101) and (100), that have only triangular BO_3 units.

5.5 References

1. Chawla, K. K., *Composite Materials: Science and Engineering*; Springer Science & Business Media, 2012.

2. Chung Deborah, D., *Composite Materials: Science and Applications*; NY: Springer,, 2010.

3. Dos Santos-Loff, D.; Micoulaut, M.; Kerner, R., Statistics of boroxol rings in vitreous boron oxide. *EPL* **1994**, *28*, 573-578.

4. Heitjans, P.; Indris, S., Diffusion and ionic conduction in nanocrystalline ceramics. *J. Phys.: Condens. Matter* **2003**, *15*, 1257-1297.

5. Indris, S.; Heitjans, P.; Roman, H. E.; Bunde, A., Nanocrystalline versus microcrystalline Li_2O:B_2O_3 composites: anomalous ionic conductivities and percolation theory. *Phys. Rev. Lett.* **2000**, *84*, 2889-2892.

6. Chawla, N.; Kerr, M.; Chawla, K., Monotonic and cyclic fatigue behavior of high-performance ceramic fibers. *J. Am. Ceram. Soc.* **2005**, *88*, 101-108.

7. Svanson, S.; Johansson, R., The Configuration of three-coordinated boron in vitreous and crystalline boron oxide. *Acta chem. Scand* **1969**, *23*, 635-646.

8. Warren, B.; Krutter, H.; Morningstar, O., Fourier analysis of x-ray patterns of vitreous Sio_2 and B_2O_2. *J. Am. Ceram. Soc.* **1936**, *19*, 202-206.

9. Zachariasen, W. H., The atomic arrangement in glass. *J. Am. Chem. Soc.* **1932**, *54*, 3841-3851.

10. Jellison Jr, G.; Panek, L.; Bray, P.; Rouse Jr, G., Determinations of structure and bonding in vitreous B_2O_3 by means of B10, B11, and O17 Nmr. *J. Chem. Phys.* **1977**, *66*, 802-812.

11. Johnson, P. A.; Wright, A. C.; Sinclair, R. N., A neutron diffraction investigation of the structure of vitreous boron trioxide. *J. Non-Cryst. Solids* **1982**, *50*, 281-311.

12. Mozzi, R. L.; Warren, B., The structure of vitreous boron oxide. *J. Appl. Clystallogr.* **1970**, *3*, 251-257.

13. Suzuya, K.; Yoneda, Y.; Kohara, S.; Umesaki, N., High energy x-ray study of the structure of vitreous B_2O_3. *Phys. Chem. Glasses* **2000**, *41*, 282-285.

14. Gurr, G.; Montgomery, P.; Knutson, C.; Gorres, B., The crystal structure of trigonal diboron trioxide. *Acta Cryst.* **1970**, *26*, 906-915.

15. Prewitt, C.; Shannon, R., Crystal structure of a high-pressure form of B_2O_3. *Acta Cryst.* **1968**, *24*, 869-874.

16. Nieto-Sanz, D.; Loubeyre, P.; Crichton, W.; Mezouar, M., X-ray study of the synthesis of boron oxides at high pressure: phase diagram and equation of state. *Phys. Rev. B* **2004**, *70*, 214108-214114.

17. Effenberger, H.; Lengauer, C. L.; Parthé, E., Trigonal B_2O_3 with higher space-group symmetry: results of a reevaluation. *Monatsh. Chem.* **2001**, *132*, 1515-1517.

18. Li, D.; Ching, W., Electronic structures and optical properties of low-and high-pressure phases of crystalline B_2O_3. *Phys. Rev. B* **1996**, *54*, 13616.

19. Brazhkin, V.; Katayama, Y.; Trachenko, K.; Tsiok, O.; Lyapin, A.; Artacho, E.; Dove, M.; Ferlat, G.; Inamura, Y.; Saitoh, H., Nature of the structural transformations in B_2O_3 glass under high pressure. *Phys. Rev. Lett.* **2008**, *101*, 035702-035706.

20. Zeidler, A.; Wezka, K.; Whittaker, D. A.; Salmon, P. S.; Baroni, A.; Klotz, S.; Fischer, H. E.; Wilding, M. C.; Bull, C. L.; Tucker, M. G., Density-driven structural transformations in B_2O_3 glass. *Phys. Rev. B* **2014**, *90*, 024206-024218.

21. Doyle, R. J., High-molecular-weight boron oxides in the gas Phase. *J. Am. Chem. Soc.* **1988**, *110*, 4120-4126.

22. Bredow, T.; Islam, M. M., Theoretical study of low-index surfaces of trigonal B_2O_3. *Surf. Sci.* **2008**, *602*, 2217-2221.

23. Dovesi, R.; Orlando, R.; Erba, A.; Zicovich-Wilson, C. M.; Civalleri, B.; Casassa, S.; Maschio, L.; Ferrabone, M.; De La Pierre, M.; D'Arco, P., Crystal14: A Program for the ab initio investigation of crystalline solids. *Int. J. Quantum Chem.* **2014**, *114*, 1287-1317.

24. Dovesi, R.; Roetti, C.; Orlando, R.; Zicovich-Wilson, C. M.; Pascale, F.; Civalleri, B.; Doll, K.; Harrison, N. M.; Bush, I. J.; D'Arco, P.; Llunell, M.; Causà M. Noël, Y. *Crystal 2014 User's Manual*, 2014.

25. Bredow, T.; Gerson, A. R., Effect of exchange and correlation on bulkproperties of MgO, NiO, and CoO. *Phys. Rev. B* **2000**, *61*, 5194.

26. Islam, M. M.; Bredow, T.; Minot, C., Comparison of trigonal B_2O_3 structures with high and low space-group symmetry. *Chem. Phys. Lett.* **2006**, *418*, 565-568.

27. Perdew, J. P.; Chevary, J. A.; Vosko, S. H.; Jackson, K. A.; Pederson, M. R.; Singh, D. J.; Fiolhais, C., Atoms, molecules, solids, and surfaces: applications of the generalized gradient approximation for exchange and correlation. *Phys. Rev. B* **1992**, *46*, 6671.

28. Perdew, J. P.; Ruzsinszky, A.; Csonka, G. I.; Vydrov, O. A.; Scuseria, G. E.; Constantin, L. A.; Zhou, X.; Burke, K., Restoring the density-gradient expansion for exchange in solids and surfaces. *Phys. Rev. Lett.* **2008**, *100*, 136406.

29. Becke, A. D., Density-functional thermochemistry. III. The role of exact exchange. *J. chem. phys.* **1993**, *98*, 5648-5652.

30. Lee, C.; Yang, W.; Parr, R. G., Development of the colle-salvetti correlation-energy formula into a functional of the electron density. *Phys. Rev. B* **1988**, *37*, 785.

31. Stephens, P.; Devlin, F.; Chabalowski, C.; Frisch, M., Si (111) bond dissociation energy is a local prop. *J. Phys. Chem.* **1994**, *98*, 623.

32. Adamo, C.; Barone, V., Toward Reliable Density functional methods without adjustable parameters: the PBE0 model. *J. Chem. Phys.* **1999**, *110*, 6158-6170.

33. De La Pierre, M.; Bruno, M.; Manfredotti, C.; Nestola, F.; Prencipe, M.; Manfredotti, C., The (100),(111) and (110) surfaces of diamond: an ab initio B3LYP study. *Mol. Phys.* **2014**, *112*, 1030-1039.

34. Civalleri, B.; Casassa, S.; Garrone, E.; Pisani, C.; Ugliengo, P., Quantum mechanical ab initio characterization of a simple periodic model of the silica surface. *J. Phys. Chem. B* **1999**, *103*, 2165-2171.

35. Tosoni, S.; Civalleri, B.; Ugliengo, P., Hydrophobic behavior of dehydroxylated silica surfaces: a B3LYP periodic study. *J. Phys. Chem. C* **2010**, *114*, 19984-19992.

36. Massaro, F. R.; Bruno, M.; Nestola, F., Configurational and energy study of the (100) and (110) surfaces of the $MgAl_2O_4$ spinel by means of quantum mechanical and empirical techniques. *Cryst. Eng. Comm.* **2014**, *16*, 9224-9235.

37. Bruno, M.; Massaro, F.; Prencipe, M.; Demichelis, R.; De La Pierre, M.; Nestola, F., Ab Initio calculations of the main crystal surfaces of forsterite (Mg_2SiO_4): a preliminary study to understand the nature of geochemical processes at the olivine interface. *J. Phys. Chem. C* **2014**, *118*, 2498-2506.

38. Demichelis, R.; Bruno, M.; Massaro, F. R.; Prencipe, M.; De La Pierre, M.; Nestola, F., First-principle modelling of forsterite surface properties: accuracy of methods and basis sets. *J. Comp. Chem.* **2015**, *36*, 1439-1445.

39. Heyd, J.; Peralta, J. E.; Scuseria, G. E.; Martin, R. L., Energy band gaps and lattice parameters evaluated with the heyd-Scuseria-ernzerhof screened hybrid functional. *J. Chem. Phys.* **2005**, *123*, 174101.

40. Perdew, J., 34, 7406.(C) Becke, Ad. *Phys. Rev. A* **1988**, *38*, 3098-3100.

41. Monkhorst, H. J.; Pack, J. D., Special points for brillouin-zone integrations. *Phys. Rev. B* **1976**, *13*, 5188.

42. Civalleri, B.; D'Arco, P.; Orlando, R.; Saunders, V.; Dovesi, R., Hartree–fock geometry optimisation of periodic systems with the crystal code. *Chem. Phys. Lett.* **2001**, *348*, 131-138.

43. Doll, K.; Saunders, V.; Harrison, N., Analytical hartree–fock gradients for periodic systems. *Int. J. Quantum Chem.* **2001**, *82*, 1-13.

44. Doll, K., Implementation of Analytical Hartree–fock gradients for periodic systems. *Comput. Phys. Commun.* **2001**, *137*, 74-88.

45. Pascale, F.; Zicovich-Wilson, C. M.; Lopez Gejo, F.; Civalleri, B.; Orlando, R.; Dovesi, R., The calculation of the vibrational frequencies of crystalline compounds and its implementation in the crystal code. *J. Comput. Chem.* **2004**, *25*, 888-897.

46. Dovesi, R.; Civalleri, B.; Roetti, C.; Saunders, V. R.; Orlando, R., Ab initio quantum simulation in solid state chemistry. *Rev. Comput. Chem*. John Wiley & Sons, Inc.: 2005; pp 1-125.

47. Dovesi, R.; De La Pierre, M.; Ferrari, A. M.; Pascale, F.; Maschio, L.; Zicovich-Wilson, C. M., The IR vibrational properties of six members of the garnet family: a quantum mechanical ab initio study. *Am. Min.* **2011**, *96*, 1787-1798.

48. Demichelis, R.; Raiteri, P.; Gale, J. D.; Dovesi, R., Examining the accuracy of density functional theory for predicting the thermodynamics of water incorporation into minerals: the hydrates of calcium carbonate. *J. Phys. Chem. C* **2013**, *117*, 17814-17823.

49. Engberg, U., B_2O_3 crystals investigated by plane-wave pseudopotential calculations using the generalized-gradient approximation. *Phys. Rev. B* **1997**, *55*, 2824.

50. Huang, L.; Durandurdu, M.; Kieffer, J., New B_2O_3 crystals predicted from concurrent molecular dynamics simulations and first-Principles calculations. *J. Phys. Chem. C* **2007**, *111*, 13712-13720.

51. Brazhkin, V. V.; Katayama, Y.; Inamura, Y.; Kondrin, M. V.; Lyapin, A. G. e.; Popova, S. V.; Voloshin, R. N., Structural transformations in liquid, crystalline, and glassy B_2O_3 under high pressure. *J. Exp. Theor. Phys. Lett.* **2003**, *78*, 393-397.

CHAPTER 6

Probing the Chemical Reactivity of the B_2O_3 -I (101) Surface: Interaction with H_2O and H_2S

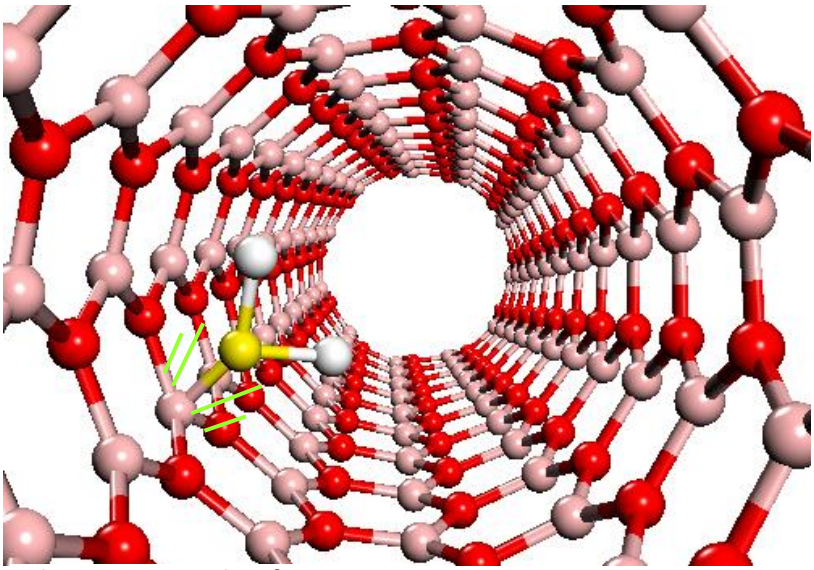

B_2O_3 as coating in H_2S oxidation process.

Beside the ease of the adsorption of H_2S molecule on B_2O_3 surface, it needs an activation energy of 76 kJ/mol to desorb the molecule from the surface which all taking into account of inhibiting H_2S oxidation process.

6.1 Introduction

Diboron oxide is an important metalloid oxide widely used in ceramic and glass technologies, enamels, alloys, fluxes, and as an inhibitor of chemical reactions.[1-6] In addition, it plays a key role from a solid state physical point of view owing to its optical characteristic.[7] Boron oxide has the advantage of being fire retardant in engineering plastics (i.e. polystyrene) owing to its extreme hardness, high refraction index, and low thermal expansion.[8-11] Despite the aforementioned technological importance of B_2O_3, there remains a paucity of studies that have investigated its structural and electronic configurations, and its inhibition characterisation.

B_2O_3 exists in two distinct crystallographic forms over a wide range of operational pressures and temperatures. This includes B_2O_3-I[12] at normal pressure and B_2O_3-II[13-14] at elevated pressures above 65 Kbar.[15] The existing accounts[16] fail to resolve the contradiction between the structure of the B_2O_3 surfaces and the chemical inertness of this compound. In Chapter 5, we performed a comprehensive investigation on selected low-index (*hkl*) surfaces of B_2O_3-I. We successfully identified new low energy surface structures, providing significant connections to the inertness of B_2O_3 and the structure of its vitreous form.

As an important inhibitor, diboron trioxide has been extensively used as unreactive coating material for the walls of chemical reactors. For instance, experimental investigations of H_2 and hydrocarbon oxidation processes indicated that the boric acid coating exhibits an inert effect on the decomposition of peroxy species.[17-20] Similar to these observations, Zhou et al.[21] investigated the use of B_2O_3 as a coating in H_2, S_2, and H_2S systems, respectively. The authors developed a detailed mechanism for H_2S oxidation in lean fuel conditions. They attempted to draw fine distinctions between H_2S oxidation in an uncoated silica reactor and analogue

reactions in a B_2O_3-coated silica reactor, showing that the oxidation process in the coated reactor is considerably less reactive than the uncoated one. Most importantly, the inhibition mechanism of diboron trioxide in this process is poorly understood, leading to uncertainties in determining the precise function of B_2O_3 in the system.

Having discussed the inert functionalities of B_2O_3, it is interesting to clarify the hygroscopic nature of this material. Diboron trioxide remains important to a wide range of scientific and industrial processes. Earlier experimental data[22] explored the behaviour of self-lubricating films of boric acid generated at the surface of materials rich in boron (i.e. vanadium diboride VB_2). Heating of such materials leads to the formation of diboron trioxide films as a result of the interaction of boron with an oxygen molecule.[23-24] During cooling, the B_2O_3 film spontaneously interacts with environmental moisture, forming a layered solid lubricant film, H_3BO_3, which exhibits a self-lubricating behavior.[23, 25-26]

$$4B + 3O_2 \rightarrow 2B_2O_3 \qquad \text{R6.1}$$

(ΔH_{298} = 1271.6 kJ/mol)[27]

$$^1/_2\ B_2O_3 + {}^3/_2\ H_2O \rightarrow H_3BO_3 \qquad \text{R6.2}$$

(ΔH_{298} = -28.84 kJ/mol)[11]

Owing to the high heating output of theses process, materials rich in boron can be used as fuels, especially in devices that use water as an oxidiser, as well as energy increasing admixtures to fuels (i.e. hydrocarbon fuels).[28-29]

Moreover, the airbreathing propulsion system is one of the most important scenarios where diboron trioxide and boric acid exist undesirably. Boron, as a unique element with a high gravimetric and volumetric heat value, serves as fuel in airbreathing propulsion systems. However, the use of boron in such processing may be linked to performance problems. For instance, the formation of both diboron trioxide and boric acid on the surface of boron increases the viscosity and accordingly complicates the propellant processing, ignition, and combustion qualities.[30-34] Thus far, a number of studies have attempted to inhibit the surface oxidation of boron either by use of surface passivating agents such as hydroxyl amine[35] and ceramic B_4C[36] or by employing coating agents.[37-38] In contrast, the formation of H_3BO_3 on the oxidised layer during the sliding test, as another scenario, has received considerable critical attention owing to the shear capability of the boric acid, which is generally considered as a factor strongly related the unique crystal structure of H_3BO_3.[39-47]

To summarise, the interaction of B_2O_3 with water molecules occurs in two stages, the formation of metaboric (HBO_2), followed by the formation of orthoboric (H_3BO_3).[48] However, heating can reversibly remove the water molecules on the B_2O_3 surfaces. The surface loses part of the water and forms HBO_2 at approximately 403.15 K and is completely dehydrated at approximately 523.15 K.[49-50]

$$B_2O_3 + H_2O \rightarrow HBO_2 \qquad \text{R6.3}$$

$$HBO_2 + H_2O \rightarrow H_3BO_3 \qquad \text{R6.4}$$

Addressing the adsorption and subsequent decomposition of water and H_2S molecules on a clean diboron trioxide surface constitutes a limiting case scenario, which is instrumental in attaining a detailed understanding of the reaction mechanisms governing the unique role of dehydrated B_2O_3 surfaces in the aforementioned H_2S/H_2O circumstances. In this Chapter, we employed DFT to examine the interaction of hydrogen sulphide and water molecules with a clean B_2O_3 -I (101) surface, substantiating the latter experimentally by diffuse reflectance infrared spectroscopy. Our results show that the diboron-trioxide surface is very active toward the molecular adsorption of both H_2S and H_2O molecules. The surface shows high reactivity towards dissociative adsorption of H_2O, whereas it exhibits a noticeable inertness regarding the dissociative adsorption of H_2S. This Chapter begins by describing the computational and experimental methods. Following this, we display a detailed investigation of the molecular and ionic interactions of both molecules over the (101) B_2O_3-I surface, drawing reasonable conclusions from the evaluated kinetic parameters.

6.2 Computational Technique

6.2.1 First-Principle DFT Settings

The DMol^3 code[51-52] that deploys the generalised gradient approximation of Perdew and Wang (GGA-PW91) is used to calculate the total energy and electronic structures. The performance of the GAA-PW91[53-54] functional in predicting the band gap for bulk B_2O_3-I has been benchmarked against the hybrid functional of B3LYP, PBE0 and PW1PW (Chapter 5), known for their accurate predictions of band gaps.[55-58] However, significant memory requirements prevent calculations of complex surfaces with this functional. We set the space cutoff to 3.4 Å and sampled the surface Brillouin zones (SBZ) on a 4×4×1 mesh of **k**-points generated by the

Monkhorst-Pack scheme.[59] Test calculations using 4.1 Å for the space cutoff and a mesh of 5×5×1 **k**-point changed the total energy by a few meV. A vacuum of 30 Å in length separated adjacent slabs in the z-direction.

The modelled (101) B_2O_3-I surface consists of vacuum-terminated symmetric slabs within 1×1 surface unit cells. The relaxation of the slabs proceeds until the total energy and forces on each atom converge with tolerances greater than 10^{-8} Ha and 10^{-5} Ha/Å, respectively.

6.2.2 Theoretical Thermodynamic and Kinetic Analysis

We estimate average binding energies for on-surface adsorption (E_b) using the following formula:

$$E_b = E_{slab+H_2X} - E_{slab} - E_{H_2X} \quad (6.1)$$

where E_{slab+H_2X}, E_{slab}, and E_{H_2X} denote the energies of a H_2X/B_2O_3 system (where X represents the chalcogen elements, i.e. S in hydrogen sulphide structures and O in water molecules), the clean B_2O_3-I (101) surface, and an isolated H_2X molecule, respectively.

Transition state calculations are investigated using the complete LST/QST method. Reaction rate constants are fitted to the Arrhenius equation (i.e. $k(T) = A \exp(-E_a/RT)$) in the temperature range of 298.15 to 1000 K, according to the classical transition state theory (TST)[60]:

$$k(T) = \frac{k_B T}{\sigma_e h} \exp\left(\frac{\Delta S^{\neq}}{R}\right) \exp\left(\frac{-\Delta H^{\neq}}{RT}\right) \qquad 6.2$$

where: k_B is Boltzmann's constant, h signifies Plank's constant, and R is the universal gas constant. $\Delta S^{\neq}$ and $\Delta H^{\neq}$ represent the entropy and enthalpy of activation, respectively, at a certain temperatures T, and σ_e is the reaction degeneracy number.

6.3 Experimental

6.3.1 Sample Preparation

We performed water adsorption and desorption experiments using B_2O_3 surface purchased from Sigma-Aldrich (Boric anhydride, 99.98 % trace metals basis) without further purification. PIKE Technologies supplied potassium bromide powder (KBr, 100 %), serving as spectroscopically pure matrix to dilute B_2O_3 samples. We set the dilution ratio to 2 % (w/w) by weighing 0.020 g of B_20_3 and 0.980 g of KBr directly into a small mortar. We applied a two-stage process to enhance the particle size consistency based on breaking larger agglomerates with a pestle, and vortex mixing (VELP F202A0175) at a maximum stirring rate for approximately 120 s inside a Pyrex test tube. A portion of the 0.050 g of unified mixture was then transferred directly into a crucible with a porous base to enable all sampling modes, including the use of reaction gases. We supplemented the loading process by setting a sample surface at 1 mm lower than the top face of the crucible by using a sample-press stick.

6.3.2 Apparatus and Method

Figure 6.1 illustrates the experimental setup for diffuse reflectance infrared Fourier transform (DRIFT) spectroscopy. We performed spectral measurements using an Agilent Cary 670 FTIR spectrometer coupled with DiffusIR accessory (041-60XX) assembled by PIKE Technologies. We supplied dry air purge gas to the spectrometer enclosure and the optical housing of the diffuse reflectance instrument to eliminate water vapour interference from the spectral measurements. The optical components of 041-60XX were gold-coated for highest reflectance in the mid-IR spectral region. This device was further equipped with a variable temperature cell within which the sample could be heated from room temperature to 1273.15 K under the achievable vacuum of 13×10^{-4} Pa. The heat chamber has a wide sampling area that allows the use of a large capacity heater with an opening for a ceramic sample cup with a porous base for gas permeation. The screw cap of the heating chamber contained the zinc selenide (ZnSe) window, selected because of its low absorptivity at infrared wavelengths and high resistance to thermal shock. Furthermore, the window acts as a mechanical barrier to conduct the experiment under steady conditions and prevent products of the reaction from damaging the optical parts of the DiffusIR accessory. The enclosed design coupled with a larger 1/8 inch gas tubing lines enables thermal experiments under various gaseous atmospheres. We eliminated overheating of the stainless-steel structure and ZnSe window by connecting a coolant line (water fed by a mini peristaltic pump head at 1 cm^3/s). We controlled the heating rate using a resistively heated temperature module from PIKE Technologies (076-2450) using TempPRO software, which is capable of setting and monitoring isothermal or multi-ramped temperature profiles.

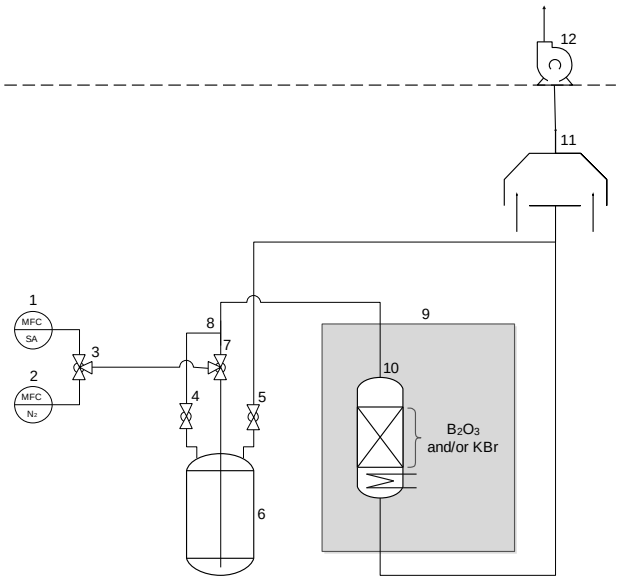

1, 2	Brooks 4800 Series Elastomer Sealed Thermal Mass Flow Controllers, Model 4850; 1: Synthetic Air (0-5 mL/s); 2: Nitrogen (0-25 mL/s)
3, 7	B1V3H 4T S316 (1/4"T 112 Series (3way) Ball Valve)
4, 5	B1VH 4T S316 (1/4"T 112 Series (2way) Ball Valve)
4	OMEGA FGR Rope Heater FGR-030 coupled with OMEGA Temperature process controller CN142
5	1/2"T Union Tee CTA 8 S316 + 1/8"T x 1/2"T Reducers CR 2- 8 S316
6	Stainless Steel 316L vessel - custom made, total volume 1000 mL
8	CLA 4 S316 (1/4"T Union Elbow) + CTA 4 S316 (1/4"T Union Tee) + CUR 4- 2 S316 (1/4"T x 1/8"T Reducing Union)
9	Agilent Cary 670 FTIR Spectrometer
10	DiffusIR Accessory with Gold-Coated Optics (041-60XX) + DiffusIR Environmental Chamber (HTV), ambient to 1000 °C (162-4200) + PC Controlled Temperature Module, HTV Chambers (076-2450)
11	Exhaust hood
12	Ventilation fan
Tubing	Stainless Steel 316L Seamless Round Tubing: 1/8" or 1/4" PTFE Tubing: O.D. x I.D. 1/4" x 3/16"

Figure 6.1. Experimental set-up for diffuse reflection measurements of H_2O adsorption/desorption on the B_2O_3 surface.

After inserting the environmental chamber into the DiffusIR accessory, we connected a stream of nitrogen (N_2, 99.9995 %) or synthetic air (20.5 % oxygen in nitrogen, Zero Grade). We did not attach a simultaneous vacuum line to the outlet of the chamber as implemented in the studies of Christy and Nodland.[61] Instead, we used a substantially higher flow rate, which was set to 3.3 mL/s by the elastomer sealed thermal mass flow controller from Brooks (4800 Series). Passing the gas through the chamber under these conditions prevents the accumulation of pyrolysis-derived products, especially in the form of condensation on the internal surface of the ZnSe window. In contrast, the inert N_2 served as a carrier gas for H_2O vapour during adsorption studies. $H_2O_{(vap.)}$ was introduced into the system by purging N_2 through a stainless-steel scrubber (total volume 1000 mL) filled with 300 mL of H_2O (ultra-high purity, Sartorius Arium Pro UV/DI system). The N_2-$H_2O_{(vap.)}$ saturated stream assembly was designed to facilitate instantaneous switching between gases by fitting a three-way valve within the lid of the vessel.

We predefined all temperature profiles using the TempPRO software interface, which allows the entry of a maximum of 20 set points in the ramp and soaking mode. Prior to each experiment run, we performed a calcination of sample using a segment of rapid heating with ramp rate of 1.6 K/s, and then holding it isothermally at 823.15 K for 900 s to eliminate H_2O and remaining impurities from previous runs. The main H_2O adsorption/desorption trials were conducted in two consecutive stages: isothermal at 303.15 K with a soak time of 5400 s, preceded by manual stabilization at 303.15 K for 600 s; and dynamic with three different heating rates of 0.04, 0.08, and 0.17 K/s, reaching the set point of 773.15 K. Data collection occurred at specific programmed timed set points (60 s intervals) from the TempPRO software. We set up the triggering method by coupling IR bench through the Agilent's Resolutions Pro software within the Spectrometer tab of the TempPRO interface. The spectrum collection method was automated to ensure that all experimental conditions remained steady and replicable. For each B_2O_3 spectrum, we collected two additional, parallel spectra: background (KBr purged with N_2) and blank (KBr purged with N_2 saturated with H_2O vapour), both measured under the same conditions and temperature profiles. We adopted this approach as a standard procedure to ratio out any water adsorbed on KBr from the final spectrum owing to its hygroscopic nature, and to compensate for the temperature-based deviations in the background spectrum. The collection method was based on a 4 cm^{-1} spectral resolution over the range of 6000–700 cm^{-1} owing to the limitation of the nominal range of a liquid nitrogen cooled MCT detector. We added 25 scans using symmetric interferograms at each sampling interval to maximise the quantitative accuracy. The optical throughput was set at 50% to prevent overflowing or saturating of the detector. We performed a separate routine alignment for the spectrometer (weekly basis) and the DiffusIR accessory (before each run) to maximize the throughput energy.

The reflectance spectra assumed Kubelka-Munk transformation to compensate for weak peak intensities at high wavenumbers and rounded line shapes. This transformation enabled us to create a true linear relationship for spectral intensity and sample concentration. Each sample and blank spectrum was reprocessed to express it as a ratio of the corresponding single beam background spectrum. Analogically, we used the blank spectrum as a subtrahend for the subtraction process (subtraction factor = 1). Further transformation included linear baseline correction and the moving of all existing baseline points vertically to the actual value of the sample original spectrum. Each spectrum was then assigned a broad peak of the following specification for the integration of the O-H bands: centre (extreme in region) left limit 3800 cm^{-1}, right limit 2700 cm^{-1}; left edge (at point) 3800 cm^{-1}; right edge (at point) 2700 cm^{-1}; and left and right baseline (at point) 3800 cm^{-1}. We applied these results as an input data to the Excel spreadsheet to calculate the fractions reacted and plot the H_2O adsorption/desorption profiles. These processed results were subsequently treated for kinetic analysis.

6.3.3 Desorption Kinetics

In solid-state reactions, the reaction rate can be described in terms of three main variables: temperature *T*, extent of conversion α (already defined), and pressure *P*, according to the following equation:

$$\frac{d\alpha}{dt} = k(T)f(\alpha)h(P) \qquad 6.3$$

Ignoring the pressure dependence $h(P)$, the process rate depends on the temperature function $k(T)$ and the conversion parameter $f(\alpha)$, otherwise termed the reaction model. The application of the isoconversional principle[61] provides the model-free activation energy as a function of the conversion α. This calculation relies on the advanced isoconversional method of Vyazovkin[62-63] (Eq. 6.4) that provides an accurate estimation of activation energy values from the temperature integral, in contrast to the Lyon,[64] Kissinger-Akahira-Sunose,[65] and Starink's[66] approximate approaches. For a series of runs performed at different heating rates, the appropriate activation energy value minimises the following function:

$$\emptyset(E_\alpha) = \sum_{i=1}^{n} \sum_{j \neq i}^{n} \frac{I(E_\alpha, T_{\alpha,i})\beta_j}{I(E_\alpha, T_{\alpha,j})\beta_i} \qquad 6.4$$

We experimented with three temperature ramps (0.04, 0.08, and 0.17 K/s), repeating each run twice. The activation energy can be estimated at any particular value of α by finding E_α for which the function attains a global minimum. The subscripts i and j represent the integer numbers of different experiments performed under varying heating programs, and $I(E,T)$ denotes the Arrhenius temperature integral, as shown in Eq. 6.5:

$$I(E_\alpha, T_\alpha) = \int_{T_{\alpha-\Delta\alpha}}^{T_\alpha} \exp\left(-\frac{E}{RT}\right) dT \qquad 6.5$$

in which α varies from $2\Delta\alpha$ to $1\text{-}\Delta\alpha$, with a step of $\Delta\alpha = (m+1)^{-1}$, and m defines the number of equidistant values of α selected for the analysis. We applied the fourth-order Senum and Yang approximation[67] for the integral function, and minimised Eq. 6.7 by employing the solver tool

in Microsoft Excel. The minimisation task was repeated for each value of α to obtain the dependency of E_α on α.

6.4 Results and Discussion

6.4.1 Bulk Properties

Figure 6.2 illustrates the optimised atomic configuration of the primitive unit cell of B_2O_3-I, consisting of nine atoms of O and six atoms of B. The configuration represents a hexagonal structure of a space group of $P3_121$ (152).[14, 68] Table 6.1 enlists calculated lattice parameters (a and c), bulk modulus (B), band gap energy (E^{gap}), and B-O bond lengths of bulk B_2O_3-I. The obtained values agree with well with both with the experimental measurement and the theoretical data of previous investigators.[14, 68-73]

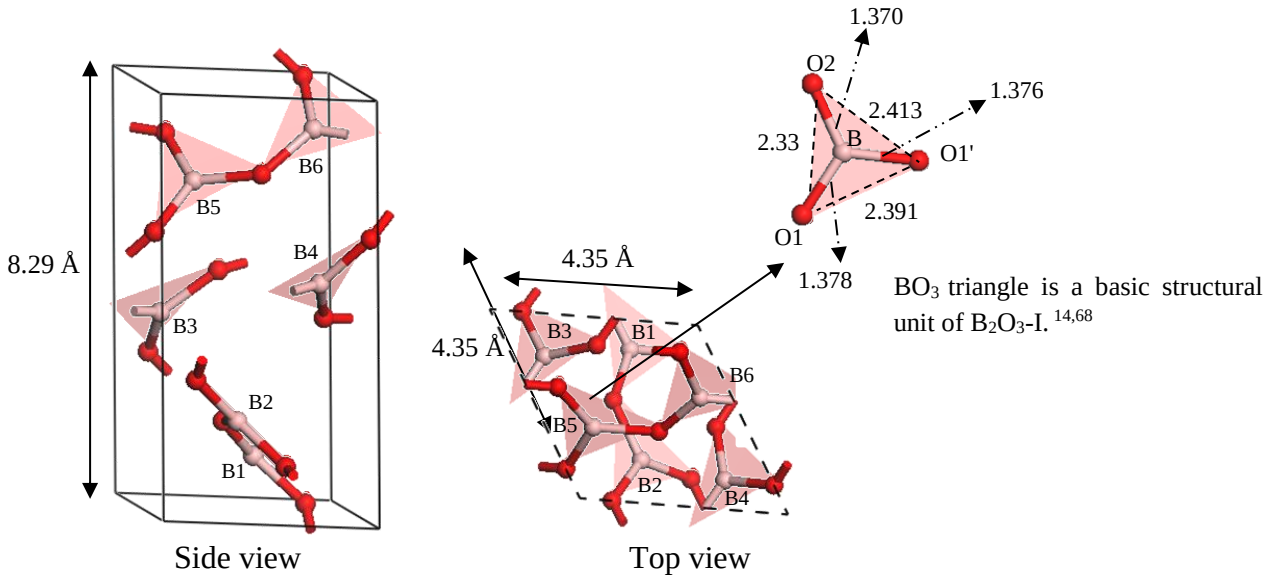

Figure 6.2. Primitive unit cell of bulk B_2O_3-I (top and side view). Red and light pink spheres represent oxygen and boron atoms, respectively.

Figure 6.2 also elucidates the three-dimensional networks of the planar triangles of BO_3,[12, 14] with all B atoms having equivalent planar coordination sites, whereas the O atoms located at the corners of the triangles occupy two non-equivalent positions.[14, 68] The latter results in two different B-O bond lengths in the bulk structure. Figure 6.3 shows the relationship between the total system energy and the volume of the unit cell, fitted to the Murnaghan[74] equation of state. Based on these results, our estimated bulk modulus at 0 K of 58 GPa coincides well with the experimental and prior theoretical values quoted in Table 6.1.

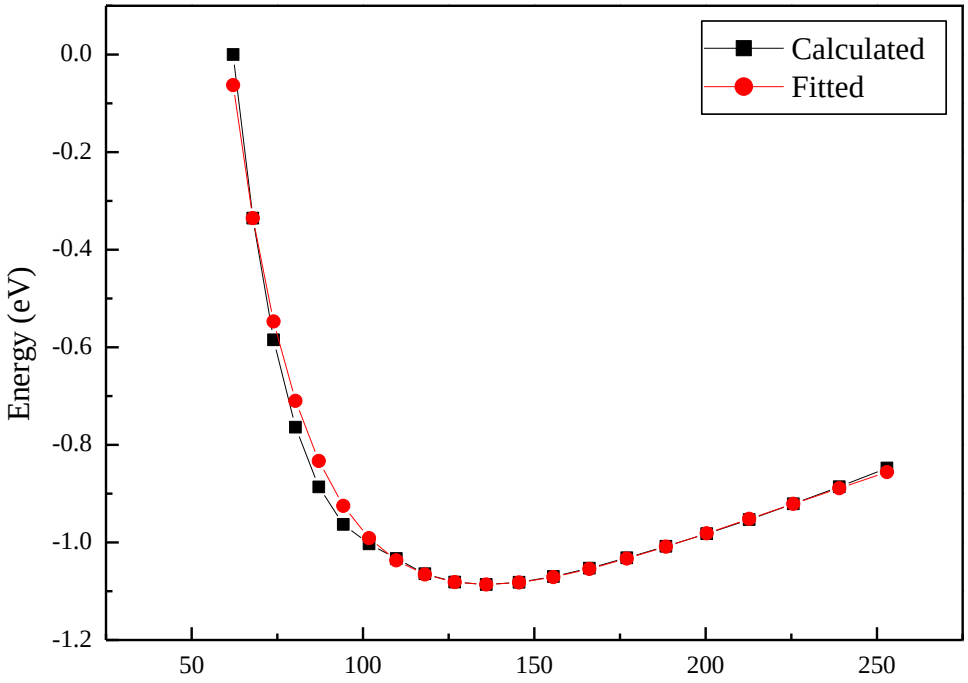

Figure 6.3. Calculated total energy versus volume for bulk B_2O_3-I.

Table 6.1. Calculated structural properties of bulk B_2O_3–I. General position of O1 is other than x,y,z: -x+1, -x+y+1,-z+1/3.[14,68]

	Current study	**Our results from hybrid functional**						
					Other results			
Properties	**PW91**	**B3LYP[73]**	**PBE0[73]**	**PW1PW[73]**	**PW91[68]**	**PW1PW[68]**	**B3LYP[68]**	**Exp.**
a/Å	4.35	4.37	4.33	4.33	4.39	4.35	4.36	4.34[14]
c/Å	8.30	8.72	8.37	8.38	8.44	8.39	8.43	8.34[14]
B-O1 /Å	1.38	1.37	1.37	1.37	1.38	1.38	1.39	1.38[14]
B-O1'/Å	1.38	1.37	1.37	1.37	1.38	1.37	1.37	1.37[14]
B-O2 /Å	1.36	1.36	1.36	1.36	1.37	1.37	1.37	1.36[14]
E^{gap}/eV	6.4	8.57	9.21	8.66	6.5, 6.2[69]	9.1	8.8	-
Bulk modulus/GPa	58	-		-	59[70]	56[71]	-	55.0 ± 15.0[72]

Figure 6.4 displays the calculated total density of states and projected DOS on the B and O atoms of bulk B_2O_3-I. The data demonstrate a wide insulating gap of B_2O_3-I. This is consistent with the results reported by Goclon et al.[75] and Bredow and Islam[16] for the V_2O_5 and B_2O_3-I systems, respectively. However, it is well-documented that the E^{gap} values are sensitive to the deployed theoretical method in which plain functionals often underestimate band gaps[76] or even describe metallic behaviour for narrow band insulators, as it is the case in Ce_2O_3.[77] On the contrary, hybrid DFT functionals, such as PW1P1, PBE0 and B3LYP, yield satisfactory agreement with experimental E^{gap} values.[73, 78] Chapter 5, we calculate E^{gap} for a bulk B_2O_3-I of 8.66 eV based on the PW1PW[73] hybrid DFT. As indicated in Table 6.1, the PBE0 value coincides with the results reported by Bredow and Islam[16] using other hybrid functionals (i.e.

PW1PW and B3LYP). Nonetheless, both methodologies (plain DFT and hybrid DFT) share the wide-gap insulating character of bulk B_2O_3-1

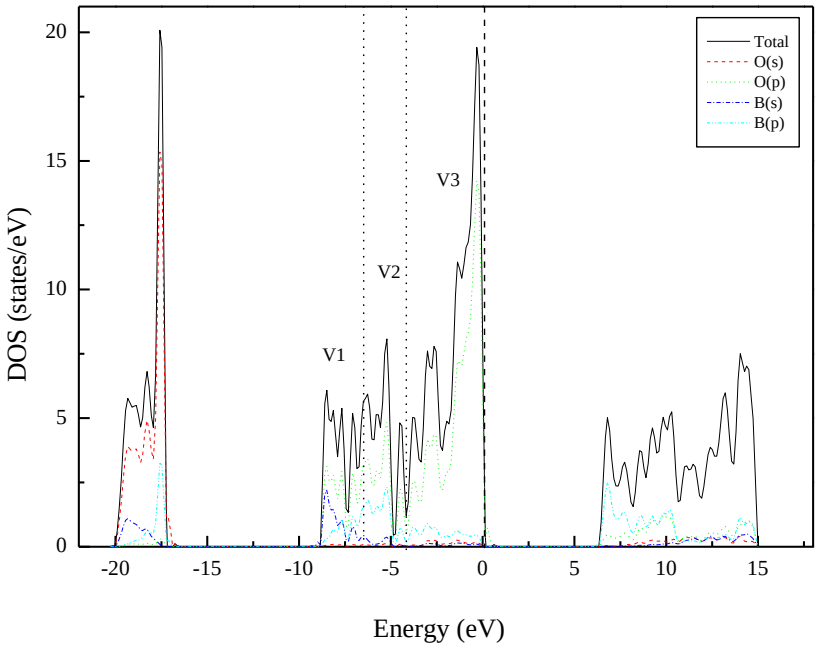

Figure 6.4. Total (DOS) and projected (PDOS) density of stats for bulk B_2O_3-I.

The calculated DOS of bulk B_2O_3-I contains four sub-bands in the valence band. The lower sub-band stretches from -20 to -17 eV and consists mainly of the O(s) orbitals. The upper three sub-bands—V1, V2, and V3—extend from -8.75 eV to the Fermi level. The V1 band consists predominantly of the B(s) and O(p) orbitals; the V2 band combines the B(p) and O(p) states; and the O(p) orbitals dominate the V3 band. The lower energy part of the conduction band (6 to 15 eV) comprises mainly the B(p) orbitals. Figure 6.4 illustrates the DOS spectrum obtained using the GGA-PW91 method. For comparison, Figure 5.2 of Chapter5 depicts the corresponding spectrum for the PW1PW hybrid functional.

6.4.2 Clean B_2O_3 -I (101) Surface

Our results in Chapter 5[73] along with the recent theoretical investigations by Bredow and Islam[16] of the B_2O_3 -I crystalline structure demonstrated the 101 surface as the most energetically stable. Accordingly, we performed the total energy calculations for this surface. Figure 6.5 presents the optimized geometry of the clean B_2O_3 -I (101) surface.

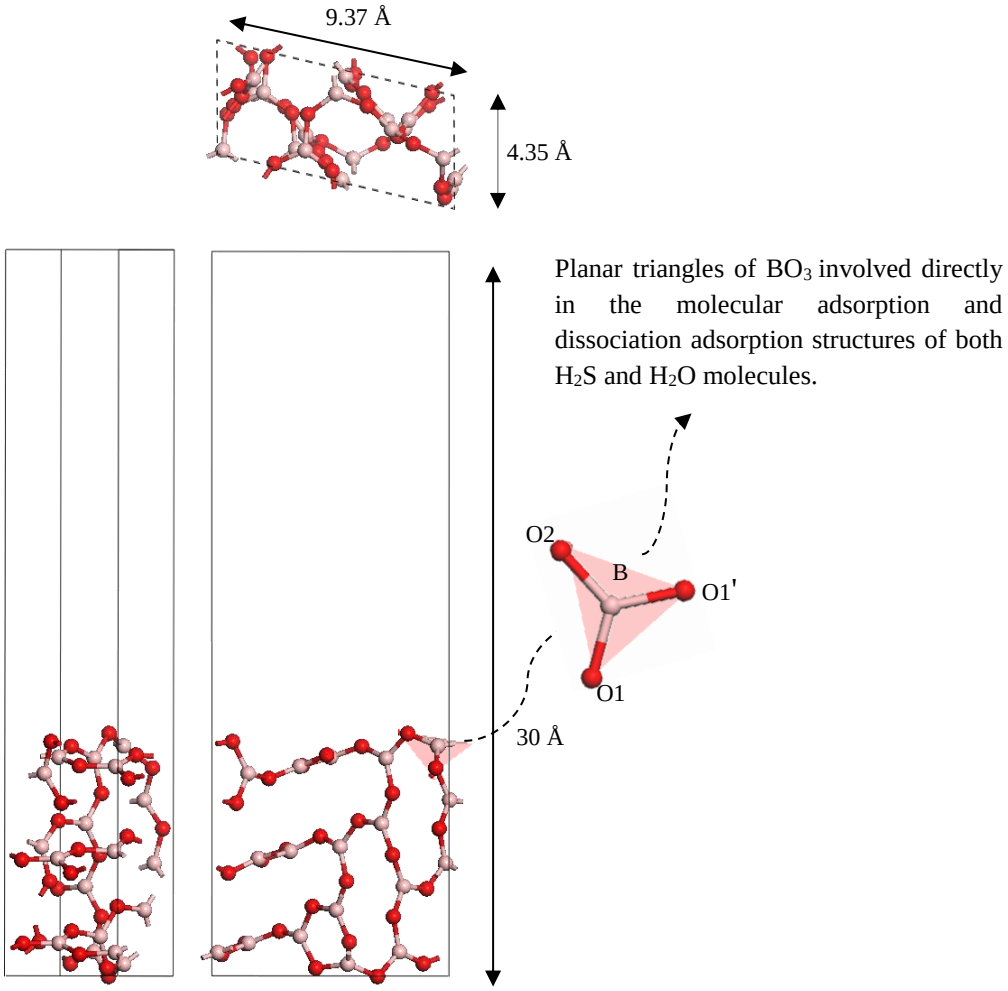

Figure 6.5. Unit cell (with slab and vacuum) employed in the periodic slab calculation for the B_2O_3-I (101) surface.

Table 6.2 lists some of the structural parameters calculated for the optimised B_2O_3 -I (101) surface. We observe that the majority of the geometries of the slab seem similar to the bulk geometry. For example, the bond lengths of the three inequivalent O-O bonds—O1-O2, O1'-O2, and O1'-O1 (see Figure 6.5)—in the slab depart from the corresponding bulk values by only -0.42 %–1.25 % , -1.25 %–0.85 %, and -0.43 %–0.85 %, respectively. Similarly, the surface B-O bonds in the slab deviate by ~0.80 % with respect to those in the bulk. To clarify how the surface geometry changes upon the employed methodology, the surface B-O bond length using the less accurate GAA-PW91 functional (employed in this Chapter) has been benchmarked against the hybrid functional (our results in Chapter 5). A comparison is presented in Table 6.3

Table 6.2. Summary of optimised geometries of the B_2O_3-I (101) surfaces. Bulk distances of B-O1, B-O2, O1-O1′, and O1-O2 are 1.37, 1.38, 2.40, and 2.34 Å, respectively. Figure 6.5 presents the atom labels.

Bond	**surface layer/Å**
B-O1	1.35 - 1.37
B-O2	1.37-1.39
O1-O1'	2.39-2.43
O1-O2	2.33-2.34

Table 6.3. Comparison of optimised geometries of the B_2O_3-I (101) surfaces among two employed methodologies, Hybrid functional and GAA-PW91 functional. Figure 5.6 (Chapter 5) presents the atom labels.

B-O bond	B-O bond length by employing Hybrid functional/Å (Results from Chapter 5)	B-O bond length by employing GAA-PW91 functional/Å (Current Chapter)
B2-O4	1.35	1.37
B2-O1	1.38	1.39
B2-O5	1.38	1.39
B3-O6	1.35	1.35
B3-O4	1.37	1.38
B3-O7	1.38	1.39

6.4.3 Molecular Adsorption

We studied the adsorption of hydrogen sulphide and water molecules on the B_2O_3 -I (101) surface in several initial configurations. These configurations comprise the physisorbed interaction of the H_2S/H_2O molecule with the B_2O_3-I (101) surface, where the molecule associated with the surface via hydrogen bonding between the hydrogen atom of the molecule and the nearest oxygen atom of the surface with a distance of 2.12-3.19 Å. . Figure 6.6 displays the optimised configuration of the physisorbed interaction of hydrogen sulphide and the water molecule over the B_2O_3 -I (101) surface.

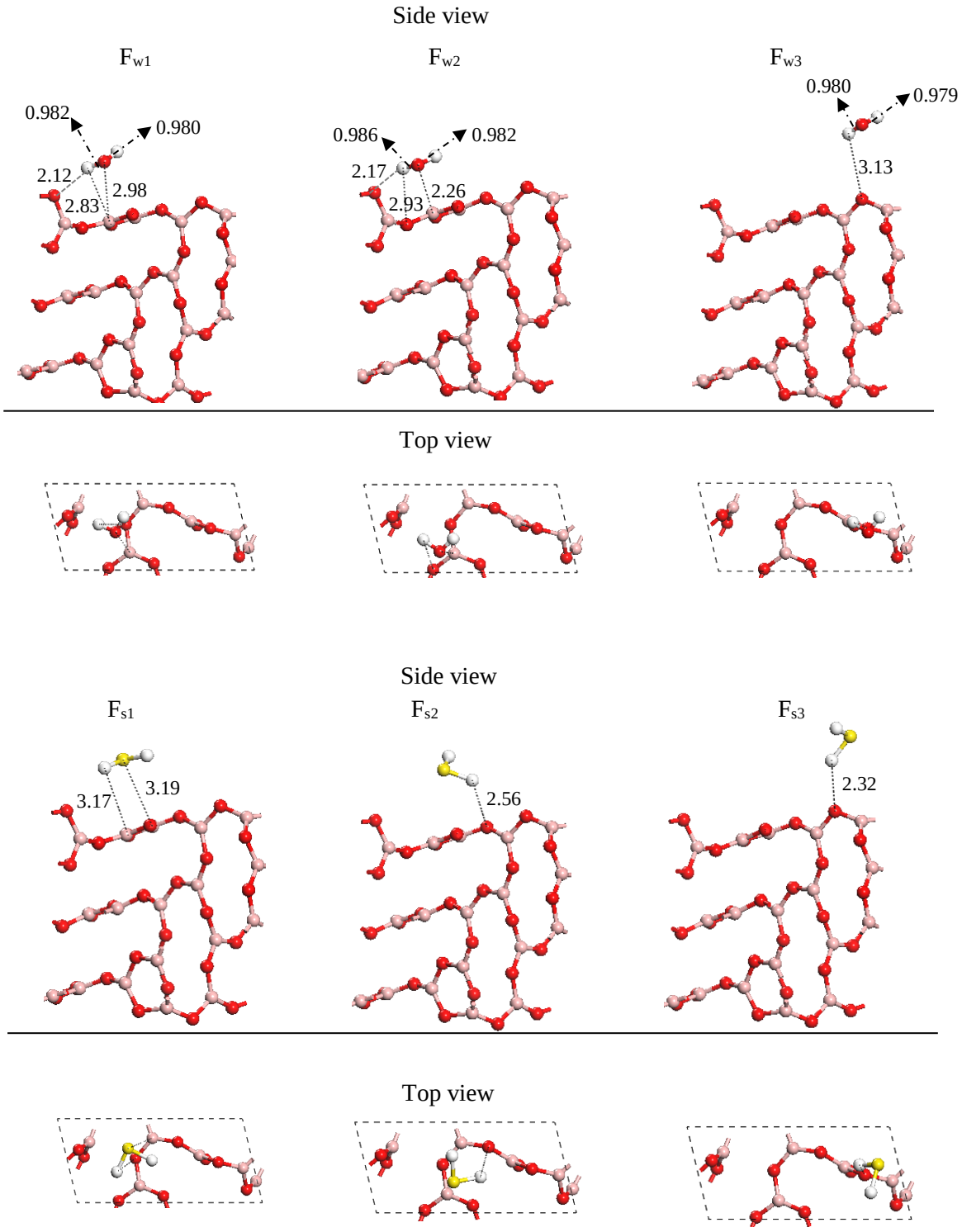

Figure 6.6. Top and side views of the stable geometries induced by molecular hydrogen sulphide and water physisorbed on B_2O_3-I (101) configurations. Distances are in Å. Yellow spheres represent sulphur atoms.

Table 6.4 summarises the calculated binding energy, X-H bond distance (where X represents the chalcogen elements, i.e. S in hydrogen sulphide structures and O in water molecules), and the distance between the hydrogen atom of the H_2X molecule and the nearest oxygen atom of the surface. Calculated binding energies for the hydrogen sulphide structures, F_{s1}, F_{s2}, and F_{s3}, are predicted to be -40, -43, and -25 kJ/mol, respectively. In contrast, the calculated binding energies for the water molecule, F_{w1}, F_{w2}, and F_{w3} are calculated to be -77, -80, and -54 kJ/mol, respectively. All values reveal a weak interaction between the hydrogen sulphide/water molecules and the B_2O_3 -I (101) surface. Moreover, we observe that the X-H bond lengths in the physisorbed interaction correspond closely to the values calculated in the gas phase H_2S and H_2O molecule (1.363 Å and 0.979 Å, respectively).

Table 6.4. Binding energies and geometric parameters for molecular H_2X physisorbed on a clean B_2O_3-I (101) surface. X represents S (sulphur) in $F_{s1,}$ $F_{s2,}$ and F_{s3} , and O (oxygen) in $F_{w1,}$ $F_{w2,}$ and F_{w3}, respectively.

Structure	**H_2X - surface interaction distance (nearest distance) (Å)**	**X-H bond distances (Å)**	**Binding energy (kJ/mol)**
F_{w1}	2.12	0.98/0.98	-77
F_{w2}	2.17	0.99/0.98	-80
F_{w3}	3.13	0.98/0.98	-54
F_{s1}	3.17	1.36/ 1.36	-40
F_{s2}	2.56	1.36/ 1.37	-43
F_{s3}	2.32	1.36/ 1.37	-25

What follows is an account of the crystallographic structure of B_2O_3-I. The structure with a three triangular- planar bonds of boron and oxygen, where the oxidation number of boron is (+3), is resulted from the sp^2 hybridization. A primary concern of the low-energy fourth orbital of the boron valence shell leads to an understanding of the transformation of the coordination number of boron which is mainly responsible for the Lewis acid properties of B_2O_3-I. The acceptance of an electron pair into this orbital results in sp^3 hybridization, and therefore the formation of fourfold tetrahedral coordination.[79] In this aspect, both the hydrogen sulphide molecule and the water molecule donate electrons from their lone pair orbital to the surface boron atom. This results in stable optimised structures of M_s and M_w with calculated binding energies of -129 and -172 kJ/mol, respectively. The stable optimised geometries of both molecules adsorbed on the surface are shown in Figure 6.7.

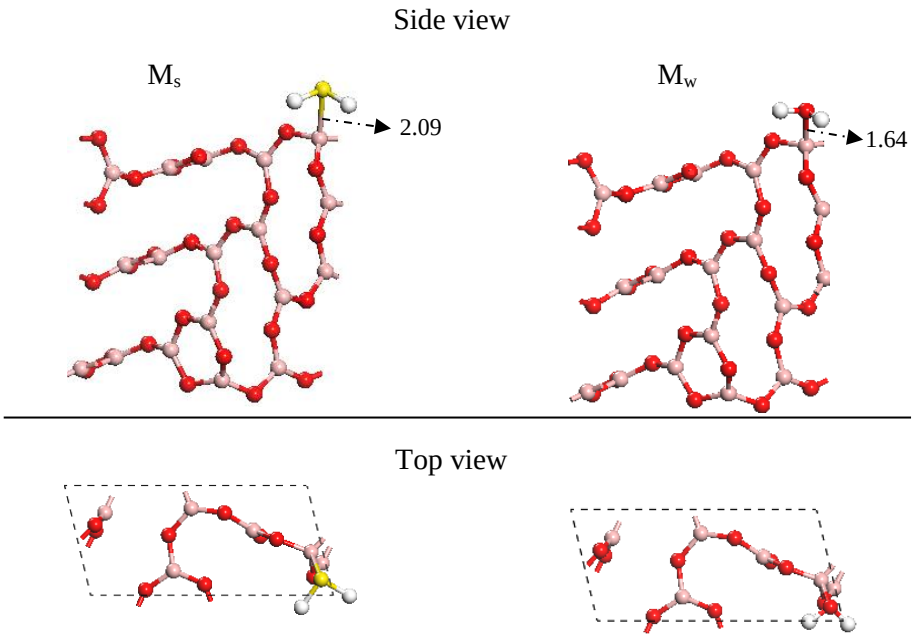

Figure 6.7. Molecular adsorption of H_2S and H_2O over the B_2O_3 -I (101) surface.

The formation of the two products M_s and M_w are found to be highly exothermic without having to overcome an energy barrier. Two concluding remarks can be drawn from this finding. First, as expected, the B_2O_3 -I (101) surface display highly hygroscopic behaviour. This has been confirmed experimentally in the literature.[80-81] Moreover, this observation concurs with those reported by Slutskii et al.[49] in their ab initio study of reactions in the $H_3BO_3/B_2O_3/H_2O$ system. The authors found that the interaction of water with diboron trioxide proceeded without an activation energy. The second important finding is that the zero energy barrier of the molecular adsorption of H_2S over the B_2O_3 -I (101) surface may explain the inhibition characterisation of B_2O_3 in the H_2S oxidation process. Herein, the H_2S molecule adsorbs easily over the B_2O_3 surface and accordingly prefers to link itself with the B_2O_3 surface rather than to interact with O_2, leading to inhibition of the oxidation process.

Furthermore, by employing classical transition state theory, desorption of the adsorbed H_2X molecules into the vacuum was found to be endothermic with an energy barrier of 76 kJ/mol and 124 kJ/mol for H_2S and H_2O, respectively. Potential energy diagram for H_2X molecule removal along with the one corresponding to molecular adsorption is presented in Figure 6.9. These results provide further support for the hypothesis that the B_2O_3 coating inhibits the oxidation process. Thus, besides the ease of the adsorption of the H_2S molecule on the B_2O_3 surface, it requires an activation energy to desorb the molecule from the surface, which takes into account the inhibition of the oxidation process. Together, these results provide important insights into the exact role of B_2O_3 in such processes, which cannot be determined by experiment.

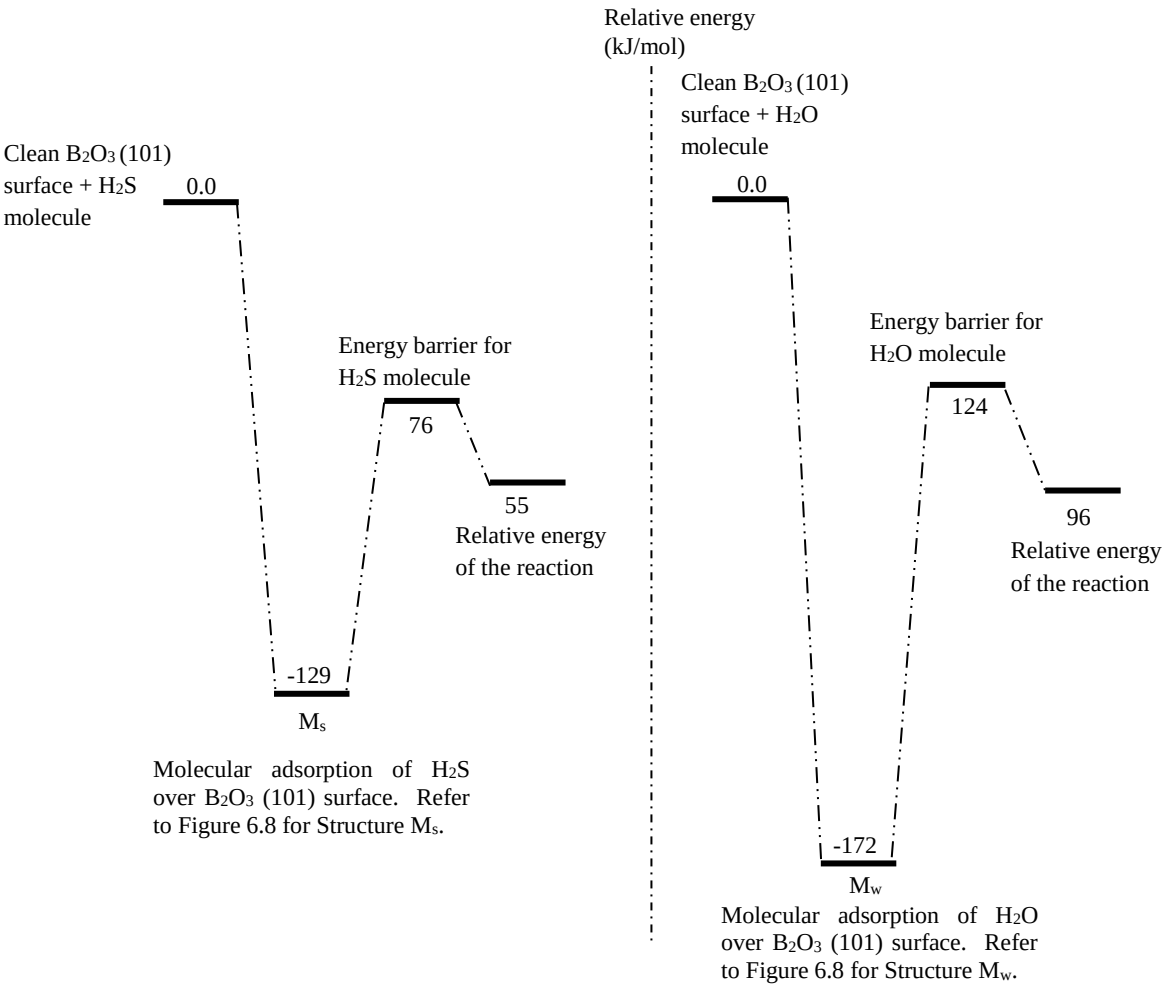

Figure 6.8. Potential energy diagram for H_2X molecule removal. Values (in kJ/mol) of energies are in reference to physisorbed reactant.

6.4.4 Dissociative Adsorption

In this section, we investigate the chemisorbed (dissociative) adsorption of both hydrogen sulphide and water molecules on the B_2O_3 -I (101) surface. Two pathways are considered, pathway 3 and pathway 4, which result in two different dissociated structures, namely D_s and D_w, with a calculated binding energy of 108 kJ/mol and -155 kJ/mol, respectively. As shown in Figure 6.9, in D_s the dissociated HS adduct attaches itself to the O_{surf} atom and the detached

hydrogen atom bonds with the B_{surf} atom, whereas in the D_w configuration, water molecule dissociate in the opposite way where OH links with the B atom and the detached hydrogen atom bonds with the O_{surf} atom. It is clear that, unlike the water molecule, the dissociation of H_2S over the B_2O_3 -I (101) surface is not favourable.

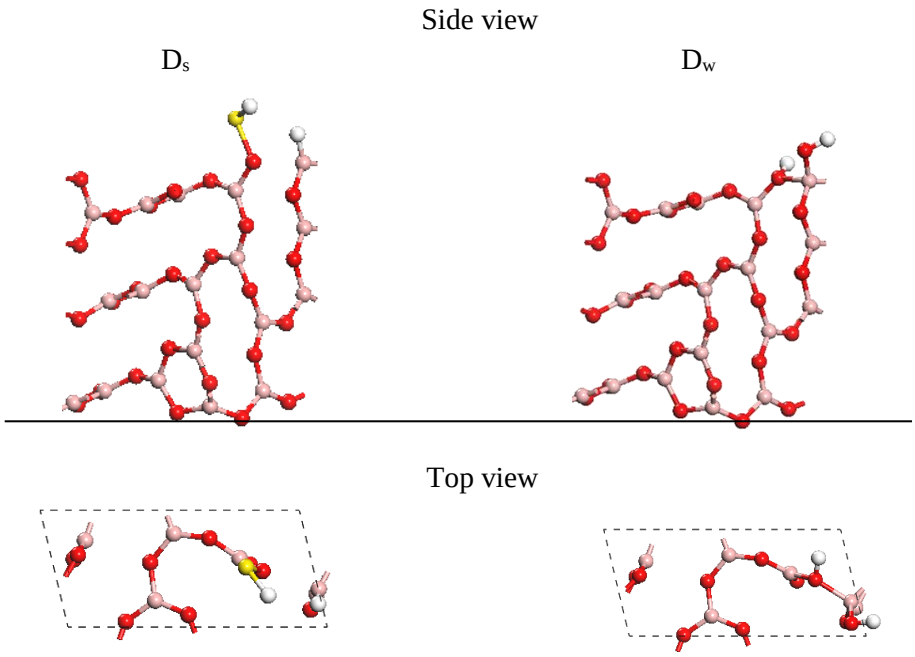

Figure 6.9. Dissociative structures of H_2S and H_2O over the B_2O_3 -I (101) surface.

Table 6.5 lists the binding energies and geometrical features pertinent to the planar triangles of BO_3 involved directly in the molecular adsorption and dissociation adsorption structures of both the H_2S and H_2O molecules. We observe that, to a large extent, molecular adsorption of H_2S and H_2O molecules induce minimal structural change on both the B-O and O-O bonds (i.e. 0.02-0.08 Å) compared to the corresponding value of the clean B_2O_3 -I (101) surface. In contrast, in the dissociative structures, D_s and D_w, structural changes in the B_2O_3 -I (101) surface is considerably larger. For example, the B-O2 values in D_s and D_w depart from the corresponding clean surface values by 1 Å and 0.29 Å, respectively. Importantly, the new

fourth B-O bond lengths of the sp^3 hybridization are very long compared to the sp^2 hybridization bonds (i.e. 2.09Å and 1.64Å both M_s and M_w, respectively).

Table 6.5. Structural changes induced in the molecular and dissociated structures of the interaction of H_2S and H_2O with the B_2O_3 -I (101) surface. Refer to Figures 6.7 and 6.9 for M_s, M_w, D_s, and D_w.

Calculated parameters	**Clean surface**	**M_s**	**M_w**	**D_s**	**D_w**
B-O1/Å	1.396	1.43	1.43	1.40	1.44
B-O1'/Å	1.396	1.47	1.48	1.41	1.46
B-O2/Å	1.372	1.44	1.43	2.37	1.66
B-XH_2/Å (sp^3 hybrids)	-	2.09	1.64	-	-
O1-O2/Å	2.394	2.41	2.42	2.58	2.45
O1-O1'/Å	2.411	2.45	2.46	2.44	2.47
O1'-O2/Å	2.398	2.31	2.39	2.77	2.43
Binding energy/kJ/mol	-	-129	-172	+108	-155

The energy profile for the two reaction pathways is considered. Figure 6.10 displays the optimized structures of the H_2S/H_2O molecule dissociated on the diboron trioxide surface, including the reactant, TS, and the product. Both dissociation paths initiate with the physisorbed state of molecular H_2X (F_{s3} and F_{w1}). Reaction pathway 3 represents the endothermic process with a very high activation energy barrier of 310 kJ/mol whereas pathway 4 appears exceedingly exothermic with a modest activation energy of 39 kJ/mol.

It is apparent from the figure that pathway 4 is not favourable, confirming that the B_2O_3 surface is inert toward dissociation of the H_2S molecule. Another important finding is that the B_2O_3

surface is very active toward the water molecule, not only in the formation of the molecular adsorption of the water molecule, but also in the formation of the dissociative hydroxy groups over the surface.

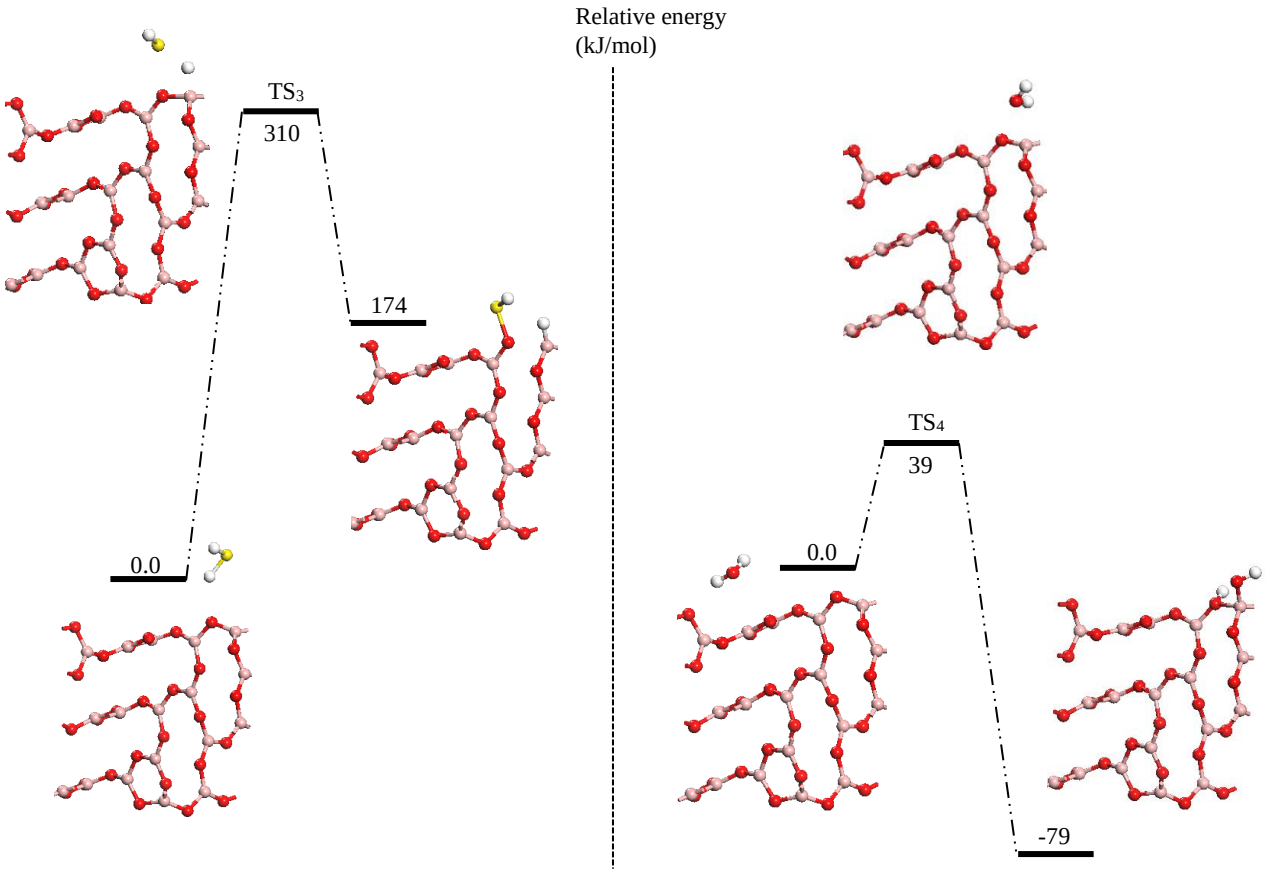

Figure 6.10. Relative energy describing the dissociative adsorption structures of H_2S and H_2O over B_2O_3 -I (101) surface. Pathway 3 and Pathway 4.

Since the dissociation of H_2S over the B_2O_3 surface requires a very high energy barrier and accordingly is not favourable, we explored the desorption calculation for the dissociated water molecule only. The reformation of the water molecule appears to be extremely endothermic with an activation barrier of 127 kJ/mol. Figure 6.11(a) displays the infrared spectral of the fully hydrated and fully dehydrated powdered B_2O_3 sample from the temperature programmed

DRIFT experiments. The shaded region represents the disappearance of broad O-H bands in the range of 3800 – 2700 cm^{-1}. The integral area of these peaks enabled the estimation of fractions reacted, i.e. the conversion as a function of temperature, as shown in Figure 6.11(b), facilitating the evaluation of isoconversional activation energies.

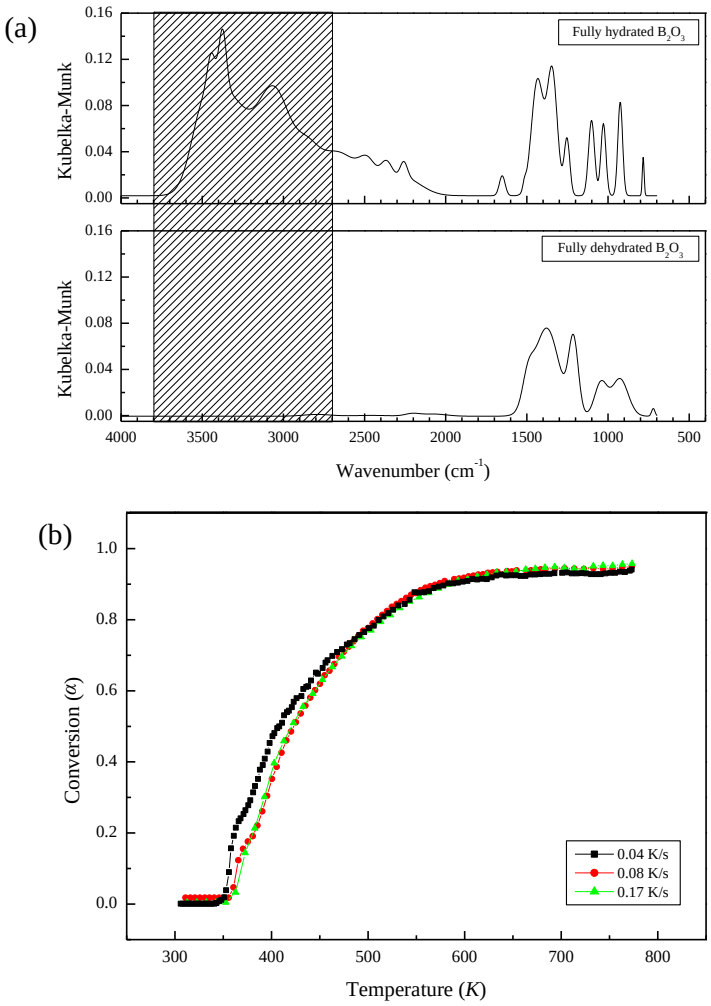

Figure 6.11. (a) Infrared spectral of fully hydrated and fully dehydrated powdered B_2O_3. (b) Fractions reacted as a function of temperature.

Figure 6.12 plots the activation energies for the desorption of adsorbed H_2O and dissociated radicals on the neat B_2O_3 surface. The dependency of activation energies on α triggers evidence

of kinetic complexity. With respect to conversion (α), the trend indicates three remarkable processes. Decreasing activation energy at conversions below 0.2 typify reversible (usually physical) reactions.[82] In the present context, this corresponds to desorption of physically (and molecularly) adsorbed water molecules. Furthermore, the increasing activation energies for conversion values in the range of ca 0.2 – 0.6 represent the competitive desorption of dissociated water species, with the activation energy averaged within the computed value of 127 kJ/mol. The final sharp spike in activation energy can be related to the reluctant desorption of residual OH/H surface-bounded species that are equidistant.

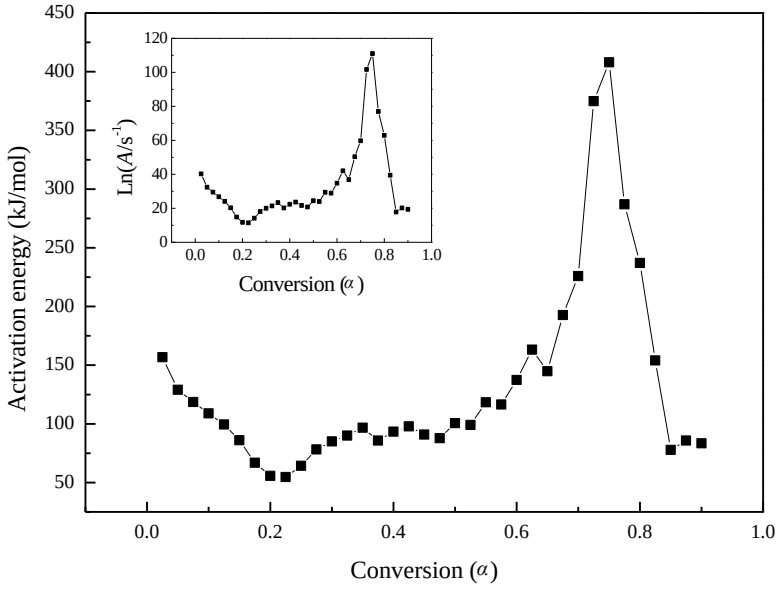

Figure 6.12. Plot of activation energies for desorption of adsorbed H_2O and dissociated radicals on the neat B_2O_3 surface.

6.4.5 Computed Kinetic Parameters

To this end, we implemented a microkinetic analysis of the aforementioned reactions in this Chapter. Figure 6.13 represents the Arrhenius plots and Table 6.6 displays the calculated reaction rate parameters. Reactions pathway 3, which represents the chemisorbed interaction of H_2S n the B_2O_3 -I (101) surface, clearly shows a high activation energy and relatively high dependence on temperature when assisted by the other reactions. Apart from this, the molecular adsorption of H_2S and H_2O and the chemisorbed interaction of H_2O, pathways 1, 2, and 4, are the least dependent on the temperature with lower energy barriers. For the most part, the calculated energy barrier of all reactions are consistent with those presented in Figures 6.8 and 6.10.

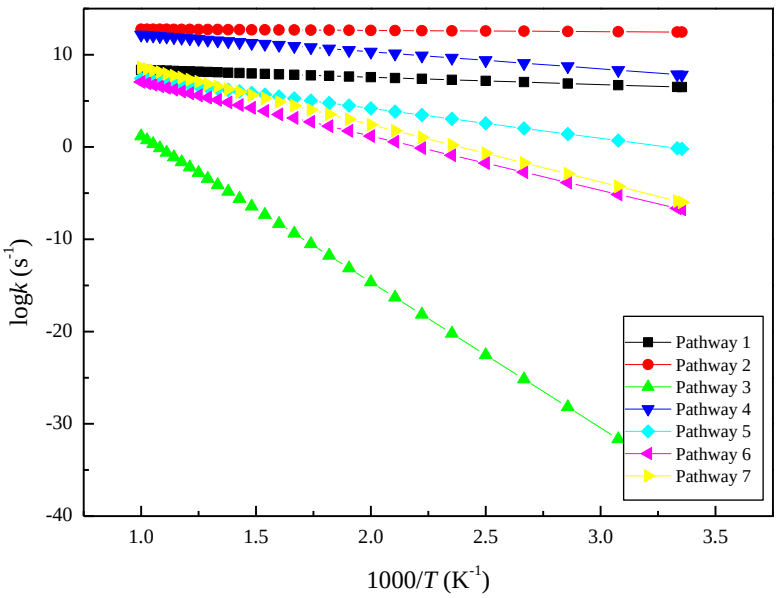

Figure 6.13. Arrhenius plots for the studied reactions. Pathways 1 and 2 correspond to molecular adsorption over the B_2O_3 -I (101) surface; Pathways 3 and 4 represent dissociation

interaction; and Pathways 5, 6, and 7 denote desorption pathways. The exact description of each pathway is presented clearly in Table 6.6.

Table 6.6. Kinetic parameters of reactions with activated complexes.

Reaction	**Description**	***Ea*** **(kJ/mol)**	***A*** **($s^{-}1$)**
Pathway 1	Molecular adsorption of H_2S over B_2O_3 -I (101) surface	15	1.42×10^{9}
Pathway 2	Molecular adsorption of H_2O over B_2O_3 -I (101) surface	3	8.02×10^{12}
Pathway 3	Dissociative (chemisorbed) adsorption of H_2S over B_2O_3 -I (101) surface	302	9.06×10^{16}
Pathway 4	Dissociative adsorption (chemisorbed) of H_2O over B_2O_3 -I (101) surface	35	1.02×10^{14}
Pathway 5	Desorption of H_2S adsorbed molecularly over B_2O_3 -I (101) surface	62	4.52×10^{10}
Pathway 6	Desorption of H_2O adsorbed molecularly over B_2O_3 -I (101) surface	112	8.52×10^{12}
Pathway 7	Desorption of chemisorbed H_2O over B_2O_3 -I (101) surface	121	6.61×10^{14}

6.5 Conclusions

In this Chapter, we confirmed the hygroscopic nature of diboron trioxide and its inhibition characteristics, e.g. towards H_2S. First, we showed that the calculated structural and electronic properties of bulk B_2O_3-I agree with published data. Second, we performed a detailed investigation on the interaction of H_2O and H_2S with B_2O_3 -I (101). For the hygroscopic nature

of diboron trioxide, we demonstrated that the water molecule adapts molecular adsorption and dissociative adsorption on B_2O_3 -I (101) surface with an activation energy of zero and 39 kJ/mol, respectively. This was followed by an investigation into the inhibition characterisation of diboron trioxide. One of the more significant findings to emerge from this study is that the current finding of the interaction of the H_2S molecule with the B_2O_3 -I (101) surface confirms the role of the B_2O_3 coating in the oxidation process of hydrogen sulphide. For instance, H_2S molecularly adsorbed on the B_2O_3 -I (101) surface with no energy barrier through forming and sp^3 hybridisation. However, desorption of this molecule requires an activation barrier of 76 kJ/mol. This explains how the B_2O_3 coating inhibits the oxidation process. Most Importantly, the interaction of H_2S molecule with B_2O_3 surface was only by the molecular adsorption in which the surface exhibist an inhibiting behaviour toward dissociating of the hydrogen sulfide.

6.6 References

1. Chawla, N.; Kerr, M.; Chawla, K., Monotonic and cyclic fatigue behavior of high-performance ceramic fibers. *J. Am. Ceram. Soc.* **2005**, *88*, 101-108.

2. Riabov, A.; Yartys, V.; Hauback, B.; Guegan, P.; Wiesinger, G.; Harris, I., Hydrogenation behaviour, neutron diffraction studies and microstructural characterisation of boron oxide-doped Zr–V alloys. *J. Alloys Compd.* **1999**, *293*, 93-100.

3. Patil, P. T.; Malshe, K. M.; Kumar, P.; Dongare, M. K.; Kemnitz, E., Benzoylation of anisole over borate zirconia solid acid catalyst. *Catal. Commun.* **2002**, *3*, 411-416.

4. El-Alaily, N.; Mohamed, R., Effect of irradiation on some optical properties and density of lithium borate glass. *Mater. Sci. Eng., B* **2003**, *98*, 193-203.

5. Ding, X.; Huang, Z.; Huang, X.; Gan, Z.; Cheng, C.; Tang, C.; Qi, S., Synthesis of gallium borate nanowires. *J. Cryst. Growth* **2004**, *263*, 504-509.

6. Krasnoperov, L. N.; Niiranen, J. T.; Gutman, D.; Melius, C. F.; Allendorf, M. D., Kinetics and thermochemistry of Si (Ch3) 3+ no reaction: Direct determination of a Si-N bond energy. *J. Phys. Chem.* **1995**, *99*, 14347-14358.

7. Muramatsu, Y.; Takenaka, H.; Oyama, T.; Hayashi, T.; Grush, M. M.; Perera, R. C., Valence band structure and decay process in the inner-shell excitation of boron oxide. *X-Ray Spectrom.* **1999**, *28*, 503-508.

8. Demir, H.; Şahin, Ö.; Izgi, M. S.; Fıratoglu, H., Production of granular boron oxide by calcination of ammonium tetraborate tetrahydrate. *Thermochim. Acta* **2006**, *445*, 1-6.

9. Buc, D.; Bello, I.; Caplovicova, M.; Mikula, M.; Kovac, J.; Hotovy, I.; Chong, Y. M.; Siu, G. G., Analysis of magnetron sputtered boron oxide films. *Thin Solid Films* **2007**, *515*, 8723-8727.

10. Ramos, M.; Moreno, J.; Vieira, S.; Prieto, C.; Fernandez, J., Correlation of elastic, acoustic and thermodynamic properties in B_2O_3 glasses. *J. Non-Cryst. Solids* **1997**, *221*, 170-180.

11. Hu, Z.-B.; Li, H.-J.; Fu, Q.-G.; Hui, X.; Sun, G.-L., Fabrication and tribological properties of B_2O_3 as friction reducing coatings for carbon-carbon composites. *New Carbon Mater.* **2007**, *22*, 131-134.

12. Gurr, G.; Montgomery, P.; Knutson, C.; Gorres, B., The crystal structure of trigonal diboron trioxide. *Acta Crystallogr. Sect. B: Structural Crystallography and Crystal Chemistry* **1970**, *26*, 906-915.

13. Nieto-Sanz, D.; Loubeyre, P.; Crichton, W.; Mezouar, M., X-ray study of the synthesis of boron oxides at high pressure: Phase diagram and equation of state. *Phys. Rev. B* **2004**, *70*, 214108.

14. Effenberger, H.; Lengauer, C. L.; Parthé, E., Trigonal B_2O_3 with higher space-group symmetry: Results of a reevaluation. *Monatsh. Chem./Chemical Monthly* **2001**, *132*, 1515-1517.

15. Prewitt, C.; Shannon, R., Crystal structure of a high-pressure form of B_2O_3. *Acta Crystallogr. Sect. B: Structural Crystallography and Crystal Chemistry* **1968**, *24*, 869-874.

16. Bredow, T.; Islam, M. M., Theoretical study of low-index surfaces of trigonal B_2O_3. *Surf. Sci.* **2008**, *602*, 2217-2221.

17. Egerton, A.; Warren, D. In Kinetics of the Hydrogen/Oxygen reaction. I. The explosion region in boric acid-coated vessels, *Proc. R. Soc. London, Ser. A*: *Mathematical, Physical and Engineering Sciences, The Royal Society*, **1951**; *465-476*.

18. Baldwin, R.; Mayor, L., The mechanism of the Hydrogen+ Oxygen reaction in aged boric-acid-coated vessels. *T. Faraday Soc.* **1960**, *56*, 103-114.

19. Baldwin, R.; Walker, R.; Langford, D., Oxidation of propionaldehyde in aged boric-acid-coated vessels. Part 1.—Kinetic results. *T. Faraday Soc.* **1969**, *65*, 792-805.

20. Lodhi, Z. H.; Walker, R. W., Decomposition of 4, 4-dimethylpent-1-ene in the presence of Oxygen between 400 and 500 C: Oxidation chemistry of allyl radicals. *J. Chem. Soc., Faraday Trans.* **1991**, *87*, 681-689.

21. Zhou, C. R.; Sendt, K.; Haynes, B. S., Experimental and kinetic modelling study of H_2S oxidation. *Proc. Combust. Inst.* **2013**, *34*, 625-632.

22. Erdemir, A.; Halter, M.; Fenske, G., Preparation of ultralow-friction surface films on vanadium diboride. *Wear* **1997**, *205*, 236-239.

23. Erdemir, A.; Bindal, C.; Zuiker, C.; Savrun, E., Tribology of naturally occurring boric acid films on boron carbide. *Surf. Coat. Technol.* **1996**, *86*, 507-510.

24. Assaf, N. W.; Altarawneh, M. K.; Radny, M. W.; Jiang, Z.-T.; Dlugogorski, B. Z., Interaction of Oxygen with A-rhombohedral boron (001) surface. *J. Phys. Chem. C* **2016**, *120*, 5968-5979.

25. Hernandez-Sanchez, E.; Chino-Ulloa, A.; Velazquez, J.; Herrera-Hernández, H.; Velázquez-Mancilla, R.; Carrera-Espinoza, R., Effect of relative humidity on the tribological properties of self-lubricating H_3BO_3 films formed on the surface of steel suitable for biomedical applications. *Adv. Mater. Sci. Eng.* **2015**, *2015*.

26. Erdemir, A.; Fenske, G.; Erck, R., A study of the formation and self-lubrication mechanisms of boric acid films on boric oxide coatings. *Surf. Coat. Technol.* **1990**, *43*, 588-596.

27. Wang, Y.; Trenary, M., Surface Chemistry of Boron Oxidation. 2. The reactions of boron oxides B_2O_2 and B_2O_3 with Boron films grown on Tantalum (110). *Chem. Mater.* **1993**, *5*, 199-205.

28. Slutskii, V.; Tsyganov, S.; Severin, E.; Kazakov, O., Kinetics of high-temperature oxidation of Boron-containing clusters by water vapor. *Chem. Phys. Rep. C/C OF KHIMICHESKAIA FIZIKA* **1999**, *18*, 697-704.

29. Kuo, K. K., Principles of Combustion. **1986**.

30. King, M. K., Ignition and combustion of Boron particles and clouds. *J. Spacecr. Rockets* **1982**, *19*, 294-306.

31. Glassman, I.; Williams, F.; Antaki, P. In *A Physical and Chemical Interpretation of Boron Particle Combustion*, Symposium (International) on Combustion, Elsevier: 1985; pp 2057-2064.

32. Meinköhn, D., The ignition of Boron particles. *Combust. Flame* **1985**, *59*, 225-232.

33. Hsieh, W.-H.; PERETZ, A.; KUO, K. K.; Huang, I.-T., Combustion behavior of Boron-based bamo/nmmo fuel-rich solid propellants. *J. Propul. Power* **1991**, *7*, 497-504.

34. Nandi, A. K.; Ghosh, M.; Newale, S. P.; Jadhav, A. J.; Prasanth, H.; Pandey, R. K., Formation of boric acid by surface oxidation of amorphous Boron powder: Characterization and quantitative estimation. *Cent. Eur. J. Energ. Mat.* **2012**, *9*, 387-398.

35. Nieder, E. G., Chemical Passivation of Amorphous Boron Powder. Google Patents: 1987.

36. Trowbridge, J. C.; Breazeale, J. D., Coating of Boron Particles. Google Patents: 1989.

37. Liu, T. K.; Luh, S. P.; Perng, H. C., Effect of Boron particle surface coating on combustion of solid propellants for ducted rockets. *Propellants Explos. Pyrotech.* **1991**, *16*, 156-166.

38. Shyu, M.; Liu, T.-K., Combustion characteristics of gap-coated Boron particles and the fuel-rich solid propellant. *Combust. Flame* **1995**, *100*, 634-644.

39. Unal, H.; Yetgin, S.; Sen, U.; Mimaroglu, A., Evaluation of the performance of H_3BO_3-filled polyamide composite. *J. Reinf. Plast. Compos.* **2010**, *29*, 986-993.

40. Su, J.-M.; Yang, J.; Xiao, Z.-C.; Zhou, S.-J.; Peng, J.-G.; Li, R.; Han, M.; Zhao, S.-L.; Gu, L.-M., Structure and properties of Carbon/ Carbon composite materials for aircraft brake discs. *New Carbon Mater.* **2006**, *21*, 81-89.

41. Sen, U.; Sen, S.; Yilmaz, F., Structural characterization of boride layer on boronized ductile irons. *Surf. Coat. Technol.* **2004**, *176*, 222-228.

42. Habig, K.-H.; Chatterjee-Fischer, R., Wear behaviour of boride layers on alloyed steels. *Tribol. Int.* **1981**, *14*, 209-215.

43. Carbucicchio, M.; Bardani, L.; Palombarini, G., Mössbauer and Metallographic Analysis of borided surface layers on armco iron. *J. Mater. Sci.* **1980**, *15*, 711-719.

44. Carbucicchio, M.; Palombarini, G., Effects of alloying elements on the growth of iron boride coatings. *J. Mater. Sci. Lett.* **1987**, *6*, 1147-1149.

45. Sen, U.; Sen, S., The fracture toughness of borides formed on boronized cold work tool steels. *Mater. Charact.* **2003**, *50*, 261-267.

46. Venkataraman, B.; Sundararajan, G., The high speed sliding wear behaviour of boronized medium Carbon Steel. *Surf. Coat. Technol.* **1995**, *73*, 177-184.

47. Atık, E.; Yunker, U.; Merıç, C., The effects of conventional heat treatment and boronizing on abrasive wear and corrosion of Sae 1010, Sae 1040, D2 and 304 steels. *Tribol. Int.* **2003**, *36*, 155-161.

48. Myers, J. E., Xix.—Boric Anhydride and its hydrates. *J. Chem. Soc., Trans.* **1917**, *111*, 172-179.

49. Slutskii, V.; Severin, E.; Polenov, L., An Ab initio study of reactions in the $H_3BO_3/B_2O_3/H_2O$ system. *Russ. J. Phys. Chem. B, Focus on Physics* **2007**, *1*, 549-552.

50. Mülazim, Y.; Kızılkaya, C.; Kahraman, M. V., Thermal and neutron shielding properties of $10B_2O_3$/polyimide hybrid materials. *Polym. Bull.* **2011**, *67*, 1741-1750.

51. Delley, B., An all-electron numerical method for solving the local density functional for polyatomic molecules. *J. Chem. Phys.* **1990**, *92*, 508-517.

52. Delley, B., From molecules to solids with the Dmol 3 approach. *J. Chem. Phys.* **2000**, *113*, 7756-7764.

53. Burke, K.; Perdew, J. P.; Wang, Y., Derivation of a generalized gradient approximation: The Pw91 density functional. In *Electronic Density Functional Theory*, Springer: 1998; pp 81-111.

54. Perdew, J. P.; Burke, K.; Wang, Y., Generalized gradient approximation for the exchange-correlation hole of a many-electron system. *Phys. Rev. B* **1996**, *54*, 16533.

55. Mietze, C.; Landmann, M.; Rauls, E.; Machhadani, H.; Sakr, S.; Tchernycheva, M.; Julien, F.; Schmidt, W.; Lischka, K.; As, D., Band offsets in cubic Gan/Aln superlattices. *Phys. Rev. B* **2011**, *83*, 195301.

56. Islam, M. M.; Bredow, T.; Heitjans, P., The ionic conductivity in Lithium-Boron oxide materials and its relation to structural, electronic and defect properties: Insights from theory. *J. Phys.: Condens. Matter* **2012**, *24*, 203201.

57. Bredow, T.; Gerson, A. R., Effect of exchange and correlation on bulk properties of MgO, NiO, and CoO. *Phys. Rev. B* **2000**, *61*, 5194.

58. Islam, M. M.; Bredow, T.; Minot, C., Theoretical analysis of structural, energetic, electronic, and defect properties of Li_2O. *J. Phys. Chem. B* **2006**, *110*, 9413-9420.

59. Monkhorst, H. J.; Pack, J. D., Special points for Brillouin-zone integrations. *Phys. Rev. B* **1976**, *13*, 5188.

60. Laidler, K. J.; King, M. C., Development of transition-state theory. *J. Phys. Chem.* **1983**, *87*, 2657-2664.

61. Christy, A. A.; Nodland, E.; Burnham, A. K.; Kvalheim, O. M.; Dahl, B., Determination of kinetic parameters for the dehydration of Calcium Oxalate Monohydrate by diffuse reflectance Ft-Ir spectroscopy. *Appl. Spectrosc.* **1994**, *48*, 561-568.

62. Vyazovkin, S.; Burnham, A. K.; Criado, J. M.; Pérez-Maqueda, L. A.; Popescu, C.; Sbirrazzuoli, N., Ictac kinetics committee Recommendations for performing kinetic computations on thermal analysis data. *Thermochim. Acta* **2011**, *520*, 1-19.

63. Vyazovkin, S., Advanced isoconversional method. *J. Therm. Anal. Calorim.* **1997**, *49*, 1493-1499.

64. Lyon, R. E., An integral method of nonisothermal kinetic analysis. *Thermochim. Acta* **1997**, *297*, 117-124.

65. Akahira, T.; Sunose, T., Method of determining activation deterioration constant of electrical insulating materials. *Res. Rep. Chiba Inst. Technol. (Sci. Technol.)* **1971**, *16*, 22-31.

66. Starink, M., The determination of activation energy from linear heating rate experiments: A comparison of the accuracy of isoconversion methods. *Thermochim. Acta* **2003**, *404*, 163-176.

67. Senum, G.; Yang, R., Rational Approximations of the integral of the Arrhenius Function. *J. Therm. Anal. Calorim.* **1977**, *11*, 445-447.

68. Islam, M. M.; Bredow, T.; Minot, C., Comparison of trigonal B_2O_3 structures with high and low space-group symmetry. *Chem. Phys. Lett.* **2006**, *418*, 565-568.

69. Li, D.; Ching, W., Electronic Structures and optical properties of low-and high-pressure phases of crystalline B_2O_3. *Phys. Rev. B* **1996**, *54*, 13616.

70. Engberg, U., B_2O_3 crystals investigated by plane-wave pseudopotential calculations using the generalized-gradient approximation. *Phys. Rev. B* **1997**, *55*, 2824.

71. Huang, L.; Durandurdu, M.; Kieffer, J., New B_2O_3 crystals predicted from concurrent molecular dynamics simulations and first-principles calculations. *J. Phys. Chem. C* **2007**, *111*, 13712-13720.

72. Brazhkin, V. V.; Katayama, Y.; Inamura, Y.; Kondrin, M. V.; Lyapin, A. G. e.; Popova, S. V.; Voloshin, R. N., Structural transformations in liquid, crystalline, and glassy B_2O_3 under high pressure. *JETP Lett.* **2003**, *78*, 393-397.

73. Assaf, N. W.; De La Pierre, M.; Altarawneh, M. K.; Radny, M. W.; Dlugogorski, B. Z., Structure, stability and (non) reactivity of the low-index surfaces of crystalline B_2O_3-I. *J. Phys. Chem. C* **2017**, *121*, 11346–11354.

74. Murnaghan, F., The compressibility of media under extreme pressures. *Proc. Nat. Acad. Sci.* **1944**, *30*, 244-247.

75. Goclon, J.; Grybos, R.; Witko, M.; Hafner, J., Relative stability of low-index V_2O_5 surfaces: A density functional investigation. *J. Phys.: Condens. Matt.* **2009**, *21*, 095008.

76. Muscat, J.; Wander, A.; Harrison, N., On the prediction of band gaps from Hybrid Functional Theory. *Chem. Phys. Lett.* **2001**, *342*, 397-401.

77. Gillen, R.; Clark, S. J.; Robertson, J., Nature of the electronic band gap in lanthanide oxides. *Phys. Rev. B* **2013**, *87*, 125116.

78. Xiao, H.; Tahir-Kheli, J.; Goddard III, W. A., Accurate band gaps for semiconductors from Density Functional Theory. *J. Phys. Chem. Lett.* **2011**, *2*, 212-217.

79. Doyle, R. J., High-molecular-weight boron oxides in the gas phase. *J. Am. Chem. Soc.* **1988**, *110*, 4120-4126.

80. Pérez-Enciso, E.; Ramos, M.; Vieira, S., Low-temperature specific heat of different B_2O_3 glasses. *Phys. Rev. B* **1997**, *56*, 32.

81. Boesch, L.; Napolitano, A.; Macedo, P., Spectrum of volume relaxation times in B_2O_3. *J. Am. Ceram. Soc.* **1970**, *53*, 148-153.

82. Vyazovkin, S.; Linert, W., Kinetic analysis of reversible thermal decomposition of solids. *Int. J. Chem. Kinet.* **1995**, *27*, 73-84.

CHAPTER 7

Formation of Environmentally-Persistent Free Radicals (EPFR) on α-Al_2O_3

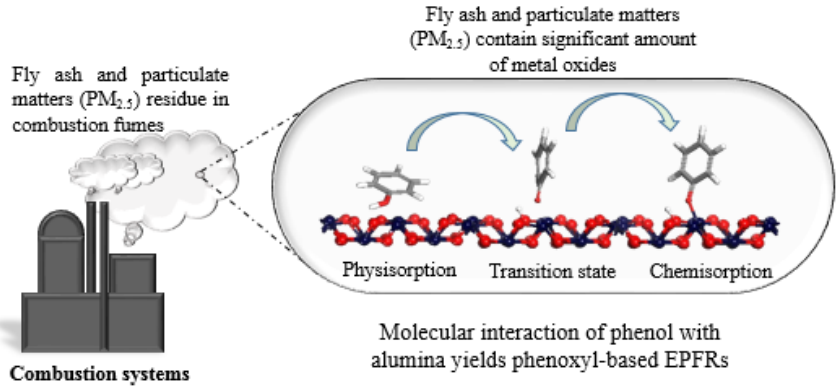

The following is a modified version of the published paper:

Assaf, N. W.; Altarawneh, M.; Oluwoye, I.; Radny, M.; Lomnicki, S. M.; Dlugogorski, B. Z. ; Formation of Environmentally-Persistent Free Radicals (EPFR) on α-Al_2O_3, Environ. Sci. Technol, **2016**, *50*, 11094-11102.

2016 impact factor: 6.198

7.1 Introduction

Environmentally-persistent free radicals represent a group of species that have prolonged life span in ambient environment. Over the last two decades, EPFR have gained tremendous interest in a wide range of scientific explorations. The major area of interest have focused on the their formation mechanisms and their associated impact on human health,[1-2] from chronic respiratory and cardiopulmonary dysfunction as a result of oxidative stress imposed by reactive oxygen species. These chemical species include hydroxyl radicals, hydrogen peroxide and superoxide anion radicals that form in the redox cycling of EPFR, in particulate matters of an aerodynamic diameter < 2.5 μm ($PM_{2.5}$) generated in combustions and thermal processes. The chemical make-up of $PM_{2.5}$ constitutes a key factor in clarifying the formation mechanisms of EPFR.

Metal oxides, present on surfaces of particulates from combustion processes,[3-6] promote the formation of ROS.[7-9] For this reason, considerably attention has also focused on investigating the catalytic role of metal oxides in forming EPFR. Lomnicki et al.[10] and Vejerano et al.[11] performed a series of experimental studies to examine the surface-mediated formation of EPFR over two transition metal oxides - Fe_2O_3 and CuO - deposited on the silicon oxide surface. These researchers provided a detailed account of physiochemical interaction of five different aromatic hydrocarbons (phenol, hydroquinone, 2-monochlorophenol, 1,2-dichlorobenzene and catechol) with the selected metal oxide surfaces. They indicated that in the progressive physisorption and chemisorption processes, the surface metal atoms transfer electrons to the adsorbed organic precursors, successively leading to generation of persistent surface bound radicals. Owing to higher oxidation potential of Fe_2O_3, the authors proposed that the surface potentially produces more stable EPFR with longer lifetime compared to those produced over

the CuO surface. The same authors have also compared EPFR formation over NiO[12] and ZnO[13] surfaces. In particular, ZnO exhibit potential for producing EPFR with long lifetime, ranging from 3-73 days, such as semiquinone-type species.[13] Along the same line of enquiry, Patterson and co-workers[14] demonstrated that the TiO_2 surfaces produce EPFR, such as phenolate, from their respective stable molecules. Even seemingly inactive surfaces, such as those of silica can generate EPFR, as reported by Mosallanejad et al.[15] in a recent study on activation of 2-chlorophenols to yield polychlorinated dibenzo-*p*-dioxins and polychlorinated dibenzofurans.

Alumina exists as one of the most abundant metal oxides in the $PM_{2.5}$ encountered in combustion systems.[16-18] Its concentration in $PM_{2.5}$ varies between 13-16 % by mass.[19] Alumina represent an active catalytic oxide[20] in its own right and provides a powerful support for different catalytic systems.[21-22] The electron energy loss spectrometry elucidated the mechanism of EPFR formation over a γ-Al_2O_3 surface, by reporting a noticeable shift in π-π^* transition of the chemisorbed phenol, suggesting that the appearance of this precursor governs the generation of phenoxyl EPFR.[23] Despite the results of these experiments, the literature lacks detailed theoretical confirmation of the role of Al_2O_3 surfaces to produce EPFR. This realisation has prompted us to investigate the EPFR formation mechanism from a mechanistic point of view.

Several studies have investigated the interaction of water molecule with α-Al_2O_3(0001) surface. It seems that α-Al_2O_3(0001) surface is highly reactive toward water molecule in producing surface hydroxyl groups.[24-29] Hass et al.[26] proposed that the binding energy of the adsorbed water molecule relies strongly on the surface adsorption sites. The most stable configuration arises for the dissociated hydrogen atom and hydroxyl group bonding to the oxygen and aluminium atoms in the same O–Al group. Based on this finding, under ambient conditions,

the α-Al_2O_3 surfaces normally features a hydroxyl-terminated surface layer. However, heating can reversibly remove the hydroxyl groups on α-Al_2O_3 surfaces,[30] as confirmed by IR and NMR measurements.[31-32] The surface is completely dehydroxylated by heating to 450-600 ℃,[30] corresponding to temperature window of the cooling-down zone of the combustor that typically extends between 180 and 600 ℃.[33] This means that the reaction between alumina and phenol, in the post combusion zone of municipal waste incinerators (MWI), involves the dehydroxylated surfaces of α-Al_2O_3, most notably near the higher edge of the temperture window. Nonetheless, the existence of water vapour may initiate the re-hydroxylation of the surface. This may implay co-current surface rehydroxylation and formation of EPFR.

By monitoring the change in IR spectra as the temperature increases, Ballinger and Yates[34] demonstrated that the adjacent OH groups attached to surface Al atoms depart the surface at around 520 ^{o}C. Full dehydroxylation of the surface becomes complete at around 900 ^{o}C, with the last stage of the process comprising the removal of isolated OH groups. The acidity of alumina surfaces (i.e., as measured by the uptake of CO molecules) correlates with the increase in temperature, as a consequence of the creation of unsaturated Al^{3+} sites upon the loss of OH groups. Detailed examination of formation of crystallographic Al_2O_3 nanomaterials from the solid waste by Singh et al.[35] demonstrated that dehydration and dehydroxylation of alumina takes place in the temperature range of 200-450 ℃; the temperature that could readily occur in commercial combustors. Along the same line of inquiry, Hollitt et al.[36] have confirmed that the dehydration and dehydroxylation processes of alumina take place in earlier stages of alumina treatment. Together these studies confirm the presence of dehydroxylated alumina under conditions encountered in typical MWIs.

By employing density functional theory, the present Chapter explores the catalytic role of dehydroxylated α-Al_2O_3(0001) in surface-mediated formation of phenoxy-type EPFR. Because of its thermodynamic stability, this surface arises naturally in combustion systems.[37-42] The thermokinetic results presented here confirm the role of alumina-rich particulate matters and fly ash as a potential source of EPFR in any system in which aromatic compounds co-exsist with dehydrated alumina.

7.2 Computational Methodology

All calculations involved the DMol^3 code[43-44] that afforded the generalised gradient approximation of the Perdew-Burke-Ernzerhof functional[45] and the Grimme dispersion correction.[46] The latter accounts for all non-bonding interactions in the system. We adopted the double numerical plus polarisation basis set, integrated the Brillouin zone on the mesh of 4×4×1 *k*-points, and converged the total energies with a tolerance of 1×10^{-6} Ha. Test calculations using 5×5×1 **k**-point changed the total energy by ~6.0 meV.

Calculation of cohesive energy (E^{coh}) of bulk Al_2O_3 followed from Eq. 7.1:

$$E^{coh} = E^{bulk}_{Al_2O_3} - 2E^{gas}_{Al} - 3E^{gas}_{O} \qquad 7.1$$

where $E^{bulk}_{Al_2O_3}$, E^{gas}_{Al} and E^{gas}_{O} denote energies of a bulk Al_2O_3 (i.e., for one unit formula), a gas-phase aluminium atom, and a gas-phase oxygen atom, respectively.

We computed the average binding energies (E_b) for the on-surface adsorption from energies of a phenol/Al_2O_3 system $E_{slab + phenol}$, energy of the clean α-Al_2O_3(0001) surface E_{slab}, and energy of an isolated phenol molecule E_{phenol}:

$$E_b = E_{slab\ +\ phenol} - E_{slab} - E_{phenol} \qquad 7.2$$

Furthermore, as implemented in the DMol^3 program, the complete linear synchronous and quadratic synchronous transit approaches (LST/QST) locate all transition states associated with the dissociation reactions. The DMol^3 package also affords computation of vibrational frequencies to obtain the temperature-dependent thermochemical parameters of the optimised structures. This allows us to compute the reaction rate parameters (E_a and A) as a slope and an intersect of the fitted linear line of Ln k vs $1/T$

Estimation of the reaction rate constants comprised fitting the rates to the Arrhenius equation - $k(T) = A \exp(-E_a/(RT))$ - in the temperature range of 300 K to 1000 K, according to the classical transition state theory:[47]

$$k(T) = \frac{k_B T}{\sigma_e h} \exp\left(\frac{\Delta S^{\neq}}{R}\right) \exp\left(\frac{-\Delta H^{\neq}}{RT}\right) \qquad 7.3$$

In Eq. 7.3, reaction degeneracy number σ_e equals unity, $\Delta S^{\neq}$ and $\Delta H^{\neq}$ represent entropy and enthalpy of activation at temperature T in that order, and k_B, h, and R denote Boltzmann's, Planck's and the universal gas constants, respectively.

7.3 Results and Discussion

7.3.1 Bulk Properties of *α*-Al_2O_3.

The crystal structure of *α*-Al_2O_3 belongs to the $R\bar{3}c$ space group, with the hexagonal unit cell of six formula units consisting of thirty atoms in total. As illustrated in Figure 7.1 in Appendix II, the *α*-Al_2O_3 unit cell displays a close-packed ABAB alternating sequence stack of oxygen ions and Al ions which occupy two thirds of the six-fold coordinated sites between the oxygen layers.[48-49] Table 7.1 presents calculated bulk parameters of the optimised *α*-Al_2O_3 structure in terms of the lattice constants (*a* and *c*), band gap energy (E^g) and cohesive energy (E^{coh}). The calculated parameters concur with experimental measurements and other theoretical data published in literature.[37, 42, 50-54] Closer inspection of the table shows that calculated value of the bulk band gap energy underestimates the experimental value. Such underestimation is a notable feature of plain DFT, mostly in the case of insulators and semiconductors. This inconsistency may be due to the false interpreting of the true unoccupied states of the system by the corresponding Kohn-Sham states of DFT.[55]

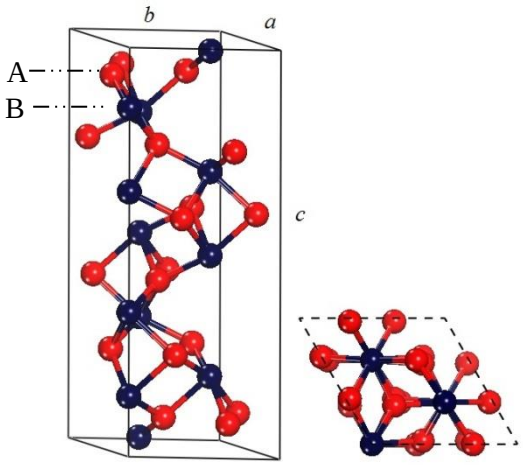

Figure 7.1. Side (left) and top (right) views of the hexagonal unit cell of bulk *α*-Al_2O_3. Blue spheres denote Al atoms and red spheres represent O atoms.

Table 7.1. Calculated parameters for α-Al_2O_3.

Applied methods	Energetics and geometrical properties			
	***a* (Å)**	***c* (Å)**	***E*^{g} (eV)**	***E*^{coh} (eV)**
Present work (PBE)	4.80	13.01	6.3	32.6
PW91[37]	4.79	13.07	-	33.0
LDA[37]	4.83	12.61	-	-
BLYP[50]	4.81	13.18	6.8	-
PW91[42]	4.83	12.6	-	32.1
PBE[51]	4.81	13.12	6.0	-
Experiment	4.76[52]	13.00[52]	8.8[53]	31.8[54]

7.3.2 Clean Al_2O_3 Surface

Recent theoretical investigations[56-61] of the α-Al_2O_3 demonstrated the (0001) Al-terminated surface as the most energetically stable. Accordingly, we performed the total energy calculations for this surface. Figure 7.2 illustrates the eight-layer slab with 2×2 surface unit cell that consists of 76 atoms, with the vacuum space of 30 Å in size above the surface. We have found that the clean α-Al_2O_3(0001) surface displays a significant inward relaxation. This observation agrees with the findings of other studies,[42, 50, 62-66] with Rohman et al.[51] explaining

the strong relaxation behaviour of α-Al_2O_3(0001) by charge redistribution accompanies the electron transfer from Al atoms to O atoms on the surface.[50]

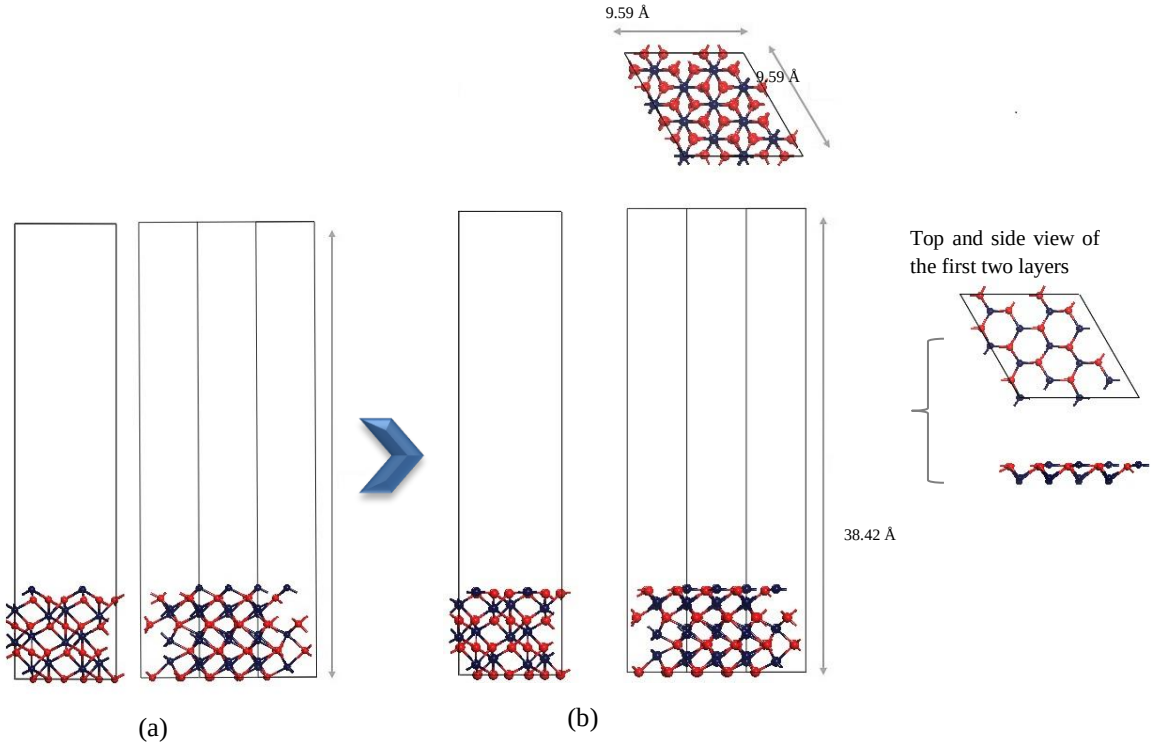

Figure 7.2. (a)Unit cell (with slab and vacuum), employed the beginning of the coordinates in the periodic slab calculation for the α-Al_2O_3(0001) surface. (b) Unit cell (with slab and vacuum), employed in the periodic slab calculation for the α-Al_2O_3(0001) surface. Blue spheres denote Al atoms and red spheres represent O atoms. This code applies to colour in all Figures.

Due to the downward movement of the Al atoms towards the O atoms beneath them, the calculated inter-layer distance between the two topmost layers decreases by 82 % relatively to the bulk inter-layer distance. The topmost layer contains both Al and O atoms. By contrast, interlayer spacing between the second and third layers configuration exhibit a minimal change (7 %) compared to the adjustment in the first two layers. On the other hand, reconstruction

shortens the Al-O bond length by 8 - 3 % with respect to the corresponding bulk values. This finding reflects those reported by Alavi et al.[42] Our deployed surface behaves as a strong Lewis acid, because of the low coordination of the Al surface atoms. Typically, Al atoms on surface display three-fold coordination, whereas those in bulk lie in octahedral cavities and are six-fold coordinated.[26, 67]

7.3.3 O-H and C-OH Bond Fissions in the Gas Phase

In order to address the formation of hydroxy and phenoxy radicals mediated by an alumina surface, we investigated the gas-phase dissociation of phenol by direct fission of H atom from the hydroxyl group (Sa, C_6H_5O-H) and scission of the hydroxyl radical (Sb; C_6H_5-OH));

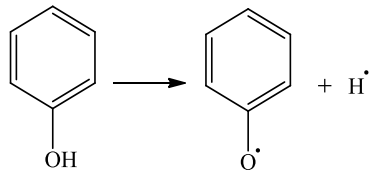

(Sa)

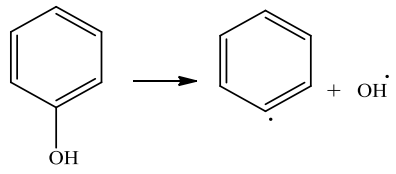

(Sb)

Scheme 7.1. Dissociation of phenol in gas phase.

Applying, $\Delta E = \sum E_{Products} - \sum E_{Reactants}$, both reactions represent highly endothermic processes, and require 362 kJ/mol and 473 kJ/mol at 298.15 K, respectively. The calculated enthalpy

value for Sa concurs with the results of the previous experimental (353 - 378 kJ)[68-76] and theoretical (360.6 -382.8 kJ)[74, 77-83] studies. Therefore, in practical systems, these reactions can only proceed in the presence of a catalyst. Figure 7.3 documents the calculated bond length of phenol and phenoxy radical and compares the relevant values to those reported in the earlier studies,[84-85] indicating good reproducibility. We conclude this section by a remark on the effect of the deployed DFT functional on the geometries of the two title species. Optimising the phenol and phenoxy species within the framework of LDA-DFT change the GGA-DFT obtained values only marginally in the range of 0.01 Å.

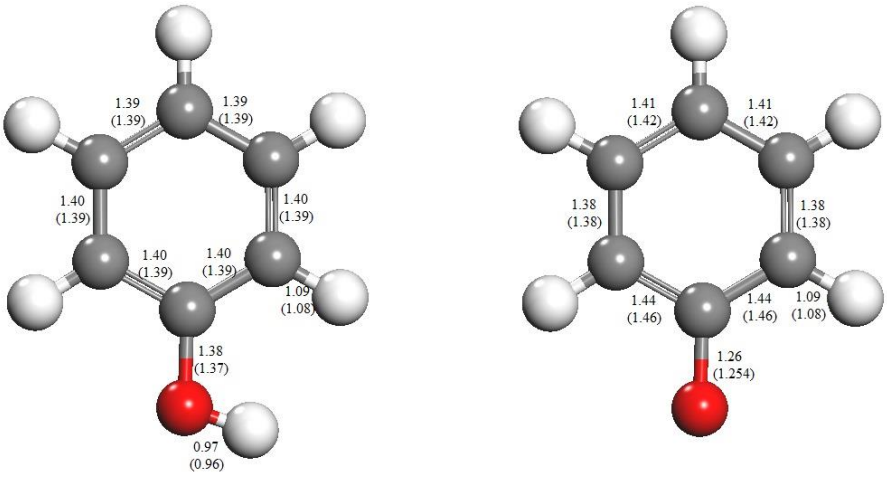

Figure 7.3. Coloured structure of a phenol molecule (left) and the phenoxy radical (right). Red, grey and white spheres represent O, C and H atoms, respectively. Bond lengths in parentheses signify the corresponding experimental or theoretical values from the previous studies.[84-85]

7.3.4 Molecular Physisorption of Phenol

We studied the molecular adsorption of phenol on the α-Al_2O_3(0001) surface in several initial vertical and flat configurations. These configurations comprise: (i) eclipsed arrangement, when

the molecular ring lies directly above a surface atom (O or Al); and, (ii) staggered structure, when the ring sits between Al-O bonds on the surface. Figure 7.4 illustrate four stable molecular adsorption patterns that were found in the calculation, namely A1, A2, A3 and A4. We observe that a moledule of a physisorbed phenol adopts a slightly tilted geometry, in agreement with the previous results.[86]

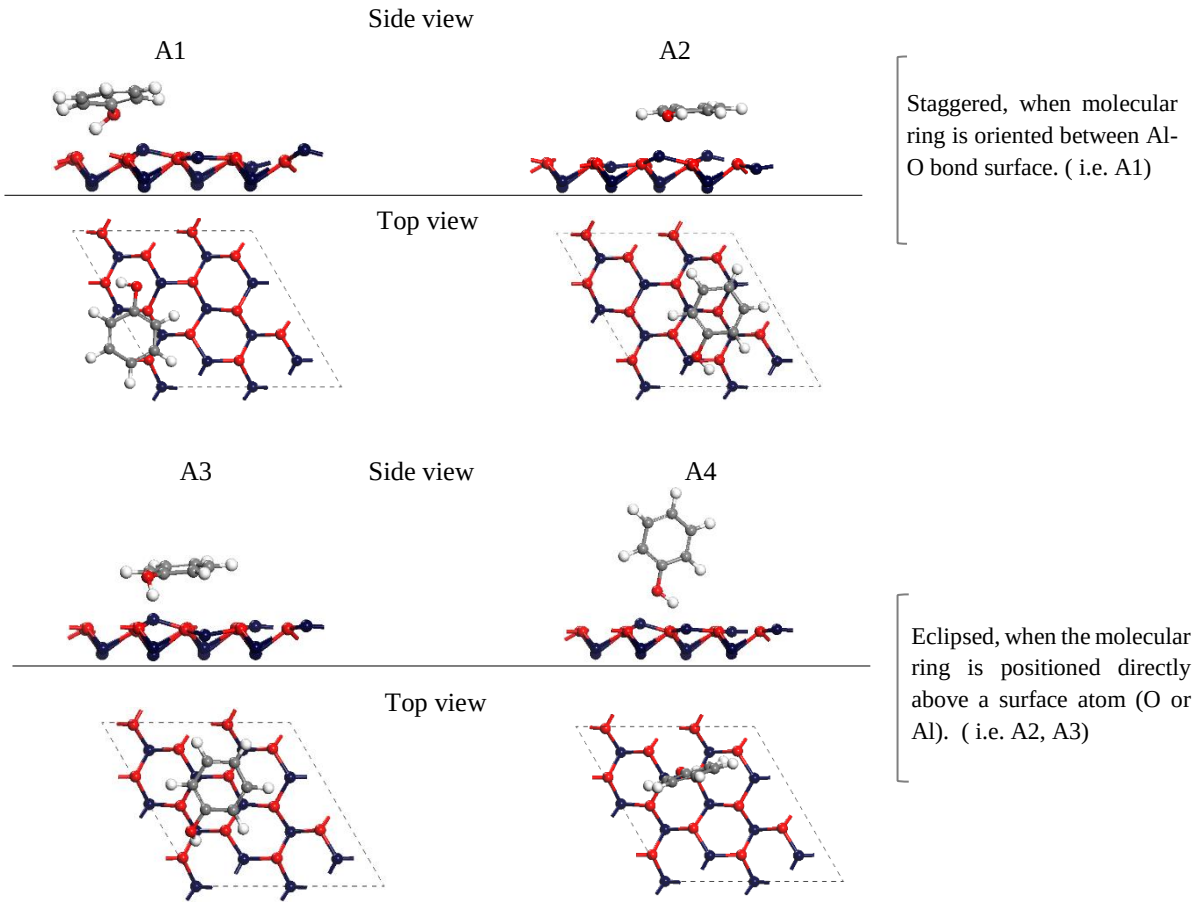

Figure 7.4. Top and side views of the stable geometries induced by molecular phenol physisorbed on α-Al_2O_3 configurations. Grey and white spheres represent carbon and hydrogen atoms; respectively.

Table 7.2 assembles the calculated binding energy (as defined in Eq. 7.2), O-H bond distance and tilt angles of the phenol molecule for the molecular physisorption configurations. What is interesting in this data is a correlation arisng between the molecular tilt angle and the binding energy where the higher molecular tilt angle (80˚ of A4) is associated with the lower binding energy (-127 kJ/mol). Optimisation attepms commencing with tilt angles of 0°, 90 amd 180° converge to one of the stable A1-A4 structures."

Table 7.2. Binding energies, O-H bond distance and tilt angle for the adsorption configuration. (1 eV = 96.49 kJ/mol)

Structure	Description	Binding energy (kJ/mol)	O- H bond distance (Å)	Tilt angle (°)
A1	Staggered, when molecular ring is oriented between Al-O bond surface	-202	1.07	13.32
A2		-201	0.98	5.40
A3	Eclipsed, when the molecular ring is positioned directly above a surface atom (O or Al)	-171	0.99	8.13
A4		-127	1.03	80.20

Sorescu et al.[87] reported similar behaviour, in their study on the interaction between nitromethane and the α-Al_2O_3(0001) surface. The authors attributed this observation to intermolecular hydrogen bonding between the hydrogen atom of the adsorbed molecule and an oxygen on the alumina surface. The direct position of a hydrogen atom, pointing toward an oxygen atom on the surface, underpins the high binding energies associated with structures A1-A4. We have also found that a slight increase in the O-H bond lengths in A1-A4 structures

(0.98 – 1.07 Å), in reference to values for the gas phase configurations (0.97 Å), provides further evidence of the strong interaction. Concisely, the calculated binding energies that are listed in Table 7.2 relate to the van der Waals states established between the hydroxyl group of a phenol molecule and the alumina surface.

7.3.5 Surface-Mediated Dissociation of Phenol

7.3.5.1 Formation of Adsorbed Phenolate Moiety

We have followed two possible pathways for the dissociation of hydrogen atom from a phenol molecule on the α-Al_2O_3(0001) surface. Firstly, we have optimised the pseudo-dissociative structures by placing $C_6H_5O^{\cdot}$ and $H^{\cdot}$ above a selected pair of oxygen and aluminium surface atoms (Al_{surf} and O_{surf}), while maintaining the relative distance between hydrogen atom and phenolate moiety beyond the effective O-H bond length. This has resulted in different dissociation structures, namely D_{H1} and D_{H2}. As shown in Figure 7.5, in D_{H1}, the dissociated phenolate adduct attaches itself to Al_{surf} ($C_6H_5O^{\cdot}$-Al_{surf}), and the detached hydrogen atom bonds with the neighbouring O_{surf} ($H^{\cdot}$-O_{surf}) as H^+, with the Al_{surf}-O_{surf} distance of 1.83 Å. In the D_{H2} configuration, the phenolate and H^+ link to Al_{surf} and O_{surf}, respectively, separated by 4.21 Å. Despite of out best attempts, we were unable to locate an analogous homolytic decomposition route affording a phenoxy radical and hydrogen atom. Such pathway seem to operate only as a homogenous gas phase route. The electro negatively charged O atom in the phenolate prefers to attach to a surface Al atom while the hydrogen proton forms a strong bond with a surface O atom. As discussed in our recent stud,[15] desorption of a phenolate from the surface (when deploying SiO_2 clusters) affording phenoxy is a highly endothermic process.

This infers that adsorbed phenolate either undergo self-condensation to produce dioxin compounds or to decompose to commence the formation of soot on the surface.

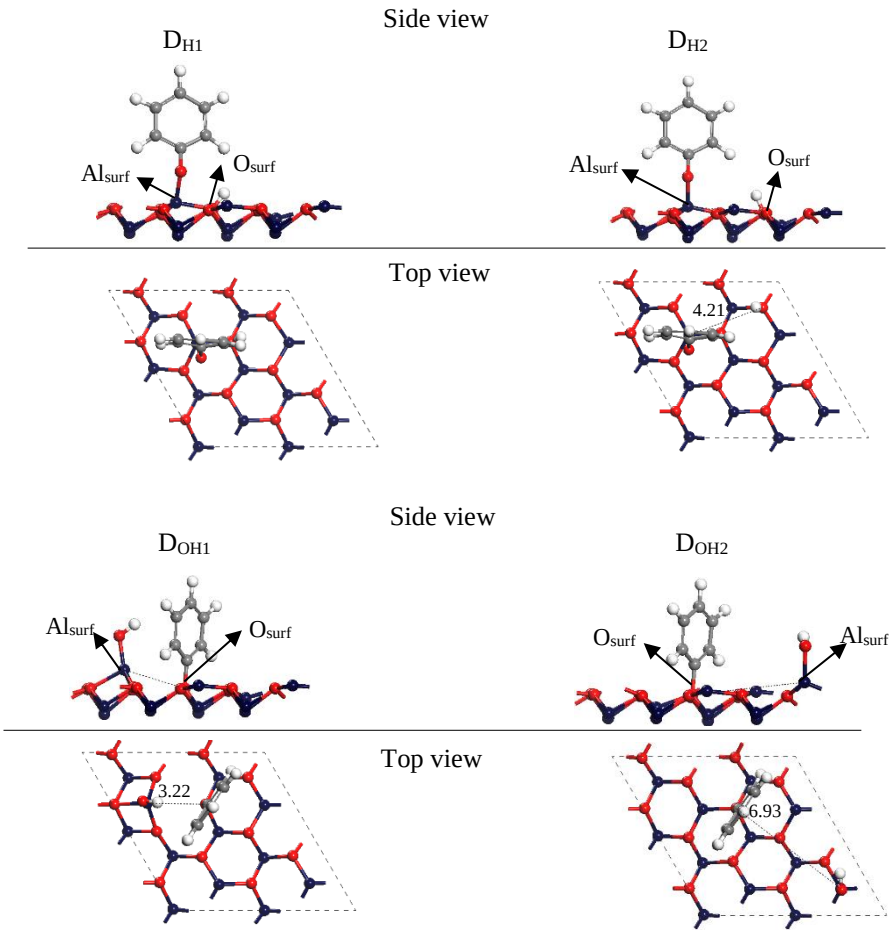

Figure 7.5. Top and side view of the chemisorbed phenol/α-Al_2O_3 configurations. All atoms derived from the phenol display stick style, whereas spheres illustrate those initially present in the alumina surface.

We have explored structural effects induced by the adsorption of phenol for the two dissociation structures on the α-Al_2O_3(0001) surface. With respect to the reconstruction, we observe that when the dissociated phenol adsorbs on the same Al_{surf}-O_{surf} bond (structure D_{H1}),

the length of this bond increases by 7 % with respect to that of the clean α-Al_2O_3(0001) surface (1.71 Å). However, in configuration D_{H2}, which represents the adsorption of dissociated phenol on two different Al-O surface groups, the distances of Al-O surface bond, where hydrogen atom and phenolate moiety are attached to, decrease by 2-12 % in reference to that of a clean surface. These values concur with the results obtained by Wang et al.[50] in their study of the dissociative adsorption of water on the α-Al_2O_3(0001) surface. They have found that dissociation of H_2O that involves the same Al-O group causes the 6 % elongation of the Al-O bond, while the dissociation on two different Al-O groups shortens the lengths of the surface Al-O bonds by 7 %. Changes in the interlayer distance between the first two layers remain negligible (~ 0.1 Å).

Structure D_{H2} appears relatively more stable than D_{H1}. This is evident from inspecting Figure 7.6 that displays the potential energy surface for the formation of dissociative structures, D_{H1} and D_{H2}. The exothermic formation of D_{H1} necessitates a modest activation enthalpy of 48 kJ/mol. However, the path leading to the second dissociation structure (D_{H2}) exhibits endothermicity over a comparable barrier height of 73 kJ/mol. Furthermore, desorption of the phenolate moiety from the two dissociated structures D_{H1} and D_{H2} (producing the product of the homolytic O-H bond cleavage), displays very high endothermicity (394 kJ/mol) rendering such a corridor inaccessible. The profound stability of the phenolate moiety on the α-Al_2O_3(0001) surface enables it to act as a catalyst for formation of the notorious halogenated dioxin compounds, as demonstrated experimentally.[88] The stability of phenolate adduct on the α-Al_2O_3(0001) surface also accords with the general consensus in literature of the very endothermic nature of the formation of gaseous phenoxy radicals from adsorbed phenolate species.[89-90]

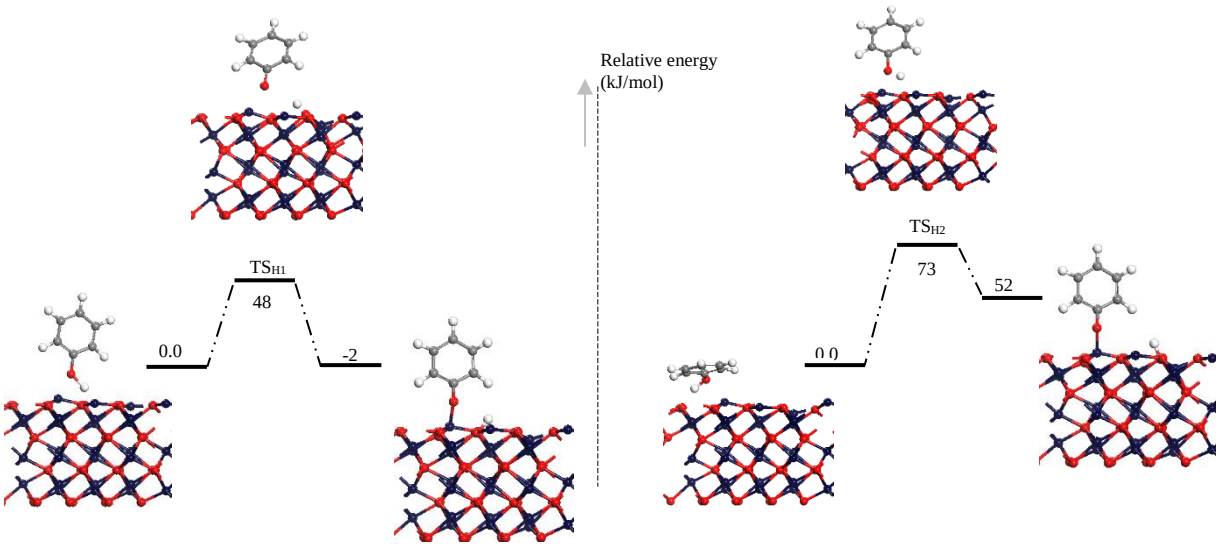

Figure 7.6. Relative energy for the formation of phenoxy radical over Al_2O_3 surface via dissociation paths leading to D_{H1} (left) and D_{H2} (right).

The most obvious finding to emerge from this study is that the α-Al_2O_3(0001) surface can actively dissociate phenol molecules, produce phenolate species, and subsequently generate persistent surface bound radicals. This could serve as a benchmark for investigating the formation of ROS via redox cycling of the persistent complexes over α-Al_2O_3 surfaces.

7.3.5.2 Formation of Hydroxyl Radical

We now turn our attention to investigating the formation of hydroxyl and phenyl radicals over the same alumina surface. Figure 7.5 reveals the stable dissociative structures. D_{OH1} characterises phenyl moiety attached to O_{surf} ($C_6H_5^{\cdot}$-O_{surf}), with the hydroxyl group linked to the adjacent Al_{surf} ($OH^{\cdot}$-Al_{surf}), and the Al_{surf}-O_{surf} bond distance amounting to 3.22 Å. For

D_{OH2}, which involves the transfer of a phenyl moiety in D_{OH1} to another O_{surf} atom, the dissociated $C_6H_5^{\cdot}$ and $OH^{\cdot}$ are separated by a distance of 6.93 Å. Adsorption of dissociated phenol on the same O_{surf}-Al_{surf} group induces an elongation in the O_{surf}-Al_{surf} bond length by 88 %, in comparison to the equilibrium bond length. While in D_{OH2}, when the distance between the two dissociated moieties attains 6.93 Å, the related O_{surf}-Al_{surf} bond lengths, where phenyl moiety is attached, increase by 6 - 10 % in refecrnce to the clean surface. The calculated binding energies of these structures reach -137 kJ/mol and -185 kJ/mol, for D_{OH1} and D_{OH2}, respectively.

Figure 7.7 illustrates the energy profiles for the two dissociation paths (D_{OH1} and D_{OH2}). Both dissociation reactions appear slightly exothermic with high activation enthalpy of 333 kJ/mol and 390 kJ/mol, for D_{OH1} and D_{OH2}, respectively. The results indicate no catalytic potential of the α-Al_2O_3(0001) surface to engender the formation of the adsorbed hydroxyl groups from surface-mediated dissociation of a phenol molecule. Based on the energies in Figure 7.6 and 7.5, the overall reaction of phenol with the α-Al_2O_3(0001) surface represents the generation of an adsorbed phenolate-like moiety rather than a phenyl-type radical.

Dissociative adsorption of phenol, both direct fission of H atom from the hydroxyl group (Sa, C_6H_5O-H) and scission of the hydroxyl radical (Sb; C_6H_5-OH), was found to have noticeable effect on the electronic structure of the α-Al_2O_3(0001) surface. Calculated Mulliken atomic charges (***e***) on the bonded Al_{surf} and O_{surf} atoms in the dissociative adsorption structures (Figure 7.3) and its corresponding ones in the clean α-Al_2O_3(0001) surface are presented in Table 7.3. The charge on the Al_{surf} atoms, for all dissociative structures (D_{H1}, D_{H2}, D_{OH1} and D_{OH2}), increases by ~ 0.1 - 0.3 *e*, when compared to Al_{surf} atoms of the clean surface (1.09 *e*). In comparison, the charge on the O_{surf} atoms, when bonded to the dissociated hydrogen atom (D_{H1}

and D_{H1}), differs than that when bonded to phenyl moiety. In the former (D_{H1} and D_{H1}), the charges of O_{surf} atoms decreases by ~ 0.10 *e*, whereas in the latter it decreases by 0.17*e* and 0.02*e* in D_{OH1} and D_{OH2}, respectively, both when compared to O_{surf} atoms of the clean surface (-0.92 *e*). A possible explanation for lower atomic charges on D_{OH1}, when compared to D_{OH2} is the increased distance between O_{surf} atom and the adjacent Alsurf (3.22 Å). Our calculated neutral charge herein serves as an additional benchmark for the accuracy of reported results.

Table 7.3. Mulliken atomic charges (***e***) on the bonded Al_{surf} and O_{surf} atoms in the dissociative adsorption structures (Figure 7.3) and its corresponding ones in the clean *α*-Al_2O_3(0001) surface. Figure 7.3 presents the atom labels.

	clean	**D_{H1}**	**D_{H2}**	**D_{OH1}**	**D_{OH2}**
Al_{surf}	1.09	1.22	1.20	1.20	1.21
O_{surf}	-0.92	-1.01	-1.00	-0.75	-0.89

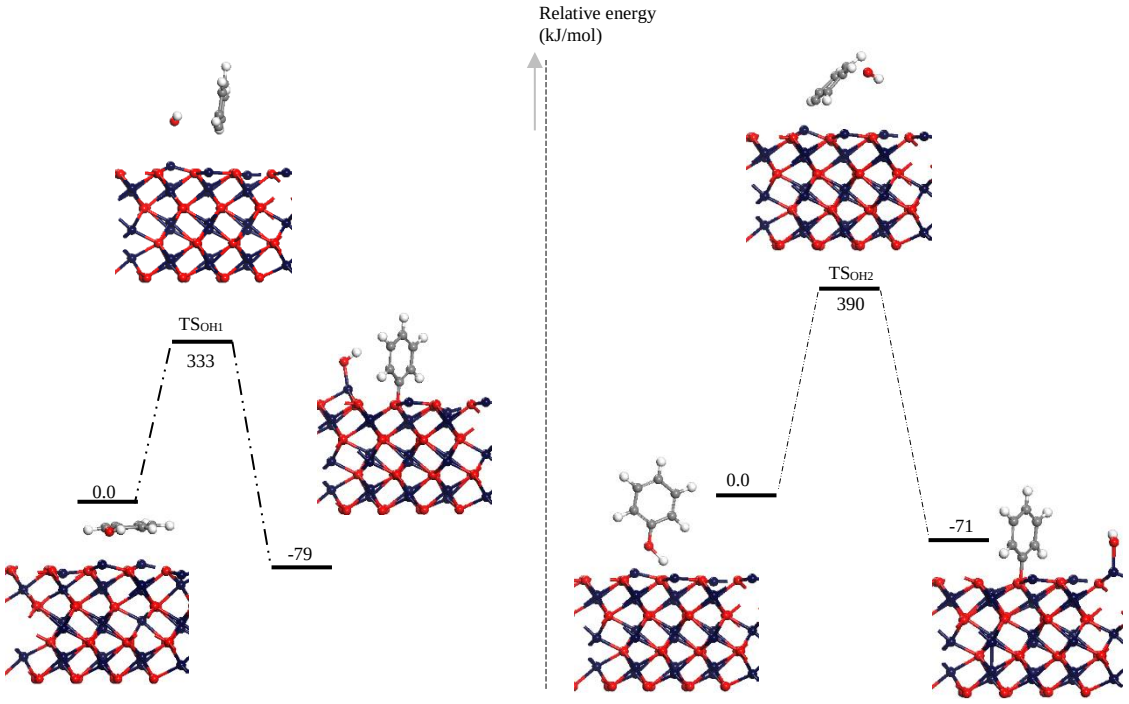

Figure 7.7. Relative energy describing the dissociation of hydroxyl group of phenol over the Al_2O_3 surface via dissociation paths leading to DO_{H1} (left) and DO_{H2} (right).

7.3.6 Kinetic Considerations

Figure 7.8 depicts the microkinetic Arrhenius plots for the four dissociation reactions investigated in this Chapter, and Table 7.3 itemises the reaction rate parameters in terms of activation energies (E_a) and the Arrhenius pre-exponential *A* factors. Reaction rate coefficients in Table 7.4 are based on a physisorbed phenol molecule (i.e., the A4 intermediate). Clearly, constructing a catalytic mechanism in practice requires inclusion of the partial pressure of phenol and the concentration of the available adsorption sites. To the best of our knowledge, there are no experimental or theoretical measurements for the interaction of phenol with *α*-

Al_2O_3 in the literature. Within the considered temperature limit, the paths leading to D_{HO1} and D_{HO2} exhibit high activation energies, with the reaction rate being highly sensitive to temperature. Reactions D_{H1} and D_{H2}, display a relatively weak dependence on temperature.

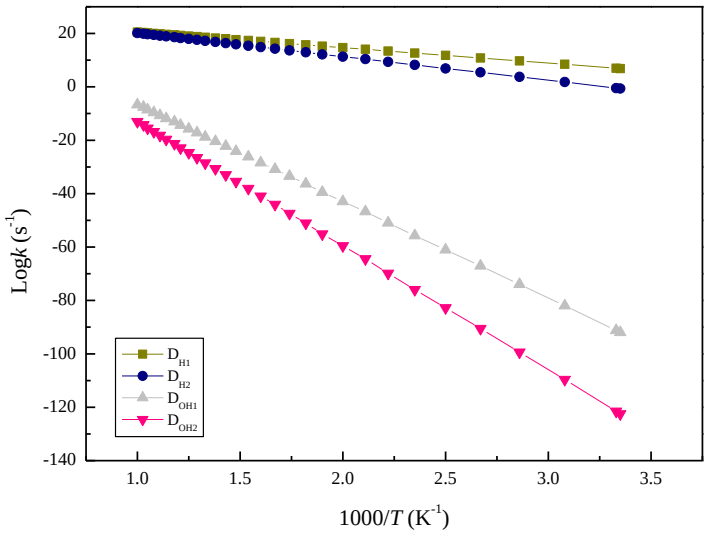

Figure 7.8. Arrhenius plots for the studied dissociation reactions.

Table 7.4. Kinetic parameters for the surface dissociation reactions.

Name	Reaction	E_a (kJ/mol)	A (s^{-1})
D_{H1}	$C_6H_5OH \rightarrow C_6H_5O^{\cdot}\text{-}Al_{surf} + H^{\cdot}\text{-}O_{surf}$	48	2.57×10^{11}
D_{H2}	$C_6H_5OH \rightarrow C_6H_5O^{\cdot}\text{-}Al_{surf} + H^{\cdot}\text{-}O_{surf}$	73	3.92×10^{12}
D_{OH1}	$C_6H_5OH \rightarrow C_6H_5^{\cdot}\text{-}O_{surf} + HO^{\cdot}\text{-}Al_{surf}$	301	6.90×10^{12}
D_{OH2}	$C_6H_5OH \rightarrow C_6H_5^{\cdot}\text{-}O_{surf} + HO^{\cdot}\text{-}Al_{surf}$	386	3.41×10^{14}

7.4. Conclusion

In conclusion, the present Chapter has evaluated the catalytic effect of α-Al_2O_3(0001) in producing EPFR. We have performed a detailed investigation on the interaction of phenol with the dehydrated α-Al_2O_3(0001) surface. The calculated structural and electronic properties of bulk α-Al_2O_3 and the α-Al_2O_3(0001) surface agree with the corresponding literature data. A noticeable inward relaxation exists within the macromolecular structure of clean α-Al_2O_3(0001). Phenol adsorbs strongly in four configurations on the α-Al_2O_3(0001) surface. Ultimately, α-Al_2O_3(0001) is catalytically very active in producing phenolate, an important candidate of persistent surface-bound radicals. Such formation requires an energy barrier in the range of 48 kJ/mol to 73 kJ/mol. Furthermore, our results show lack of activity of α-Al_2O_3(0001) to produce hydroxyl radicals, as this process necessitates an energy barrier of around 333 kJ/mol to 390 kJ/mol. Our findings provide insights into the role of α-Al_2O_3(0001) in promoting the production of EPFR.

7.5. References

1. Peters, A.; Dockery, D. W.; Muller, J. E.; Mittleman, M. A., Increased particulate air pollution and the triggering of myocardial infarction. *Circulation* **2001,** *103*, 2810-2815.

2. Nel, A., Air pollution-related illness: effects of particles. *Science* **2005,** *308*, 804-806.

3. Kennedy, I. M., The health effects of combustion-generated aerosols. *Proc. Combust. Inst.* **2007,** *31*, 2757-2770.

4. Cass, G. R.; Hughes, L. A.; Bhave, P.; Kleeman, M. J.; Allen, J. O.; Salmon, L. G., The chemical composition of atmospheric ultrafine particles. *Philos. Trans. R. Soc. London Ser. A-Math. Phys. Eng. Sci.* **2000,** *358,* 2581-2592.

5. Lighty, J. S.; Veranth, J. M.; Sarofim, A. F., Combustion aerosols: factors governing their size and composition and implications to human health. *J. Air Waste Manag. Assoc.* **2000,** *50,* 1565-1618.

6. Allouis, C.; Beretta, F.; D'Alessio, A., Structure of inorganic and carbonaceous particles emitted from heavy oil combustion. *Chemosphere* **2003,** *51,* 1091-1096.

7. Rasmussen, P. E.; Wheeler, A. J.; Hassan, N. M.; Filiatreault, A.; Lanouette, M., Monitoring personal, indoor, and outdoor exposures to metals in airborne particulate matter: risk of contamination during sampling, handling and analysis. *Atmos. Environ.* **2007,** *41,* 5897-5907.

8. Bondy, S. C.; Guo-Ross, S. X.; Truong, A. T., Promotion of transition metal-induced reactive oxygen species formation by *β*-amyloid. *Brain Res.* **1998,** *799,* 91-96.

9. Valavanidis, A.; Fiotakis, K.; Bakeas, E.; Vlahogianni, T., Electron paramagnetic resonance study of the generation of reactive oxygen species catalysed by transition metals and quinoid redox cycling by inhalable ambient particulate matter. *Redox Rep.* **2005,** *10,* 37-51.

10. Lomnicki, S.; Truong, H.; Vejerano, E.; Dellinger, B., Copper oxide-based model of persistent free radical formation on combustion-derived particulate matter. *Environ. Sci. Technol.* **2008,** *42,* 4982-4988.

11. Vejerano, E.; Lomnicki, S.; Dellinger, B., Formation and stabilization of combustion-generated environmentally persistent free radicals on an $Fe(III)_2O_3$/silica surface. *Environ. Sci. Technol.* **2010,** *45,* 589-594.

12. Vejerano, E.; Lomnicki, S. M.; Dellinger, B., Formation and stabilization of combustion-generated, environmentally persistent radicals on Ni(II)O supported on a silica surface. *Environ. Sci. Technol.* **2012,** *46*, 9406-9411.

13. Vejerano, E.; Lomnicki, S.; Dellinger, B., Lifetime of combustion-generated environmentally persistent free radicals on Zn(II)O and other transition metal oxides. *J. Environ. Montor* **2012,** *14*, 2803-2806.

14. Patterson, M. C.; Thibodeaux, C. A.; Kizilkaya, O.; Kurtz, R. L.; Poliakoff, E.; Sprunger, P. T., Electronic signatures of a model pollutant–particle pystem: chemisorbed Phenol on TiO_2(110). *Langmuir* **2015,** *31*, 3869-3875.

15. Mosallanejad, S.; Dlugogorski, B. Z.; Kennedy, E. M.; Stockenhuber, M.; Lomnicki, S. M.; Assaf, N.; Altarawneh, M., Formation of PCDD/Fs in oxidation of 2-chlorophenol on neat silica surface. *Environ. Sci. Technol.* **2015**, 10.1021.

16. Takasuga, T.; Makino, T.; Tsubota, K.; Takeda, N., Formation of dioxins (PCDDs/PCDFs) by dioxin-free fly ash as a catalyst and relation with several chlorine-sources. *Chemosphere* **2000,** *40*, 1003-1007.

17. Seames, W. S., An initial study of the fine fragmentation fly ash particle mode generated during pulverized coal combustion. *Fuel Process. Technol.* **2003,** *81*, 109-125.

18. Cains, P. W.; McCausland, L. J.; Fernandes, A. R.; Dyke, P., Polychlorinated dibenzo-*p*-dioxins and dibenzofurans formation in incineration: effects of fly ash and carbon source. *Environ. Sci. Technol.* **1997,** *31*, 776-785.

19. Ma, B.-Y.; Li, Y.; Cui, S.-G.; Zhai, Y.-C., Preparation and sintering properties of zirconia-mullite-corundum composites using fly ash and zircon. *T. Nonferr. Metal Soc.* **2010,** *20*, 2331-2335.

20. Corma, A., From microporous to mesoporous molecular sieve materials and their use in catalysis. *Chem. Rev.* **1997,** *97*, 2373-2420.

21. Kroschwitz, J. I., *Kirk-Othmer Encyclopedia of Chemical Technology*. J. Wiley: 2007.

22. Eng, P. J.; Trainor, T. P.; Brown Jr, G. E.; Waychunas, G. A.; Newville, M.; Sutton, S. R.; Rivers, M. L., Structure of the hydrated α-Al_2O_3(0001) surface. *Science* **2000,** *288*, 1029-1033.

23. Patterson, M. C.; Keilbart, N. D.; Kiruri, L. W.; Thibodeaux, C. A.; Lomnicki, S.; Kurtz, R. L.; Poliakoff, E.; Dellinger, B.; Sprunger, P. T., EPFR formation from phenol adsorption on Al_2O_3 and TiO_2: EPR and EELS studies. *Chem. Phys.* **2013,** *422*, 277-282.

24. McHale, J.; Auroux, A.; Perrotta, A.; Navrotsky, A., Surface energies and thermodynamic phase stability in nanocrystalline aluminas. *Science* **1997,** *277*, 788-791.

25. Elam, J.; Nelson, C.; Cameron, M.; Tolbert, M.; George, S., Adsorption of H_2O on a single-crystal α-Al_2O_3(0001) surface. *J. Phys. Chem. B* **1998,** *102*, 7008-7015.

26. Hass, K.; Schneider, W.; Curioni, A.; Andreoni, W., First-principles molecular dynamics simulations of H_2O on α-Al_2O_3(0001). *J. Phys. Chem. B* **2000,** *104*, 5527-5540.

27. Shapovalov, V.; Truong, T. N., Ab initio study of water adsorption on α-Al_2O_3(0001) crystal surface. *J. Phys. Chem. B* **2000,** *104*, 9859-9863.

28. Ranea, V. A.; Schneider, W. F.; Carmichael, I., DFT characterization of coverage dependent molecular water adsorption modes on α-Al_2O_3(0001). *Surf. Sci.* **2008,** *602*, 268-275.

29. Ranea, V. c. A.; Carmichael, I.; Schneider, W. F., DFT investigation of intermediate steps in the hydrolysis of α-Al_2O_3(0001). *J. Phys. Chem. C* **2009,** *113*, 2149-2158.

30. Meurant, G., *Advances in Catalysis*. Elsevier Science: 1966.

31. Glemser, O.; Rieck, G., Die bindung des wassers in den durch thermische zersetzung von aluminiumhydroxyden entstandenen phasen. *Angew. Chem.* **1956,** *68*, 182-182.

32. Glemser, O., Ergebnisse und probleme von verbindungen der systeme oxyd-wasser. *Angew. Chem.* **1961,** *73*, 785-805.

33. Cormier, S. A.; Lomnicki, S.; Backes, W.; Dellinger, B., Origin and health impacts of emissions of toxic by-products and fine particles from combustion and thermal treatment of hazardous wastes and materials. *Environ. Health Perspect.* 2006, *114*, 810–817.

34. Ballinger, T. H.; Yates Jr, J. T., IR spectroscopic detection of lewis acid sites on alumina using adsorbed carbon monoxide. Correlation with aluminum-hydroxyl group removal. *Langmuir* **1991,** *7*, 3041-3045.

35. Singh, S.; Srivastava, V. C.; Mandal, T. K.; Mall, I. D., Synthesis of different crystallographic Al_2O_3 nanomaterials from solid waste for application in dye degradation. *RSC Adv.* **2014,** *4*, 50801-50810.

36. Hollitt, M.; Grocott, S.; Kisler, J. P.; Beeby, C. J., Feed processing for improved alumina process performance. U.S. Patent No. 6, 582, 670, 2003.

37. Siegel, D. J.; Hector Jr, L. G.; Adams, J. B., Adhesion, atomic structure, and bonding at the Al (111)/α-Al_2O_3(0001) interface: a first principles study. *Phys. Rev. B* **2002,** *65*, 085415-085434.

38. Yang, Z.; Wu, R., First-principles study of the electronic structure and magnetic properties of 3 *d* single or multilayers on a Cu(001) substrate: Ni_1(or Ni 4)/Cu(001), Cu_2/Ni 4/Cu (001), and Co/Cu $_2$/Ni_4/Cu (001). *Phys. Rev. B* **2001,** *63*, 064413.

39. Wong, K.; Zeng, Q. H.; Yu, A. B. In electronic structure of bilayer (Fe, Ni) metallic α-Al_2O_3(0001) catalysts towards CH_4 adsorption and dissociation, *Mater. Sci. Forum*, **2010**, *654*, 2747-2750.

40. Ruan, M.; Hou, H.; Li, W.; Wang, B., Theoretical study of the adsorption/dissociation reactions of formic acid on the α-Al_2O_3(0001) surface. *J. Phys. Chem. C* **2014,** *118*, 20889-20898.

41. Wefers, K.; Misra, C., *Oxides and Hydroxides of Aluminum*. Alcoa Laboratories: 1987.

42. Alavi, S.; Sorescu, D. C.; Thompson, D. L., Adsorption of HCl on single-crystal *α*-Al_2O_3(0001) surface: a DFT study. *J. Phys. Chem. B* **2003,** *107*, 186-195.

43. Delley, B., An all-electron numerical method for solving the local density functional for polyatomic molecules. *J. Chem. Phys.* **1990,** *92*, 508-517.

44. Delley, B., From molecules to solids with the $DMol^3$ approach. *J. Chem. Phys.* **2000,** *113*, 7756-7764.

45. Perdew, J. P.; Burke, K.; Ernzerhof, M., Generalized gradient approximation made simple. *Phys. Rev. Lett.* **1996,** *77*, 3865.

46. Grimme, S., Semiempirical GGA-type density functional constructed with a long-range dispersion correction. *J. Comput. Chem.* **2006,** *27*, 1787-1799.

47. Laidler, K. J.; King, M. C., Development of transition-state theory. *J. Phys. Chem.* **1983,** *87*, 2657-2664.

48. Hosseini, M., Comparison of electronic and optical properties of the *α* and *k* phase alumina using density functional theory. *Chin. J. Phys.* **2009**, *48*, 862-873.

49. Mousavi, S. J., Structural and thermodynamic properties of alumina. *CSM.* **2013,** *1*, 15-24.

50. Wang, B.; Hou, H.; Luo, Y.; Li, Y.; Zhao, Y.; Li, X., Density functional/all-electron basis set slab model calculations of the adsorption/dissociation mechanisms of water on *α*-Al_2O_3(0001) surface. *J. Phys. Chem. C* **2011,** *115*, 13399-13411.

51. Rohmann, C.; Metson, J. B.; Idriss, H., A DFT study on carbon monoxide adsorption onto hydroxylated *α*-Al_2O_3(0001) surfaces. *Phys. Chem. Chem. Phys.* **2014,** *16*, 14287-14297.

52. Touloukian, Y.; Kirby, R.; Taylor, R.; Lee, T., *Thermophysical Properties of Matter*. Plenum, New York, , 1977.

53. French, R. H.; Müllejans, H.; Jones, D. J., Optical properties of aluminum oxide: determined from vacuum ultraviolet and electron energy-loss spectroscopies. *J. Am. Ceram. Soc.* **1998,** *81*, 2549-2557.

54. Wheast, R., *Handbook of Chemistry and Physics*. CRC press, 1984.

55. Lundqvist, S., Density Oscillations in Nonuniform Systems. In *Theory of the Inhomogeneous Electron Gas*, Springer: 1983; pp 149-188.

56. Manassidis, I.; Gillan, M. J., Structure and energetics of alumina surfaces calculated from first principles. *J. Am. Ceram. Soc.* **1994**, *77*, 335-338.

57. Gautier-Soyer, M.; Jollet, F.; Noguera, C., Influence of Surface Relaxation on the Electronic states of the α-Al_2O_3 (0001) surface: A self-consistent tight-binding approach. *Surf. Sci.* **1996**, *352*, 755-759.

58. Wander, A.; Searle, B.; Harrison, N., An ab initio study of α-Al_2O_3 (0001): The effects of exchange and correlation functionals. *Surf. Sci.* **2000**, *458*, 25-33.

59. Tepesch, P.; Quong, A., First-principles calculations of α-Alumina (0001) surfaces energies with and without hydrogen. *Phys. Status Solidi B* **2000**, *217*, 377-387.

60. Ma, L.; Lu, Y.; Li, S.-y.; Zuo, W.; Ji, Z.-q.; Ding, M., First-principles investigation of Sn9zn (0001)/α-Al_2o_3 (0001) interfacial adhesion. *Appl. Surf. Sci.* **2018**, *435*, 863-869.

61. Liu, P.; Han, X.; Sun, D.; Wang, Q., First-principles investigation on the structures, energies, electronic and defective properties of Ti_2Aln surfaces. *Appl. Surf. Sci.* **2018**, *433*, 1056-1066.

62. Lodziana, Z.; Nørskov, J. K., Adsorption of Cu and Pd on α-Al_2O_3(0001) surfaces with different stoichiometries. *J. Chem. Phys.* **2001,** *115*, 11261- 11267.

63. Hinnemann, B.; Carter, E. A., Adsorption of Al, O, Hf, Y, Pt, and S atoms on α-Al_2O_3(0001). *J. Phys. Chem. C* **2007,** *111*, 7105-7126.

64. Verdozzi, C.; Jennison, D.; Schultz, P.; Sears, M., Sapphire (0001) surface, clean and with *d*-metal overlayers. *Phys. Rev. Lett.* **1999,** *82*, 799-802.

65. Carrasco, J.; Gomes, J. R.; Illas, F., Theoretical study of bulk and surface oxygen and aluminum vacancies in α-Al_2O_3. *Phys. Rev. B* **2004,** *69*, 064116-064129.

66. Wallin, E.; Andersson, J. M.; Münger, E. P.; Chirita, V.; Helmersson, U., Ab initio studies of Al, O, and O_2 adsorption on α-Al_2O_3(0001) surfaces. *Phys. Rev. B* **2006,** *74*, 125409-125419.

67. Shukla, M. K.; Hill, F., Plane-wave density functional theory investigation of adsorption of 2, 4, 6-trinitrotoluene on al-hydroxylated (0001) surface of (4× 4) α-alumina. *J. Comput. Chem.* **2014,** *35*, 1977-1985.

68. Colussi, A.; Zabel, F.; Benson, S., The very low-pressure pyrolysis of phenyl ethyl ether, phenyl allyl ether, and benzyl methyl ether and the enthalpy of formation of the phenoxy radical. *Int. J. Chem. Kinet.* **1977,** *9*, 161-178.

69. DeFrees, D. J.; McIver Jr, R. T.; Hehre, W. J., Heats of formation of gaseous free radicals via ion cyclotron double resonance spectroscopy. *J. Am. Ceram. Soc.* **1980,** *102*, 3334-3338.

70. Peters, K. S., Time-resolved photoacoustic calorimetry. *Pure Appl. Chem.* **1986,** *58*, 1263-1266.

71. Oehlschlaeger, M. A.; Davidson, D. F.; Hanson, R. K., Thermal decomposition of toluene: overall rate and branching ratio. *Proc. Combust. Inst.* **2007,** *31*, 211-219.

72. Lucarini, M.; Mugnaini, V.; Pedulli, G. F.; Guerra, M., Hydrogen-bonding effects on the properties of phenoxyl radicals. An EPR, kinetic, and computational study. *J. Am. Ceram. Soc.* **2003,** *125*, 8318-8329.

73. Cowley, R. E.; Bontchev, R. P.; Sorrell, J.; Sarracino, O.; Feng, Y.; Wang, H.; Smith, J. M., Formation of a cobalt (III) imido from a cobalt (II) amido complex. Evidence for proton-coupled electron transfer. *J. Am. Ceram. Soc.* **2007,** *129*, 2424-2425.

74. Wang, J.; Domin, D.; Austin, B.; Zubarev, D. Y.; McClean, J.; Frenklach, M.; Cui, T.; Lester Jr, W. A., A diffusion Monte Carlo Study of the O− H bond dissociation of phenol. *J. Phys. Chem. A* **2010,** *114*, 9832-9835.

75. Angel, L. A.; Ervin, K. M., Competitive threshold collision-induced dissociation: gas-phase acidity and OH bond dissociation enthalpy of phenol. *J. Phys. Chem. A* **2004,** *108*, 8346-8352.

76. Luo, Y.-R., *Handbook of Bond Dissociation Energies in Organic Compounds*. CRC press: 2002.

77. Wright, J. S.; Carpenter, D. J.; McKay, D. J.; Ingold, K., Theoretical calculation of substituent effects on the OH bond strength of phenolic antioxidants related to vitamin E. *J. Am. Ceram. Soc.* **1997,** *119*, 4245-4252.

78. DeTuri, V. F.; Ervin, K. M., Proton transfer between Cl− and C_6H_5OH. O-H bond energy of phenol. *Int. J. Mass Spectrom. Ion Processes* **1998,** *175*, 123-132.

79. Behrman, E., The Elbs and Boyland-Sims peroxydisulfate oxidations. *Beilstein J. Org. Chem.* **2006,** *2*, 1-10.

80. Chandra, A. K.; Uchimaru, T., The OH bond dissociation energies of substituted phenols and proton affinities of substituted phenoxide ions: a DFT study. *J. Mol. Sci.* **2002,** *3*, 407-422.

81. Cabral, B. C.; Canuto, S., The enthalpy of the O–H bond homolytic dissociation: Basis-set extrapolated density functional theory and coupled cluster calculations. *Chem. Phys. Lett.* **2005,** *406*, 300-305.

82. Mulder, P.; Korth, H.-G.; Pratt, D. A.; DiLabio, G. A.; Valgimigli, L.; Pedulli, G.; Ingold, K., Critical re-evaluation of the OH bond dissociation enthalpy in phenol. *J. Phys. Chem. A* **2005,** *109*, 2647-2655.

83. Gómez, I.; Rodríguez, E.; Reguero, M., New insights into the interconversion mechanism between phenol and its isomers. *J. Mol. Struct-Theochem* **2006,** *767*, 11-18.

84. Larsen, N., Microwave spectra of the six mono-^{13}C-substituted phenols and of some monodeuterated species of phenol. Complete substitution structure and absolute dipole moment. *J. Mol. Struct.* **1979,** *51*, 175-190.

85. Liu, R.; Morokuma, K.; Mebel, A. M.; Lin, M., Ab initio study of the mechanism for the thermal decomposition of the phenoxy radical. *J. Chem. Phys.* **1996,** *100*, 9314-9322.

86. Chakarova-Käck, S. D.; Borck, Ø.; Schröder, E.; Lundqvist, B. I., Adsorption of phenol on graphite (0001) and α-Al_2O_3(0001): nature of van der waals bonds from first-principles calculations. *Phys. Rev. B* **2006,** *74*, 155402-155407.

87. Sorescu, D. C.; Boatz, J. A.; Thompson, D. L., First-principles calculations of the adsorption of nitromethane and 1, 1-diamino-2, 2-dinitroethylene (FOX-7) molecules on the α-Al_2O_3(0001) surface. *J. Phys. Chem. B* **2005,** *109*, 1451-1463.

88. De Jong, V.; Cieplik, M. K.; Louw, R., Formation of dioxins in the catalytic combustion of chlorobenzene and a micropollutant-like mixture on Pt/γ-Al_2O_3. *Environ. Sci. Technol.* **2004,** *38*, 5217-5223.

89. Altarawneh, M.; Dlugogorski, B. Z.; Kennedy, E. M.; Mackie, J. C., Mechanisms for formation, chlorination, dechlorination and destruction of polychlorinated dibenzo-*p*-dioxins and dibenzofurans (PCDD/Fs). *Prog. Energy Combust. Sci.* **2009,** *35*, 245-274.

90. Flikkema, E.; Bromley, S. T., Dedicated global optimization search for ground state silica nanoclusters:(SiO_2) N (N= 6-12). *J. Phys. Chem. B* **2004,** *108*, 9638-9645.

CHAPTER 8

Formation of Phenoxy-Type EPFR over Hydrated Pure Alumina and Si-alumina Surfaces

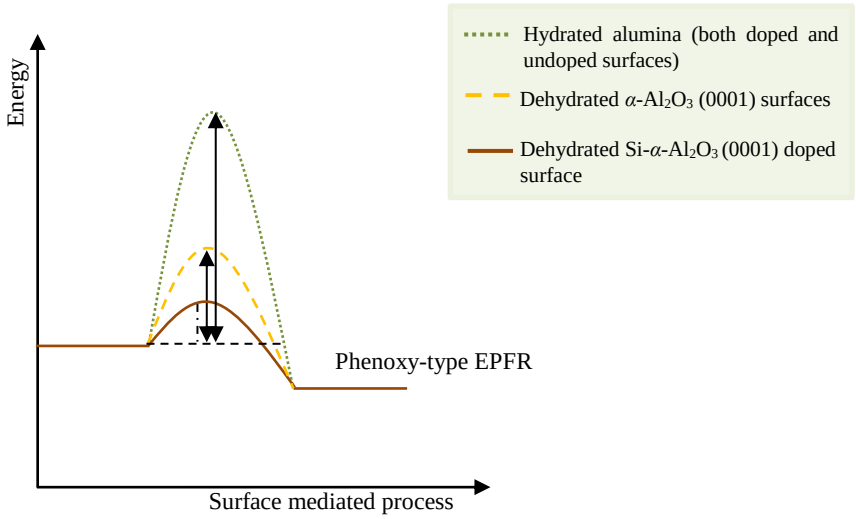

Catalytic activity of alumina surfaces toward the formation of phenoxy-type EPFR.

Si atom has enhanced the catalytic activity of the dehydrated alumina surface by ~36 %.

Hydration layer over alumina surface (both doped and undoped surfaces) increase the energy requirement for the formation of the attached phenolate adducts on the surface.

8.1 Introduction

Phenols and phenolic compounds constitute major precursors for the synthesis of polychlorinated dibenzo-*p*-dioxins and dibenzofurans.[1-6] Their principle sources are coal conversion plants, petroleum, municipal waste treatment plants, synthetic processing and phenol producing industries.[7-9] In municipal waste incinerators (MWIs), these species reach concentrations of up to 1000 μg/m^3.[10] In the cool zone of a typical MWI, metal oxides, typically dispersed on alumina and titania provide catalytic surfaces that facilitate the production of environmentally persistent free radicals from phenol[11-12] via physisorption and chemisorption processes.

The appreciable concentrations of alumina in MWIs enable it to serve as an important surface mediator for the heterogeneous formation of PCDD/Fs. Its concentration in fly ash can reach up to 25–30%, by mass.[13] In light of the temperature window of the cooling-down zone of the combustor, which is typically 200-600℃[14-16], the alumina surface can be present as a combination of hydrated and dehydrated facets. The interplay of alumina and water has been a thematic topic of a great deal of research.[17-25] In the course of water interaction with alumina, the hydroxyl groups on the alumina surface can reversibly be removed by heating, producing a fully dehydrated surface of alumina at a temperature of 450-600 °C.[26] Hence, the lower and higher temperature ends of the cooling zone involves the hydrated and dehydrated surfaces of alumina, respectively. In Chapter 7[27], we investigate the interaction of phenol with the dehydrated alumina (0001) surface. We find that the mixed Al/O surface termination along the (0001) place facilitates rupture of the phenol's O-H bond, producing phenolate—a species that signifies an important candidate of persistent surface bound radicals. Nonetheless, by

considering the temperature range of interest, a dehydrated alumina surface represents a limiting case scenario for alumina configurations in which hydrated and dehydrated entities coexist. Thus, propping all modes of interaction between phenol and alumina necessitates addressing the pathways underlying the generation of EPFR on a hydrated alumina surface. Likewise, in real scenarios, trace loads of elements (Si, Cd, Zn, Fe) in combustion systems could readily be deposited on pure termination of alumina. Thus, it is important to investigate the effect of atomic dopants on the efficiency of hydrated alumina surfaces in producing phenoxy-type EPFR.

To this end, this Chapter has a threefold aim, (i) to report the modes of interactions between phenol and hydrated α-Al_2O_3 (0001) surfaces, (ii) to offer some important insights into the Si-Al_2O_3 doping system and its effect on the catalytic activity of the surface, and (iii) to improve our current understanding of chemical phenomena operating in the formation of EPFR over both doped and undoped alumina surfaces. This Chapter begins by describing the computational method, and this is followed by a detailed investigation of the molecular interaction of phenol over a hydrated alumina surface. Finally, we describe the mechanism of surface-mediated dissociation of the hydroxyl bond in phenol over doped hydrated and dehydrated alumina surfaces and undoped hydrated alumina surfaces.

8.2 Computational Methodology

As in the preceding Chapters, the DMol^3 program performs structural optimisations, energy computations, and estimation of vibrational frequencies.[28-29] Chemisorbed and chemisorbed

structures were fully optimised using the Perdew-Burke-Ernzerhof[30] function as the exchange-correlation within the generalised gradient approximation family. Final energies were corrected by incorporating a Grimme dispersion correction[31]. A double-polarised numeric basis set of DNP is considered.[28] A total of 4×4×1 κ-points was employed to integrate the Brillouin zone. A 2×2 α-Al_2O_3 (0001) surface was used in all calculations. A 30 Å vacuum distance separates the slab and its image in the periodic system along the *z*-direction. The energies and total forces converge with a tolerance of 1×10^{-6} Ha and 1×10^{-5} Ha/Å, respectively.

We estimate the average binding energies for on-surface adsorption (E_b) using the following formula:

$$E_b = E_{slab + phenol} - E_{slab} - E_{phenol} \quad 8.1$$

where $E_{slab + phenol}$, E_{slab}, and E_{phenol} denote the energies of a phenol/Al_2O_3 system, the α-Al_2O_3 (0001) surface, and the energy of an isolated phenol molecule, respectively.

Reaction rate constants are fitted to the Arrhenius equation (i.e. $k(T) = A \exp(-E_a/RT)$) in the temperature range of 298.15 to 1000 K, according to the classical transition state theory[32]:

$$k(T) = \frac{k_B T}{\sigma_e h} \exp\left(\frac{\Delta S^{\neq}}{R}\right) \exp\left(\frac{-\Delta H^{\neq}}{RT}\right) \quad 8.2$$

where: k_B is Boltzmann's constant, h signifies Plank's constant, R is the universal gas constant. $\Delta S^{\neq}$ and $\Delta H^{\neq}$ represent the entropy and enthalpy of activation, respectively, at a certain temperatures, T, and σ_e is a reaction degeneracy number.

8.3 Results and Discussion

8.3.1 Bulk Properties of Aluminium Oxide

Our study in Chapter 7 contrasts the geometries and energies of the optimized bulk unit cell of amorphous alumina (i.e. the thermodynamically stable phase, α-Al_2O_3[33-34]) with analogous experimental values. The calculated bulk lattice parameters a= 4.80 and c= 13.01 Å[27] are in accordance with the experimental values at 4.76 and 13.00 Å, respectively.[35] The estimated cohesive energy, E^{coh}, per Al_2O_3 rhombohedral unit is 32.6 eV; this value is in good agreement with the experimental measurement of 31.8 eV.[36]

8.3.2 Clean Al_2O_3 Surface

We constructed the structure of the hydrated alumina surface by adding four water molecules to the dehydrated alumina surface deployed in Chapter 7.[27] Figure 8.1 presents the optimized geometry of the hydrated alumina surface. As shown in the Figure, each surface Al atom is bonded by three oxygen surface atoms (O1, O2, and O3). It has been found that the most thermodynamically stable configuration for the dissociated water molecules comprises a 1,2-

addition pathway. [22] Accordingly, each Al surface Al atom is attached to a hydroxyl group leaving a protonated nearby oxygen atom (i.e. O1 in Figure 8.1).

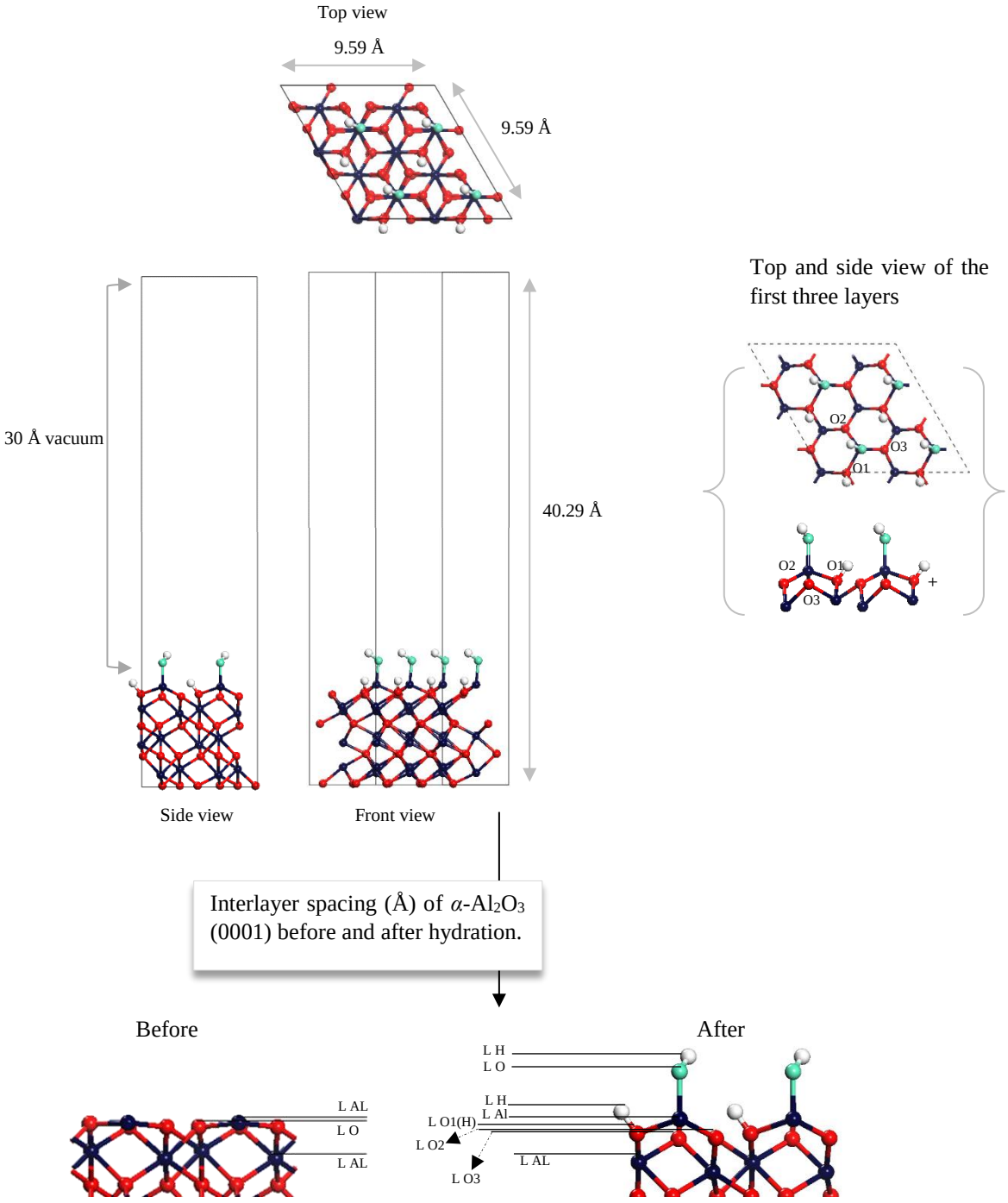

Figure 8.1. Unit cell (with slab and vacuum) employed in the periodic slab calculation for the α-Al_2O_3 (0001) hydrated surface. Blue, red, green and white spheres denote Al atoms, O surface atoms, water O atoms and H atoms, respectively.

To clarify how the surface geometry changes with interaction with water molecules, we measured the surface relaxations and reconstructions of the hydrated alumina surface depicted in Figure 8.1. We found that hydration leads to a significant change in both relaxation and reconstruction of the surface. For instance, the second layer, oxygen layer LO, is relaxed into three sub-layers (i.e. LO1, LO2, and LO3), as shown in Figure 8.1. The first sub-layer containing the protonated O1(H) experienced a downward displacement by 0.53 Å below the Al layer. In comparison to the dehydrated alumina surface, such an interlayer distance is found to be 0.15 Å. Accordingly, the inter-layer distance between the Al and O layers increased by 0.38 Å. The downward displacements in the second and the third sub-layers were measured to be 0.16 and 0.03 Å, respectively. The inter-layer distances between the top two layers of the dehydrated alumina surface and its corresponding layers in the hydrated surface are presented in Table 8.1. Our results are in good agreement with those obtained by Shukia and Hill[37], i.e. the interlayer spacings in both studies are within 0.01 Å.

Table 8.1. Interlayer spacing (Å) of α-Al_2O_3 (0001) before and after hydration (i.e. water addition).

	Current study		**Literature (37)**	
Layer	Before hydration	After hydration	Before hydration	After hydration
H	-	-	-	-
O	-	0.55	-	0.55
H	-	1.46	-	1.48
Al	-	0.26	-	0.23
O1(H)	0.15	0.53	0.12	0.56
O2	-	0.16	-	0.17
O3	-	0.03	-	0.03
Al	0.89	0.85	0.89	0.84

Now we address the deviations in the surface reconstruction; the three surface Al-O bond distances, Al-O1, Al-O2, and Al-O3, increased asymmetrically in the order of 8.48% for Al-O1(H) and 2.63%, 3.99% for the other two bonds, respectively, all with respect to the clean dehydrated alumina surface where the three bonds are equivalent (1.71 Å). (Refer to Figure 8.1 for atoms numberings). Our observations concur with those reported by Shukia and Hill in their study of the interaction of trinitrotoluene (TNT) with a hydrated alumina surface.[37] The authors reported that, after adding water molecules to the surface, the Al-O1 (H) bond distance increased by 9.8% compared to the Al-O bond of the dehydrated alumina surface (1.693 Å), while the other two Al-O bonds elongated by 3.19% and 3.84%, respectively.

8.3.3 Molecular Physisorption of Phenol

In this section, we investigate the physisorbed (non-dissociative) adsorption of molecular phenol on the (0001) hydrated alumina surface. Phenol molecules were initially positioned horizontally and vertically above the surface. We found that all optimizations starting from the horizontally adsorbed phenol molecule converged to a slightly titled geometry (i.e. M_h). This is consistent with the corresponding optimized geometries of phenol molecules over dehydrated alumina surfaces presented in Chapter 7.[27, 38] The stable optimised geometries of the phenol molecule adsorbed on the surface are shown in Figure 8.2.

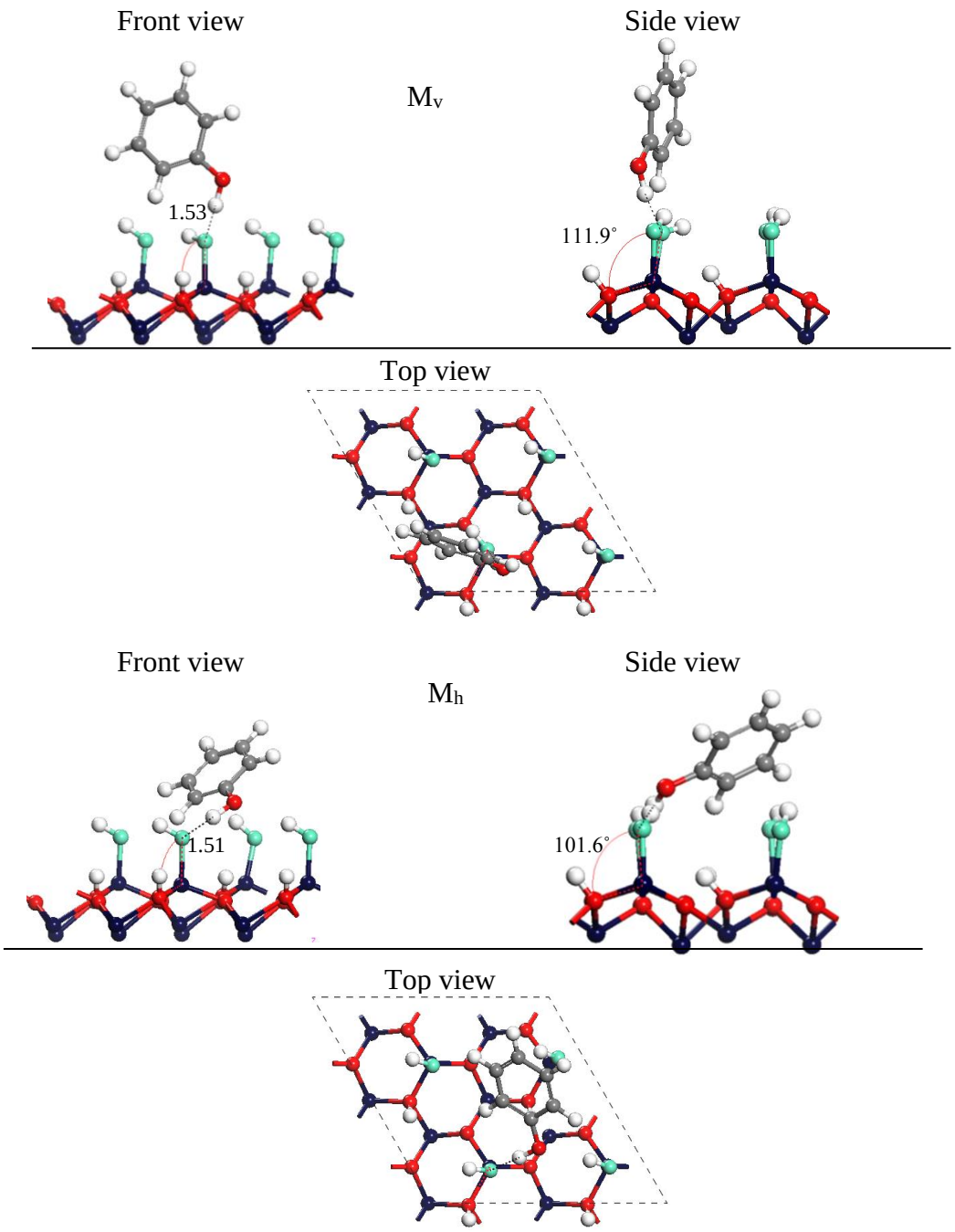

Figure 8.2. Top, side, and front views of the stable geometries of molecular phenol physisorbed on hydrated α-Al_2O_3 (0001) configurations. Distances are in Å.

Table 8.2 summarises the calculated binding energies, the percentage increase of B-O bond length in reference to gas phase phenol, tilt angle (with respect to the ground level), and the

distance between the hydrogen atom of phenol molecule and the nearest oxygen atom of the hydroxyl group attached to the alumina surface. The calculated binding energies for the M_v and $M_{h,}$ structures are predicted to be -91 kJ/mol and -136 kJ/mol, respectively (based on eq. 8.1 in reference to separated reactants). In Chapter 7 on the interaction of phenol molecules with dehydrated alumina surfaces[27] we found that molecular adsorption of phenol molecule entails binding energies of -127 kJ/mol and -171- -202 kJ/mol for the vertical and tilted configurations, respectively. Evidently, the hydration layer over α-Al_2O_3 (0001) systematically reduces the molecular adsorption energy. The same behaviour was observed by Shukla and Hill[37] in their study of the interaction of TNT over a hydroxylated alumina surface. The authors found that hydration of the α-Al_2O_3 (0001) surface leads to a decrease the molecular adsorption of TNT by 85 kJ/mol.

Table 8.2. Binding energies, O-H bond distance, phenol-surface interaction distance, and tilt angle for the adsorption configurations.

Structure	**Binding energy (kJ/mol)**	**% increase of B-O bond length in reference to gas phase phenol (Å)**	**Phenol-Surface interaction distance (Å)**	**Tilt angle (˚)**
M_v	-91	6.2 %	1.533	70.8
M_h	-136	7.0%	1.514	25.3

By comparing the geometric parameters of the alumina surface with and without the phenol molecule for both orientations, we can predict the geometrical changes induced in the surface by phenol adsorption. One obvious characteristic is the marginal rotation of the involved

surface hydroxyl groups. For example, the corresponding angle in the M_v structure increases by 3° compared with the corresponding value of the clean hydrated surface of alumina (i.e. 108.9°). The interatomic distance between O_w and Al_{surf} increased by 0.041Å, in both orientations. Furthermore, a very minimal shrinkage in the Al_{surf}-O_{surf} (H) bond is observed (~0.02 Å).

8.3.4 Surface-Mediated Dissociation of Phenol

8.3.4.1 Undoped α-Al_2O_3 (0001) Surface

Dissociation of phenol molecule over the alumina surface results in the formation of either a phenoxy moiety (i.e. phenolate anion) or a phenyl moiety. In Chapter 7, we found that rupture of the aromatic C-H bond over the dehydrated surface causing an OH-phenyl adduct to incur a very high energy barrier of approximately 333 to 390 kJ/mol. Accordingly, herein we only limit our analysis on pathways leading to the formation of a phenoxy moiety.

Two possible pathways are considered; water elimination mechanism and hydrogen elimination corridor. Scheme 8.1 displays both mechanisms. The first mechanism signifies a concentric pathway for the elimination of a surface group along with the phenolic H atom as a water molecule and the attachment of the phenoxy's O to a surface Al atom. In the second pathway, a hydrogen molecule is produced upon fission of the phenolic' O-H and hydroxyl O-H bonds in a process that forms a peroxy linkage between the phenolic's O and the surface hydroxyl's O. Two dissociative structures are produced from the water and hydrogen

elimination mechanisms, which results in two different dissociative structures, termed D_1 and D_2.

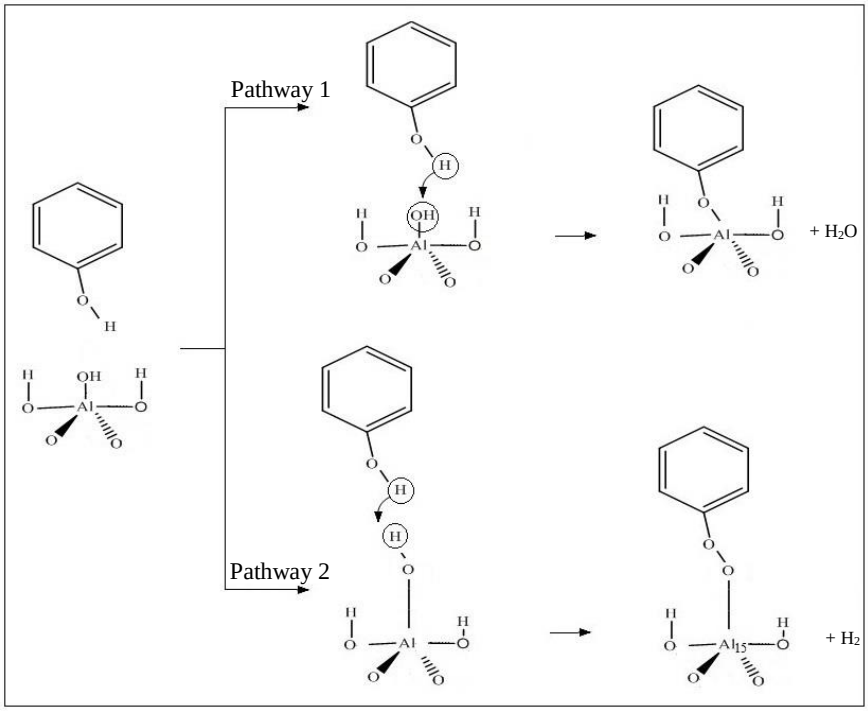

Scheme 8.1. Reaction pathway for the interaction of phenol with hydrated alumina surface.

As shown in Figure 8.3, in D_1 the dissociated phenolate adduct attaches itself to Al_{surf} and the detached hydrogen atom bonds with the dissociated hydroxyl group (OH_w) forming a water molecule. In the D_2 configuration, a hydrogen molecule is eliminated in a process that forms a peroxy-type bond between the phenoxy radical and a surface Al(O) site.

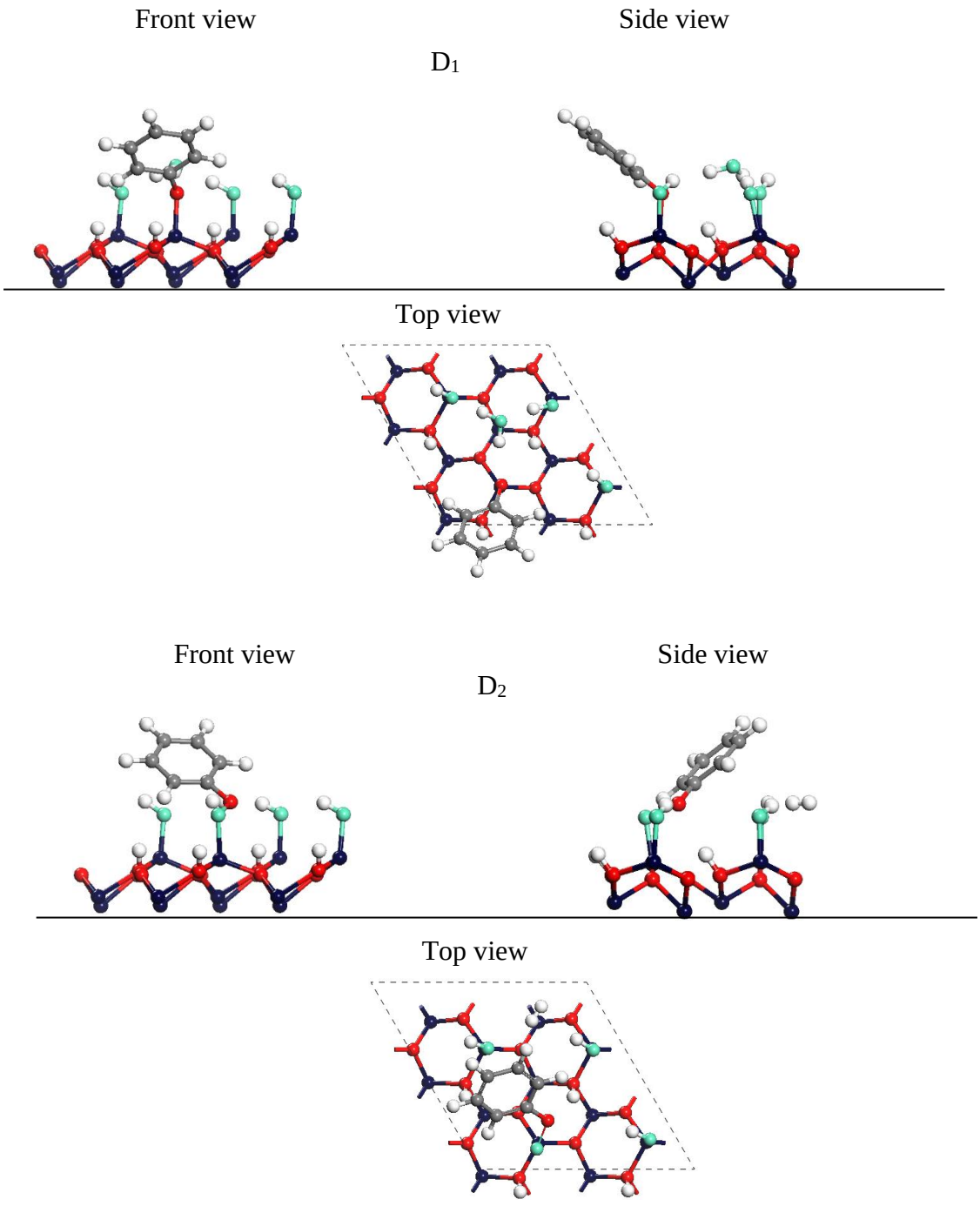

Figure 8.3. Top and front views of the stable dissociated structures of phenol over the hydrated α-Al_2O_3 (0001) surface.

Energy profiles for the two reaction corridors are depicted in Figure 8.4. Both dissociative pathways are assumed to initiate from the physisorbed state of M_v. The formation of the two

products D_1 and D_2 was found to be endothermic. Water elimination via pathway requires an activation energy of 195 KJ/mol, which is significantly lower than the tremendous energy barrier required for H_2 elimination in the pathway i.e. 432 kJ/mol. Therefore, the formation of a phenoxy moiety is thermodynamically preferred via the H_2O elimination mechanism.

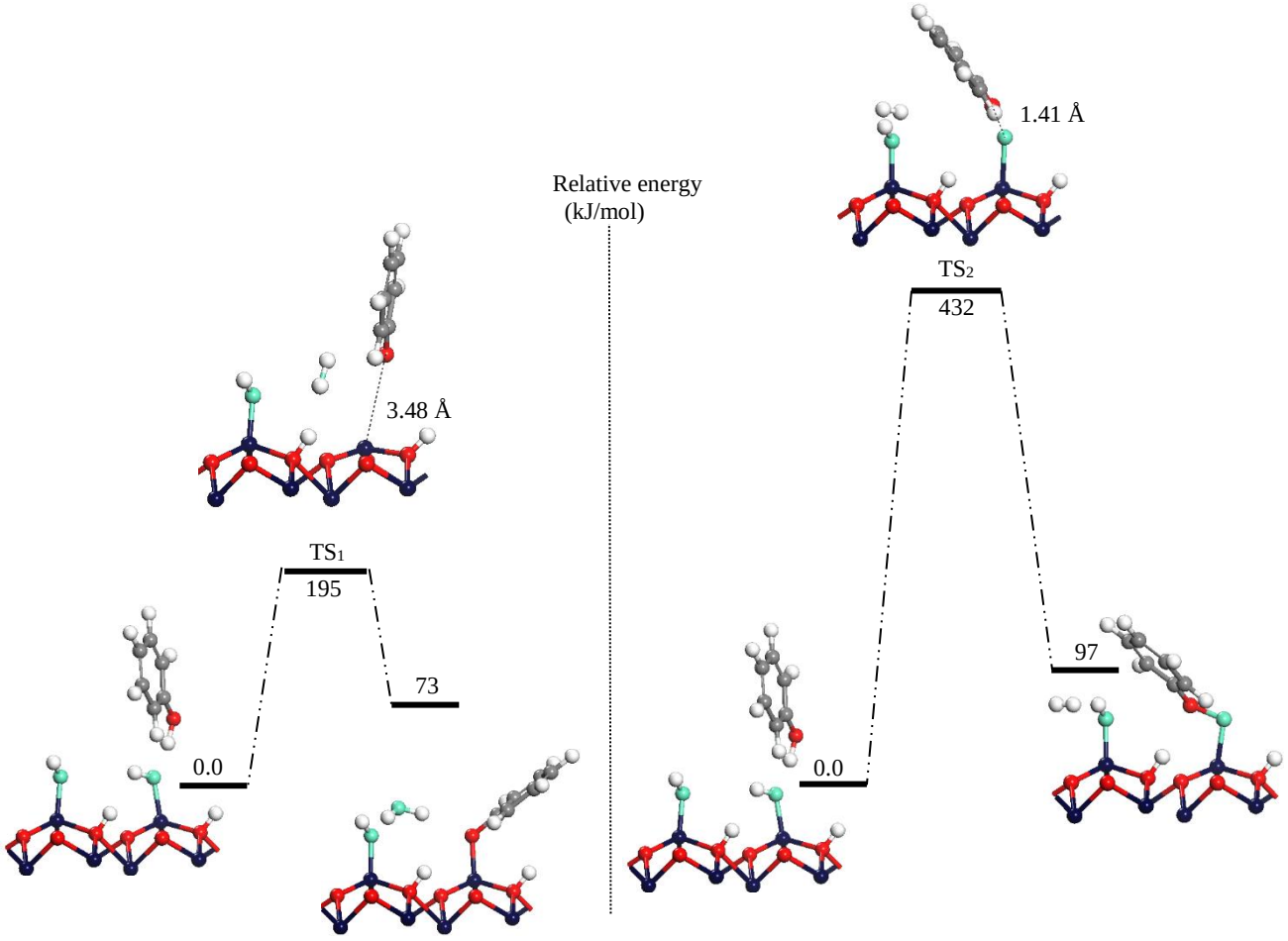

Figure 8.4. Relative energy describing the dissociated structures of phenol over the α-Al_2O_3 (0001) hydrated surface. Pathway 1 (TS_1) and Pathway 2 (TS_2). Values (in kJ/mol) of energies are in reference to physisorbed reactant.

Chapter 7[27] investigated the interaction of phenol with the dehydrated alumina surface. We found that the dehydrated alumina produces surface-bound phenolate through an energy barrier of only 48 kJ/mol.[27] In reference to the energy barrier of pathway 1 (195 kJ/mol), it is inferred

that hydroxyl radicals attached to surface Al atoms substantially increase the energy requirement for the formation of the attached phenolate adducts on the surface. Over the dehydrated surface, the underlying mechanism is characterised by direct fission of the hydroxyl's O-H bond over the surface Al-O bond. On the contrary, surface-bounded phenolate motilities are generated over the hydrated alumina via water elimination; this process that typically requires a higher energy barrier.

8.3.4.2 Doping α-Al_2O_3 (0001) Surface with Silicon

Recently, there has been a renewed interest in examining a potential improvement in the catalytic activity of transitional metal oxides by replacing a fraction of the surface oxide cations with another cation.[39-40] The emerging role of dopants in the catalytic activity of oxide catalysts has been investigated from many aspects. For example, some dopants, via the Mars-van Krevelen mechanism,[41-42] display a profound ability to weaken nearby surface oxygen atoms and accordingly producing oxygen vacancies.[43-46] Such doping enhances the performance of environmental catalysts such as ceria, widely deployed in the so-called three-ways catalysts.[40, 47] Dopants of a higher valence, compared to surface cations, tend to increase the rate of surface adsorption of O_2 molecules.[47] In other scenarios, the presence of the dopant in the surface oxide increases the uptake of gas phase molecules and subsequent dissociative adsorption of molecules. An example of this is a theoretical study by Pala and Metiu (2008)[48], who investigate the dissociative adsorption of methanol on a ZnO $(10\bar{1}0)$ surface doped with K, Au, Ag, Cu, Al, Na, Ti, and Mg atoms. The authors found that, unlike the undoped surface, where

methanol preferred to adsorb molecularly, certain doped surfaces triggered dissociation of the hydroxyl's OH bonds, thereby forming an adsorbed methoxy adduct.

Mounting evidences suggests that silica is among the most important metal oxides in the formation of EPFR.[49-50] It represents the core component of fly ash (5-50%), and in catalytic systems it plays a key role either as the catalyst itself and/or as support for transition metals. For this reason, we selected silica in particular in our study. Herein, we investigate the dissociative adsorption of a phenol molecule over a Si-α-Al_2O_3 (0001) doped surface. The underlying aim is to assess to what extent doping alumina, either hydrated or dehydrated form, can modify its catalytic activity in producing phenoxy-type EPFR.

8.3.4.2.1 Structural Changes Caused by Si Doping

The structure of the dehydrated α-Al_2O_3 (0001) surface with Si dopant in the surface layer is shown in Figure 8.5. Al surface atoms in the (0001) dehydrated alumina surface are coordinated by three oxygen surface atoms with equivalent Al-O bond distances of 1.71 Å and by the three oxygen atoms from the layer below with an Al-O bond distance of 2.85 Å (see Figure 8.5). The doping α-Al_2O_3 (0001) surface with the Si atom leads to significant changes in the atomic arrangements. Unlike the Al atom, which does not form a genuine chemical bond with oxygen atoms in the layer below (Al-O distance is 2.85 Å), the Si doped atom links with oxygen atoms with a bond distance of 2.13 Å. The interatomic distances between the dopant and the three surface oxygen atoms are 0.05 Å shorter than the analogous Al-O bonds (1.66 Å in Si doped surface versus 1.7 Å in undoped alumina surface). Clearly, this shortening stems from the fact that the Si atom is pulled down toward the oxygen atoms from the layer below.

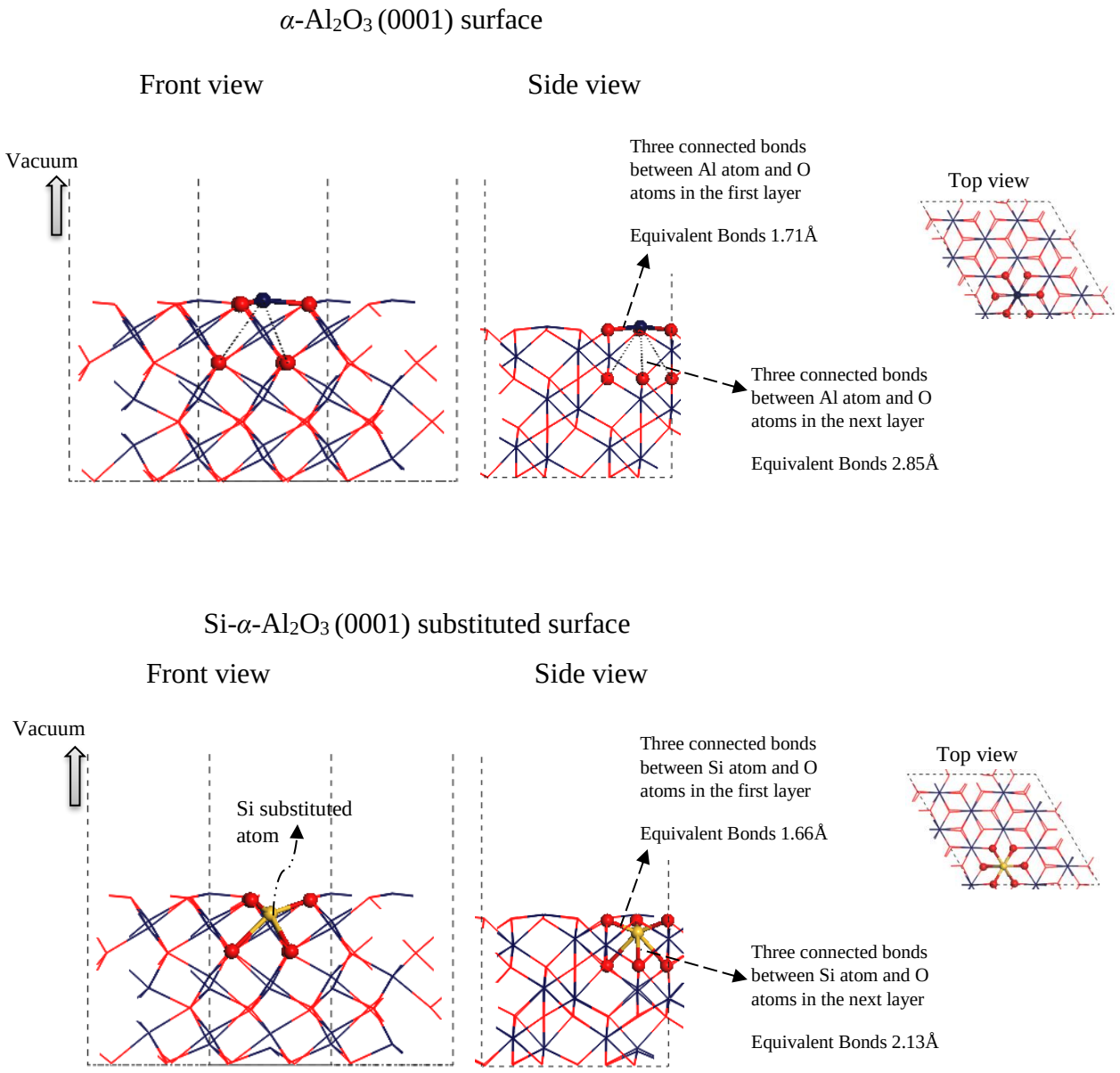

Figure 8.5. Front, side, and top views of the clean α-Al_2O_3 (0001) surface and the Si-α-Al_2O_3 (0001) substituted surface

The change in the hydrated alumina surface caused by the Si dopant becomes more evident with the presence of the hydrated layer over the surface. Figure 8.6 and Table 8.3 display in detail the structural change in the hydrated alumina surface induced by doping the surface with

the Si atom. The bond lengths between the dopant Si atom and the three oxygen atoms O_1, O_2, and O_3 are 1.729, 1.626, and 1.643 Å, respectively, i.e., these are ~0.14 Å shorter than the corresponding bond length of the hydrated alumina surface (refer to data in Table 8.3).

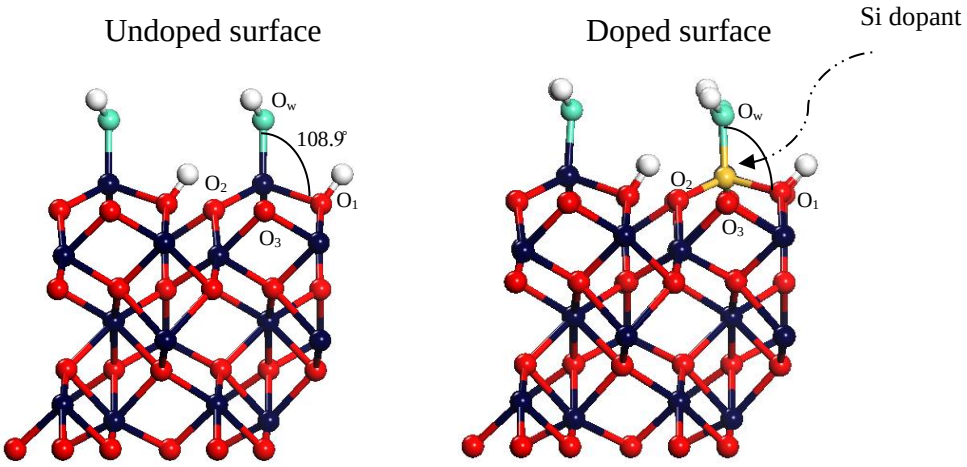

Figure 8.6. Side view of the hydrated α-Al_2O_3 (0001) surface and the Si-α-Al_2O_3 (0001) substituted surface.

Table 8.3. Distances and bond angle between the dopant in the surface layer of the hydrated alumina surface and its neighbouring atoms (as shown in Figure 8.6).

Bond	**Undoped surface / *X*=Al**	**Doped surface / *X*=Si**
X-O_1 /Å	1.86	1.729
X-O_2 /Å	1.759	1.626
X-O_3 /Å	1.768	1.628
X-O_w /Å	1.737	1.643
O_w-Al-O(H) angle /°	108.9	106.4

8.3.4.2.2 Effect of Doping on the Catalytic Activity of the α-Al_2O_3 (0001) Surface

Figure 8.7 displays the energy profile for the interaction of a phenol molecule with the Si-*α*-Al_2O_3 (0001) substituted surface. The reaction proceeds via the physisorbed interaction between the phenol molecule and the surface at a binding distance of 1.62 Å above the surface. The phenol molecule dissociates over the surface through a trivial energy barrier of only 31 kJ/mol, where the phenoxy moiety attaches to the Si atom and the hydrogen atom binds to a nearby O atom. This leads to the dissociated structure M_{sd} with a binding energy of -108 kJ/mol (based on eq. 8.1 in reference to separated reactants).

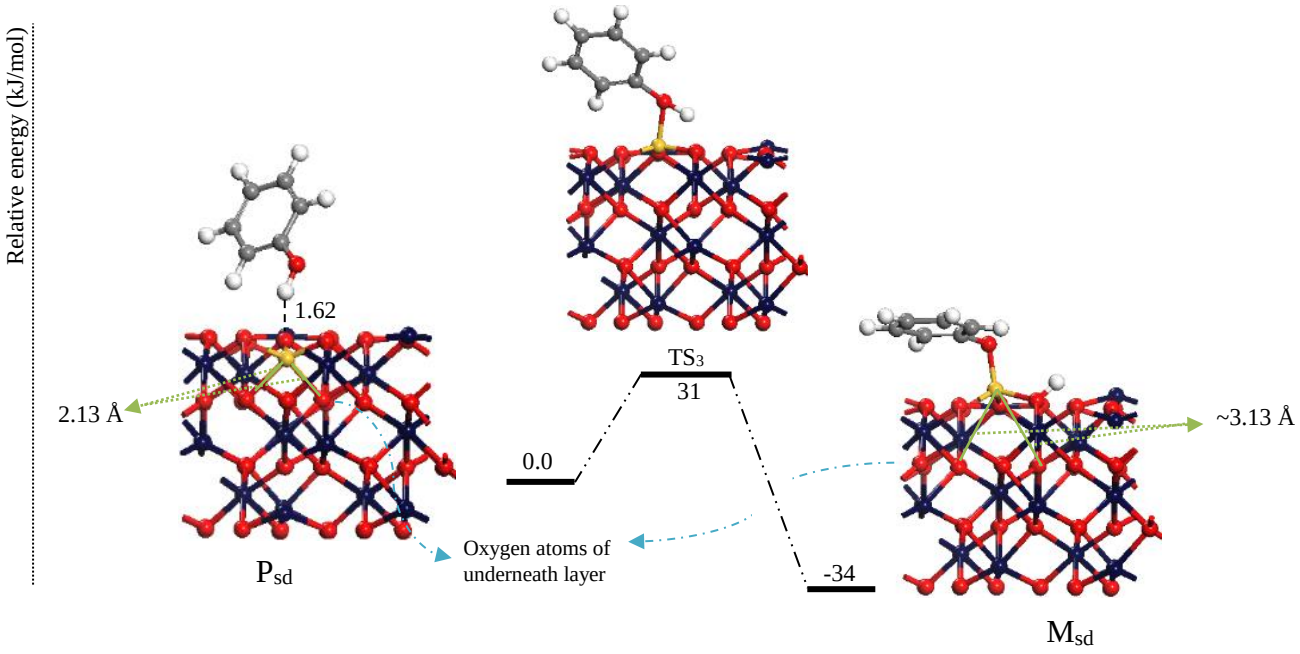

Figure 8.7. Relative energy for phenol molecule dissociation over the Si-*α*-Al_2O_3 (0001) substituted surface via dissociation pathway 3 (TS_3). Values (in kJ/mol) of energies are in reference to physisorbed reactants.

The Si doped atom was found to increase the catalytic activity of the dehydrated alumina surface in producing phenolate adduct, in which the required energy barrier for the formation of phenoxy moiety decreased by 17 kJ/mol compared to the undoped surface (i.e. 48 kJ/mol, reported in Chapter 7[27]). A possible explanation for this trend originates from the high coordination number of the Si atom compared to the Al surface atom. The Si atom is saturated by its attachment to phenolic's oxygen atom. A closer inspection of the structure of the alumina surface in the dissociated product M_{sd} (Figure 8.7) reveals noticeable structural changes induced in the Si atom. Unlike the physisorbed structure, P_{sd}, where the Si atom moved down and bonded to three oxygen atoms from the layer below, the Si atom in the M_{sd} product is pulled up toward the phenoxy moiety and accordingly become truly unbounded to the oxygen atoms from the layer below. The distance between the Si atom and the oxygen atoms from layer below increases by ~2.00 Å compared to the corresponding value in the clean doped surface (2.13 Å in Figure 8.5). Furthermore, the calculated Mulliken atomic charges for the substituted Si atom and the Al atom in the undoped dehydrated alumina surface were found to be 1.74 and 1.47 *e*, respectively. This indicates that the surface Si atom exhibits more acidity than the Al atom. Such variation in this electronic attribute explains the difference in energy barrier between clean alumina and Si-doped alumina surfaces; i.e. 31 kJ/mol versus 48 kJ/mol.

In an analysis of the catalytic effect of silica on the surface-mediated reactions, Pan et al.[50] found that the silica surface mediates formation of polychlorinated Dibenzo-*p*-Dioxins from the oxidation of 2-chlorinated. The authors theoretically examined the interaction of 2-chlorophenol (2-CP) over both hydrated and dehydrated silica clusters. They found that dehydrated silica clusters produce 2-chlorophenolate from the 2-CP molecule through energy barriers of 27 and 49 kJ/mol over bridge and defect (double bonded) sites, respectively.

Similarly, in our recent study on the formation of PCDD/Fs from 2-CP over neat SiO_2 clusters,[49] we investigated the formation of pre-PCDD/F intermediates. In line with the previous finding of Pan et al.[50], we found that silica facilitates the synthesis of pre-PCDD and pre-PCDF intermediates via the Eley−Rideal mechanism through two different channels that eliminate HCl and Cl_2, demanding accessible energy barriers of 61 and 82 kJ/mol, respectively.

Next, we describe the effect of Si doping on the catalytic activity of the hydrated α-Al_2O_3 (0001) surface. The mechanistic details of the interaction are similar to that discussed in Section 8.3.4.1. Two reaction pathways have been considered, namely pathway 4 and pathway 5, characterising the H_2O and H_2 elimination mechanisms, respectively. Figure 8.8 displays the energy profile for the interaction of a phenol molecule with the hydrated Si-α-Al_2O_3 (0001) substituted surface. The formation of the phenoxy moiety in both reaction pathways is endothermic with very sizable energy barriers of 247 and 418 kJ/mol, respectively. By considering the water elimination pathway, the Si-OH-site results in a noticeable increase in the reaction barrier for the formation of phenolate over the Al-OH site (195 kJ/mol versus 247 kJ/mol). This is clearly in contrast to the case of the dehydrated alumina surface, in which the energy barrier for the water elimination mechanism was reduced by doping (48 kJ/mol versus 31 kJ/mol). Nonetheless, doping of the hydrated surface does not modify the energy barrier for the hydrogen elimination channel; 418 kJ/mol versus 432 kJ/mol.

There is a positive correlation between the calculated energy barriers for the H_2O elimination mechanism, in both doped and undoped surfaces, and the O-Si/Al bond dissociative energies. For instance, the calculated bond dissociation energies for O-Si and O-Al are 798 kJ/mol[51] and 512 kJ/mol[51], respectively. The difference in the bond dissociation energies of O-Al/Si

correlates with the difference in the energy barriers for the water elimination corridors for the Si(O) and Al(O) sites at 247 and 195 kJ/mol, respectively.

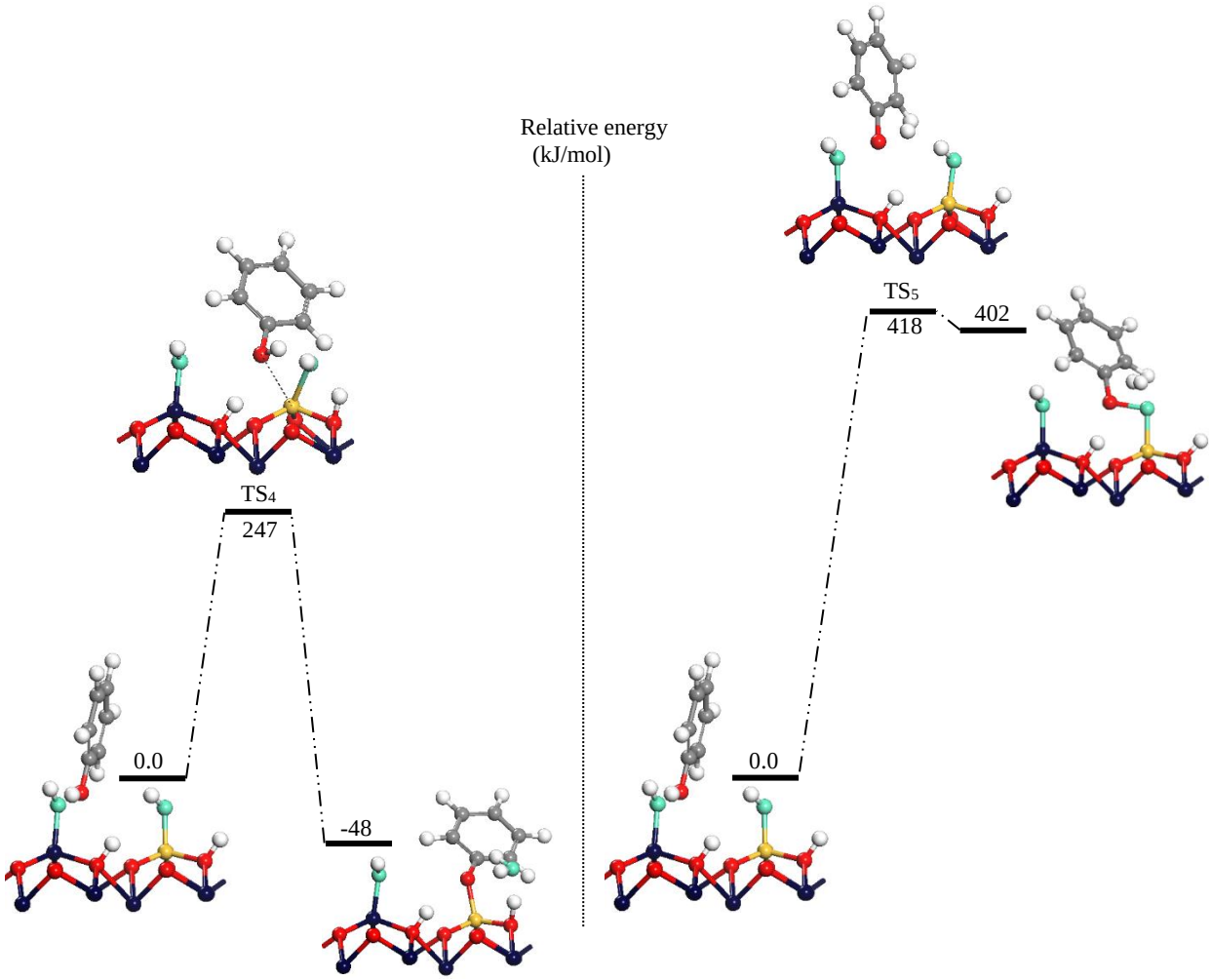

Figure 8.8. Relative energy describing the dissociated structures of phenol over Si-α-Al_2O_3 (0001) substituted surface via dissociation pathway 4 (TS_4) and pathway 5(TS_5). Values (in kJ/mol) of energies are in reference to physisorbed reactants.

Furthermore, desorption of the phenolate moiety into a vacuum, from both Si-doped alumina surfaces, was found to be highly endothermic at 300 kJ/mol. This finding is in accordance with

those reported in our studies for the interaction of phenol[27] (Chapter 7) and chlorophenol[49] molecules over an alumina surface and a silica cluster at 394 kJ/mol and 379 kJ/mol, respectively. These high energy values indicate that the desorption of the phenolate moiety from the surface renders such a corridor largely inaccessible. As discussed in the literature,[49] the profound stability of the phenolate species over alumina and silica surfaces enable these adducts to yield PCDD/Fs using the so-called LH and LR mechanisms.

8.3.5 Kinetic Considerations

Herein, we report the reaction rate constants for all investigated pathways. As discussed in Section 8.2, the search of the transition state is carried out by synchronous and quadratic synchronous transit approaches (LST/QST). Calculated reaction rate constants are fitted to the Arrhenius equation. Figure 8.9 represents the Arrhenius plots and Table 8.4 lists the calculated reaction rate parameters. Reaction pathway 3, representing water elimination over the Si-doped dehydrated alumina surface, incurs the lowest activation energy and displays almost a temperature-independent behaviour, in reference to other reaction pathways of the hydrated system.

Table 8.4. Kinetic parameters for surface dissociation reactions.

Name	**Reaction**	E_a **(kJ/mol)**	A **(s^{-1})**
Pathway 1	Formation of phenolate moiety over hydrated α-Al_2O_3 (0001) surface via H_2O elimination mechanism	186	1.06×10^{16}
Pathway 2	Formation of phenyl moiety over hydrated α-Al_2O_3 (0001) surface via H_2 elimination mechanism	419	5.44×10^{17}
Pathway 3	Formation of phenolate moiety over Si- α-Al_2O_3 (0001) doped dehydrated surface	33	4.94×10^{15}
Pathway 4	Formation of phenoxy moiety over Si- α-Al_2O_3 (0001) doped hydrated surface via H_2O elimination mechanism	231	1.81×10^{11}
Pathway 5	Formation of phenoxy moiety over Si- α-Al_2O_3(0001) doped hydrated surface via H_2 elimination mechanism	385.6	4.59×10^{12}

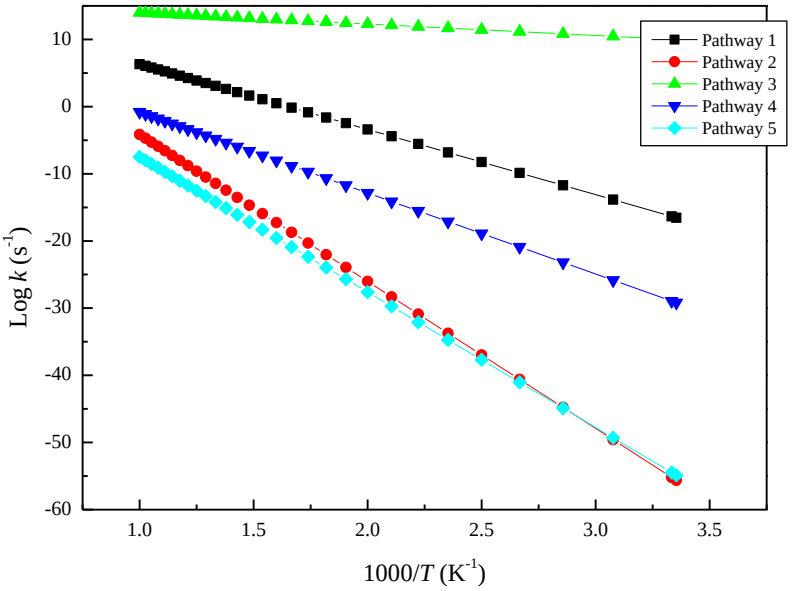

Figure 8.9. Arrhenius plots for the studied reactions.

8.4 Conclusions

This Chapter sets out to determine the catalytic potential of the hydrated α-Al_2O_3 (0001) surface and the Si modified α-Al_2O_3 (0001) surface in producing phenoxy-type EPFR. We investigated the physisorbed and chemisorbed interaction of phenol with the hydrated α-Al_2O_3 (0001) surface. Dissociative adsorption of phenol molecule occurs via either H_2O or H_2 elimination mechanisms. In view of the calculated energy barriers, the production of a phenolate adduct through the water elimination mechanism largely prevails over that entailing elimination of a hydrogen molecule over all considered structural configurations. Our results based on the estimated activation energies show that the hydroxyl layers attached to the hydrated surface form a shield against attack of the phenol molecules on the surface. A major finding to emerge from this Chapter is that dehydrated alumina surface doped with Si atoms enhances the catalytic activity of the surface in reference to Al sites by ~36% (based on the difference in

analogous activation energies). On the contrary, this effect was not observed in the hydrated alumina surface owing to the presence of the OH- layer.

8.5 References

1. Jansson, S., *Thermal Formation and Chlorination of Dioxins and Dioxin-Like Compounds*, Umeå University, **2008**.

2. Hell, K.; Stieglitz, L.; Dinjus, E., Mechanistic aspects of the De-Novo synthesis of PCDD/PCDF on model mixtures and MSWI fly ashes using amorphous 12C-and 13C-labeled carbon. *Environ. Sci. Technol.* **2001**, *35*, 3892-3898.

3. Iino, F.; Imagawa, T.; Takeuchi, M.; Sadakata, M., De Novo synthesis mechanism of polychlorinated dibenzofurans from polycyclic aromatic hydrocarbons and the characteristic isomers of polychlorinated naphthalenes. *Environ. Sci. Technol.* **1999**, *33*, 1038-1043.

4. Sidhu, S.; Maqsud, L.; Dellinger, B.; Mascolo, G., The homogeneous, gas-phase formation of chlorinated and brominated dibenzo-*p*-dioxin from 2, 4, 6-trichloro-and 2, 4, 6-tribromophenols. *Combust. Flame* **1995**, *100*, 11-20.

5. Iino, F.; Imagawa, T.; Takeuchi, M.; Sadakata, M.; Weber, R., Formation rates of polychlorinated dibenzofurans and dibenzo-*p*-dioxins from polycyclic aromatic hydrocarbons, activated carbon and phenol. *Chemosphere* **1999**, *39*, 2749-2756.

6. Wiater, I.; Louw, R., Reactions of diphenyl ether with chlorine and bromine atoms around 750 K–relevance for gas-phase “dioxin” formation. *Eur. J. Org. Chem.* **1999**, *1999*, 261-265.

7. Asmaly, H. A.; Ihsanullah; Abussaud, B.; Saleh, T. A.; Laoui, T.; Gupta, V. K.; Atieh, M. A., Adsorption of phenol on aluminum oxide impregnated fly ash. *Desalination Water Treat.* **2015**, *57*, 1-8.

8. Mukhopadhyay, A. K., *Industrial Chemical Cresols and Downstream Derivatives*. CRC Press, **2004**.

9. Cooper Sr, A. R., *Cooper's Toxic Exposures Desk Reference with Cd-Rom*. CRC Press, **1996**.

10. Dempsey, C. R., A comparison of organic emissions from hazardous waste incinerators versus the 1990 toxics release inventory air releases. *J. Air Waste* **1993**, *43*, 1374-1379.

11. Patterson, M. C.; Keilbart, N. D.; Kiruri, L. W.; Thibodeaux, C. A.; Lomnicki, S.; Kurtz, R. L.; Poliakoff, E.; Dellinger, B.; Sprunger, P. T., EPFR formation from phenol adsorption on Al_2O_3 and TiO_2: EPR and EELS studies. *J. Chem. Phys.* **2013**, *422*, 277-282.

12. Akgerman, A.; Zardkoohi, M., Adsorption of phenolic compounds on fly ash. *J. Chem. Eng. Data* **1996**, *41*, 185-187.

13. Ahmaruzzaman, M., A review on the utilization of fly ash. *Prog. Energy Combust. Sci.* **2010**, *36*, 327-363.

14. Altwicker, E. R., Some laboratory experimental designs for obtaining dynamic property data on dioxins. *Sci. Total Environ.* **1991**, *104*, 47-72.

15. Nganai, S.; Lomnicki, S.; Dellinger, B., Ferric oxide mediated formation of PCDD/Fs from 2-monochlorophenol. *Environ. Sci. Technol.* **2008**, *43*, 368-373.

16. Lomnicki, S.; Dellinger, B., A detailed mechanism of the surface-mediated formation of PCDD/F from the oxidation of 2-chlorophenol on a CuO/Silica surface. *J. Phys. Chem. A* **2003**, *107*, 4387-4395.

17. McHale, J.; Auroux, A.; Perrotta, A.; Navrotsky, A., Surface energies and thermodynamic phase stability in nanocrystalline aluminas. *Science* **1997**, *277*, 788-791.

18. McHale, J.; Navrotsky, A.; Perrotta, A., Effects of increased surface area and chemisorbed H_2O on the relative stability of nanocrystalline γ-Al_2O_3 and α-Al_2O_3. *J. Phys. Chem. B* **1997**, *101*, 603-613.

19. Elam, J.; Nelson, C.; Cameron, M.; Tolbert, M.; George, S., Adsorption of H_2O on a single-crystal α-Al_2O_3 (0001) surface. *J. Phys. Chem. B* **1998**, *102*, 7008-7015.

20. Liu, P.; Kendelewicz, T.; Brown, G. E.; Nelson, E. J.; Chambers, S. A., Reaction of water vapor with α-Al_2O_3 (0001) and α-Fe_2O_3 (0001) surfaces: Synchrotron x-ray photoemission studies and thermodynamic calculations. *Surf. Sci.* **1998**, *417*, 53-65.

21. Hass, K. C.; Schneider, W. F.; Curioni, A.; Andreoni, W., The chemistry of water on alumina surfaces: Reaction dynamics from first principles. *Science* **1998**, *282*, 265-268.

22. Hass, K.; Schneider, W.; Curioni, A.; Andreoni, W., First-principles molecular dynamics simulations of H_2O on α-Al_2O_3 (0001). *J. Phys. Chem. B* **2000**, *104*, 5527-5540.

23. Eng, P. J.; Trainor, T. P.; Brown Jr, G. E.; Waychunas, G. A.; Newville, M.; Sutton, S. R.; Rivers, M. L., Structure of the hydrated α-Al_2O_3 (0001) surface. *Science* **2000**, *288*, 1029-1033.

24. Al-Abadleh, H. A.; Grassian, V., Ft-Ir study of water adsorption on aluminum oxide surfaces. *Langmuir* **2003**, *19*, 341-347.

25. Zhang, L.; Tian, C.; Waychunas, G. A.; Shen, Y. R., Structures and charging of α-alumina (0001)/water interfaces studied by sum-frequency vibrational spectroscopy. *J. Am. Chem. Soc.* **2008**, *130*, 7686-7694.

26. Meurant, G., *Advance in Catalysis*. Elsevier Science, 1966.

27. Assaf, N. W.; Altarawneh, M.; Oluwoye, I.; Radny, M.; Lomnicki, S. M.; Dlugogorski, B. Z., Formation of environmentally persistent free radicals on α-Al_2O_3. *Environ. Sci. Technol.* **2016**, *50*, 11094-11102.

28. Delley, B., An all-electron numerical method for solving the local density functional for polyatomic molecules. *J. Chem. Phys.* **1990**, *92*, 508-517.

29. Delley, B., From molecules to solids with the $DMol^3$ approach. *J. Chem. Phys.* **2000**, *113*, 7756-7764.

30. Perdew, J. P.; Burke, K.; Ernzerhof, M., Generalized gradient approximation made simple. *Phys. Rev. Lett.* **1996**, *77*, 3865.

31. Grimme, S., Semiempirical GGa-type density functional constructed with a long-range dispersion correction. *J. Comput. Chem.* **2006**, *27*, 1787-1799.

32. Laidler, K. J.; King, M. C., Development of transition-state theory. *J. Phys. Chem.* **1983**, *87*, 2657-2664.

33. Shackelford, J. F.; Doremus, R. H., *Ceramic and Glass Materials. Structure, Properties and Processing.* Springer **2008**.

34. Matori, K. A.; Wah, L. C.; Hashim, M.; Ismail, I.; Zaid, M. H. M., Phase transformations of α-Alumina made from waste Aluminum via a precipitation technique. *Int. J. Molec. Sci.* **2012**, *13*, 16812-16821.

35. Touloukian, Y.; Kirdby, R.; Taylor, R.; Lee, T., *Thermophysical Properties of Matter Plenum.* New York-Washington **1970**.

36. Wheast, R., *Handbook of Chemistry and Physics*; CRC press, 1984.

37. Shukla, M. K.; Hill, F., Plane-wave density functional theory investigation of adsorption of 2, 4, 6-trinitrotoluene on Al-hydroxylated (0001) surface of (4× 4) α-alumina. *J. Comput. Chem.* **2014**, *35*, 1977-1985.

38. Chakarova-Käck, S. D.; Borck, Ø.; Schröder, E.; Lundqvist, B. I., Adsorption of phenol on graphite (0001) and $\alpha - Al_2O_3$ (0001): Nature of van der waals bonds from first-principles calculations. *Phys. Rev. B* **2006**, *74*, 155402.

39. Hegde, M.; Madras, G.; Patil, K., Noble metal ionic catalysts. *Acc. Chem. Res.* **2009**, *42*, 704-712.

40. Li, B.; Metiu, H., DFT studies of oxygen vacancies on undoped and doped La_2O_3 Surfaces. *J. Phys. Chem. C* **2010**, *114*, 12234-12244.

41. Doornkamp, C.; Ponec, V., The universal character of the mars and van krevelen mechanism. *J. Mol. Catal. A: Chem.* **2000**, *162*, 19-32.

42. Mars, P.; Van Krevelen, D. W., Oxidations carried out by means of vanadium oxide catalysts. *Chem. Eng. Sci.* **1954**, *3*, 41-59.

43. Kim, H. Y.; Lee, H. M.; Pala, R. G. S.; Shapovalov, V.; Metiu, H., Co oxidation by rutile TiO_2 (110) doped with V, W, Cr, Mo, and Mn. *J. Phys. Chem. C* **2008**, *112*, 12398-12408.

44. Shapovalov, V.; Metiu, H., Catalysis by doped oxides: Co oxidation by $Au_XCe_{1-X}O_2$. *J. Catal.* **2007**, *245*, 205-214.

45. Pala, R. G. S.; Metiu, H., Modification of the oxidative oower of ZnO (1010) surface by substituting some surface Zn atoms with other metals. *J. Phys. Chem. C* **2007**, *111*, 8617-8622.

46. Chrétien, S.; Metiu, H., Density functional study of the co oxidation on a doped rutile TiO_2 (110): Effect of ionic Au in catalysis. *Catal. Lett.* **2006**, *107*, 143-147.

47. Pala, R. G. S.; Tang, W.; Sushchikh, M. M.; Park, J.-N.; Forman, A. J.; Wu, G.; Kleiman-Shwarsctein, A.; Zhang, J.; McFarland, E. W.; Metiu, H., Co oxidation by Ti-and Al-doped ZnO: Oxygen activation by adsorption on the dopant. *J. Catal.* **2009**, *266*, 50-58.

48. Pala, R. G. S.; Metiu, H., Selective Promotion of different modes of methanol adsorption via the cation substitutional doping of a ZnO surface. *J. Catal.* **2008**, *254*, 325-331.

49. Mosallanejad, S.; Dlugogorski, B. Z.; Kennedy, E. M.; Stockenhuber, M.; Lomnicki, S. M.; Assaf, N. W.; Altarawneh, M., Formation of PCDD/Fs in oxidation of 2-chlorophenol on neat silica surface. *Environ. Sci. Technol.* **2016**, *50*, 1412-1418.

50. Pan, W.; Zhong, W.; Zhang, D.; Liu, C., Theoretical study of the reactions of 2-chlorophenol over the dehydrated and hydroxylated Silica clusters. *J. Phys. Chem. A* **2011**, *116*, 430-436.

51. Dean, J., *Properties of Atoms, Radicals, and Bonds. Lange's Handbook of Chemistry* **1999**, 36.

CHAPTER 9

Formation of Environmentally-Persistent Free Radicals (EPFR) on α-Al_2O_3 Clusters

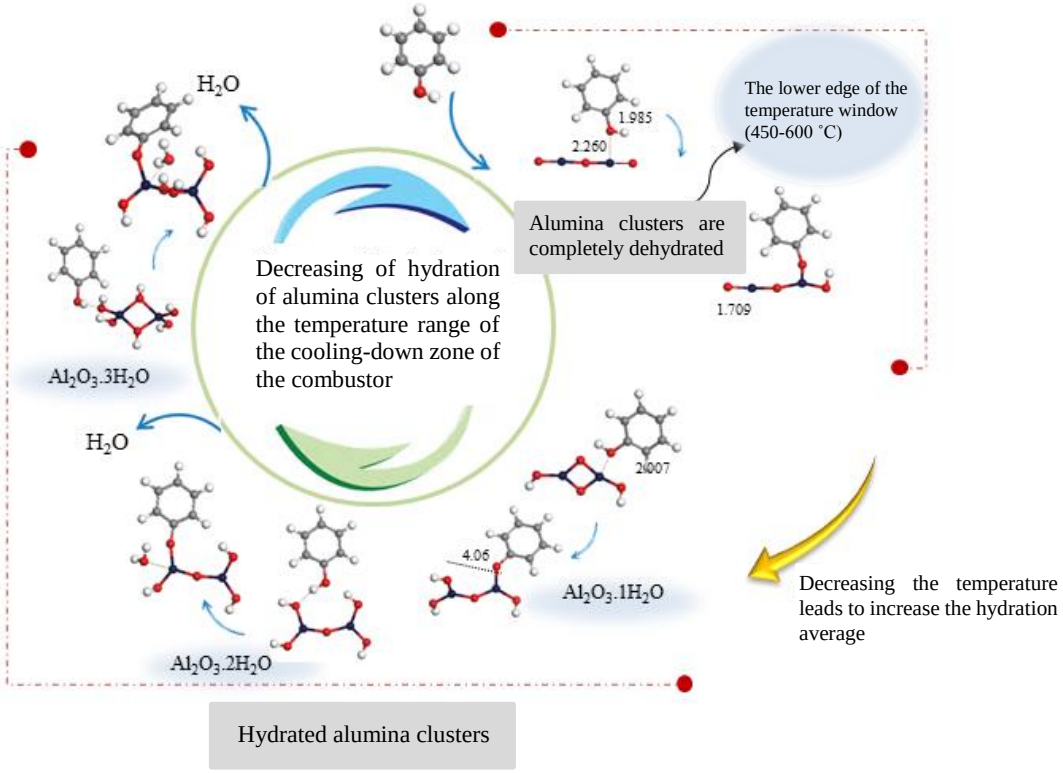

The following is a modified version of the published paper:

Assaf, N. W.; Altarawneh, M.; Radny, M.; Al-Nu'airat, J.; Dlu**gogor**ski, B. Z.; Formation of environmentally-persistent free radicals (EPFR) on α-Al_2O_3 clusters, **RSC Adv. 7 (2017) 52672-526683.**

2016 impact factor: 3.108

9.1 Introduction

Alumina represents one of the most important catalytic and catalyst-support materials,[1-3] for chemical reactions. It also finds direct applications in dielectric materials, substrates for electronics, packing materials and radiation doimeters.[4-5] Over the last two decades, surface chemistry of alumina has been a thematic research topic in catalysis chemistry. Most of these studies have focused on the surface/water interface conditions, where the chemistry of the surface is greatly affected and accordingly mark its reactivity and catalytic performance.[6-8] The interaction of alumina surfaces with water molecules,[6, 9-14] results in water- and hydroxyl-covered surfaces, in which the degree of coverage is highly sensitive to temperature.[15] Heating and cooling processes can reversibly either add or remove hydroxyl groups on the surfaces, as confirmed experimentally by IR and NMR measurements.[16-17] For instance, X-ray diffraction data by Dyer et al.[18] revealed the formation of $Al(OH)_3$ on the γ-Al_2O_3 surface, which disappeared after heating to 473.15 K. This has also been confirmed by Raman and infrared spectroscopy where several sharp peaks in the region around 3600 cm^{-1} have been observed after hydration of the γ-Al_2O_3 powder. X-ray photoemission experiments by Liu et al.[19] pointed out to water dissociation; most likely at surface defect sites.

It has become evident that,[3, 15, 20-21] the differences of the coordination of Al atoms of the alumina surface lead to form different terminal hydroxyl termination or interactive phases. An experimental study by Pimentel and McClellan[22] revealed that, surfaces encompasses two main categories of surface hydroxyl groups; isolated hydroxyl groups with a sharp infrared bands (>3600 cm^{-1}), and self-associated hydroxyl groups with a broad, intense band (<3600 cm^{-1}). Apart from this, self-associated hydroxyl groups differ from the isolated groups in the presence of the hydrogen bond connection between adjacent moieties. Detailed examination

of chemical sites on Al_2O_3 surface[23-24] confirmed the findings of Pimentel and McClellan.[22] Overall, five different classes of isolated hydroxyl groups have been detected by IR spectroscopy.[21, 24] Knozinger et al.[3] attribute the difference in vibrational frequencies among these classes to the coordination number of alumina (i.e.; either tetrahedral and/or octahedral coordination).

The chemical makeup (i.e.; adsorption and decomposition) of the hydroxyl groups over alumina surface constitutes a key factor in clarifying the reactive/catalytic nature of alumina. As stated earlier, heating can reversibly remove the hydroxyl groups from the alumina surface,[16-17, 25] leading to the formation of Lewis acid-base pair sites, and thus increases the catalytic activity of the surface. Along a similar line of enquiry, Ballinger and Yates[26] have performed a detailed investigation into the correlation between Al-OH group removal and the number of Lewis acid sites via CO molecular adsorption. The authors have found that, heating leads to the decomposition of the associated hydroxyl groups, leaving only isolated hydroxyl groups on the surface at a temperature range of 475-800 K. This has been viewed as the driving force of the catalytic activity of alumina, either via hydrogen bonding to the hydroxyl group and/or via lone pair donation to Lewis acid sites. A study by Hendriksen et al.[27] measure the heat of adsorption of water on both α- and γ-alumina powders via immersion calorimetry. It has been indicated that, the heat of adsorption on both termination depends primarily on the degree of hydration prior to water adsorption.

Over a wide range of operational pressure and temperatures, alumina exhibits a variety of crystallographic structures such as α phase or corundum, which is the most thermodynamically stable phase,[28] and other aluminas such as δ, β, κ, η, θ and γ. [29-30] Literature Density function theory investigations have considered water adsorption and dissociation over α-Al_2O_3 surfaces

from the dry to the fully hydroxylated surface. A detailed analysis and discussion on the subject was presented by Wang et al.[31] The authors have found that, a fully hydrated alumina α-Al_2O_3 (0001) surface, when the surface Al atom is triply hydroxylated, exhibits relatively inertness toward further hydroxylation. In an insightful analysis into the interaction of water molecules and a α-Al_2O_3 (0001) surface, Wirth and Saalfrank[32] found that 1,2-dissociation pathway is the most kinetically feasible mechanism, where Al surface atoms are hydroxylated and the nearby oxygen atoms are protonated.

Recent theoretical investigations addressed the interaction of hydrated and dehydrated α-Al_2O_3 surfaces towards different molecules.[33-35] Shukla and Hill[33] have performed a detailed investigation of the molecular interaction of 2,4,6-Trinitrotoluene (TNT) molecule with α-Al_2O_3 (0001) surface demonstrating that TNT acquires strong covalent interaction in a parallel orientation with the surface. The same group[34] found that molecular adsorption of TNT over hydroxylated alumina surface is much weaker when compared to the dehydrated surface. Similarly, Rohman et al.[35] investigated molecular interaction of carbon monoxide with hydroxylated alumina surface, reporting that molecular CO exhibits strong interaction with a 25% degree of hydroxylated surface and this interaction is significantly stronger when compared with that over the clean dehydrated alumina. In a follow-up study on H_2S removal via γ-Al_2O_3 surfaces with different hydroxyl coverage, Ren et al.[36] revealed that, the bonding strength of H_2S on hydrated alumina surface is lower than that the over a dehydrated termination. For example, calculated binding energy for 8.9 OH per nm^2 hydroxyl coverage for γ-Al_2O_3 (110) amounts to -68 kJ/mol whereas the corresponding value of the dehydrated surface stands at -114 kJ/mol. XPS studies by Keller et al.[37] investigated the interaction between Cu and the hydrated α-Al_2O_3 (0001) surface to report an enhanced interaction of copper to the surface of alumina owing to the presence of a surface hydrated layer. There is a

rather limited literature account on reactions of hydrocarbons on alumina clusters. Most of relevant studies have considered extended surfaces of alumina.[34-35, 38] Nonetheless, it has been shown that alumina clusters encompass effective catalytic active sites present on surfaces; i.e., the surface Al-O bonds.[39-40] Therefore, alumina clusters in many theoretical studies (i.e. $(Al_2O_3)_{n=4}$) are being applied as representative models for both α-Al_2O_3 and γ-Al_2O_3 surfaces. Alumina clusters imitate both the experimental measurements and DFT surface properties. Additionally, clusters[41-42] were shown to illustrate an effective stability against relaxation often encountered in extended alumina surfaces.

Phenol molecule is among the most commonly discussed precursors for the synthesis of poly chlorinated dibenzo-*p*-dioxins and dibenzofurans[43-45]. Heterogeneous formation of PCDD/Fs via surface-mediated coupling of chlorinated phenols were investigated on many oxide systems, including Al_2O_3,[46-47] Co_3O_4,[46] CuO,[48-49] TiO_2[47] and Fe_2O_3.[50] In our recent Study,[51] we theoretically investigate the interaction of phenol molecule with the dehydrated α-Al_2O_3(0001) surface. We have found that, alumina surface is catalytically very active in producing phenolate (i.e., surface-bounded phenoxy) with a modest activation energy of 43 kJ/mol, thus, signifying as an accessible route for the formation of persistent surface-bound radicals. However, when considering the temperature range of the cooling-down zone of the combustor (i.e.; 746 -1146 K), all models of alumina (i.e.; polymorphs, surfaces and\or clusters) assume different hydration coverage. Therefore, the effect of the degree of hydration, on dissociative adsorption of phenol, can play an important role in attaining a detailed understanding of the catalytic activity of the surface. Thus, it is very important to shed light into the generation of the environmentally persistent free radicals[52-53] on alumina surface with varying hydroxyl coverages.

In summary, the current Chapter is part of our ongoing effort to reveal mechanistic and kinetic factors dictating the catalytic role of alumina surfaces in surface-mediated formation of phenoxy-type EPFR. The study provides a detailed investigation of the interaction of a phenol molecule with different hydration coverage of alumina clusters and therefore offers important insights into the role of the surface adsorbed water in the catalytic activity of alumina toward the generation of adsorbed phenoxy radicals. The present Chapter expands on our investigation in Chapter 7,[51] in which we considered a dehydrated α-Al_2O_3 (0001) surface. Overall, this study has a three-fold aim; (i) to report modes of interaction of phenol with different hydration coverages of alumina clusters, (ii) to compare between the catalytic activity of hydrated and dehydrated alumina clusters toward the formation of the adsorbed phenolate via two distinct pathways; namely direct fission of the phenol' O-H bond and elimination of water molecules (iii) to construct a simplified kinetic model for the conversion of phenol into adsorbed phenoxy radicals.

9.2 Methodology

DMol^3 program[54-55] performs all structural optimization, energy calculations and vibrational frequencies based on the generalized gradient approximation of the Perdew-Burke-Ernzerhof functional[56] . The computational methodology comprises Grimme dispersion correction,[57] together with the basis set of double numerical plus polarization. Total energy and forces on each atom converge with tolerance to less than 10^{-6} Ha and 10^{-4} Ha/Å, respectively.

We computed the binding energies (E_b) for the adsorption based on the energies of a phenol/Al_2O_3 system $E_{cluster + phenol}$, the clean alumina cluster $E_{cluster}$, and an isolated phenol molecule E_{phenol}:

$$E_b = E_{cluster + phenol} - E_{cluster} - E_{phenol} \quad 9.1$$

Reaction rate constants were estimated based on the conventional transition state theory,[58] We fit reaction rate constants to the two-parameters Arrhenius formula, $k(T) = A \exp(-E_a/(RT)$, over the temperature range of 300 K to 1000 K, according to:

$$k(T) = \frac{k_B T}{\sigma_e h} \exp\left(\frac{\Delta S^{\neq}}{R}\right) \exp\left(\frac{-\Delta H^{\neq}}{RT}\right) \quad 9.2$$

where: k_B is Boltzmann's constant, h signifies Plank's constant, R is the universal gas constant. Calculated vibrational frequencies enable to calculate thermodynamic functions; i.e., entropies and enthalpies. $\Delta S^{\neq}$ and $\Delta H^{\neq}$ stand for temperature-depended entropy and enthalpy of activation, correspondingly. σ_e represents the reaction degeneracy number. DMol^3 computes entropy values based on well-documented statistical thermodynamics equations.[59] The enthalpy (at the desired temperature) has been competed relatively to the zero-point energy at 0 K.

9.3 Results and Discussions

9.3.1 Water Adsorption on Al_2O_3 Cluster

Starting with dehydrated alumina clusters, Figure 9.1 displays two water-free geometrical monomers of alumina near-cyclic AlO_3Al that adapt D_{3h} symmetry, and a linear O=Al-O-Al=O chain structure. As illustrated in Figure 9.1, the cyclic dehydrated alumina, AlO_3Al, contains three Al-O bonds with distances of ~ 1.82 Å. This structure was found to be energetically less stable[60] than the linear chain structure due to the repulsion between the two cations (Al^{+3}). In the latter configuration, alumina adapts a linear structure with one bridging and two non-bridging oxygen atoms. Calculated bond angle and bond lengths, in both structures, are in agreement with the literature analogous values.[60-61]

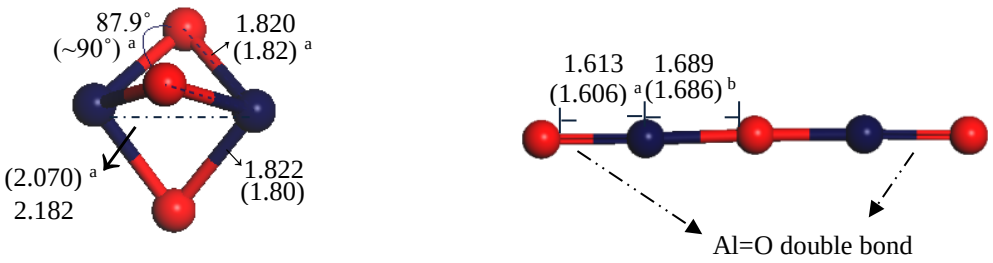

Figure 9.1. Optimised geometries for dehydrated Al_2O_3 clusters with the main geometrical parameters (in Å). Bond lengths in parentheses signify the corresponding experimental or theoretical values from the literature. a[ref 60], b[ref 61]

Moving on now to consider how the geometries of alumina cluster are compared with those in alumina surface. Figure 9.2 displays top and side views of α-Al_2O_3(0001) surface (i.e., the thermodynamically most stable alumina surface[62-63]) and the D_{3h} structure. As can be seen from the Figure, Al-O bonds lengths in both structures are within 0.01 Å. This close agreement serves to testify that considered cyclic dehydrated structure contains similar active sites to those present in the surface.

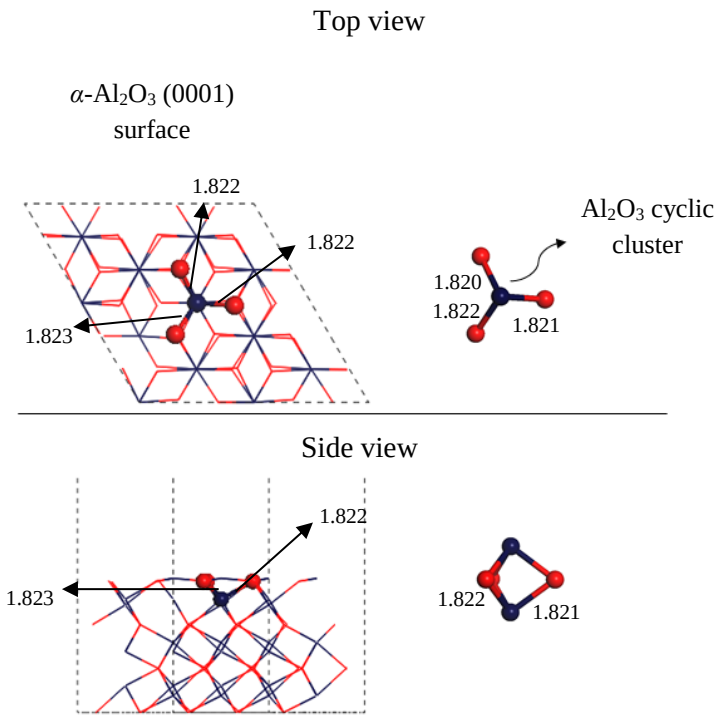

Figure 9.2. Geometric comparison between Al_2O_3 cyclic cluster and the α-Al_2O_3(0001) surface.

A study by Johnson and Panas[60] examine water adsorption and hydrolysis on molecular Al oxides and hydroxides solvation versus cluster formation. They found that, dehydrated alumina clusters, both cyclic and linear chain, reacts with water molecules through accessible energy barriers in the range of 33 - 310 kJ/mol. Further addition of water molecules leads to a series of $Al_2O_3.nH_2O$ structures.

Figure 9.3 illustrates mechanism of successive addition of water molecules to the dehydrated cluster of alumina (i.e.; cyclic and linear clusters). Starting with the cyclic structure of alumina, D_{3h}, the addition of a water molecule to the Al_2-O_1 bond results in the formation of the $Al_2O_3.1H_2O_{(c)}$ cluster (c) which has been reported to be the most stable structure among the various configurations of $Al_2O_4H_2$ clusters.[60] Typically, this structure assumes cis and trans

configurations, with very similar thermodynamic stability.[60] Thus, we have performed our subsequent calculations considering the cis planar molecule configurations with the C_{2v} symmetry as it is marginally more thermodynamically stable than its trans counterpart; by 3 kJ/mol. Calculated Al_2-O_2 and Al_2-O_{w1} bond lengths amount to 1.75 Å and 1.70 Å, respectively. These values concur very well with the corresponding literature values by Johnson and Panas;[60] i.e., 1.75 Å and 1.69 Å, respectively.

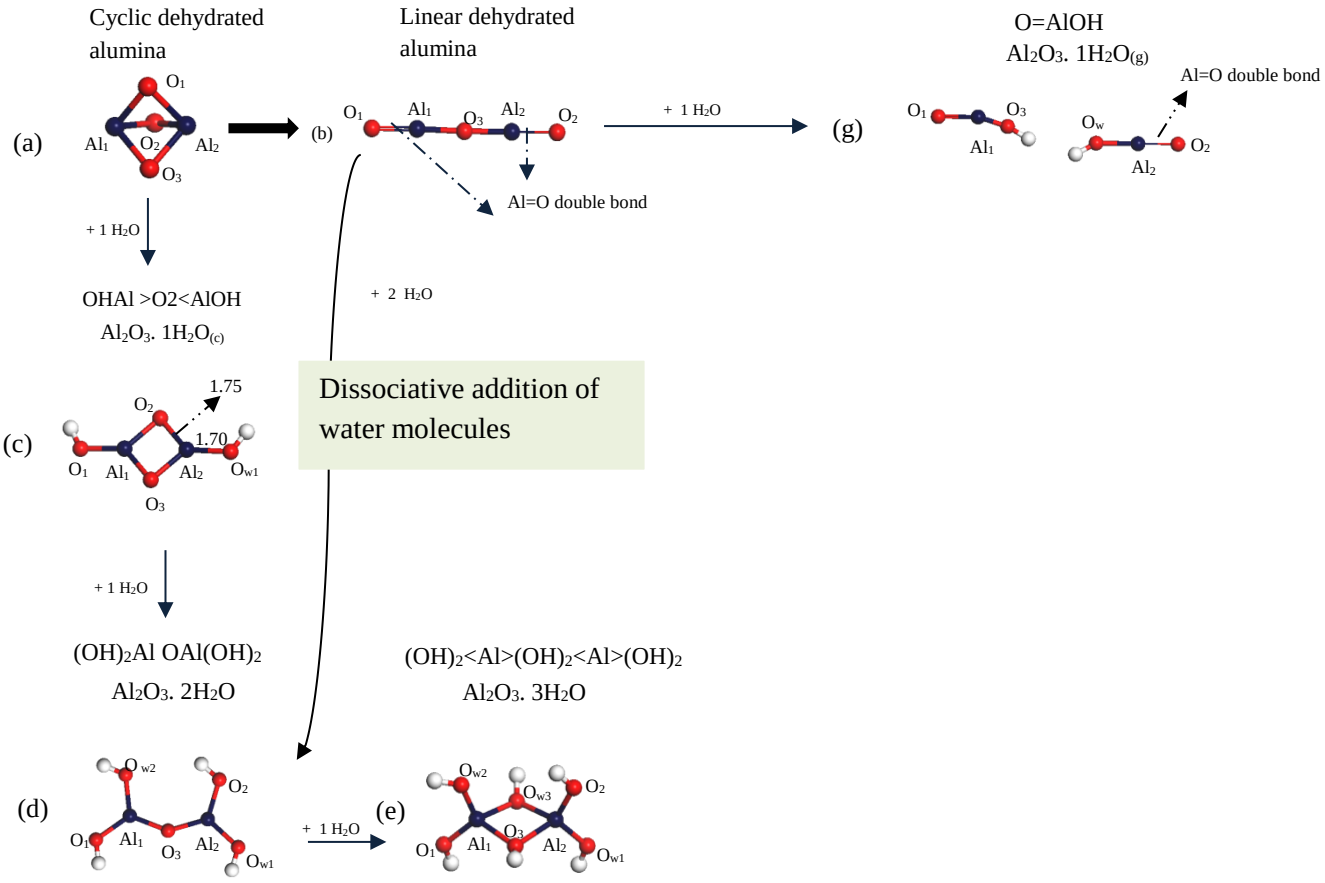

Figure 9.3. Structures of the Al_2O_3 + nH_2O.

Turning now to the linear chain structure, the addition of water can proceeds either via cluster Al=O double bond site or via cleaving the central Al-O-Al bond.[60] This results in the formation

of the $Al_2O_3.2H_2O$ cluster (d) and O=AlOH (g), respectively. Considering the double bond pathway; further addition of a water molecule produces the cluster $Al_2O_3.3H_2O$ (e), with the C_{2h} symmetry. Energetics for the formation of the hydrated alumina structures in Figure 9.3 has been reported by Johnson and Panas.[60] The authors found that formation of (c) and (e) structures display an exothermic process with calculated enthalpies of - 310 kJ/mol and - 184 kJ/mol, respectively. The formation of structure (g) is slightly endothermic with a low activation enthalpy at 33 kJ/mol. [60]

9.3.2 Reaction of Phenol with Dehydrated Alumina Cluster

In Chapter 7, we investigate the interaction of a phenol molecule with a dehydrated alumina surface without incorporating the effect of water molecules on the dissociative adsorption mechanism. In this section, we elect to study the interaction of a dehydrated alumina cluster based on two compelling grounds. First, to provide an accuracy benchmark for results obtained on clusters in general and how they compare with analogous values obtained over an extended surface. Second, reaction and activation barriers obtained on the dehydrated cluster constitute a base for comparison with subsequent corresponding values reported on hydrated clusters. The underlying aim is to contrast energetic values between dehydrated and hydrated clusters in order to underpin the effect of added water/hydroxyl radicals in facilitating formation of an adsorbed phenolate.

We studied the interaction of a phenol molecule with the two dehydrated alumina clusters (i.e.; cyclic and linear clusters in Figure 9.3, a and b). Two different reactions have been considered, denoted as pathway a and pathway b. These pathways involve the interaction of phenol

molecule with cyclic and linear dehydrated alumina clusters, respectively. The optimized geometries for the reactants, transition states and products are presented in Figure 9.4. Table 9.1 lists energies for physisorbed configurations and dissociative structures as well as prominent interatomic distances for all pathways.

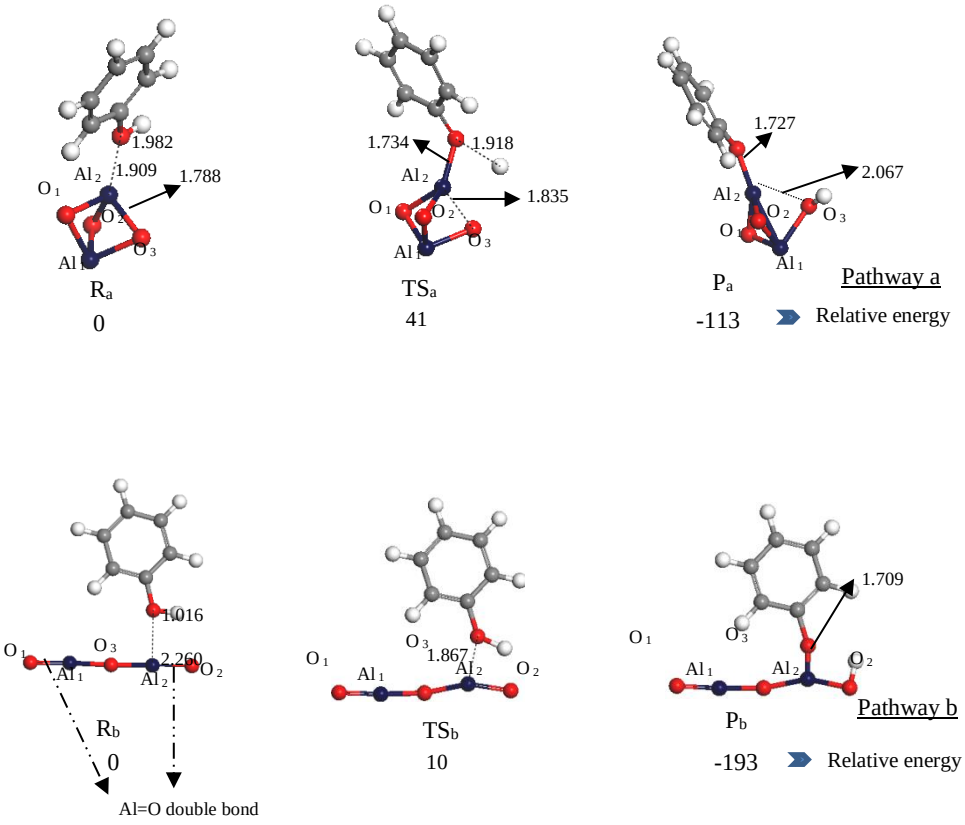

Figure 9.4. Optimised geometries for species the reaction of phenol with dehydrated alumina clusters. Values (in kJ/mol) of energies are in reference to physisorbed reactant.

Table 9.1. Binding energies (using Eq. 9.1) and geometrical parameters for phenol interaction with Al_2O_3 and Al_2O_3. nH_2O clusters.

Structure	**Phenol-cluster spacing in the reactant (Å)**	**O-H phenol bond distance in the reactant (Å)**	**Al-O bond distance in the reactant (Å)**	**Binding energies for reactants and products (kJ/mol)**
Pathway a	1.909	0.982	1.788	R_a= -129 P_a= -241
Pathway b	2.260	0.985	2.260	R_b= -152 P_b= -345
Pathway c_1	2.007	0.997	1.793	R_{c1}= -143 P_{c1}= -225
Pathway c_2	1.979	0.881	1.739	R_{c2}= -147 P_{c2}= -167
Pathway c_3	1.997	0.990	1.742	R_{c3}= -129 P_{c3}= 17
Pathway g	1.940	1.009	1.630	R_g= -166 P_g= -360
Pathway d	1.725	1.004	1.733	R_d= -81 P_d= -74
Pathway e	1.75	1.007	1.738	R_e= -99 P_e= -135

We first consider the interaction along the cyclic alumina structure, pathway a. Figure 9.4a. shows, phenol molecule physically adsorbs on the cluster through a van der Waals interaction between O_{phenol} atom and $Al_{cluster}$ atom with a binding distance of 1.909 Å. The interaction proceeds via fission of the hydroxyl's bond over Al-O cluster bond where phenoxy moiety attaches to $Al_{cluster}$ and deducted hydrogen atom binds to $O_{cluster}$ atom. This has resulted in the optimised dissociation product P_a. Hence, the length of this bond increases by 13.4 % with respect to that of the clean cyclic cluster (1.822 Å). This value concurs with results obtained in Chapter 7[51] of the dissociative adsorption of phenol on the dehydrated α-Al_2O_3(0001) surface (11.9 %). In comparison, Wang et al.[31] showed that the elongation of Al-O bond increased by 6.4 % upon the dissociation of a water molecule over this Al-O bond.

The reaction is highly exothermic with an energy barrier of only 41 kJ/mol. Calculated binding energy of the reactant, R_a, and the product, P_a, are -129 kJ/mol and -241 kJ/mol, respectively (based on Eq. 9.1 in reference to separated reactants). These values also agree with the results obtained in Chapter 7.[51] We found that, phenol molecule strongly interacts with the dehydrated α-Al_2O_3(0001) surface via physisorbed binding energies in the range of -127 kJ/mol - -202 kJ/mol), leading to the formation of an adsorbed phenolate with a modest activation energy of 48 kJ/mol.

Considering the second reaction, where phenol molecule interacts with the linear cluster chain of alumina (pathway b), phenol molecule physically adsorbs on the active Al=O double bond site of the cluster with a calculated binding distance of 2.26 Å. The O-H bond length of phenol molecule in R_b (Figure 9.4) increases from the equilibrium 0.97Å distance in the gas phase to 1.016 Å. The exothermic formation of the product P_b requires a trivial activation energy of 10 kJ/mol (via direct fission of the phenol's O-H bond catalysed by the cluster's Al-O linkage).

Calculated binding energies of the reactant, R_b, and the product, P_b, are -152 kJ/mol and -345 kJ/mol, respectively (in reference to the separated reactants, Figure 9.4). P_b appears relatively more stable than P_a. Activation barrier via pathway b is lower by 31 kJ/mol than that along pathway a. This indicates that, the linear chain cluster of alumina is catalytically more active in producing phenolate than the cyclic dehydrated cluster.

Test computations employing the dependence of the reactivity of alumina cluster on the cluster size has been considered. We investigated physisorption and a chemisorption interactions of phenol with the larger $(Al_2O_3)_4$ reported in the literature.[64] Stable optimised structures are shown in Figure 9.5 Calculated binding energies of the physisorbed and the chemisorbed structures are -150 kJ/mol and -315 kJ/mol, respectively, both values are in good agreement with the corresponding values we obtained for the smaller dehydrated clusters (i.e.-129 - -152 kJ/mol)and -241 - -345 kJ/mol), respectively). Furthermore, binding energies obtained for the larger $(Al_2O_3)_4$ cluster are consistent with the calculated binding energies in Chapter 7[51] for the interaction of phenol with a seven-layer slab of the 2 × 2 (0001) surface alumina (-127 kJ/mol - -202 k J/mol). Thus, it can be concluded that energies of the surface interaction of phenol with alumina surface do not display sensitivity toward the cluster size. The same observation has been observed by Pan et al.[65] in their study of the reaction of 2-Chlorophenol over the dehydrated and hydroxylated silica clusters with $(SiO_2)_3$ and $(SiO_2)_8$ clusters. They have found that binding energies of reactants and products using both structures are within (0.4 - 17) kJ/mol.

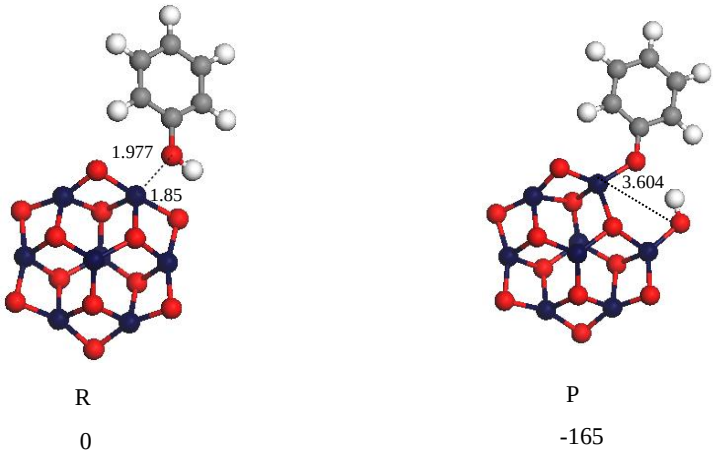

Figure 9.5. Optimised geometries for the reaction of phenol with the $(Al_2O_3)_4$.

9.3.3 Reaction of Phenol with $Al_2O_3.nH_2O$ Cluster

We now turn our attention to investigate the interaction of a phenol molecule with hydrated alumina clusters entailing different hydroxylation coverages, (i.e., all the hydrated alumina clusters shown in Figure 9.3). The detailed mechanism of the interaction is presented in Scheme 9.1. Figure 9.6 depicts optimised geometries of reactants, transition states, and products; along with their energy profiles.

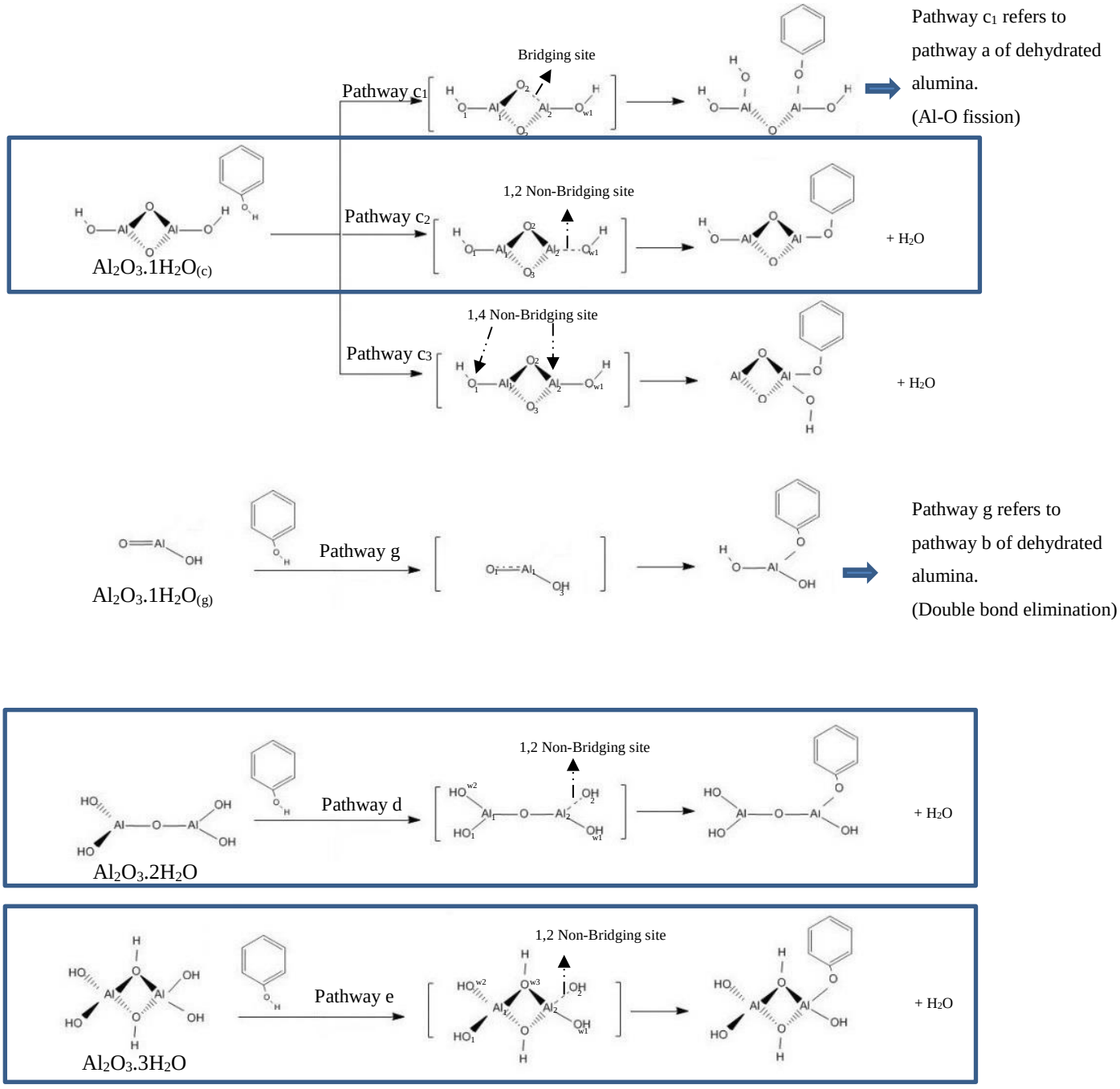

Scheme 9.1. Reaction of phenol with hydrated Al_2O_3 cluster. The highlighted reactions proceed via H_2O elimination (presenting H_2O elimination mechanism over the same Al-OH bond (1,2 non-bridging)).

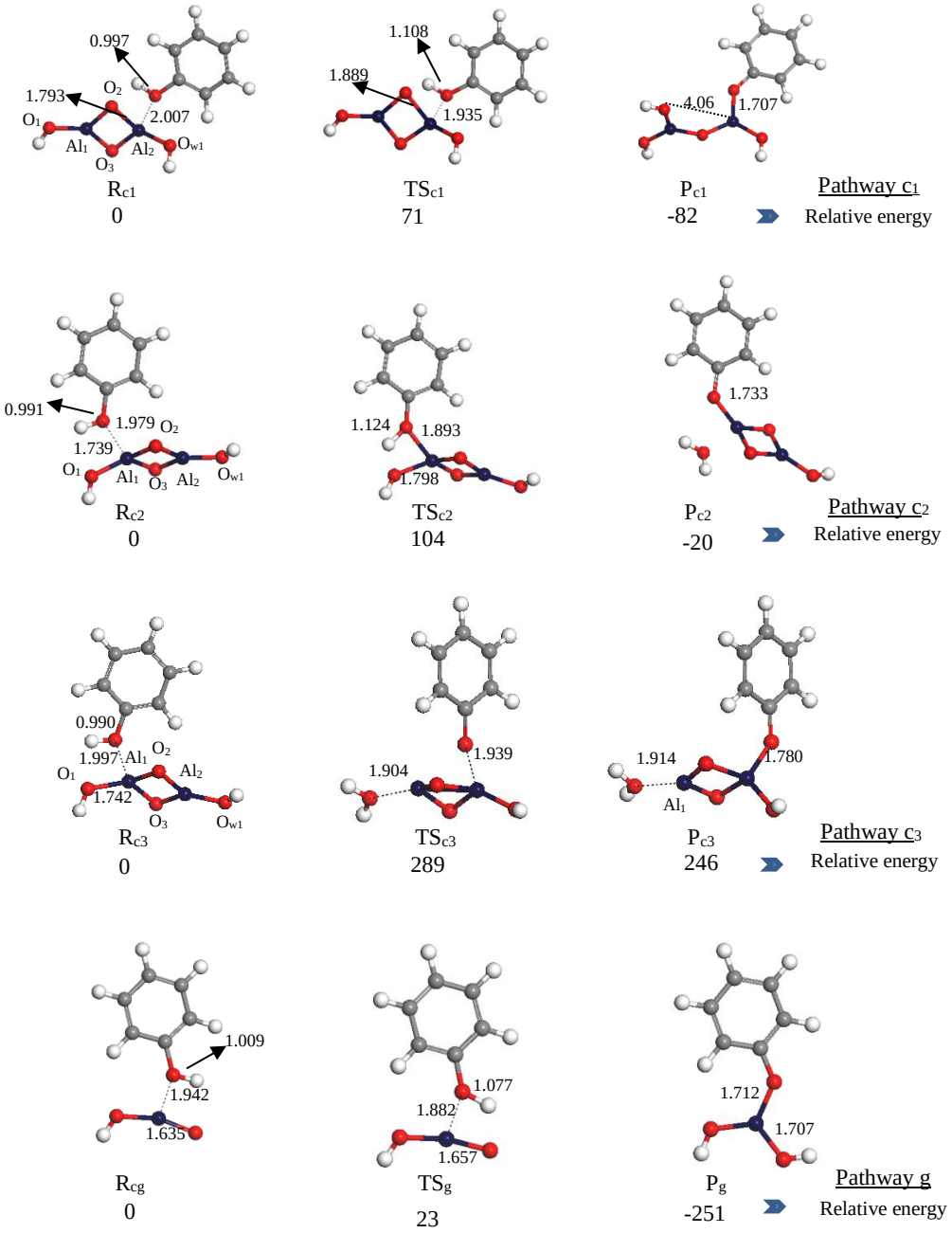

Figure 9.6. Optimised geometries involved in the reaction of phenol with c and g clusters. Values (in kJ/mol) of energies are in reference to physisorbed reactants.

First, we have studied the interaction of a phenol molecule with the (c) structure, Figure 9.3. Three possible pathways have been considered, denoted as c_1, c_2 and c_3 in Scheme 1. As Scheme 1 demonstrates, these reaction pathways characterise (i) fission of hydroxyl's bond

over the same Al_2-O_2 bond (bridging bond), (ii) H_2O elimination mechanism over the same Al-OH bond (1,2 non-bridging) and (iii) H_2O elimination route over two Al-OH bonds (1,4 non-bridging linkage), respectively (Figure 9.3 illustrates atomic numberings). The reaction is initiated by the physisorbed-type interaction between O_{phenol} and $Al_{cluster}$ via binding spacings of 2.007 Å, 1.979 Å and 1.997 Å in the reactants R_{c1}, R_{c2} and R_{c3}, respectively (Figure 9.6). Calculated binding energies of the three reactants stand at -143 kJ/mol, -147 kJ/mol and -129 kJ/mol, respectively. (in reference to the separated reactants). Regarding to the structural changes induced to the cluster; we observe that Al_2-O_2 bridging bond in Figure 9.6, R_{c1} elongates by 2.4% when compared with the corresponding value in the Figure 9.3 (c) structure while Al_1-O_1 in R_{c2} and Figure 9.6, R_{c3} increases by 8.1% and 8.2 %, respectively. Dissociative desorption of phenol via these pathways leads to the formation of P_{c1}, P_{c2} and P_{c3} (Figure 9.6) intermediates with binding energies of -225 kJ, -167 kJ/mol and 17 kJ/mol, respectively. The thermodynamic penalty associated with the product P_{c3} most likely stem from the low coordinated Al_1 that display a 2-fold coordination.[66]

Next, we examine the dissociative adsorption of phenol over the Figure 9.3 (g) structure. The reaction proceeds via the active Al=O double bond site of the cluster. We found a slight increase in the O-H bond length of the physisorbed phenol in pathway g (1.009Å, Scheme 1), in reference to the gas phase value (0.97Å). The corridor g in scheme 1 characterises fission of the O-H bond in the phenol molecule in a noticeably exothermic reaction of 360 kJ/mol. The physisorbed state Figure 9.6 (R_g) in this channel resides 166 kJ/mol below the separated reactants. Compered to Figure 9.3(*d*), the size of hydrated alumina cluster (*g*) with one water molecule is smaller and it has a planar structure. Therefore, as temperature increases, molecules move faster and they are more likely to collide and hence positively affect the collision frequency, *A.*

Reaction pathways c_1, p c_2 and g proceeds via modest energy barriers of 71 kJ/mol, 104 kJ/mol and 23 kJ/mol, respectively, whereas pathway c_3 incurs a very sizable energy barrier of 289 kJ/mol. Three concluding remarks can be drawn from values in Figure 9.6. First, within $Al_2O_3.1H_2O$ system (i.e.; pathways: g, c_1, c_2, c_3), as expected, reaction pathway g is the most favourable channel, presumably due to the presence of the active Al=O double bond site. Second, phenol dissociation catalysed/accompanied with water elimination (pathways c_2 and c_3) is more energy demanding than phenol decomposition through surface-assisted fission of its hydroxyl O-H bond (pathways c_1). For instance, the activation energy in pathway c_1 is lower by 33 kJ/mol than that along pathway c_2. Third, the activation energy in reaction pathway c_3 as well as the calculated binding energy of the product P_{c3} are higher when contrasted with the corresponding values in pathway c_2, This indicates that water elimination preferentially occurs at the same A-OH linkage; i.e., 1.2-elimination step rather than at different A-OH sites (i.e., 1,4-elimination). This has prompted us to exclude this mechanism (i.e.; pathway c_3) from further consideration in our subsequent discussion.

Phenol interaction with higher hydrated alumina clusters ($Al_2O_3.2H_2O$ (d) and $Al_2O_3.3H_2O$ Figure 9.3(e)) is presented in pathways d and e in Scheme 1, with Figure 9.7 illustrates optimised geometries and relative energies for species involved in pathways d and e.

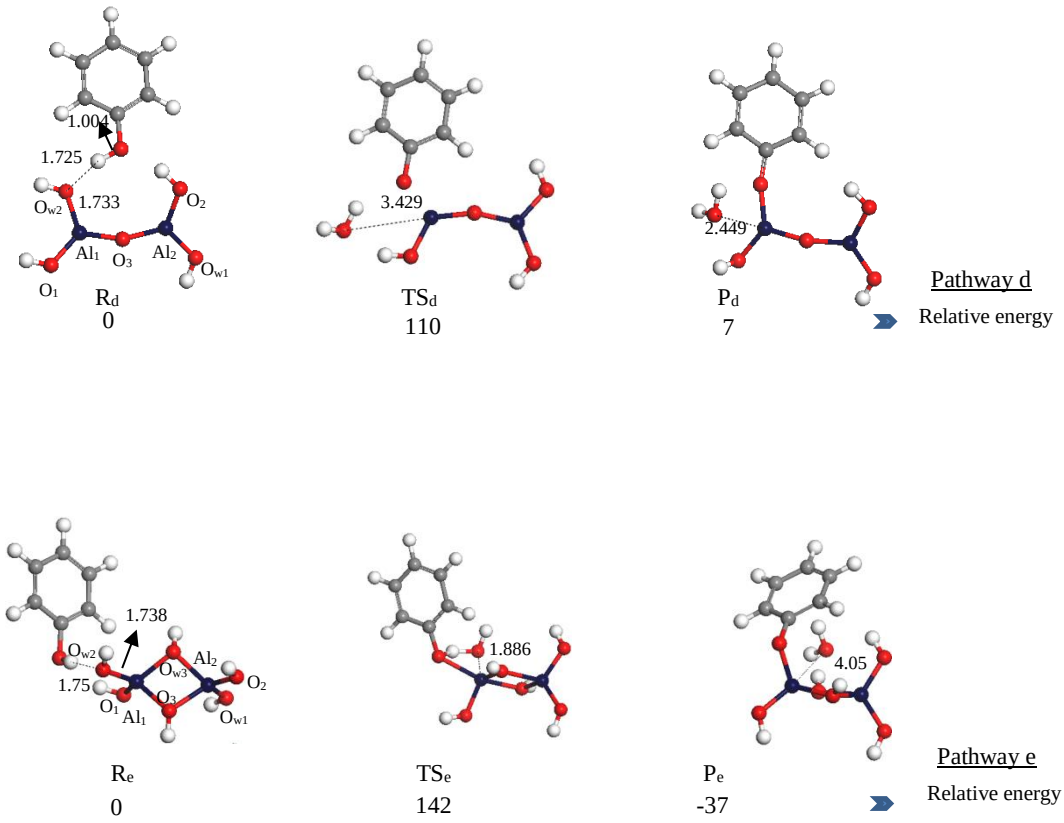

Figure 9.7. Optimised geometries involved in the reaction of phenol with d and e clusters. Values (in kJ/mol) of energies are in reference to physisorbed reactants.

Water elimination via pathways d and e results in the formation of a phenolate moiety via activation barriers of 110 kJ/mol and 142 kJ/mol, respectively. Pathways d and e characterises dissociative adsorption of phenol via water elimination through 1,2-route; i.e., attachment of the phenoxy'O at the Al atom and the simultaneous departure of the OH group attached to the same Al atom with the hydroxyl'H as a water molecule. Higher energy barrier for pathway e in reference to pathways c_2 and d can be rationalised in energy penalty required for the rupture of the Al-O linkage in the former. The degree of hydration of alumina; could be viewed as a factor that partially dictates the catalytic activity of alumina via controlling the surface-acid properties.[67] In this regard, Al atom in structure (e) (the $Al_2O_3.3H_2O$ system), is coordinated by four hydroxyl groups, whereas Al atom in c_2 and d, is less coordinated presenting more

acidic structures as illustrated in Scheme 9.2. From the Scheme, we can see that the addition of water molecule in the structure d blocks the Lewis active site and accordingly decreases the catalytic activity of the cluster. This view is supported by Digne et al.[68] who argued that the lower the Al atom coordination, the stronger generally- the Lewis acidity. Calculated atomic Mullikan charges on Al atom for (c), (d) and (e) were shown to have more positive values on the four coordinated Al atom of 1.96*e* (structure (e)) when compared to the three coordinated Al atom (i.e., 1.52*e* in structures (c) and (d)). A positive correlation is found between the calculated energy barrier and calculated Mulliken atomic charges; the higher the atomic charges on Al atom the higher energy required to break Al-OH bond toward generating water molecule (accompanied with the dissociative adsorption of phenol). Thus, the observed increase in barrier for pathway e in reference to pathways c_2 and d correlates with partial atomic charges; i.e., a prominent electronic descriptor that determines the acidity character.

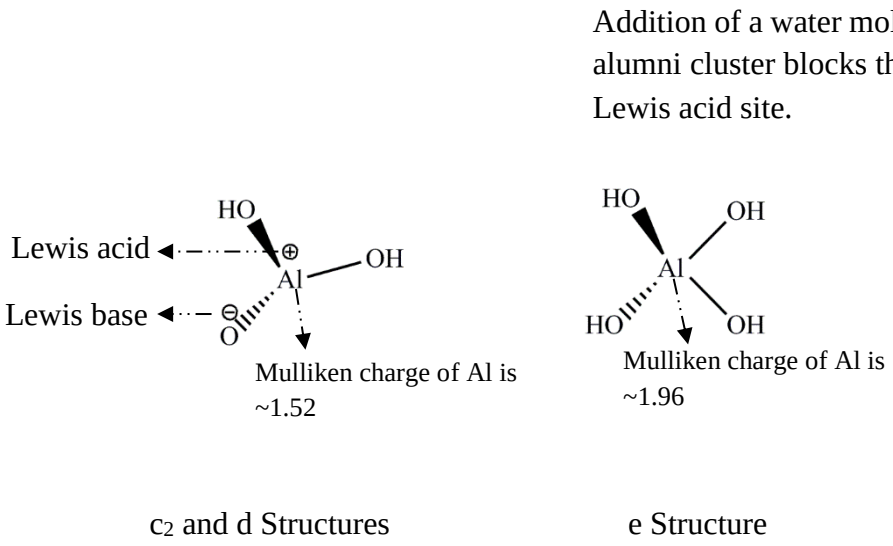

Scheme 9.2. Structure of acidic and basic site of alumina cluster.

Over all, we can compare between hydrated and dehydrated alumina from two different perspectives. First, within fission of hydroxyl's bond reactions over the same Al-O bond; contrasting pathway Figure 9.6 c_1 with pathway a reveals that the energy barrier required in hydrated alumina clusters (i.e.; c_1= 71 kJ/mol) are significantly higher than that over the dehydrated one (i.e.; a= 41 kJ/mol), respectively. Second, saturation of Al=O double bonds in the course of the hydroxylation of cluster b into d (refer to Figure 9.3) significantly increases the barrier required for water elimination from only 10 kJ/mol to 110 kJ/mol. Together, these findings indicates that dehydrated alumina cluster are more active in producing phenolate than hydrated alumina clusters. This observation agrees with the findings of Pan et al.[65] who found that, the dehydrated silica cluster (with the presence of two ends of S=O double bonds sites) produces chlorophenolate from 2-chlorophenol through an energy barrier of only 21 kJ/mol, compared with 70 kJ/mol over the hydrated cluster (the same cluster after the two Si=O double bonds sites become saturated).

The most obvious finding to emerge from inspecting data in Table 9.1 is that, in both hydrated and dehydrated alumina, the dissociated product via Al=O double bonds site of the cluster is more stable than that leading to Al-O bond cleaving. For example, reaction energies that mark the formation of P_g and P_b (double bonds sites) amount to -360 kJ/mol and -345 kJ/mol, respectively, while the analogous energies of P_{c1} and P_a are -225 kJ/mol and -241 kJ/mol, (A-O bond fission), respectively. This finding is in agreement with those obtained by Pan et al.[65] The authors found that dissociative adsorption of 2-chlorophenol through rupture of its hydroxyl's bond over a S=O double bonds site forms more stable product by 136 kJ/mol than that leading to Si-O bond cleaving. The calculated binding energies for $Al_2O_3.nH_2O$ clusters concur with our results in Chapter 8 for the interaction of phenol with (0001) hydrated alumina surface.

Desorption of the phenolate moiety from both dehydrated alumina cluster and hydrated alumina clusters, was found to be highly endothermic by 334– 373 kJ/mol. This finding is in accord with those reported in our recent study for the interaction of phenol[51] (Chapter 7) and chlorophenol[69] molecules over alumina surfaces and silica clusters, 394 kJ/mol and 379 kJ/mol respectively. This profound stability of phenolate enables it to undergo bimolecular reactions via the so called Eley-Rideal and Langmuir-Hinshelwood mechanisms[48] to produce dibenzo-*p*-dioxin and dibenzofuran; respectively. In alternative corridor, decomposition of phenolate on the surface is expected to initiate the formation of soot.

9.3.4 Kinetic Consideration

We conclude the study by implementing a microkinetic analysis of the abovementioned reactions in this Chapter. Figure 9.8 represents Arrhenius plots while Table 9.2 displays the calculated reaction rate parameters. Within the considered temperature limit, reactions pathway c_3 displays the highest activation energy and relatively high dependence on temperature. For all reactions, the fitted Arrhenius energy of activation (E_a) largely reflects corresponding energy barriers presented in Figure 9.4, 9.6 and 9.7. Calculations of the conversion-temperature profiles were carried out based on a simplified plug flow reactor (PFR) model. The material balance equations were solved by Polymath software[70]:

$$r_B = -r_A = \frac{d(F)}{d(W)} \qquad 9.3$$

In the considered reaction, ($A \rightarrow B$), *A* and *B* represents the molecularly adsorbed phenol and the dissociative structures; respectively. *r* denotes the reaction rate, *F* symbolizes the molar flow rate of phenol in mole/s, and *W* stands for alumina catalyst weight in kg. The reaction is considered to be first order with respect to phenol. The model utilises reaction rate constants given in Table 9.2. The catalytic destruction of phenol molecule over $Al_2O_3.nH_2O$ catalysts as a function of temperature is presented in Figure 9.9. It can be seen that all hydrated coverage of alumina clusters exhibits a highly catalytic destruction activity for phenol molecule, evident by high conversion at low temperatures. Calculated temperature of 90% destruction of phenol molecule (T_{90}%) occurs at 350 K, 925 K, 425 K and 425 K for pathways c_2, c_3, d and e, respectively. To the best of our knowledge, literature provides no conversion values for the interaction of phenol with α-Al_2O_3 in the literature. Considering the very high desorption energy for phenolate, formation of gas phase phenoxy should be hindered. The LR and LH mechanisms operated by the highly stable surface-bounded phenolate species, remains largely speculative.

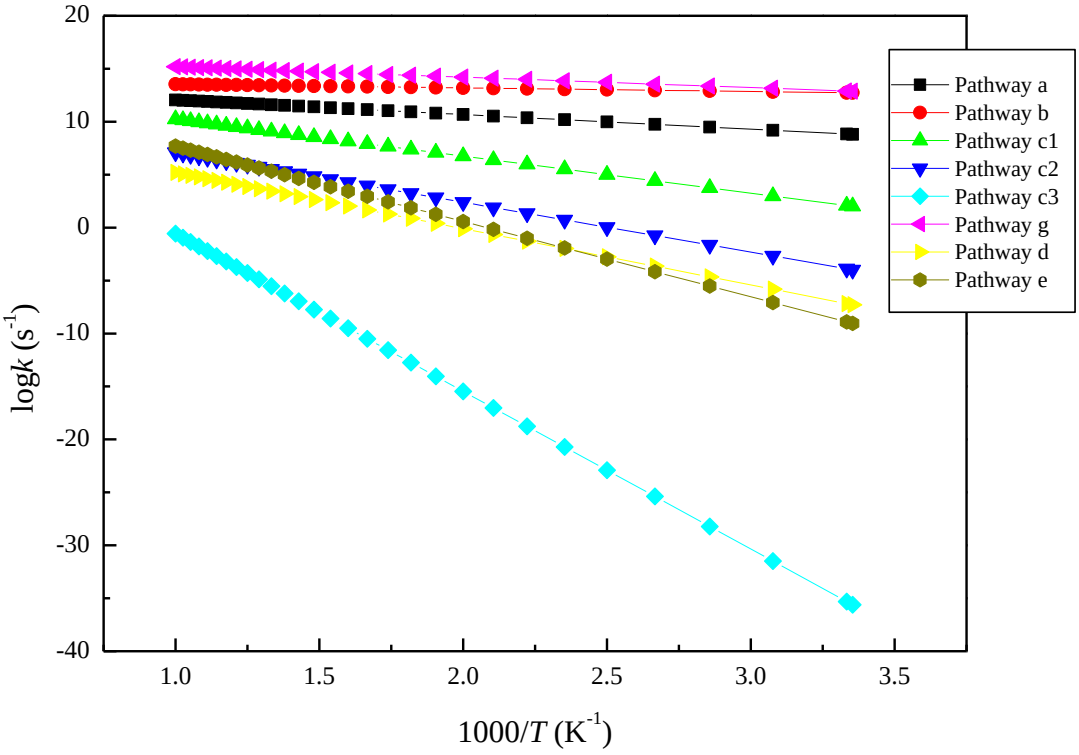

Figure 9.8. Arrhenius plots for the studied reactions.

Table 9.2. Arrhenius kinetic parameters.

Reaction	E_a **(kJ/mol)**	A **(s^{-1})**
Pathway a	27	2.76×10^{13}
Pathway b	7	7.50×10^{13}
Pathway c_1	67	5.60×10^{13}
Pathway c_2	90	6.35×10^{11}
Pathway c_3	285	2.09×10^{14}
Pathway g	19	1.50×10^{16}
Pathway d	102	3.29×10^{10}
Pathway e	136	6.28×10^{14}

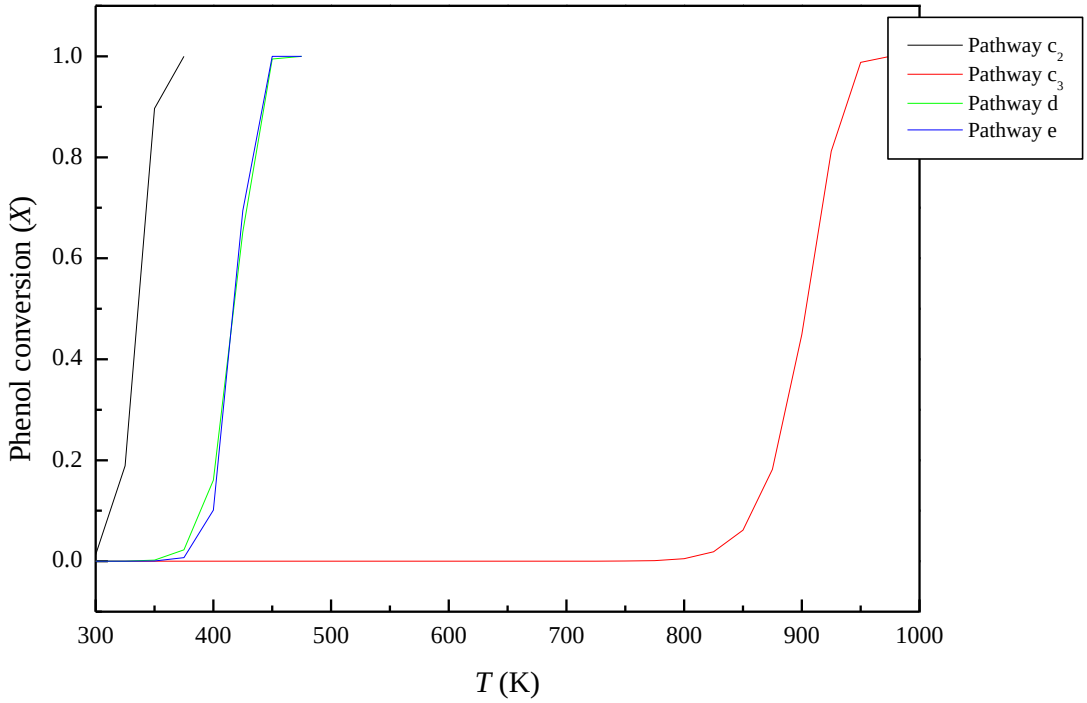

Figure 9.9. Conversion values for phenol molecule decomposition over Al_2O_3. nH_2O clusters.

9.4 Conclusion

This Chapter sets out to assess the effect of surface acidity on the interaction of alumina with phenol molecules. Interaction of phenol molecule with dehydrated alumina clusters proceeds via fission of the hydroxyl's bond over either Al-O single bond or Al=O double bond. Clusters with the active Al=O double bond (i.e., b) are catalytically more active in producing phenolate when compared structures where all bonds are saturated (i.e., a, Al-O single bonds). Overall hydrated clusters, channels that proceeds through fission of the hydroxyl's bond over Al-O (i.e,; c_1) are more favorable than that along H_2O elimination channels (i.e.; c_2 and c_3). The most obvious finding to emerge from this study is that adding water molecules increases the coordination number of Al atoms and acts to black available Lewis acid sites for uptake of

phenol molecules. Simplified kinetic calculations suggest dissociation of phenol molecules at low temperatures; however, subsequent desorption of adsorbed phenolate into gas phase phenoxy radicals is hindered by very sizable desorption energies.

9.5 References

1. Tanabe, K.; Anderson, J.; Boudart, M., *Catalysis Science and Technology*. by JR Anderson and M. Boudart, Springer-Verlag, New York: **1981**.

2. Boehm, H.-P.; Knözinger, H., *Nature and Estimation of Functional Groups on Solid Surfaces*. In Catalysis, Springer: **1983**.

3. Knözinger, H.; Ratnasamy, P., Catalytic aluminas: surface models and characterization of surface sites. *Cat. Rev. - Sci. Eng.* **1978**, *17*, 31-70.

4. Gitzen, W. H., *Alumina as A Ceramic Material*. **1970**.

5. French, R. H., Electronic band structure of Al_2O_3, with comparison to Alon and AlN. *J. Am. Ceram. Soc.* **1990**, *73*, 477-489.

6. Eng, P. J.; Trainor, T. P.; Brown Jr, G. E.; Waychunas, G. A.; Newville, M.; Sutton, S. R.; Rivers, M. L., Structure of the hydrated α-Al_2O_3 (0001) Surface. *Science* **2000**, *288*, 1029-1033.

7. Elam, J.; Nelson, C.; Cameron, M.; Tolbert, M.; George, S., Adsorption of H_2O on a single-crystal α-Al_2O_3 (0001) Surface. *J. Phys. Chem. B* **1998**, *102*, 7008-7015.

8. Hass, K.; Schneider, W.; Curioni, A.; Andreoni, W., First-principles molecular dynamics simulations of H_2O on α-Al_2O_3 (0001). *J. Phys. Chem. B* **2000**, *104*, 5527-5540.

9. Mason, S. E.; Iceman, C. R.; Trainor, T. P.; Chaka, A. M., Density functional theory study of clean, hydrated, and defective alumina (1102) surfaces. *Phys. Rev. B* **2010**, *81*, 125423-125439.

10. Argyris, D.; Ho, T.; Cole, D. R.; Striolo, A., Molecular dynamics studies of interfacial water at the alumina surface. *J. Phys. Chem. C* **2011**, *115*, 2038-2046.

11. Hass, K. C.; Schneider, W. F.; Curioni, A.; Andreoni, W., The chemistry of water on alumina surfaces: Reaction dynamics from first principles. *Science* **1998**, *282*, 265-268.

12. Thomas, A. C.; Richardson, H. H., Growth of thin film water on α-Al_2O_3 (0001): An ftir study. *J.Phys. Chem.C* **2008**, *112*, 20033-20037.

13. Zhang, L.; Tian, C.; Waychunas, G. A.; Shen, Y. R., Structures and charging of α-alumina (0001)/water interfaces studied by sum-frequency vibrational spectroscopy. *J. Am. Chem. Soc.* **2008**, *130*, 7686-7694.

14. Al-Abadleh, H. A.; Grassian, V., FT-IR study of water adsorption on aluminum oxide surfaces. *Langmuir* **2003**, *19*, 341-347.

15. Mawhinney, D. B.; Rossin, J. A.; Gerhart, K.; Yates, J. T., Adsorption and reaction of 2-chloroethylethyl sulfide with Al_2O_3 surfaces. *Langmuir* **1999**, *15*, 4789-4795.

16. Glemser, O.; Rieck, G., Die bindung des wassers in den durch thermische zersetzung von aluminiumhydroxyden entstandenen phasen. *Angew. Chem.* **1956**, *68*, 182-182.

17. Glemser, O., Ergebnisse und probleme von verbindungen der systeme oxyd-wasser. *Angew. Chem.* **1961**, *73*, 785-805.

18. Dyer, C.; Hendra, P. J.; Forsling, W.; Ranheimer, M., Surface hydration of aqueous γ-Al_2O_3 studied by fourier transform raman and infrared spectroscopy—I. Initial results. *Spectrochim. Acta Mol. Biomol.* **1993**, *49*, 691-705.

19. Liu, P.; Kendelewicz, T.; Brown, G. E.; Nelson, E. J.; Chambers, S. A., Reaction of water vapor with α-Al_2O_3 (0001) and α-Fe_2O_3 (0001) Surfaces: Synchrotron x-ray photoemission studies and thermodynamic calculations. *Surf. Sci.* **1998**, *417*, 53-65.

20. Peri, J. B.; Hannan, R. B., Surface hydroxyl groups on γ-alumina1. *J. Phys. Chem.* **1960**, *64*, 1526-1530.

21. Peri, J., A Model for the surface of γ-alumina1. *J. Phys. Chem.* **1965**, *69*, 220-230.

22. Pimentel, G. C.; McClellan, A. L., *The Hydrogen Bond.* **1960**.

23. Ballinger, T. H.; Yates, J., Interaction and catalytic decomposition of 1,1,1-trichloroethane on high surface area alumina. An infrared spectroscopic study. *J. Phys. Chem.***1992**, *96*, 1417-1423.

24. Zaki, M.; Knözinger, H., Carbon monoxide—a low temperature infrared probe for the characterization of hydroxyl group properties on metal oxide surfaces. *Mater. Chem. Phys*. **1987**, *17*, 201-215.

25. Eley, D. D.; Pines, H.; Weisz, P. B., *Advances in Catalysis*, Elsevier Science: **1966**.

26. Ballinger, T. H.; Yates Jr, J. T., IR spectroscopic detection of Lewis acid sites on alumina using adsorbed carbon monoxide. Correlation with aluminum-hydroxyl group removal. *Langmuir* **1991**, *7*, 3041-3045.

27. Hendriksen, B.; Pearce, D.; Rudham, R., Heats of adsorption of water on α-and γ-alumina. *J. Catal.* **1972**, *24*, 82-87.

28. McHale, J.; Navrotsky, A.; Perrotta, A., Effects of increased surface area and chemisorbed H_2O on the relative stability of nanocrystalline γ-Al_2O_3 and α-Al_2O_3. *J.Phys. Chem. B* **1997**, *101*, 603-613.

29. Lee, C.-K.; Cho, E.; Lee, H.-S.; Seol, K. S.; Han, S., Comparative study of electronic structures and dielectric properties of alumina polymorphs by first-principles methods. *Phys. Rev. B* **2007**, *76*, 245110.

30. Levin, I.; Brandon, D., Metastable alumina polymorphs: Crystal structures and transition sequences. *J. Am. Ceram. Soc.* **1998**, *81*, 1995-2012.

31. Wang, B.; Hou, H.; Luo, Y.; Li, Y.; Zhao, Y.; Li, X., Density functional/all-electron basis set slab model calculations of the adsorption/dissociation mechanisms of water on *α*-Al_2O_3 (0001) Surface. *J. Phys. Chem. C* **2011**, *115*, 13399-13411.

32. Wirth, J.; Saalfrank, P., The chemistry of water on *α*-alumina: kinetics and nuclear quantum effects from first principles. *J.Phys.Chem. C* **2012**, *116*, 26829-26840.

33. Shukla, M. K.; Hill, F., Computational investigation of adsorption of 2,4,6-trinitrotoluene on (0001) surface of (4× 4) *α*-alumina. *J.Phys.Chem. C* **2013**, *117*, 13136-13142.

34. Shukla, M. K.; Hill, F., Plane-wave density functional theory investigation of adsorption of 2, 4, 6-trinitrotoluene on Al-hydroxylated (0001) Surface of (4× 4) *α*-alumina. *J.comp. chem.* **2014**, *35*, 1977-1985.

35. Rohmann, C.; Metson, J.; Idriss, H., A DFT study on carbon monoxide adsorption onto hydroxylated *α*-Al_2O_3 (0001) Surfaces. *PCCP* **2014**, *16*, 14287-14297.

36. Ren, R.-P.; Liu, X.-W.; Zuo, Z.-J.; Lv, Y.-K., Theoretical investigation of H_2S removal on *γ*-Al_2O_3 surfaces of different hydroxyl coverage. *RSC Adv.* **2015**, *5*, 55372-55382.

37. Kelber, J.; Niu, C.; Shepherd, K.; Jennison, D.; Bogicevic, A., Copper wetting of *α*-Al_2O_3(0001): Theory and experiment. *Surf. sci.* **2000**, *446*, 76-88.

38. Chakarova-Käck, S. D.; Borck, Ø.; Schröder, E.; Lundqvist, B. I., Adsorption of phenol on graphite (0001) and *α*−Al_2O_3 (0001): Nature of van der waals bonds from first-principles calculations. *Phys. Rev. B* **2006**, *74*, 155402-155409.

39. Fernández, E.; Eglitis, R.; Borstel, G.; Balbás, L., Ab initio calculations of H_2O and O_2 adsorption on Al_2O_3 substrates. *Comput. Mater. Sci.* **2007**, *39*, 587-592.

40. Zdetsis, A. D.; Kunz, A. B., Ab initio cluster study of Ni adsorption on alumina. *Phys.l Rev. B* **1985**, *32*, 6358-6362.

41. Wittbrodt, J.; Hase, W.; Schlegel, H., Ab initio study of the interaction of water with cluster models of the aluminum terminated (0001) *α*-aluminum oxide surface. *J. Phys. Chem. B* **1998**, *102*, 6539-6548.

42. Biswas, S.; Pramanik, A.; Sarkar, P., Computational studies on the reactivity of alkyl halides over $(Al2O3)_N$ nanoclusters: An approach towards room temperature dehydrohalogenation. *Nanoscale* **2016**, *8*, 10205-10218.

43. Altarawneh, M.; Dlugogorski, B. Z., Formation and chlorination of carbazole, phenoxazine, and phenazine. *Environ. Sci. Technol.* **2015**, *49*, 2215-2221.

44. Altarawneh, M.; Radny, M. W.; Smith, P. V.; Mackie, J. C.; Kennedy, E. M.; Dlugogorski, B. Z.; Soon, A.; Stampfl, C., A first-principles density functional study of chlorophenol adsorption on Cu_2O(110):Cuo. *J. chem. Phys.* **2009**, *130*, 184505.

45. Altarawneh, M.; Dlugogorski, B. Z., Formation of dibenzofuran, dibenzo-*p*-dioxin and their hydroxylated derivatives from catechol. *PCCP* **2015**, *17*, 1822-1830.

46. Qian, Y.; Zheng, M.; Liu, W.; Ma, X.; Zhang, B., Influence of metal oxides on PDCDD/Fs formation from pentachlorophenol. *Chemosphere* **2005**, *60*, 951-958.

47. Patterson, M. C.; Keilbart, N. D.; Kiruri, L. W.; Thibodeaux, C. A.; Lomnicki, S.; Kurtz, R. L.; Poliakoff, E.; Dellinger, B.; Sprunger, P. T., EPFR formation from phenol adsorption on Al_2O_3 and TiO_2: EPR and EELS studies. *J. Chem. Phys.* **2013**, *422*, 277-282.

48. Lomnicki, S.; Dellinger, B., A detailed mechanism of the surface-mediated formation of PCDD/F from the oxidation of 2-chlorophenol on a CuO/silica surface. *J. Phys. Chem. A* **2003**, *107*, 4387-4395.

49. Lomnicki, S.; Dellinger, B., Formation of PCDD/F from the pyrolysis of 2-chlorophenol on the surface of dispersed copper oxide particles. *Proc. Comb. Inst.* **2002**, *29*, 2463-2468.

50. Nganai, S.; Lomnicki, S.; Dellinger, B., Ferric oxide mediated formation of PCDD/Fs from 2-monochlorophenol. *Environ. Sci. Technol.* **2008**, *43*, 368-373.

51. Assaf, N. W.; Altarawneh, M.; Oluwoye, I.; Radny, M.; Lomnicki, S. M.; Dlugogorski, B. Z., Formation of environmentally persistent rree radicals on α-Al_2O_3. *Environ. Sci. Technol.* **2016**, *50*, 11094-11102.

52. Dellinger, B.; Lomnicki, S.; Khachatryan, L.; Maskos, Z.; Hall, R. W.; Adounkpe, J.; McFerrin, C.; Truong, H., Formation and stabilization of persistent free radicals. *Proc. Comb. Inst.* **2007**, *31*, 521-528.

53. Patterson, M. C.; Thibodeaux, C. A.; Kizilkaya, O.; Kurtz, R. L.; Poliakoff, E.; Sprunger, P. T., Electronic signatures of a model pollutant–particle system: Chemisorbed phenol on TiO_2 (110). *Langmuir* **2015**, *31*, 3869-3875.

54. Delley, B., An all-electron numerical method for solving the local density functional for polyatomic molecules. *J. Chem. Phys.* **1990**, *92*, 508-517.

55. Delley, B., From molecules to solids with the $DMol^3$ approach. *J. Chem. Phys.* **2000**, *113*, 7756-7764.

56. Perdew, J. P.; Burke, K.; Ernzerhof, M., Generalized gradient approximation made simple. *Phys. Rev. Lett.* **1996**, *77*, 3865.

57. Grimme, S., Semiempirical GGA-type density functional constructed with a long-range dispersion correction. *J. Comput. Chem.* **2006**, *27*, 1787-1799.

58. Laidler, K. J.; King, M. C., Development of transition-state theory. *J. Phy. Chem.* **1983**, *87*, 2657-2664.

59. Fowler, R. H.; Guggenheim, E. A., *Statistical Thermodynamics*. **1941**.

60. Johnson, J. T.; Panas, I., Water adsorption and hydrolysis on molecular Al Oxides and hydroxides—solvation versus cluster formation. *PCCP* **2001**, *3*, 5482-5488.

61. Li, R.; Cheng, L., Structural determination of $(Al_2O_3)_n$ (n= 1–7) clusters cased on density functional calculation. *Comput. Theor. Chem.* **2012**, *996*, 125-131.

62. Manassidis, I.; Gillan, M. J., Structure and energetics of alumina surfaces calculated from first principles. *J. Am. Ceram. Soc.* **1994**, *77*, 335-338.

63. Gautier-Soyer, M.; Jollet, F.; Noguera, C., Influence of surface relaxation on the electronic states of the α-Al_2O_3 (0001) surface: A self-consistent tight-binding approach. *Surf. Sci.* **1996**, *352*, 755-759.

64. Woodley, S. M., Atomistic and electronic structure of $(X_2O_3)_n$ nanoclusters; n= 1–5, X= B, Al, Ga, in and Tl, *A Proc. R. Soc. A* **2011**, *467*, 2020-2042.

65. Pan, W.; Zhong, W.; Zhang, D.; Liu, C., Theoretical study of the reactions of 2-chlorophenol over the dehydrated and hydroxylated silica clusters. *J. Phys. Chem. A* **2011**, *116*, 430-436.

66. Cavallotti, R. m.; Goniakowski, J.; Lazzari, R. m.; Jupille, J.; Koltsov, A.; Loison, D., Role of surface hydroxyl groups on zinc adsorption characteristics on α-Al_2O_3 (0001) surfaces: First-principles study. *J. Phys.Chem. C* **2014**, *118*, 13578-13589.

67. Yoshida, S., *Quantum-Chemical Studies of the Acidity and Basicity of Alumina.* In Theoretical Aspects of Heterogeneous Catalysis, Springer: **1990**.

68. Digne, M.; Sautet, P.; Raybaud, P.; Euzen, P.; Toulhoat, H., Use of DFT to achieve a rational understanding of acid–basic properties of γ-alumina surfaces. *J. Catal.* **2004**, *226*, 54-68.

69. Mosallanejad, S.; Dlugogorski, B. Z.; Kennedy, E. M.; Stockenhuber, M.; Lomnicki, S. M.; Assaf, N. W.; Altarawneh, M., Formation of PCDD/Fs in oxidation of 2-chlorophenol on neat silica surface. *Environ. Sci. Technol.* **2016**, *50*, 1412-1418.

70. POLYMATH is copyrighted by Shacham, M. C., M. B.; Elly, M. P. h. w. p.-s. c., accessed; Feb 23.

CHAPTER10

Conclusions and Recommendations for Future work

10.1 Conclusions

The thesis set out to advance our understanding of an atomic-based understanding of reactive and non-reactive surfaces. First, we focused on diboron trioxide, B_2O_3, as an important oxidation inhibitor that assumes critical importance in many chemical and coating applications. Then, we turned our attention to the elucidation of the reactivity of alumina, Al_2O_3, as a prominent environmental catalyst. In particular, we tested the catalytic reactivity of various configurations of α-$A_{l2}O_3$ (hydrated and hydrated surfaces, Si-doped termination, and clusters) in mediating the formation of phenoxy-type EPFR.

The introductory chapters **(Chapters 1-3)** introduced general portrayal molecular modelling as an insightful tool to study solid-gas interaction. This was followed by a brief description of the thesis outlines, including an overview of each chapter (**Chapter 1**). A comprehensive and rigorous literature account was presented in **Chapter 2**. The methodology employed within the scope of this thesis was briefly introduced in **Chapter 3**. The attained results were presented, analysed, and discussed in **Chapters 4-9**.

Comprehensive accurate quantum-mechanical calculations, which afforded the investigation into diboron trioxide with the underlying objective of evaluating its unreactive functionality, were presented in **Chapters 4-6**. **Chapter 4** provided a theoretical understanding of the conversion of elemental boron into B_2O_3 via dissociative adsorption of oxygen molecules. The structure, stability, and nonreactivity of four low-index surfaces of the low pressure phase of B_2O_3 were presented in **Chapter 5**, confirming the low reactivity of this compound. **Chapter 6** provided a detailed understanding of the inhibition characteristic of diboron trioxide, particularly in the H_2S oxidation system. For instance, the H_2S molecularly was adsorbed on

the B_2O_3 -I (101) surface through the formation of sp^3 hybridisation. Desorption of this molecule required an activation barrier of 27.1 kJ/mol, which explains how the B_2O_3 coating inhibits the oxidation process. Furthermore, the B_2O_3 surface exhibited an insulating behaviour of the dissociation of the hydrogen sulphide. **Chapter 6** confirmed the hygroscopic behaviour of diboron trioxide, aided by both experimental diffuse reflectance infrared spectroscopy, and the quantum chemical calculations elucidating the corresponding enthalpic requirements for fission of the H-O bond during adsorption of water molecules on the B_2O_3–I (101) surface.

Chapters 7-9 presented detailed theoretical investigations into the role of alumina-based models in surface-mediating the formation of EPFR persistent free radical formation, a situation that is typically encountered during the interaction of aromatic compounds with generated particulate matter PM_{12} in combustion. We considered different models of alumina, encompassing: dehydrated alumina surface, fully hydrated alumina surface, clusters with different hydration coverages, and silicon-alumina doped surface. **Chapter 7** further characterised the catalytic potential of the neat α-Al_2O_3(0001) surface in producing phenolic-type EPFR, under conditions pertinent to the cooling zones of the combustion system. We found that surface-assisted rupture of the phenol's O-H bond over a dehydrated alumina surface required only 48 kJ/mol to proceed with manifestation of the facile nature of producing adsorbed phenolate. **Chapter 8** uncovered new insights into structural factors that affect the catalytic activity of alumina, either adversely or positively under certain operational conditions Most importantly, we found that the presence of the hydration layer over α-Al_2O_3(0001) decreased the catalytic activity of the surface towards the formation of the phenoxy moity, in which the calculated energy barrier for fission of the O-H bond in phenol was approximately four times higher than the dehydrated surface. A substituted Si-alumina surface was shown to have lower energy requirements in terms of the formation of adsorbed phenolate adducts.

Furthermore, the relevance of the acidity sites to the catalytic activity of alumina was clearly supported by the finding that the catalytic activity of alumina surface in producing the phenoxy/phenolate species reversibly correlated with the degree of hydroxyl coverage (**Chapter 9)**.

10.2 Recommendation for Future Work

In light of the findings of the thesis, the following suggestions are made for future related work:

1. In Chapter 4, we limited our analysis to one elemental boron surface; thus, it is interesting to assess the effect of surface boron termination on the likely reduction in the energy barrier for fission of the O-O bond by considering other phases of elemental boron. The most stable form of elemental boron has been a matter of a sweeping discussion. Obtaining phonon dispersions (i.e. vibrational frequencies) for the various phases of elemental boron will enable the construction of a *T-P* thermodynamic stability diagram. Such a diagram unequivocally determines that the most stable boron form is any combination of *T* and *P*.

2. An implication of our results in Chapter 5 is that none of the investigated low-index surfaces had dangling bonds. This likely correlates with the experimentally observed low surface reactivity of B_2O_3–I, except for the Lewis acid behaviour made possible by the empty p orbital in the three-fold coordinated B atoms. Surface terminations free from dangling bonds occur in other solids with mixed ionic–covalent bond characters

and flexible structural subunits, such as silica (SiO_2).[1] Notably, surfaces of these compounds can undergo hydroxylation to varying degrees under normal operational conditions[2]; therefore, future computational investigations of the hydroxylation of B_2O_3–I surfaces represent a promising direction in which to further improve our understanding of their chemical and physical properties.

3 A point of interest relates to the other forms of B_2O_3 found in nature. Tetrahedral BO_4 units are the only building blocks of the high-pressure crystalline polymorph B_2O_3–II; besides, they are found in increasingly large fractions in the amorphous phase *v*-B_2O_3 at high pressures.[3] The occurrence of BO_4 units on some low-index surfaces of the low-pressure B_2O_3–I polymorph provides a basis for the investigation of potentially relevant parallels in the structural and chemical properties of these forms. In particular, if the structurally complex amorphous phase has the widest technological applications, the simple structure of B_2O_3–I makes it an excellent candidate as a structural model for future computational studies on its surface properties.

4 Future research is required to address the formation of other types of EPFR (such as phenyl and ortho/para dihydroxylbenzneses), the differences between α-Al_2O_3 and other alumina configurations, and the effects of surface defects on the interaction of alumina with organic precursors for EPFR. An inspection of Chapter 7 reveals that, even when the dissociated phenolate and H moieties are significantly separated, the O-H bond surface-mediated fission is still a highly feasible process (DH_1 versus DH_2). This infers that the key to the O-H bond dissociation is the presence of surface Al and O atoms. On this basis, we envisage that all alumina surfaces with Al/O mixed termination can effectively catalyse the formation of the adsorbed phenolate.

Nonetheless, the presence of Al^{+3} vacancies in surfaces of γ-Al_2O_3 (a cubic spinal structure with ABC oxygen staking) may open up additional pathways. For example, placement of the OH group over these vacancies may facilitate C-OH bond rupture, producing phenyl-like radicals. Clearly, the interaction of phenol with γ-Al_2O_3 surfaces warrants further investigation.

5 In Chapter 8, we demonstrated that atomic doping assumes a critical importance in altering in the catalytic activity of alumina surface (in reference to neat surfaces). In addition to Si-doped alumina surface, other atomic substitutions systems could be investigated; candidates include the trace metallic content dispersed on PM encompassing Fe, Cd, and Zn.

6 Further studies need to be carried out to examine the mechanistic and energy requirements for the formation of EPFR on other transition metal oxides, such asFe_2O_3, Si_2O_3, and CuO. It is important that such studies address not only the well-structured terminations of these metal oxides, but also analogous configurations with structural defects, atomic substituents, and varying hydroxyl coverages.

7 Over the last ten years, our group has been working to map the reaction pathways operating in the homogenous and heterogeneous formation of PCDD/Fs.[4-5] While the homogenous pathway is believed to contribute only 30%, it has received more mechanistic attention than the dominant surface-assisted corridor. Appendix III summarises our current progress in constructing mechanisms for the formation of the PCDD/Fs main skeleton, i.e. dibenzo-*p*-dioxin (DD) and dibenzofuran (DF) on ZnO, CuO, SiO_2, and B_2O_3 surfaces. However, the reaction barriers obtained for prominent

steps (ring-closure; HCl elimination) still reflect to a large extent the corresponding gas phase steps. Thus, we envisage the surface-assisted reaction steps to be fundamentally different from the well-established gas phase reaction pathways. Thus, future efforts could focus on the survey and exploration of additional pathways in the pursuit to locate reaction corridors that demand substantially lower energy barriers than the equivalent gas phase steps.

10.3 References

1. Tosoni, S.; Civalleri, B.; Ugliengo, P., Hydrophobic behavior of dehydroxylated silica surfaces: A B3LYP periodic study. *J. Phys. Chem. C* **2010**, *114*, 19984-19992.

2. Rimola, A.; Costa, D.; Sodupe, M.; Lambert, J.-F.; Ugliengo, P., Silica surface features and their role in the adsorption of biomolecules: Computational modeling and experiments. *Chem. Rev.* **2013**, *113*, 4216-4313.

3. Brazhkin, V. V.; Katayama, Y.; Trachenko, K.; Tsiok, O. B.; Lyapin, A. G.; Artacho, E.; Dove, M.; Ferlat, G.; Inamura, Y.; Saitoh, H., Nature of the structural transformations in B_2O_3 glass under high pressure. *Phys. Rev. Lett.* **2008**, *101*, 035702.

4. Altarawneh, M.; Dlugogorski, B. Z.; Kennedy, E. M.; Mackie, J. C., Mechanisms for formation, chlorination, dechlorination and destruction of polychlorinated dibenzo-*p*-dioxins and dibenzofurans (PCDD/Fs). *Prog. Energy Combust. Sci.* **2009**, *35*, 245-274.

5. Altarawneh, M., Formation of Dibenzofuran, dibenzo-*p*-dioxin and their hydroxylated derivatives from Catechol. *Phys. Chem. Chem. Phys.: PCCP* **2015**, *17*, 1822-1830.

Statement of Contribution

Journal Publications

1. Assaf, N. W.; Altarawneh, M. K.; Radny, M.W.; Jiang, Z. T.; Dlugogorski, B. Z.; Interaction of oxygen with α-rhombohedral boron (001) surface, *J. Phys. Chem. C,* 120 (2016) 5968-5979.

Author's Name	**Contribution**	**Overall Percentage (%)**	**Signature**
Niveen W Assaf	1- Investigate geometric and electronic properties of bulk α-boron(B12) 2- Investigate geometric and electronic properties of clean α(001)B12 surface 3- Investigate geometric and energetic properties for on-surface and substitutional adsorption of atomic oxygen on the α(001)B12 surface 4- Assess the thermodynamic feasibility of the formation of bulk-like B_2O_3 structure via substitutional adsorption of oxygen atoms on the clean α(001)B12 surface 5- Prepare the manuscript 6- Revise the manuscript according to supervisors and co-authors comments	70	
Mohammednoor K Altarawneh	Data analysis and manuscript preparation	30	
Marian W Radny	Data analysis and manuscript preparation		
Zhong-Tao Jiang	Proof reading		
Bogdan Z Dlugogorski	Data analysis and manuscript preparation		

2. Assaf, N. W.; La Pierre, M. De; Altarawneh, M. K.; Radny, M. W.; Jiang, Z. T.; Dlugogorski, B. Z.; Structure, stability, and (non) reactivity of the low-index surfaces of crystalline B_2O_3–I, *J. Phys. Chem. C*, 121 (2017) 11346–11354.

Author's Name	**Contribution**	**Overall Percentage (%)**	**Signature**
Niveen W Assaf	1- Investigate geometric and electronic properties of bulk B_2O_3-I 2- Investigate the structural, electronic and energetic properties of four low-index surfaces of crystalline B_2O_3-I: (001), (011), (100) and (101). 3- Prepare the manuscript 4- Revise the manuscript according to supervisors and co-authors comments	70	
Marco De La Pierre	Quantum calculations, manuscript preparation and Data analysis	30	
Mohammednoor K Altarawneh	Data analysis and manuscript preparation		
Marian W Radny	Data analysis and manuscript preparation		
Zhong-Tao Jiang	Proof reading		
Bogdan Z Dlugogorski	Data analysis and manuscript preparation		

3. Assaf, N. W.; Altarawneh, M.; Oluwoye, I.; Radny, M.; Lomnicki, S. M.; Dlugogorski, B. Z.; Formation of environmentally persistent free radicals on α-Al_2O_3, *Environ. Sci. Technol.*, 50 (2016) 11094-11102.

Author's Name	**Contribution**	**Overall Percentage (%)**	**Signature**
Niveen W Assaf	1- Investigate geometric and electronic properties of bulk α-Al_2O_3 2- Investigate geometric and electronic properties of clean α-Al_2O_3(0001) 3- Investigate the molecular adsorption of phenol on the α-Al_2O_3(0001) surface 4- Explore the catalytic role of dehydroxylated α-Al_2O_3(0001) in surface-mediated formation of phenoxy-type EPFR 5- Prepare the manuscript 6- Revise the manuscript according to supervisors and co-authors comments	70	
Mohammednoor Altarawneh	Data analysis and manuscript preparation	30	
Ibukun Oluwoye	Proof reading		
Marian W Radny	Data analysis and manuscript preparation		
Slawomir M Lomnicki,	Proof reading		
Bogdan Z Dlugogorski	Data analysis and manuscript preparation		

4. Assaf, N. W.; Altarawneh, M.; Radny, M.; Al-Nu'airat, J.; Dlugogorski, B. Z.; Formation of environmentally-persistent free radicals (EPFR) on α-Al_2O_3 clusters, *RSC Adv*. 7 (2017) 52672-526683.

Author's Name	**Contribution**	**Overall Percentage (%)**	**Signature**
Niveen W Assaf	1- Investigate modes of interaction of phenol with different hydration coverages of alumina clusters. 2- Assess the effect of surface acidity on the interaction of alumina with phenol molecules 3- Compare between the catalytic activity of hydrated and dehydrated alumina clusters toward the formation of the adsorbed phenolate via two distinct pathways; namely direct fission of the phenol' O-H bond and elimination of water molecules 4- Construct a simplified kinetic model for the conversion of phenol into adsorbed phenoxy radicals. 5- Prepare the manuscript 6- Revise the manuscript according to supervisors and co-authors comments	70	
Mohammednoor K Altarawneh	Data analysis and manuscript preparation	30	
Marian W Radny	Data analysis and manuscript preparation		
Jomana Al-Nu'airat	Proof reading		

Bogdan Z Dlugogorski	Data analysis and manuscript preparation		